Vitamins vs. Antivitamins: Unmasking the Metabolism of Vitamin B_6 by Positron Emission Tomography for Detection of Lung Cancer

Aidan Torrens

Thesis submitted to the University of Ottawa in partial fulfillment of the requirements for the Masters of Science in Chemistry degree

Department of Chemistry and Biomolecular Science
Faculty of Science
University of Ottawa

Supervisor: Adam J. Shuhendler, PhD
Examining Board: Christopher N. Boddy, PhD, Chemistry and Biomolecular Sciences
Jeffrey W. Keillor, PhD, Chemistry and Biomolecular Sciences

Abstract

Drug resistance is a major challenge leading to low survival amongst diseases like lung cancer, the most diagnosed cancer in Canadians. Cisplatin is the current standard of care, but resistance is common after 4-6 months. A strong association between treatment outcomes and the metabolism of Vitamin B_6, or Pyridoxine (PN), has been found, where the active form of PN is associated with effective chemotherapy, while the inactive metabolite is associated with resistance. Previous work using contrast agents by MRI have begun addressing this need, but clinical relevance is limited due to motion of the lungs and perturbance of metabolic processes. Herein we focused on developing a non-invasive way to detect the onset of cancer resistance from Cisplatin-based chemotherapy using Positron Emission Tomography (PET). Towards this goal, three cold analogues of PN were prepared, with successful fluorine and carbon substitutions. Metabolomic analysis found interaction with pyridoxal kinase, phosphatase, and oxidase enzymes, showing cell transport and metabolic transformations were maintained. This was followed by radiolabelling efforts, where fluorination was unsuccessful due to low [^{18}F]HF concentrations. However, carbon radiolabelling showed apparent product formation, with work currently being done to optimize reaction conditions, purification, and characterization. With optimized radiotracers in-hand, future work will focus on differentiating chemotherapy responsive and resistant lung cancer by PET imaging in animal model tumour tissue. PET imaging is performed routinely in clinic, and the rapid translation of radiotracers to clinical use (18 months) suits the need for rapid response to this clinical challenge, improving patient treatment outcomes.

Acknowledgements

I would first like to thank the Natural Science and Engineering Research Council of Canada (NSERC), the Canadian Institutes for Health Research (CIHR), and the Ontario Graduate Scholarship (OGS) program for financial support for this work.

There are many people, without whom, this work would not have been possible. I would like to highlight several individuals. First, Dr. Adam Shuhendler, who I have had the pleasure to work with over the last two years. Thank you for the privilege to work in the Molecular Medicine Lab, which provided irreplaceable and boundless opportunities. I greatly appreciate that you kept me busy, allowed me to explore work on multiple projects, and encouraged learning through multiple conferences. I value your mentorship throughout my time here, and for your battles against radiochemistry we endured.

Dr. Nick Calvert, who encouraged me to move all the way to Ottawa, supported me as my cousin, but also as a role model. You provided me with opportunities to work alongside you and made the experience of living in Ottawa all the better.

My family and friends, namely my parents, brother, and friend Cameron, for helping me at my highs and lows, and providing external support from afar.

Rochelle D'mello, who supports me and celebrates with me in all stages of my life, even in this chapter in Ottawa.

My lab mates, especially Emilie, Dominic, and Lauren, who welcomed me into the lab and put up with my shenanigans and kept me fed (not an easy task).

Finally, I would like to thank the various members of Marion Floor 2, especially André, Mike, and Eric. It has been a pleasure to get to know you all, and your friendships, advice, and contributions helped me grow as a person and scientist.

Table of Contents

List of Figures

List of Tables

List of Abbreviations

[^{11}C]	Carbon-11
[^{18}F]	Fluorine-18
ATM	Ataxia Telangiectasia Mutated
ATP	Adenosine Triphosphate
CDDP	Cisplatin (cis-diamminedichloroplatinum II)
CEST-MRI	Chemical Exchange Saturation Transfer Magnetic Resonance Imaging
CNAIN	Committee on Nomenclature of the American Institute of Nutrition
CT	Computed Tomography
DMP	Dess-Martin Periodinane
DIBAL-H	Diisobutylaluminum Hydride
DMEM	Dulbecco's Modified Eagle Medium
DMSO	Dimethyl Sulfoxide
DMF	Dimethylformamide
EAS	Electrophilic Aromatic Subsitutions
ESI	Electrospray Ionization
FDG	[^{18}F]2-Fluorodeoxyglucose
FBS	Fetal Bovine Serum
FMN	Flavin Mononucleotide
GSH	Non-Oxidized Glutathione
HCl	Hydrochloric Acid
HPLC	High-Performance Liquid Chromatography
HRMS	High-resolution Mass Spectrometry
KOH	Potassium Hydroxide
LC	Liquid Chromatography
LC-MS	Liquid-Chromatography Mass Spectrometry
$LiAlH_4$	Lithium Aluminum Hydride
$LiBH_4$	Lithium Borohydride
LUMO	Lowest Unoccupied Molecular Orbital
MeI	Methyl Iodide
MeOTf	Methyl Triflate
m-CPBA	*meta*-Chloroperoxybenzoic Acid
mCi	Millicuries
MPN	4'-*O*-Methyl Pyridoxine, Ginkgotoxin
MS	Mass Spectrometry
MS/MS	Tandem Mass Spectrometry
NAC	N-Acetylcysteine
NBS	N-bromosuccinimide
NMR	Nuclear Magnetic Spectroscopy
NSCLC	Non-small cell lung cancer
PA	4-Pyridoxic Acid
PET	Positron Emission Tomography
PDXK	Pyridoxal Kinase
PDXP	Pyridoxal Phosphatase
PL	Pyridoxal

PLP	Pyridoxal 5'-Phosphate
PN	Pyridoxine
PNP	Pyridoxine 5'-Phosphate
PNPO	Pyridoxine 5'-Phosphate Oxidase
PM	Pyridoxamine
PMB	*para*-Methoxy Benzyl
PMB-Cl	*para*-Methoxybenzyl Chloride
PNPO	Pyridoxine 5'-Phosphate Oxidase
ROS	Reactive Oxygen Species
SCLC	Small-cell lung cancer
siRNA	Small Interfering RNA
S_NAr	Nucleophilic Aromatic Substitution
SPIAd	Spirocyclic Iodonium Ylides
TBAF	Tetrabutyl Ammonium Fluoride
TEA	Triethylamine
TFA	Trifluoroacetic Acid
TFAA	Trifluoroacetic Anhydride
THF	Tetrahydrofuran
uCi	Microcuries
UV	Ultraviolet
VDAC1	Voltage-dependent anion channel 1
UOHI	University of Ottawa Heart Institute

Chapter 1 – Introduction and Literature Review

1.1 Lung Cancer and Treatment in Canada

Lung cancer continues to be one of the most diagnosed cancers in Canadian men and women, accounting for approximately 24% of all cancer deaths as of 2023.[1] Non-small cell lung cancer (NSCLC) represents 87% of lung cancer cases,[2] while small-cell lung cancer (SCLC) is representative of smoking related cases.[3] Most NSCLC patients tend to be diagnosed with later-stages of the disease, and the prognosis involves a 5-year survival rate of only 17.4%, which is significantly lower than many other cancers.[4]

In both neo-adjuvant (before therapy) and adjuvant (after surgery) chemotherapy, platinum based drugs like cisplatin (cis-diamminedichloroplatinum (II) (CDDP) are the standard of care (Figure 1A).[5] Combination drugs are often employed such as paclitaxel and gemcitabin, which act synergistically by assisting in the interference of DNA synthesis and cell division.[6,7] CDDP transport into cancer cells is mediated by copper transporters, and upon cell entry, CDDP is hydrolyzed to a potent electrophile that reacts with sulfhydryl groups of proteins and N_7 reactive centres of purine residues of DNA (Figure 1B). This results in platinum complexes forming intra- and inter-strand DNA adducts that block cell division, specifically at the G2/M checkpoint, and facilitate cell death mediated by DNA damage that causes senescence and mitochondrial apoptosis.[89] CDDP can also engage poorly characterized cytoplasmic pathways that promote apoptotic or necrotic cell death by overproducing reactive oxygen species (ROS).[9] In some instances, activation of pro-apoptotic proteins, like BCL-2 members BAX, BAK, voltage-dependant anion channel 1 (VDAC1), and cytoplasmic p53 also mediate cell death (Figure 2).[9–12]

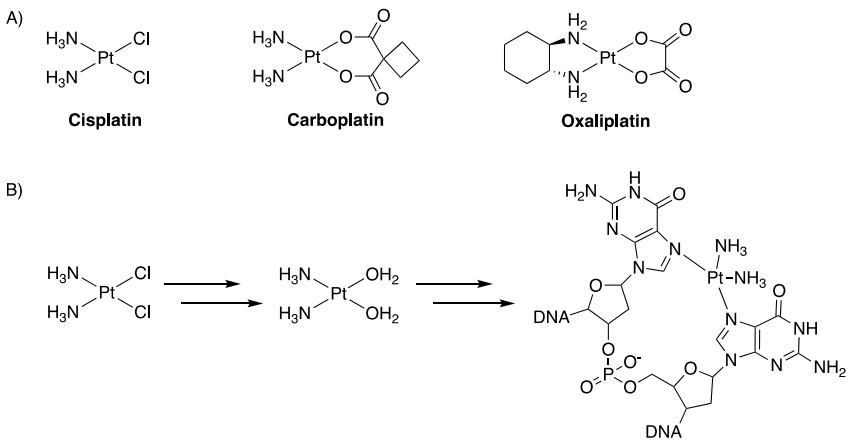

Figure 1. Clinically approved platinum-based anti-cancer drugs. A) Cisplatin (first-generation treatment), as well as carboplatin and oxaliplatin (second-generation treatments). B) Platinum based agents work by hydrolysis to potent electrophiles, reacting with N_7 reactive centres of purine residues of DNA, or sulfhydryl groups, causing DNA strand cross-links.

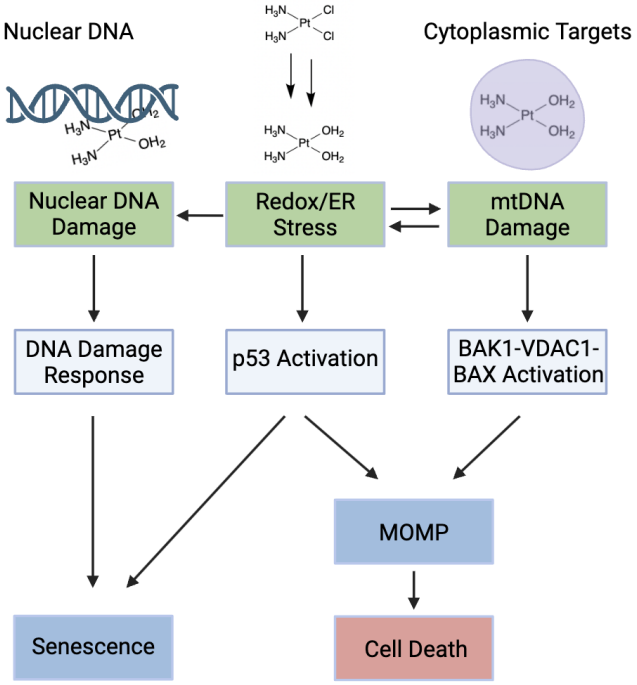

Figure 2. Cisplatin downstream mode of action as a chemotherapeutic. As a result of reduced cytoplasmic concentration of chloride ions, intracellular cisplatin (CDDP) is rapidly 'aquated', generating potent electrophiles. CDDP then cross-links nuclear DNA, as well as cytoplasmic targets like mitochondrial DNA (mtDNA) and proteins. These interactions induce oxidative and reticular stress; eliciting a signal transduction cascade that includes the pro-apoptotic BCL-2 family members BAK1 and BAX, as well as voltage-dependent anion channel 1 (VDAC1) and activates the cytoplasmic pool of p53. Asterisks tag the primary consequences of CDDP reactivity. ER, endoplasmic reticulum; MOMP, mitochondrial outer membrane permeabilization. Figure made using BioRender.

CDDP-based treatments suffer from major complications, with significant off-target effects including peripheral neurotoxicity, ototoxicity, myelosuppression, and nephrotoxicity due to its primarily kidney based excretion.[13] Resultingly, second generation complexes carboplatin and oxaliplatin were developed (Figure 1A), which result in fewer significant side effects, and have been shown to exhibit efficacy in CDDP-resistant lung cancer.[3] The success of platinum based complexes has also advanced development in drugs derived from other metals including ruthenium (NAMI-A, KP1019), which have entered clinical trials and show antitumoral effects and less off-target activity.[14] Despite the known side effects, and the presence of other treatment options, CDDP still remains the first-line treatment option for lung cancer.

Drug resistance remains one of the biggest challenges in cancer chemotherapy,[2] and is the leading cause of the low survival rates of lung cancers.[2] CDDP treatment suffers predominantly from this principal factor limiting treatment efficacy.[15] Drug resistance in chemotherapy is quite similar to infectious disease, where although early developments proved quite effective, tumour remissions are now more common due to the development of resistance. Combination chemotherapy has thus become a paradigm to cancer therapy,[16] necessitating more complex and toxic treatments with increasing dosage intensity.[17,18]

Devastatingly, many patients suffering from lung cancer acquire CDDP resistance that limits treatment efficacy. Acquired resistance mechanisms in CDDP treated patients have been tied to decreased cytoplasmic accumulation, cytoplasmic sequestration, and enhanced DNA repair.[16] Malignant cells exposed to CDDP are known to activate a multipronged adaptive response that renders them less susceptible to cytotoxic and

antiproliferative effects.[12] CDDP resistance can occur *via* pre-target, on-target, post-target, and off-target resistances, and is often a combination of non-overlapping molecular mechanisms.[19–21] Currently in clinic, CDDP resistance is only detected after 4-6 cycles of therapy (i.e. 4 to 6 months) at the earliest.[22] This delay results in futile therapy with unnecessary toxicity, and a significant period of time for tumour reprogression under selective pressure encouraging CDDP resistance. As a result, not only are therapeutic strategies in need of change, but so are diagnostic measures for earlier identification of resistance onset, better guiding treatment changes.

1.2 Vitamins and their role in Human Health

Vitamins are a group of complex functionalized compounds, present in minute quantities typically in foodstuffs, which are critical to normal metabolic and functional processes in human health.[23,24] Vitamins and minerals and their necessity for human health was demonstrated more than 100 years ago, and recommendation guides have been thoroughly produced to illustrate necessary dietary intake to ensure sufficient population health.[25] Absence of these nutrients is associated with various different disorders, where reintroduction of vitamins can counteract these symptoms, usually in the form of food or dietary supplements. Clinical deficiencies in developed countries is now quite uncommon, but insufficiencies are seen worldwide with variations depending on age and country.[25,26] While metabolic needs remain more consistent, dietary needs are more variable among individuals. In most instances, a varied and balanced diet, rich in nutrient-dense foods is sufficient for maintaining adequate levels. However, some vitamins such as vitamin D (synthesized by ultraviolet (UV) radiation), niacin (synthesized from

tryptophan), and vitamin C are produced by humans, and therefore food intake is not the only factor determining bioavailability.[24]

Traditionally, vitamins are divided into two main groups based on solubility, being fat soluble or water soluble.[24] Fat soluble vitamins include A, D, E and K, while B-complex and C-complex vitamins are water soluble. Alterations in fat absorption have impacts on fat-soluble vitamin uptake,[24] while water soluble vitamins are unaffected. As a result of their solubilities, water soluble vitamins like B-vitamins are not as well stored in the body, and are more rapidly excreted. A more continual supply is often necessary to maintain adequate levels, and excess levels are less likely to cause toxic effects.

When originally discovered, the composition of vitamins were unknown, and Casimir Funk, a pioneer in vitamin research coined the term “vitamine”,[27] with an alphabetized system being used to identify them by functional class.[24] As more variations in chemical structure were found, suffixes were adopted within each class (eg. vitamin B_6 and vitamin B_9). The final classification system was established by the Committee on Nomenclature of the American Institute of Nutrition (CNAIN), and is the standard system by which vitamins are referred to in literature and common dialogue.

The history for vitamins is quite storied, with countless review articles by pioneers like Casimir Funk (1922),[27] Scott et al. (1982),[28] and many more. Although the existence of these compounds was not recognized until the twentieth century, the existence of vitamin deficiency type disease had already become common-place, including scurvy, beriberi, night blindness, and pellagra.[29,30,31] Scientists in the field of nutrition at the time began recognizing the necessity for not only carbohydrates, fats, proteins, and salts, but also the importance of coenzymes in the early 1900s. Soon after, rat studies contributed

significantly to our knowledge base,[24,32] involving the use of diet manipulation to identify and isolate coenzymes responsible for their effects.

Vitamins are now understood to be associated with multiple diseases, with malignant or cancerous disease being of particular interest.[33] Since vitamins are required for cellular metabolism and immunity,[34] deficiency increases risk and severity of infection and cancer.[35,36] For instance, animal models have suggested that vitamin A deficiency is associated with cancer risk, with important cell membrane, protein glycosylation, and DNA replication involvement.[37–39] Associations have also been made for virtually all other vitamins,[40] but most pertinent to our research study is the role of vitamin B. Deficiency in B-vitamins like B_6 and B_{12} are associated with DNA damage, which increases risk of cancer formation.[41] Also quite interestingly, Vitamin B_9 (Folate) depletion is used as a chemotherapeutic with antifolate drugs,[42] which induce DNA insult in rapidly dividing cancer cells. Undoubtedly, a strong association has been found between blood vitamin concentrations and the risk of disease such as cancer, which has developed into significant work into using vitamins as biomarkers.[33]

1.3 Vitamin B_6 and its Metabolic Alterations

Vitamin B_6 is an essential nutrient obtained from our diet that is a coenzyme necessary for more than 140 biochemical transformations.[43] Vitamin B_6 is a complex molecule that is essential for human health, and has been implicated in inflammation-related chronic diseases, metabolism, and immune regulation.[44] However, the role of vitamin B_6 in carcinogenesis is of particular focus.

Vitamin B_6 exists in a variety of different forms, with variations in functionality present on the 4'-benzyl position (Figure 3). The predominant forms consist of pyridoxine

(PN) which carries a hydroxyl group, pyridoxal (PL) which carries an aldehyde, and pyridoxamine (PM) which carries an amine group. Sources of the different vitamin B_6 structures consist of non-citrus fruits, fish, and starchy vegetables,[45] and has been found to be synthesized by gut microbiota through de novo or salvage pathways,[46] which may explain why deficiencies are uncommon.

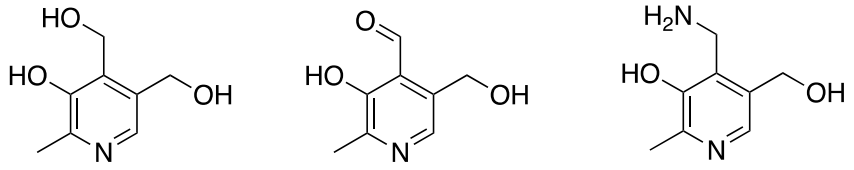

Pyridoxine (PN) **Pyridoxal (PL)** **Pyridoxamine (PM)**

Figure 3. Structures of pyridoxine, pyridoxal, and pyridoxamine. Predominant structures consist of pyridoxine (4'-hydroxyl), pyridoxal (4'-aldehyde), and pyridoxamine (4'-amine).

Absorption of vitamin B_6 begins in the intestine, and transport predominantly occurs for the native substrate PN.[45] Any modified forms of vitamin B_6 are therefore hydrolyzed by intestinal phosphatases (phosphorylated vitamin B_6) and glycosidases (glucoside of vitamin B_6) prior to transport.[47,48] Experimentation with Saccharomyces cerevisiae (Brewers Yeast) has identified the transporter TPN1, which is a member of the purine-cytosine permease family (Figure 4).[49] This protein functions as a proton symporter, localized to the plasma membrane, with high affinity for PN. Once in the cells of the intestine, PN can undergo metabolic alterations prior to transport to the liver,[50] or once within the liver. PN may first be phosphorylated by pyridoxal kinase (PDXK) to pyridoxine 5'-phosphate (PNP), and then oxidized by the flavin mononucleotide (FMN) dependant enzyme, pyridoxine 5'-phosphate oxidase (PNPO) to pyridoxal 5'-phosphate (PLP).[45] Alternatively, PN can be oxidized first by PNPO to PL, and then phosphorylated by PDXK to PLP. Phosphorylation of PN results in trapping of the molecule in the cell,

however, reversibility is possible with pyridoxal phosphatase (PDXP).[45] If vitamin B_6 vitamer levels exceed biological requirements, PLP may undergo this dephosphorylation event, and will be oxidized to 4-pyridoxic acid (PA), with excretion occurring through the urine.[51] Ultimately, the final metabolic product PLP can then be secreted from the liver, covalently bound to lysine residue 190 on human serum albumin (HSA) as a Schiff base.[52] This not only facilitates transport in the blood, but also mitigates dephosphorylation.[53]

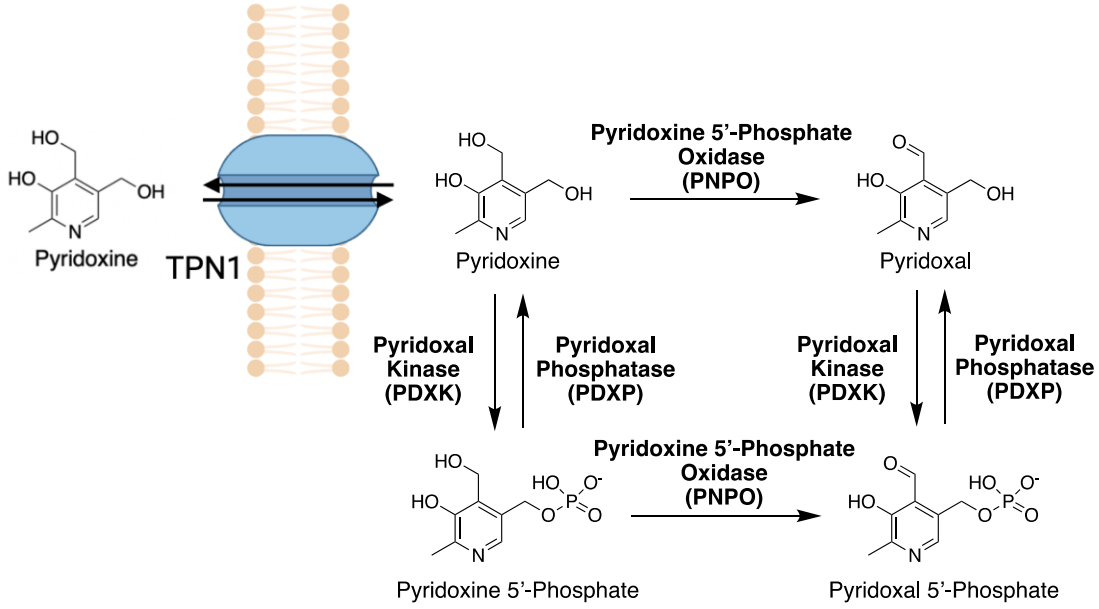

Figure 4. Metabolic alterations of pyridoxine. PDXP, pyridoxal phosphatase; PDXK, pyridoxal kinase; PNPO, pyridoxine phosphate oxidase. (**A**) Vitamin B_6 metabolism involves active transport into the cell, then oxidation by PNPO and phosphorylation by PDXK. Figure made using BioRender.

Once secreted into the circulatory system, PLP is delivered to a variety of different tissue types including the brain, red blood cells, liver, and lungs.[53] As previously mentioned, vitamin B_6 is involved in over 140 enzymatic processes, and plays a crucial role in cellular metabolism and physiological health. PLP has been reported to play roles in protein folding,[54] amino acid biosynthesis and degradation (transamination by Schiff base reactions),[53,55] glycogen storage and breakdown,[53] neurotransmitter synthesis,[56] and carbohydrate and lipid synthesis.[43]

As such an integral, multifaceted, and well-integrated substrate for so many processes, vitamin B_6 and its vitamers act as one of the most central molecules in cellular processes of living organisms. In the last several years, major discoveries have been made on its role in human health, and is continuing to develop. Consequently, such a critical coenzyme has garnered interest as an important, and underutilized biomarker for disease.

1.4 Pyridoxine's Role in Carcinogenesis and Lung Cancer

A strong clinical association has been made between the PN status of lung tumours and their sensitivity to CDDP chemotherapy.[9,57] A relatively comprehensive analysis of CDDP-resistance in NSCLC has been performed to identify CDDP response modifying factors that inhibit or exacerbate treatment.[9,57–59] Among these investigations, the metabolism of PN appears to be central in both cytotoxic response and adaptation of NSCLC cells to perturbations in homeostasis like nutrient depravation and exposure to cytotoxic agents.[57] More specifically, high expression levels of PDXK have been associated with improved disease outcomes of NSCLC patients. After ingestion, PN is taken up by TPN1, and metabolized to the active form PLP as previously described. Pre-clinically, lung cancer cells with more of the active form of PN (PLP) are more sensitive to CDDP treatment (Figure 5A).[60] However, those with more of the inactive form (PL) exhibit CDDP resistance (Figure 5B).

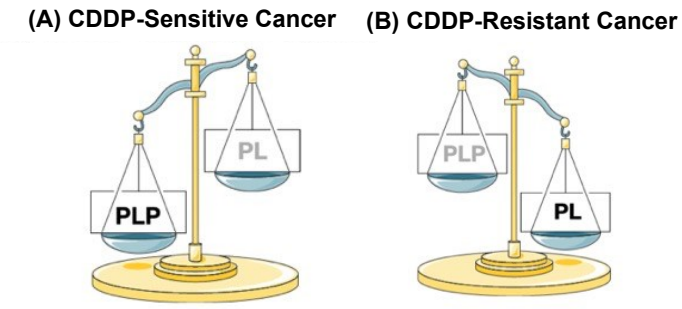

Figure 5. Biochemical CDDP resistance in lung cancer. Ultimately the PLP:PL balance, defined by PDXK and PDXP activity, dictates sensitivity to CDDP therapy. Lung cancer cells sensitive to CDDP have more PLP than PL (**A**), whereas resistant cells have more PL (**B**).

Mechanistically, PLP-conferred sensitivity to CDDP is dependent upon PDXK.[9] It was found that the loss or knockdown of PDXK *via* small interfering RNA (siRNA), protected A549 NSCLC cells against CDDP cytotoxicity.[57] Population studies have also found a negative correlation between PN serum levels and risk for developing NSCLC.[61] *In vivo* studies have shown that the anti-tumour efficacy of CDDP was enhanced by co-administration of PN to mice, increasing intracellular concentrations of vitamin B_6 vitamers, with higher than normal levels exacerbating cancer cell death.[59] *In-vitro* models sought an explanation of this effect, and suggested that acquired CDDP resistance ultimately correlated to a loss of PDXK and/or increase in PDXP. The same effects hold true for human NSCLC H460 cells, and is also a contributor to ovarian carcinoma, cervical carcinoma, and even colorectal cancer cell lines, showing the important impact of PN metabolism in cancer therapy.

PN-mediated chemosensitization has been investigated. Reduced glutathione (GSH) and N-acetylcysteine (NAC) have been shown to prevent cytotoxicity of CDDP irrespective of PN levels, while inhibition of caspases reduces CDDP cytotoxicity.[57] In the presence of PN, cells treated with sub-apoptotic concentrations of CDDP have shown increased phosphorylation of TP53, as well as increased activation of caspases 3 and 9,

which help facilitate apoptosis in cancer cells. Most notably, the accumulation of CDDP-DNA adducts as well as phosphorylation of ataxia telangiectasia mutated (ATM) and its histone (H2AX) are aggravated in the presence of PN, which are known signs of ongoing DNA damage response.[57] Ultimately, the presence of PN and its vitamer PLP are known to exacerbate the cytotoxic effects of CDDP by both caspase dependant and independent mechanisms, upstream of the DNA damage response.

Given the importance of PN and PDXK in response and resistance to CDDP based treatments of NSCLC, their quantification can provide risk assessment for disease progression and treatment response. PDXK levels as a marker for lung cancer CDDP-resistance was demonstrated to have clinical relevance in human lung cancer biopsy samples, with low tumour PDXK levels being significantly associated with poorer disease-free and overall survival.[57] While these studies reinforce the prognostic value of PDXK, it does not explain why an enzyme responsible for over 140 metabolic alterations driving cell growth and survival is lost in rapidly dividing cancer cells.

The Shuhendler group has already evaluated PN metabolism in A549 and H460 NSCLC cell lines,[62] where A549 cells have shown to be more intrinsically resistant to CDDP therapy than H460 cells.[63] Through targeted mass spectrometry (MS), it was shown that H460 cells had more intracellular PLP relative to PL than A549 cells.[62] This result was further confirmed by *in vivo* magnetic resonance imaging (MRI) of heterotopic A549 and H460 tumour xenografts. This methodology utilized chemical exchange saturation transfer magnetic resonance imaging (CEST-MRI), leveraging a hydrazine-based contrast agent that generates hydrazones with PLP to measure activity (Figure 6A), which produced results in line with previously discussed literature (Figure 6B).[9,57]

However, the clinical relevance of this contrast agent is limited due to its perturbation of the system by consuming PLP to provide imaging signal. Additionally, CEST-MRI suffers from motion sensitivity, which is incompatible with imaging organs such as the lungs.

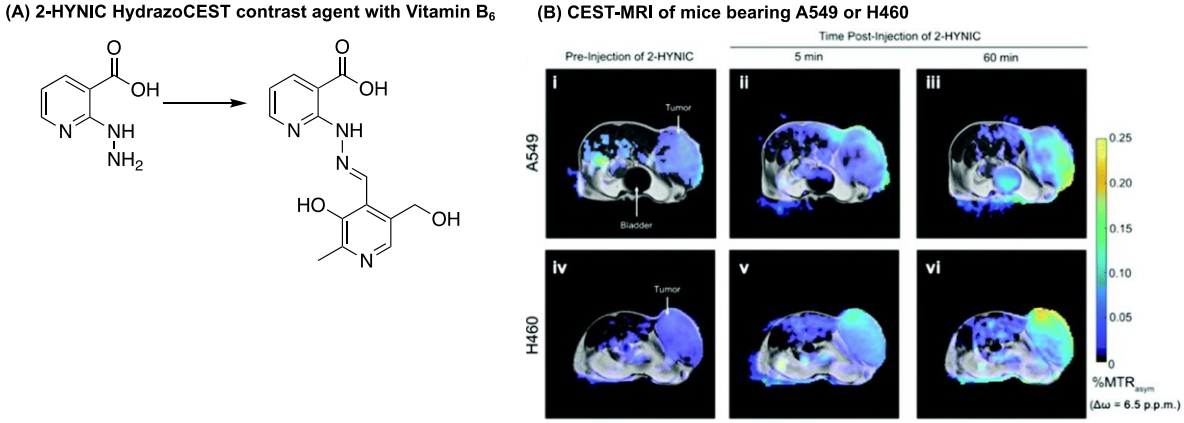

Figure 6. HydrazoCEST contrast agents' detection of vitamin B6 using 2-HYNIC in-vivo in lung tumour xenografts. The ability of HydrazoCEST contrast agent 2-HYNIC to react with pyridoxal (PL) or pyridoxal 5'-phosphate to form a hydrazone (A) through Schiff-base formation. (B) Mapping of PLP by 2-HYNIC *in vivo* in lung tumour xenografts is shown using mice bearing A549 (i-iii) or H460 (iv-vi) before (I and vi), 5 min (ii and v), and 60 min (iii and vi) after IV-injection of 2-HYNIC. Figure adapted from reference 62.

Despite these limitations, this work identified a shortcoming in literature findings of PDXK loss when assessing the expression levels of PDXK and PDXP in parental and CDDP-resistant A549 and H460 lines for three main reasons.[64] (1) While a loss of PDXK was observed in CDDP-resistant relative to parental A549 cells using previous established antibodies[57] recognizing the *N*-terminal epitope of PDXK, no PDXK was detected in parental or resistant H460 cells with the same antibody. (2) Using an anti-PDXK antibody recognizing a C-terminal epitope, PDXK was detected in both A549 and H460 cells. With the C-terminal anti-PDXK antibody, the level of PDXK expression was independent of resistance status, with A549 cells expressing more enzyme than H460 cells. (3) PDXP expression was elevated in sensitive cells, with H460 cells expressing more enzyme than A549 cells. To better understand why expression level changes were

occurring, further work was performed involving preliminary PCR studies. These alluded to a PDXK product of smaller cDNA size associated with CDDP-resistant A549 cells, which may be explained by a loss of exon 3 with the progressive onset of resistance. These findings suggest structural alterations in PDXK upon conference of resistance onset (ie. a loss of the *N*-terminal epitope) in A549 cells, and varying levels of PDXP between parental A549 and H460 cell lines. This provides a possible new hypothesis that resistance to CDDP treatment ultimately occurs as a result of varying PDXP expression and alternative splicing of PDXK.

Despite these possible foundations for CDDP-resistance onset, the fact still remains that alterations in PDXK and PLP levels are ultimately predictive of lung cancer outcomes,[57] constituting an underutilized biomarker directly addressing a clinical need to improve therapeutic outcomes for this devastating disease.

1.5 Anti-Vitamins and Ginkgotoxin as Disease Biomarkers

Similarly to vitamins, a class of molecules known as antivitamins have also undergone extensive research congruently. As early as 1926, Mellanby discovered a chemical of unknown composition that could counteract the effect of vitamin D, coined as a toxamin.[65,66] Later, this structure was identified to be phytic acid, and it is one of many antivitamins known. Antivitamins are compounds that diminish or counteract the essential functions of vitamins, mimicking the effects of vitamin deficiency in most cases.[65] With such a broad definition, many molecules have been classified as antivitamins, both with therapeutic and toxic implications.

In fact, two groups of anti-vitamins have been established due to their diversity, differentiating between structural inhibitors/analogues (Class A) and structural modifiers

(Class B).[67] Class A structural analogues are further classified into those that (A1) target proteins involved in biosynthesis, (A2) target proteins involved in cellular delivery, and (A3) target proteins involved in enzymatic transformations of the vitamin.[65] A multitude of Class A antivitamins are known, predominantly associated with therapeutic applications. Methotrexate (chemotherapy, anti-vitamin B_9) and warfarin (anticoagulant, anti-vitamin K) are two noteworthy examples, which are commonplace medical treatments.[65] Class B do not target proteins directly, but rather modify the vitamins themselves into non-functional molecules, or by interrupting necessary coenzymes, rendering them unable to participate in their native reaction pathways. Various Class B antivitamins have been identified, including phytic acid (vitamin D modifier for coenzymes), thiaminase (thiamine modifier), and even streptavidin (biotin binder) which is now a critical biotechnology.[65,68] Unlike class A antivitamins, class B represent mostly antinutritional factors, and are recognized as toxins rather than therapeutics.

As suggested, the history of antivitamins and their toxic nature has ingrained these molecules as dangerous. Despite this, antivitamin research has been an important pillar in the understanding of vitamin deficiency and metabolic processes, with deliberate vitamin deficiency in bacteria, animals, and even humans shaping our understanding.[69–72] Notably, the antivitamin deoxypyridoxine has been used to understand skin lesion formations as a symptom of deficiency, with subsequent readministration of PN counteracting its effects (Figure 6).[71] Of all explored antivitamins, the B-family has undoubtedly gathered significant interest in recent years. Vitamin B_9 is of particular interest, due to the implications of folic acid in DNA synthesis for antiproliferative drugs.[65]

Vitamin B_{12} is also tightly associated with folic acid, and has seen a multitude of analogues for medical applications that failed before clinical trials in the late 1900s.

4'-*O*-Methylpyridoxine (MPN, Ginkgotoxin) is a known Class A3 antivitamin of PN, which causes severe neuronal issues in mammals that often result in epileptic seizure (Figure 6).[73] Ginkgotoxin originates from the *Ginkgo biloba* tree, within nut-like gametophytes inside its' seeds.[74] Full plant extracts are commonly used in dietary supplements, as well as medicines for cough and infections.[75] Leaf extracts are even utilized for treating memory loss and cognitive disorders, and are sold as herbal supplements in health stores in North America.[74] With a reported LD_{50} (lethal dose causing 50% death) of 1.1 g/kg intravenously,[74] low dosages in supplements exhibit limited toxic effects. It is evident that although Ginkgotoxin poses adverse health effects, there is significant interest into its application in medicine.

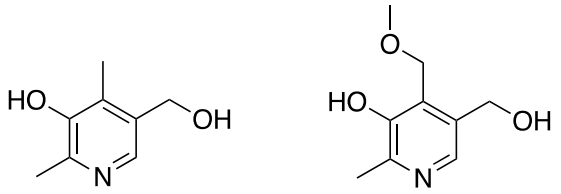

4-Deoxypyridoxine **Ginkgotoxin (4'-*O*-Methyl Pyridoxine)**

Figure 6. Anti-vitamins of pyridoxine of pyridoxine including 4-deoxypyridoxine and Ginkgotoxin (4'-O-methyl pyridoxine).

Until recently, Ginkgotoxin research has provided limited understanding beyond nutritional supplementation. However, it has recently been suggested that Ginkgotoxin acts as a competitive inhibitor for PDXK.[76] Incubation of PDXK with Ginkgotoxin and adenosine triphosphate (ATP) has shown time-dependent product formation through high-performance liquid chromatography (HPLC) detection of a 5'-phophorylated Ginkgotoxin product, with reversibility through alkaline phosphatase. Kinetic analysis after

this discovery was performed against other PN vitamers, with K_M and K_I reported. Ginkgotoxin (K_M = 4.95 µM) showed an almost 2-fold increase in binding affinity compared to PN (K_M = 9.87 µM), with a comparable specificity constant to PN (k_{cat}/K_M, 9.30 x 10^4 $mol^{-1}s^{-1}$ versus 1.25 x 10^5 $mol^{-1}s^{-1}$). They also elucidated a seemingly competitive inhibition mechanism by using a fixed concentration of Ginkgotoxin, whose inhibitory effects on PDXK could be alleviated using increasing concentrations of PL. To understand the increased affinity of Ginkgotoxin, molecular modelling of the crystallographic structure of sheep PDXK was performed using substrate and co-factor binding.[76] Modelling showed the 4'-*O*-methyl group of Ginkgotoxin extends into the most hydrophobic portion of the binding pocket, containing two hydrophobic side chains of tyrosine. The hydrophobic interactions in this region may be what contributes to the increased affinity of Ginkgotoxin, helping elucidate its potency as an inhibitor (Figure 7).

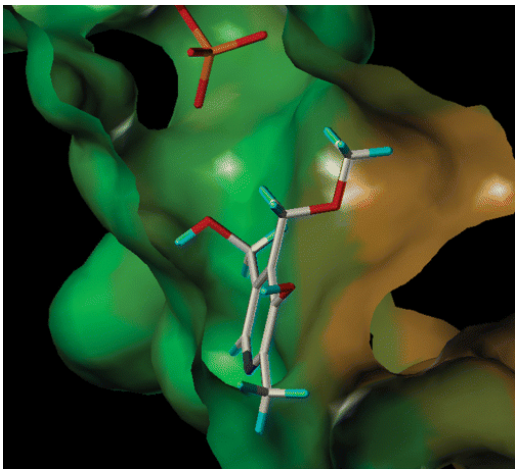

Figure 7. View into the active site of human pyridoxine kinase binding Ginkgotoxin. The hydrophobic properties are colour coded from hydrophobic (brown) to more hydrophilic (green). Shown are one phosphate residue of ATP and Ginkgotoxin as docked using the program Gold. Figure is from reference 76.

With an understanding of Ginkgotoxin and its interactions with PDXK and its high binding affinity relative to PN, this substrate acts as an appealing way to monitor changes in PDXK function. Unlike PN, Gingkotoxin can be taken up and reversibly phosphorylated

using the same mechanisms, allowing cell trapping, but further metabolic alterations cannot occur due to the 4'-position being chemically blocked (Figure 8). As a result, Ginkgotoxin only interacts with the enzymes of interest, PDXK and PDXP, providing a simplified metabolic system. Due to the low concentrations of radiotracers used for imaging, typically in the nanomolar range, toxicity is also not a concern.[74] As a result of these combined features, Ginkgotoxin and its interactions with PDXK were also considered for CDDP-resistant lung cancer monitoring.

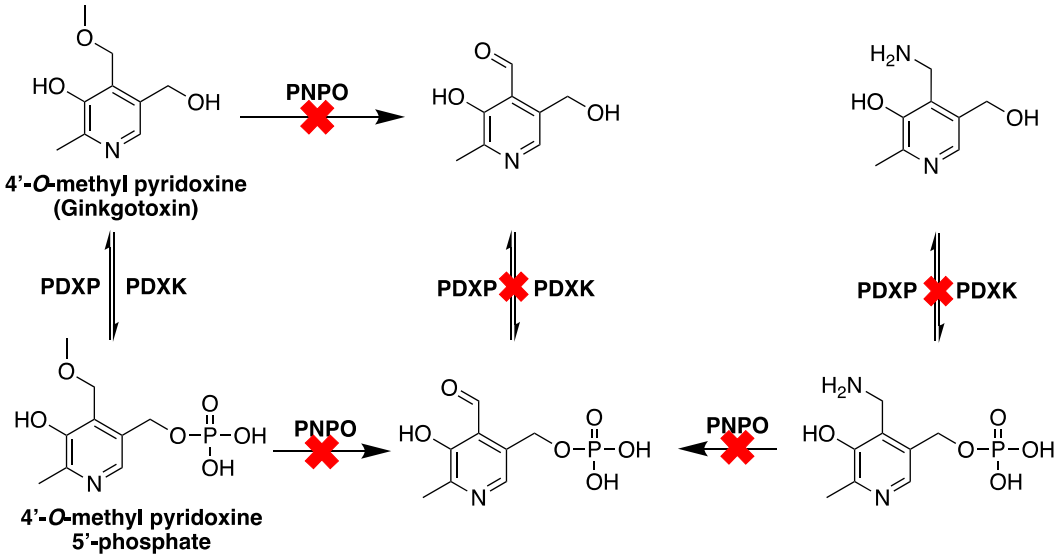

Figure 8. Metabolic alterations of Ginkgotoxin. Ginkgotoxin metabolic alterations are limited to a simplified model, with phosphorylation possible at the 5'-position. Further metabolic alterations at the 4'-benzyl position are limited by methylation, which simplifies metabolism and prevents further shuttling to downstream metabolites.

1.6 Positron Emission Tomography (PET), Computed Tomography (CT) and Metabolic Imaging

Translational molecular imaging has improved our ability to diagnose and treat numerous pathologies in clinical applications, seeing daily use in the fields of cardiology, neurology, and oncology.[77–79] Unlike anatomical imaging, molecular imaging provides detailed information on the interactions of a probe within biological systems, with real time

monitoring for disease.[80] In nuclear medicine, the probe of interest consists of a radionuclide bearing molecule that interacts with the system, which is called a radiotracer. Radiotracers are utilized in non-invasive imaging modalities for detection of minute biochemical alterations for early disease monitoring,[80] leveraging imaging techniques like positron emission tomography (PET).

The fundamentals of PET imaging begin with the utilization of radionuclides, which are generated from a cyclotron or generator with a specific decay mechanism. These radionuclides are then incorporated through a variety of radiochemical transformations with a precursor molecule on a commercial module, producing the desired radiotracer, like the commonly used [^{18}F]2-fluorodeoxyglucose (FDG) in clinic.[80,81] After quality control, the radiotracer is injected intravenously, distributing through the bloodstream to the desired target systems. The patient is then subsequently scanned in a round-shaped PET scanner (Figure 9). PET radiotracers are labelled with positron-emitting radionuclides, which decay and emit a positron, a positively charged particle or antielectron.[82] This positron is emitted from the nucleus and travels a short distance in the surrounding tissue, eventually colliding with an electron, known as annihilation.[81] This travelled distance before annihilation is known as positron range, with shorter ranges providing better spatial resolution.[83] This annihilation produces two 511-keV gamma rays (photons), which are emitted simultaneously in opposite directions (Figure 10). The detectors of a PET system are in a full ring-array,[80] where the photon pairs are detected as a coincidence event by striking opposing detectors simultaneously. Approximately 6-70 million detector pair combinations record these events from different angles around the patient, providing many coincidences to localize the site of annihilation, which is

transferred to a computer.[84] Three dimensional images can then be reconstructed into a map with information on the spatial distribution of radioactivity. A special advantage to PET is that the measured activity in the target tissue can provide absolute units of radioactivity, like Becquerel/mL, allowing for accurate quantitation of molecular processes. However, major challenges in PET reconstruction including correction for scattering, random coincidence events, and attenuation of signal through body tissue effect anatomical and quantitative processes.[85] As such, PET imaging in pre-clinical and clinical settings is often combined with computed tomography (CT) scans for anatomical positioning and attenuation correction.

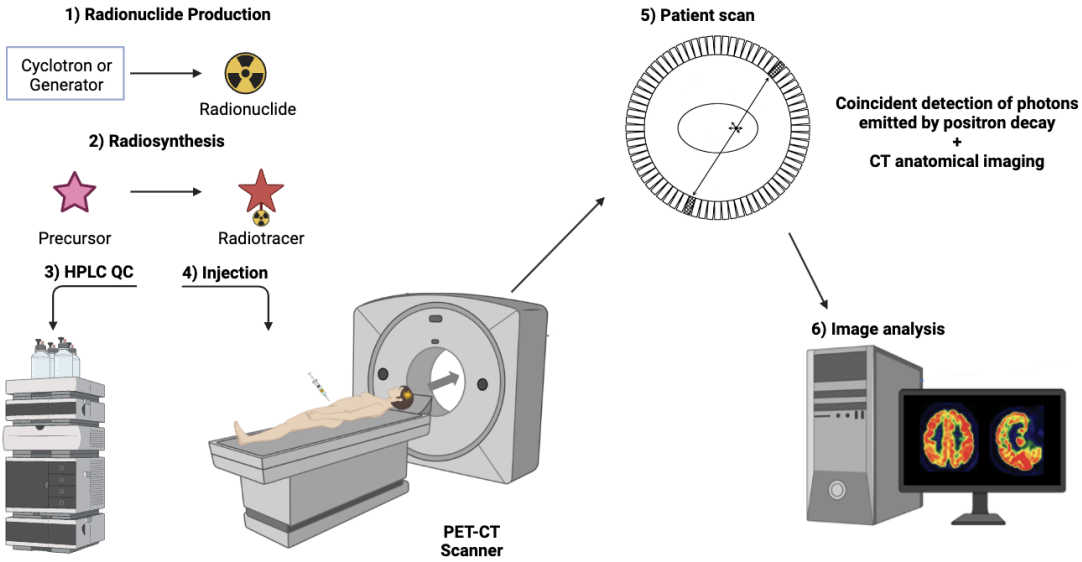

Figure 9. Principles of PET-CT imaging. Imaging of PET-CT radiotracers consists of: 1) radionuclide generation, 2) radiosynthesis, 3) quality control *via* HPLC and radioactivity detection, 4) intravenous (IV) injection in patients, 5) PET-CT annihilation and coincidence detection, and 6) image analysis and data quantifications *via* computer software. Figure adapted from reference 80 using BioRender.

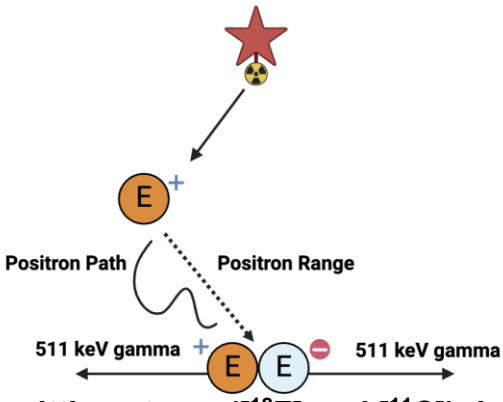

Figure 10. Positron emitting atoms ([^{18}F] and [^{11}C]) decaying by emitting a positron. Radionuclides bearing a positron emitting nuclide, predominanly [^{18}F] and [^{11}C] in literature, emit a positively charged electron from their nucleus. After a short distance travelled in tissue, known as positron range, collision with an electron causes annihilation. Two 511-keV gamma rays (photons) are emitted simultaneously in opposite directions, where PET detectors in a ring-array are detected as a coincidence event by striking opposing detectors simultaneously. Figure made using BioRender.

Using PET tracers, visualization of molecular and cellular events early in the course of disease and treatment is possible. PET gives access to prognostic information and can offer a risk-evaluation tool in clinical practice when applied to CDDP-resistant lung cancer. Changes in metabolic alterations at the cellular level in lung cancer can be monitored with a tailored radiotracer, providing a mechanism to monitor resistance onset earlier than anatomical changes to prevent devastating outcomes.

1.7 Translational Radiochemistry Using Fluorine-18 and Carbon-11

The development of successful radiotracers depends not only on biological characteristics and application, but also on the use of radionuclides that are compatible with the molecule of interest and current automated tracer modules. The selection of the PET radionuclide, radiosynthetic methods, and stability are important considerations when devising synthetic conditions that are appropriate between benchtop and radiochemistry applications. The availability of these radionuclides is also important, and can depend upon access to a cyclotron facility.[28] Commonly employed cyclotron-based

radionuclides include carbon-11 (half-life ($t_{1/2}$)= 20.4 min), nitrogen-13 ($t_{1/2}$ = 10 min), oxygen-15 ($t_{1/2}$ = 2 min), fluorine-18 ($t_{1/2}$ = 109.8 min), and iodine-124 ($t_{1/2}$ = 4.2 days).[80] These radionuclides are introduced through extensive synthetic approaches either covalently or as a salt. Radiometals are also possible, including gallium-68 ($t_{1/2}$ = 67.7 min), copper-64 ($t_{1/2}$ = 12.7 h), and zirconium-89 ($t_{1/2}$ = 78.4 h), which are integrated through addition of a chelator and coordination chemistry.[80] The use-case of radionuclides is dependent upon synthetic applicability, half-life duration, and spatial resolution requirements. Of all mentioned nuclides, fluorine-18 and carbon-11 are by far the most commonly employed.

Among the existing positron-emitting nuclides, fluorine-18 ([^{18}F]) is the most widely utilized positron emitter. [^{18}F] provides an optimal half-life of 109.8 minutes that enables longer reaction times and off-site clinical use.[86] Additionally, the low positron range of 0.6 mm enables high spatial resolution, coupled with a 97% positron efficiency that enables ideal imaging conditions.[87] [^{18}F] is produced in a cyclotron by proton irradiation of liquid [^{18}O]H_2O, producing an aqueous solution of [^{18}F]HF.[88] Proton irradiation of gaseous [^{18}O]O_2 is also possible, and produces [^{18}F]F_2 gas; however, electrophilic F_2 is rarely utilized in modern radiochemistry due to hazards and synthetic difficulties.[89] [^{18}F] is introduced *via* bioisosteric substitution of hydrogen or hydroxyl groups, with limited steric implications.[82] Introduction is most commonly mediated by nucleophilic substitution of sulfonate based leaving groups (mesyl, tosyl, triflate), halogens (Br, I), or aromatic S_NAr leaving groups (-N+Me_3, NO_2) with [^{18}F]F- in the forms of potassium fluoride (KF) and tetrabutyl ammonium fluoride (TBAF).[80] Polar aprotic solvents such as acetonitrile (MeCN), dimethyl sulfoxide (DMSO), or dimethyl formamide (DMF) are typically employed

to enhance nucleophilicity in the short reaction times, and are permissible for higher temperatures. Other methodologies have been employed using deoxyfluorination,[90] enzymes,[91] and even transition metal chemistry,[92,93] highlighting the universal applicability of this radionuclide.

Besides [^{18}F], carbon-11 ([^{11}C]) labelling is commonly employed and has experienced significant advancement in synthetic strategies to enable access. Given that carbon atoms are abundant in biologically active molecules, this strategy acts as an alternative to [^{18}F] bioisosteric replacement. [^{11}C] has a significantly shorter half-life of 20.4 minutes, which is ideal for limiting patient exposure but imparts synthetic challenges from time constraints.[94] [^{11}C] also provides a 99.8% positron efficiency, and moderate 1.2-mm positron range that provides good spatial resolution.[87] Production of [^{11}C] begins with proton bombardment of nitrogen gas (^{14}N to ^{11}C) in the presence of oxygen, producing [^{11}C]CO_2. As a result, [^{11}C]CO_2 can be used for carbonylation,[95,96] or be converted using various conditions to [^{11}C]CO,[97] [^{11}C]HCN,[98] and [^{11}C]CS_2 (Figure 11).[99] A plethora of radiolabelling handles have been developed for radiopharmaceuticals including [^{11}C]-methyl-, [^{11}C]-carbonyl-, and [^{11}C]-trifluoromethyl. Of these handles, methylation of amines, alcohols, and carboxylates with [^{11}C]CH_3I (methyl iodide, MeI) or the more reactive [^{11}C]CH_3OTf (methyl triflate, MeOTf, by reacting [^{11}C]CH_3I with silver triflate) is most common.[100101] Commercially available modules are designed for these reliable methylation strategies, and allow for automated synthesis in research and clinical settings. Despite methylation being more common, [^{11}C]CO_2 can be used for carbonylation,[95,96] or be converted using various conditions to [^{11}C]CO[97], [^{11}C]HCN[98], and [^{11}C]CS_2[99] (Figure 11) for a variety of different carbon labelled funcitonalities.[102] Although

[^{11}C] suffers from a significantly lower half-life, its clinical relevance and synthetic versatility makes it a powerful tool for radiotracer production, still being used for the production of clinically relevant radiotracers like [^{11}C]Raclopride[103] and [^{11}C]HED.[103]

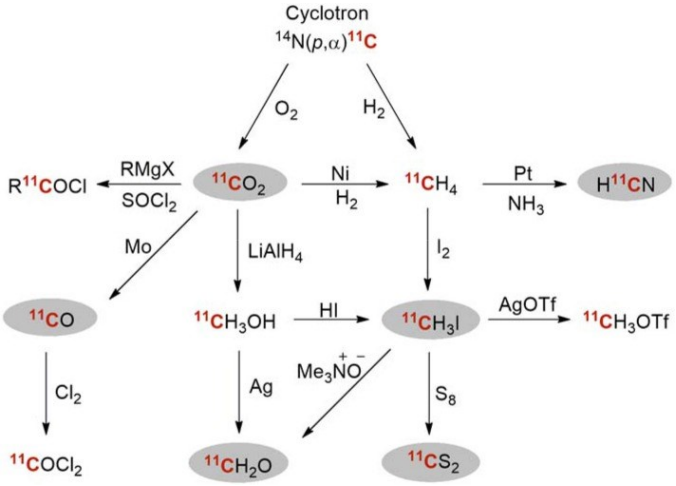

Figure 11. Cyclotron production of [^{11}C] synthetic agents. Multiple stationary phases facilitate conversion of [^{11}C]CO_2 gas into carbonylating, methylating, and other carbon derived agents for radiochemical synthesis strategies. Figure adapted from reference 102.

1.8 Goals and Objectives

Conventional strategies for the detection and diagnosis of lung cancer rely on the commonly used FDG radiotracer, which maps the increased metabolic activity of cancer cells.[104] However, due to limitations in low FDG uptake in cancer subtypes,[105] infection or inflammation mimicking metastases[106], and overall low specificity for NSCLC with variable uptake,[106] the current standard is limited in consistency in providing prognostic information on treatment outcomes for CDDP treatment. Fortunately, a strong clinical association has been made between the PN and PLP status of lung tumours and their sensitivity to CDDP chemotherapy. The expression level changes of PDXK during CDDP-resistance onset provides a changing metabolic process that can be leveraged for PET-CT imaging. Through the utilization of radiochemical transformations, a suitable

radiotracer based on PN can be synthesized to monitor changes in metabolic alterations to provide insight on CDDP-resistance onset during treatment.

To achieve this goal, three main objectives were established for the completion of this project:

Objective 1: Synthesize cold standards, characterizing and ensuring purity of products.

Cold standards for use as a radiotracer are based upon both [^{19}F]/[^{18}F] and [^{12}C]/[^{11}C] analogues of pyridoxine. Four cold standard and radiotracer pairs were hypothesized (Figure 12), with the aromatic carbon-6 **1** being the first option with fluorine substitution next to the pyridine nitrogen. Second, fluorine substitution at the 2'-benzyl position was also of interest, as this is a non-metabolically modified position, giving cold standard/radiotracer **2**. Cold standard and radiotracers **3** and **4** were then based upon anti-vitamins of pyridoxine, with methylations at the 2' and 4'-benzyl positions to provide comparison of radionuclide and analogue suitability *in vivo*. All proposed cold-standard modifications focused on positions translatable to radiochemical analogues, while limiting modification to metabolically active positions involving PDXK and PDXP.

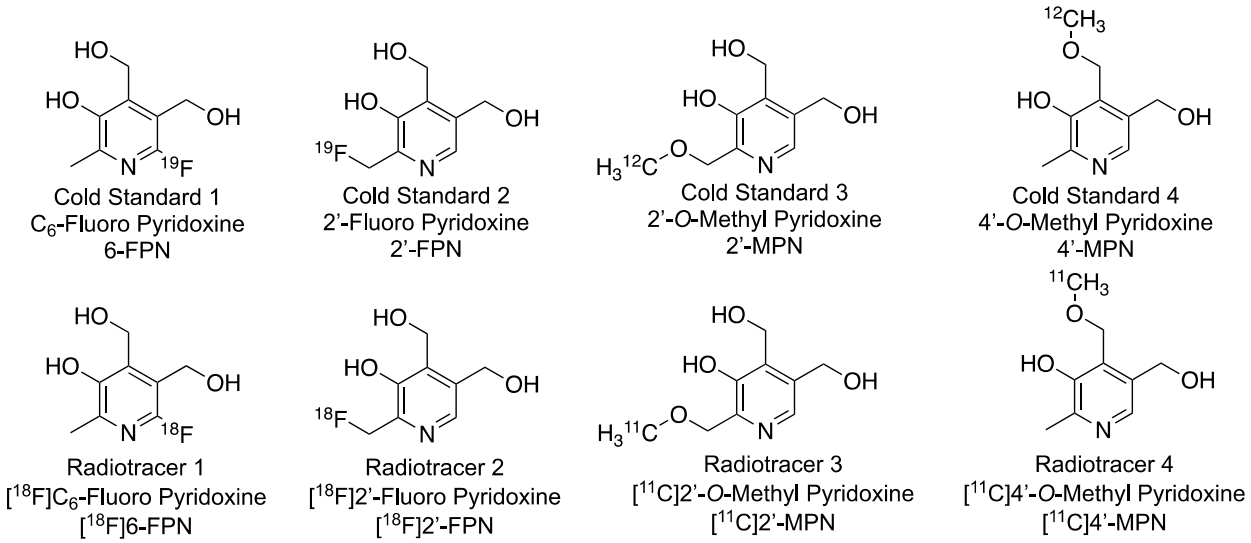

Figure 12. Proposed structures for cold-standard and radiotracer analogues of pyridoxine.

Objective 2: Assess the biochemical and metabolic alterations of cold vitamin B_6 derivatives using *in vitro* metabolomic analysis to ensure metabolic conversions through interactions with known enzyme pathways.

Objective 3: Synthesize radiolabelled tracers, validating production through HPLC. We will then demonstrate that reduced [^{18}F] and [^{11}C]vitamin B_6 retention in tumour tissue is associated with lung cancer resistance to CDDP, whether intrinsic or acquired.

If successful, this work can provide a new strategy for monitoring the early onset of CDDP-resistant NSCLC lung cancer in the clinic. Utilization of PET-CT imaging and our most effective radiotracer can track changes in metabolic activity through qualitative and quantitative changes in imaging contrast, guiding informed decisions on patient treatment plans before cancer reprogression and devastating outcomes.

Chapter 2 – Results and Discussion

2.1 Synthesis of C_6-Fluoro Pyridoxine using S_NAr

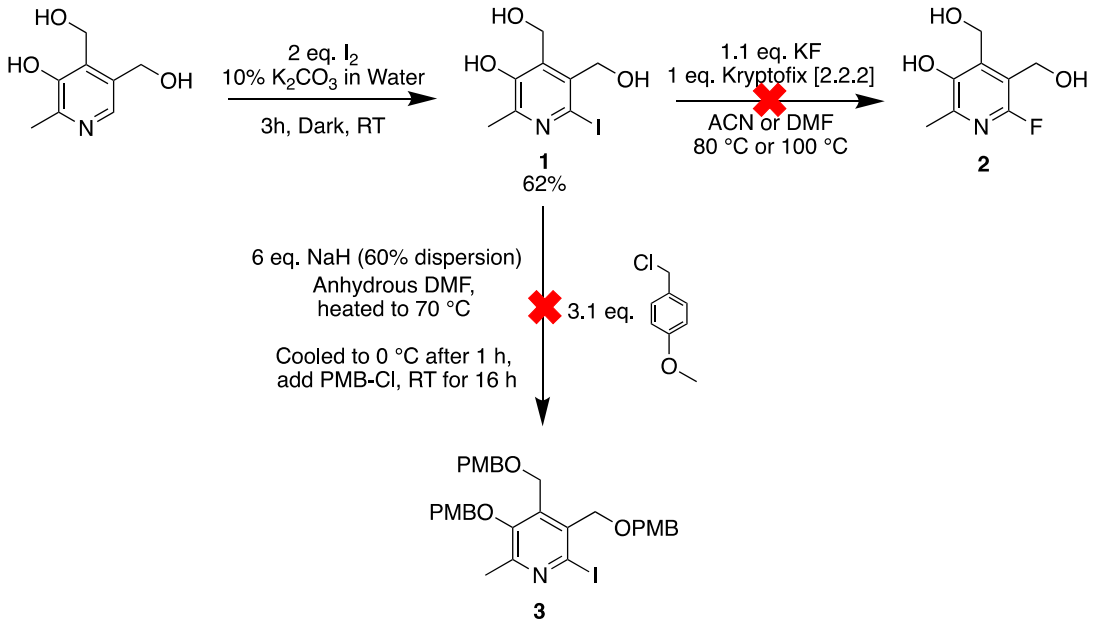

Scheme 1. Proposed synthesis of C6-fluoro pyridoxine cold-standard 1 using nucleophilic aromatic substitution.

We began our investigation by attempting to synthesize the carbon-6 aromatic fluorinated cold-standard **1** of PN. Scheme 1 shows the first synthesis, which began with a simple two step procedure adapted from Yu *et al.*, where PN was reacted with iodine in 10% aqueous K_2CO_3 with exclusion of light.[107] This afforded **1** with 62% yield, which was reacted with KF and the cryptand Kryptofix [2.2.2] *via* nucleophilic aromatic substitution (S_NAr) for attempted formation of **2**. Despite varying conditions including the use of MeCN and DMF at 80 °C and 100 °C respectively, no desired product could be observed by liquid chromatography mass spectrometry (LC-MS) analysis (see Appendix Figures S56/S57). This was speculated to be due to the high electron density from the electron donating alcohol groups present at the *ortho* and *para* positions of pyridoxine, limiting reactivity. To try and circumvent this issue, a protection of the alcohol groups of **1** was

attempted using *para*-methoxybenzyl chloride (PMB-Cl) and sodium hydride to form **3**. However, once pyridoxine was substituted on the carbon-6 position, the substrate exhibited little to no reactivity, with most of the mixture still containing starting material after 16 hours (see Appendix Figures S58-S60). Other possible leaving group options were also considered, specifically chlorine and nitro groups based on other pyridine-based probes.[108] The chlorinated derivative could be synthesized, but didn't improve reactivity, while the nitro group could not be installed. Trialkyl ammonium groups are also commonly employed, synthesized through pyridine-*N*-oxides using trifluoroacetic anhydride and trimethylammonium.[109] However, due to the presence of the methyl group on the carbon-2 position of pyridoxine, functional group compatibility became an issue, with preference for Boekelheide rearrangement to the 2'-benzyl alcohol (Figure 13).[110,111]

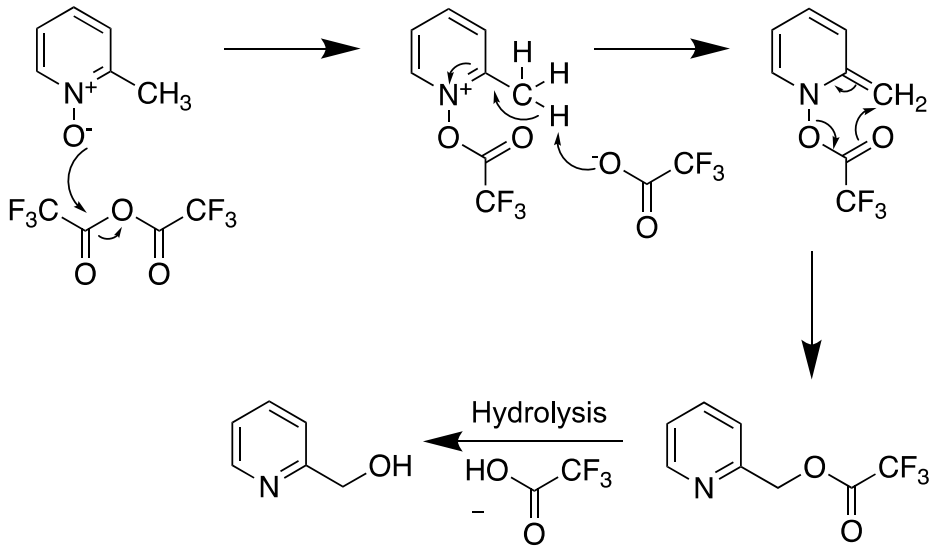

Figure 13. Mechanism of the Boekelheide rearrangement of pyridine compounds with *ortho*-methyl substitution.

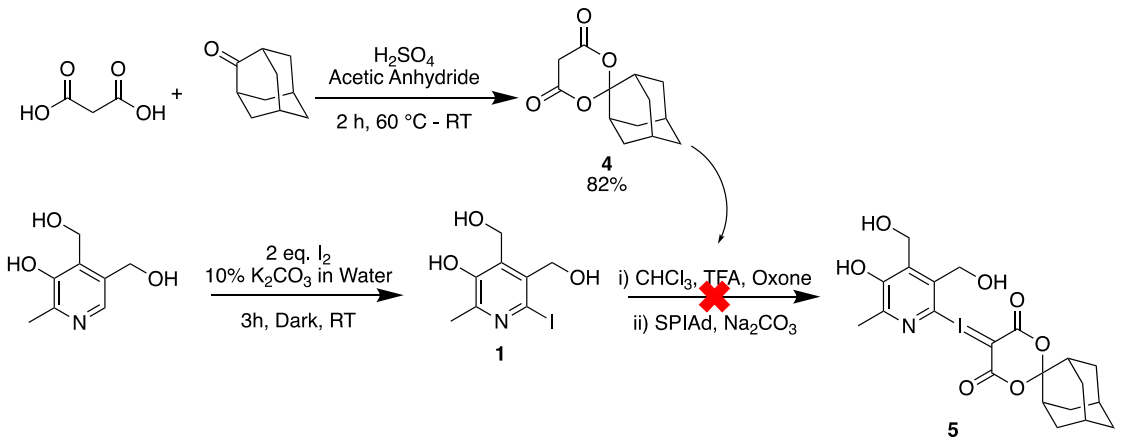

Scheme 2. Proposed synthesis of C_6-fluoro pyridoxine cold-standard 1 using nucleophilic aromatic substitution on hypervalent iodine.

Due to the limited leaving group compatibility and reactivity toward S_NAr at carbon-6, we searched for strategies to decrease electron density or further activate this position. One common strategy used for the introduction of $[^{18}F]F^-$ into electron rich arenes is diaryliodonium salt-based precursors using hypervalent iodine (III).[112–114] More specifically, spirocyclic iodonium ylides (SPIAd) have been made popular due to synthetic ease and stability as precursors.[114] Adapting this strategy, **4** was first synthesized using malonic acid and 2-adamantone in the presence of cat. H_2SO_4 and acetic anhydride (solvent) with 82% yield according to scheme 2. Using conditions established by Rotstein *et al.*,[114] 6-iodopyridoxine **1** was combined with **4** in the presence of trifluoroacetic acid and oxone to activate the pyridine nitrogen, followed by introduction of SPIAd to make the iodonium ylide. Despite multiple attempts, **5** was not observed by LC-MS analysis (see Appendix Figures S61/S62). It is speculated that due to the highly acidic and oxidative conditions, PN undergoes significant side-reactivity that prevents any notable conversion. Implementation of protecting group strategies may be a possibility, including the use of benzyl ethers,[115] but due to the requirement of precursors for radiochemistry containing fast and acid-labile protecting groups, the conditions of the reaction remain unsuitable.

In addition to previously described substitutions, electrophilic aromatic substitutions (EAS) were considered for this substrate. However, pyridine is known to preferably react at the *meta* position, instead of the desired *ortho* position (Figure 14).[116] In Figure 14A, this can be described using resonance structures, where *meta* substitution results in only carbon atoms bearing the positive charge. In Figure 14B, *ortho* substitution results in the same number of resonance structures, but produces a resonance structure where the more electronegative nitrogen bears a positive charge and an incomplete octet, making *ortho* substitution less favourable. Additionally, the basic nitrogen of pyridine can undergo protonation under acidic conditions, which can interfere with some EAS reactions. An additional issue with EAS for fluorinated substrates is the requirement of fluorine gas (F_2),[117] which is not suitable for most organic chemistry labs and is not available for radiochemistry. Significant work has been done for fluorine suitable and more mild methods for EAS including selectfluor[118] but are not available for radiochemistry in most labs. As a result, aromatic substitution on pyridoxine appears unsuitable for development of the desired radiotracer **1**.

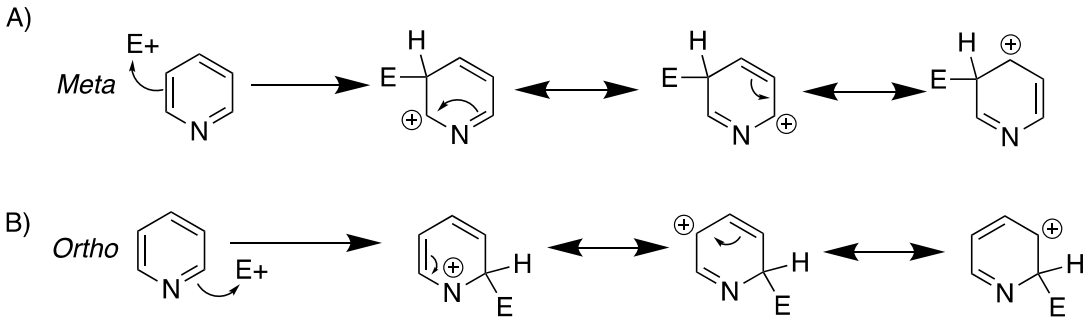

Figure 14. Complications for electrophilic aromatic substitution (EAS) of pyridine rings. (A) Pyridine rings prefer meta-addition, with resonance stability that limits the positive charge present on nitrogen. (B) Ortho substitutions result in positive charge on the pyridine nitrogen, resulting in unstable resonance structures that make this substitution less preferable.

2.2 Synthesis of C_6-fluoro pyridoxine using the Sandmeyer Reaction

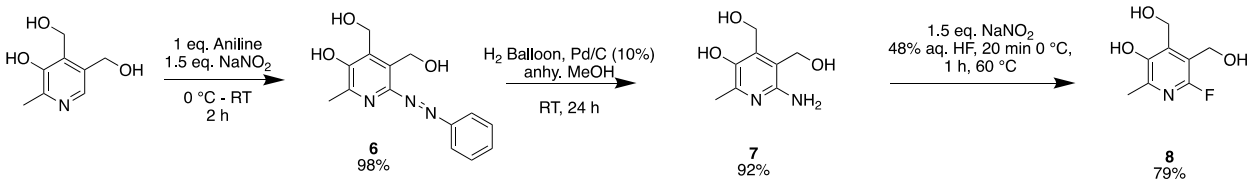

Scheme 3. Proposed synthesis of C_6-fluoro pyridoxine cold-standard 1 using the Sandmeyer reaction.

With significant difficulty limiting the potential for EAS and S_NAr on pyridoxine, a search into alternatives was performed on substrates resembling pyridoxine. Quite unexpectedly, the synthesis of cold standard **1** was previously described by Sha et al. in 1998 for the development of ^{19}F nuclear magnetic resonance spectroscopy (NMR) pH indicators.[119] Scheme 3 describes the synthesis of desired product C_6-fluoro pyridoxine using the Sandmeyer reaction. Beginning with PN, aniline and sodium nitrite were combined to yield **6** with 98% yield. This product could then be reduced to the amine using H_2 gas with palladium over carbon (10% by weight) to give **7** in 92% yield. Two potential reactions were hypothesized for fluorine introduction on **7** based on activation of the amine with sodium nitrite to a diazonium salt leaving group. One prominent reaction is the Balz-Shiemann reaction,[120] which would yield the desired product, but with difficult translation to radiochemistry due to the 1 in 4 statistical distribution of fluorine addition when performing isotopic exchange with HBF_4. The use of TBAF and KF were also attempted but were unsuccessful in yielding product. As a result, the proposed cold standard **8** was synthesized *via* the Sandmeyer reaction by combining **7** with sodium nitrite and 48% aqueous hydrofluoric acid in 79% yield after HPLC purification. [^{18}F]HF is a feasible reactant, as it is the product of cyclotron production, allowing the Sandmeyer to be a potential radiochemistry viable pathway.

2.3 Synthesis of 2'-Fluoro Pyridoxine

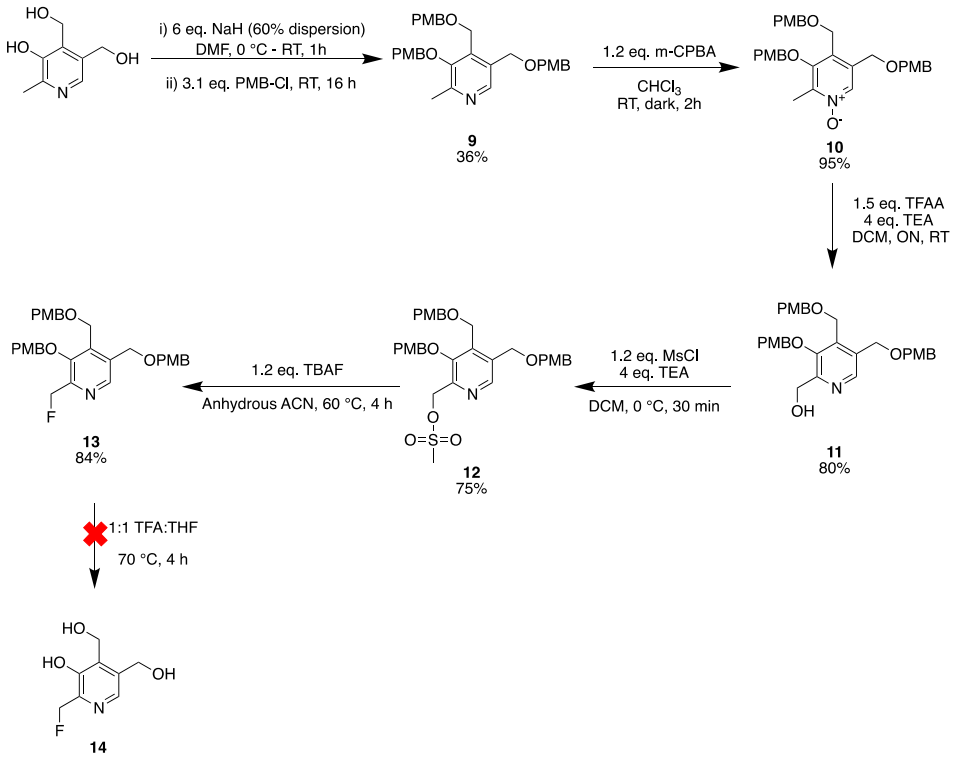

Scheme 4. Proposed synthesis of 2'-fluoro pyridoxine cold-standard 2 using nucleophilic substitution.

In addition to fluorination on the aromatic ring of pyridoxine, a fluorinated derivative on the 2'-benzyl position yielded the second proposed vitamin-B_6 analogue radiotracer. The advantage to modification of this position is its limited impact on metabolism, being an unmodified position by PN's enzymes. The synthesis of 2'-fluoro pyridoxine cold-standard **2** is shown in scheme 4, which begins with protecting groups being installed on pyridoxine to prevent side reactivity of the varying alcohol groups. Per-addition of PMB-Cl in the presence of sodium hydride in DMF was the protecting group strategy of choice. The use of sodium hydride at large scale produced a messy suspension, but after purification afforded **9** in 36% yield. Limitations in yield are attributed to various factors including complications in extraction and flash chromatography due to a black tar-like substance that is difficult to remove, as well as the presence of partially protected

products. Attempts to switch solvent to tetrahydrofuran (THF) saw poor solubility and reactivity and attempting to add PMB-Cl in greater quantities complicated chromatography. Other protecting group strategies were considered, including silyl, acetyl and benzyl ether groups. Silyl ethers proved too unstable for addition and could not effectively be added to all alcohols of pyridoxine. Additionally, previous work has shown that less stable groups like acetyl groups can migrate in the presence of fluorinating agents, which would complicate selective fluorination of the 2'-position.[121] Finally, acid-labile protecting groups for alcohols in radiochemistry are common, as the radiosynthetic TRACERlab modules require facile deprotections to limit loss in radioactivity. The module is not designed for complex catalyst introductions, with no capacity for hydrogen gas introduction, preventing the use of benzyl ethers as protecting groups.

With pyridoxine protected, synthesis of **10** could then be performed using *meta*-chloroperoxybenzoic acid (m-CPBA) in chloroform with 95% yield.[122] Transformation to the 2'-alcohol protected product **11** could be performed using a Boekelheide rearrangement, employing trifluoroacetic anhydride (TFAA) as an acylating agent which is subsequently hydrolyzed.[110,111] Due to the acidic nature of this reaction, with trifluoroacetic acid (TFA) being a by-product, the standard conditions resulted in deprotection of the PMB-ether groups previously installed. To modulate this, an excess of triethylamine (TEA) was added to the reaction, which allowed for isolation of **11** in 80% yield. Activation of the alcohol as a leaving group was then necessary for substitution with fluorine, which was first attempted with *p*-toluene sulfonyl chloride, with limited conversion and poor isolation. The milder activator, methanesulfonyl chloride (MsCl), was used in

place in the presence of TEA to sequester chlorine ions from further substitution and limit hydrochloric acid (HCl) by-product, affording **12** with 75% yield. This product exhibited poor stability, and loss of the methanesulfonyl group over prolonged storage, so the product was made, characterized, and used directly in the next step. Fluorination could be achieved using the standard fluorinating agent TBAF, affording **13** in 84% yield. Characterization of **13** included high-resolution MS (HRMS) and ^{1}H, ^{13}C, and ^{19}F NMR, which all showed desired product was formed (see Appendix Figures S20-S22). The final step of this scheme included deprotection of the PMB groups, using a commonly employed TFA and THF mixture at reflux. Reaction progress was monitored using electrospray ionization (ESI) positive mode LC-MS, where desired product with *m/z* 188 formed after 4 hours. However, alongside the desired product appeared co-elution of a product with *m/z* 186 that corresponds to the mass of a 2'-hydroxyl containing PN derivative (Figure 15).

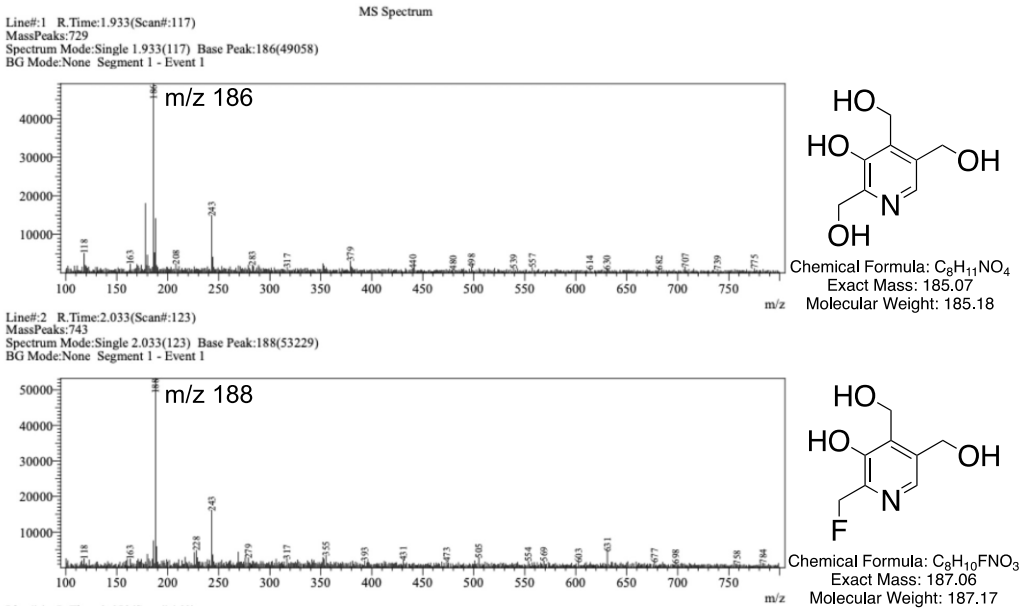

Figure 15. LC-MS analysis of 2'-fluoro pyridoxine substitution in ESI+ mode. The top ion chromatogram shows an undesired 2'-hydroxyl pyridoxine product of *m/z* 186 (1.93 min RT), while the bottom ion chromatogram shows the desired product 2'-fluoro pyridoxine of *m/z* 188 (2.03 min RT) corresponding to fluorinated product.

Despite the implementation of varying conditions of temperature, time, and acid equivalents, **14** could not be isolated and characterized. This finding prompted an investigation into the literature to find an explanation to the lability of the fluorine after deprotection of the alcohol groups. It was discovered that pyridine groups with *ortho* substitution are known to exhibit a mechanism known as the pyridinone-methide elimination.[123] This is facilitated by a neighbouring phenol oxygen group forming a ketone under aqueous conditions. This would allow for the elimination of the *ortho*-substituent (halogens and sulfonyl activators), followed by reformation of the phenol using water to generate the hydroxyl substitution (Figure 16).

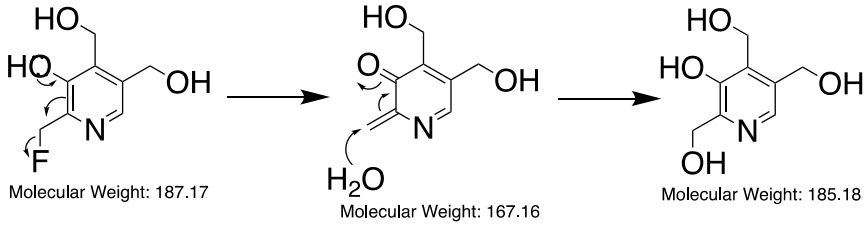

Figure 16. Proposed mechanisms for pyridinone-methide elimination of 2'-fluoro pyridoxine.

This elimination imparts an instability to the benzyl position of pyridoxine and makes 2'-benzyl substitutions most likely unsuitable for this substrate. *In vivo* this would have significant implications, because even a mixture of substrates including the desired product would exhibit defluorination, which is a known issue to PET radiotracer design with skeletal fluorosis occurring due to fluorides affinity for bone.[124,125]

2.4 One-Carbon Homologation of Pyridoxine to Prevent Elimination

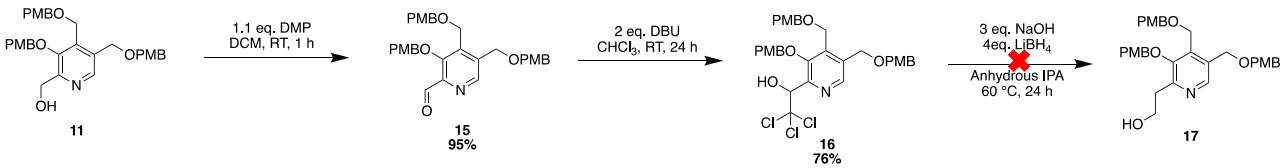

Scheme 5. Proposed synthesis of 2'-benzyl one-carbon homologated pyridoxine using the Jocic-Reeve reaction.

With the knowledge that substitution of the 2'-benzyl position of PN is unstable, it was hypothesized that a carbon homologation on this position may promote greater stability by distancing the leaving group. Due to the restraints of our tracer design, one carbon homologations were chosen as potential options to limit modifications of the structure too significantly from native pyridoxine, so metabolism was not impacted. After a literature search, Scheme 5 was proposed for synthesis *via* a modified Jocic-Reeve reaction (Figure 17).[126]

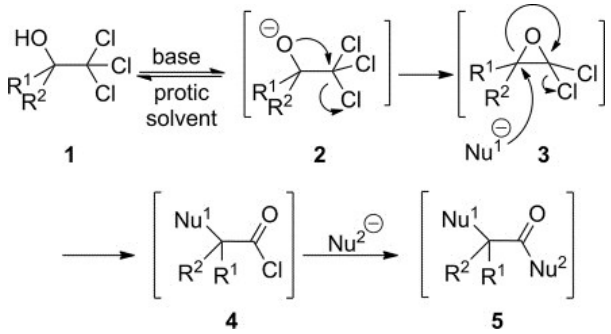

Figure 17. Jocic-Reeve reaction mechanism.

This began with the use of previously isolated **11**, which could be readily transformed to the aldehyde product **15,** using Dess-Martin periodinane (DMP) as a mild oxidative agent, in 95% yield. The trichloro-substituted **16** could then be synthesized using an excess of 1,8-diazabicyclo(5.4.0)undec-7-ene (DBU) in chloroform to form trichloromethanide *in situ*, giving **16** in 76% yield.[126] Finally, the Jocic-Reeve reaction was attempted using the best optimized conditions from Li *et al.* using sodium hydroxide (NaOH) and lithium borohydride ($LiBH_4$) to form **17**.[126] Reaction progress was monitored by LC-MS (see Appendix Figures S63/S64), which showed two main products after 24 hours, the desired homologated hydroxyl product, as well as loss of the carbon and reformation of the benzyl alcohol **11**. Attempts were made to isolate this product by column chromatography, but the desired product could not be isolated, with benzyl

alcohol **11** being the major and only isolatable product. This finding suggests that the new C-C bond was unstable, and lost during the transformation, yielding the starting material once again.

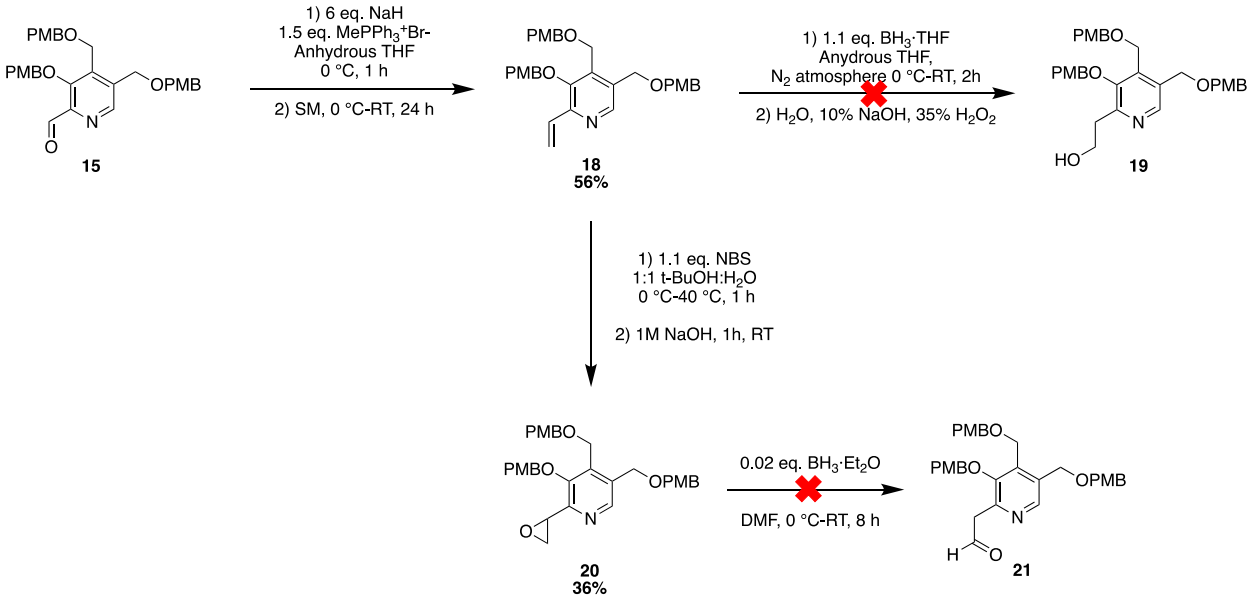

Scheme 6. Proposed synthesis of 2'-benzyl one-carbon homologated pyridoxine using asymmetric hydroboration and epoxide opening.

Another proposed pathway involved the use of a one-carbon homologated styryl containing derivative of pyridoxine through the Wittig reaction, illustrated in Scheme 6. The synthesis began with previously isolated **15**, which could then be converted to styryl containing **18** with 56% yield. This reaction required a small optimization for a suitable base to produce the Wittig reagent, where *n*-butyl lithium and sodium hydride were compared, with sodium hydride being the best choice. A variety of different reactions were attempted on this derivative, with a focus on anti-Markovnikov additions to produce the desired terminal alcohol group. A hydroboration oxidation was performed using BH_3•THF, followed by 10% aqueous NaOH to form the terminal alcohol homologated product **19**. Reaction progress was monitored using LC-MS, where the desired *m/z* of 560 was not observed. 9-BBN and BH_3•DMS complexes were also tried, but similar *m/z* species of

408 and 440 were observed by LC-MS (see Appendix Figures S65/S66). TLC analysis also showed loss of starting material, with a multitude of new UV active spots being present. The loss in mass may be attributed to an instability in the PMB protecting groups in these conditions. It is also assumed that the nitrogen in pyridine could be potentially complexing with boron in the reaction, which is known in the literature,[127,128] limiting reactivity at the desired position. Increasing equivalents of borane reagents was attempted, but similar results were found.

An alternative attempt at anti-Markovnikov addition was performed using the styryl intermediate **18**. The benzylic epoxide **20** could be synthesized from the alkene using freshly recrystallized *N*-bromosuccinimide (NBS) in a mixture of *tert*-butanol and water[129] under inert atmosphere of nitrogen. LC-MS analysis showed the major product by UV detection at 254 nm was most likely the desired product, with *m/z* of 558 (see Appendix Figures S67/S68). The product however was unstable when attempting column chromatography, making isolation and further characterization difficult. The solvent was instead removed, and the ring opening to the terminal aldehyde **21** was attempted directly using $BH_3 \bullet Et_2O$ in DMF.[130] No observable reaction occurred, with starting material being the only UV active material present after 8 hours by LC-MS (see Appendix Figures S69/S70). It is again predicted that the capacity of boron to complex with the pyridine nitrogen limits reactivity, preventing chemoselectivity for the alkene position. A literature search provided few transformations containing pyridine groups, reinforcing its poor suitability for borane complexes.

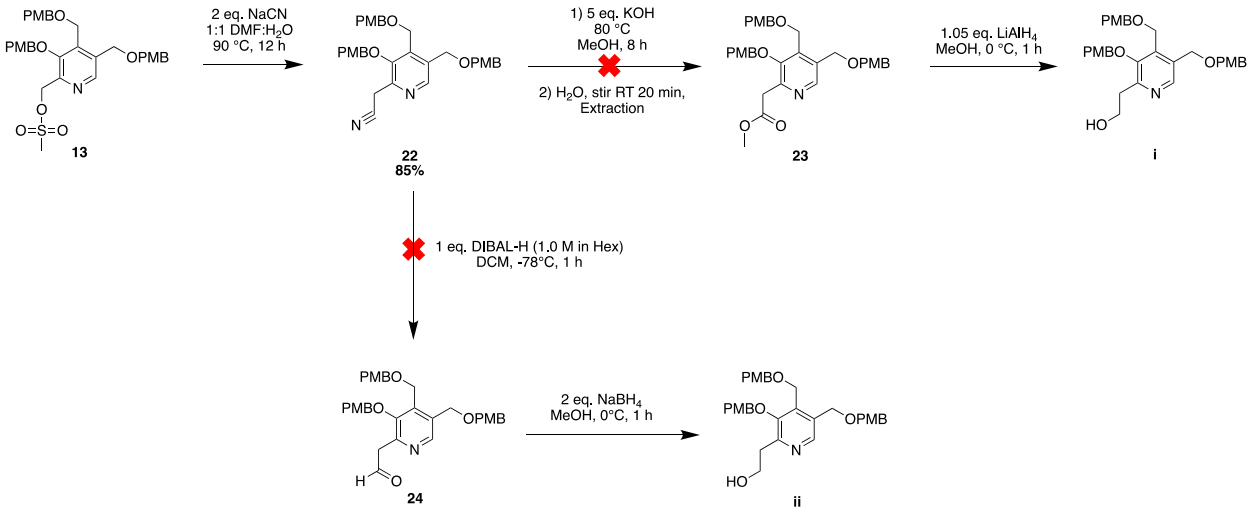

Scheme 7. Proposed synthesis of 2'-benzyl one-carbon homologated pyridoxine using a nitrile derivative.

The final pathway attempted for the one carbon homologation is proposed in Scheme 7. Using previously methanesulfonyl-substituted **13**, sodium cyanide could be introduced to homologate to the nitrile containing group **22** in 85% yield (see Appendix Figures S71/S72). From this product, the first attempt to bring the nitrile group to a reducible carbonyl functional group involved the use of a modified Pinner reaction under basic conditions using sodium hydroxide in methanol, as to avoid deprotecting the PMB groups.[131] The desired product **23** was observed by LC-MS with *m/z* 588 (see Appendix Figures S73/S74) but attempting to isolate this product by column chromatography was unsuccessful over multiple attempts. Instead, it was opted to perform an extraction, and use the semi-crude material directly in the next step. Crude **23** was reacted with lithium aluminum hydride ($LiAlH_4$) in methanol (MeOH), and the progress of product **i** formation was monitored by LC-MS. After one hour, complete consumption of starting material was seen, with new products containing *m/z* 546, 410, and 426 (see Appendix Figures S75-S77). The product of *m/z* 546 matches the mass of the original hydroxylated **11**, potentially seeing a loss of homologation. The lower masses also indicate that potentially

the PMB groups were not retained in these conditions. Finally, the Pinner reaction was also attempted using potassium hydroxide (KOH) with water present to promote the production of the carboxylic acid but did not show any significant transformation.

An alternative pathway using the nitrile derivative was attempted, where **22** was reacted with diisobutylaluminum hydride (DIBAL-H) at -78 °C to form **24**. These conditions are well known and are used in conjunction with this reducing agent to assist in a controlled reduction of nitrile groups to an intermediate imine, which is hydrolyzed in the presence of water and usually acid.[132,133] However, despite implementing careful control of temperature, and additionally performing this reaction in a Schlenk flask under nitrogen, the reduction could not be controlled and resulted in the amine with no intermediate imine observed (see Appendix Figures S78/S79).

With significant difficulty in one-carbon homologation of the 2'-benzyl position, it was decided that a new approach may be necessary to install an additional carbon.

2.5 Kondrat'eva Synthesis of Pyridoxine for Carbon Homologation

Traditionally, pyridoxine is produced in industry using an oxazole method, which involves a Kondrat'eva cycloaddition resembling a Diels-Alder reaction (Figure 18).[134]

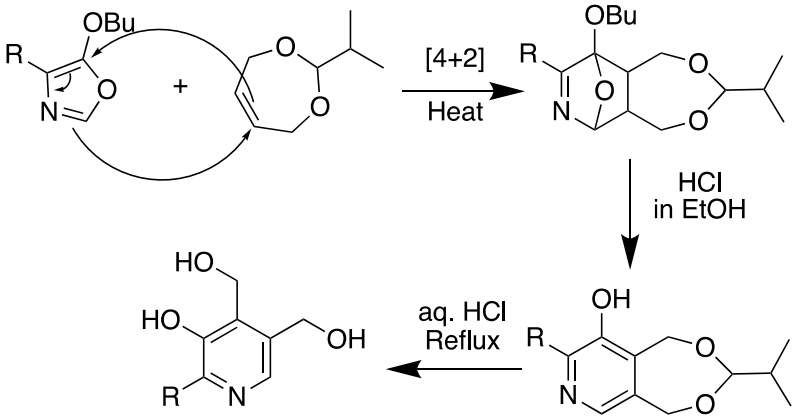

Figure 18. Diels-Alder based Kondrat'eva synthesis of pyridoxine. R-group replacement of the oxazole can produce functionalized derivatives of pyridoxine.

Significant work has been done to optimize the industrial production of pyridoxine, and the procedure has been optimized using alanine as a starting material with an improvement of yield from 1% to 56.4% overall.[134]

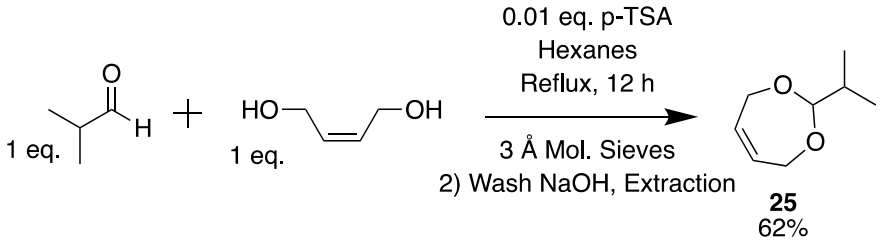

Scheme 8. Proposed synthesis of 2-(propan-2-yl)-4,7-dihydro-2H-1,3-dioxepine for Kondrat'eva synthesis of one-carbon homologated pyridoxine.

Coinciding with the oxazole synthesis, the dienophile **25** is necessary for the Diels-Alder reaction. This product could be synthesized according to Scheme 8 by combining isobutyric aldehyde and cis-1,4-butenediol with para-toluene sulfonic acid (p-TSA). To help with conversion, 3-Å molecular sieves were added, as an equivalent of water is produced during the reaction. Distillation could then be performed to afford **25** in 62% yield as a colourless oil, which was then used later for the Diels-Alder reaction.

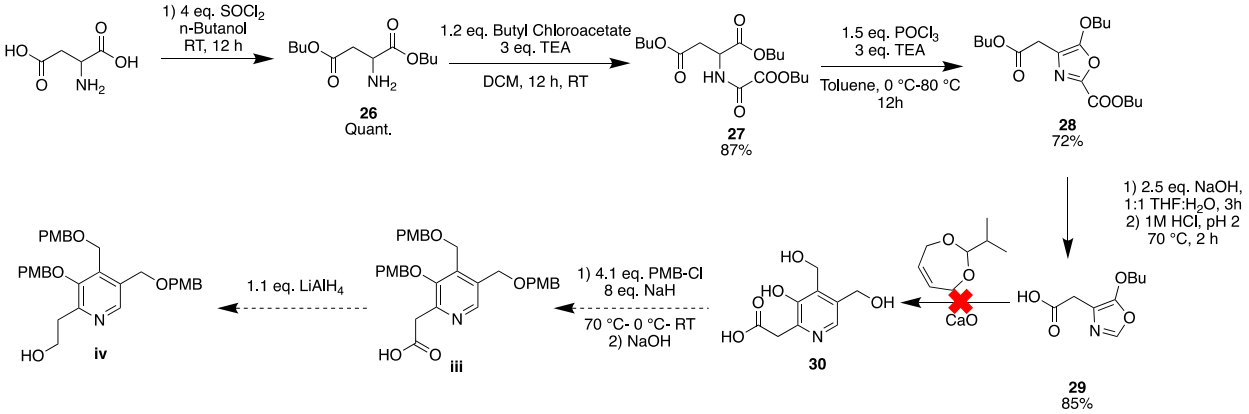

Scheme 9. Proposed synthesis of one-carbon homologated pyridoxine using Diels-Alder chemistry.

Modelling the industrial preparation of pyridoxine, it was proposed that a one-carbon homologation could be accomplished using aspartic acid, which contains a hidden

homologated carbon as a carboxyl group (Scheme 9). To achieve this, the carboxylic acid groups of aspartic acid were first esterified by combination with thionyl chloride in *n*-butanol, giving **26** in quantitative yield. Following the industrial preparation, the use of oxalic acid resulted in a poor yield of **27** of 42%, with difficult purification by azeotropic drying and distillation. Alternatively, **26** could be combined with commercially available butyl chloroacetate in the presence of TEA, with only extraction needed for purification to afford **27** in 87% yield. Formation of the oxazole was then possible using the dehydrating agent phosphorous oxychloride ($POCl_3$) in the presence of TEA, affording **28** with 72% yield. With **28** in hand, the remaining two step saponification and decarboxylation could be conducted,[134] utilizing NaOH and HCl respectively, to produce the final oxazole **29** in 85% yield.

With both the dieneophile **25** (dioxopene) and diene **29** (oxazole) in hand, a Diels-Alder reaction was attempted by adapting previously established literature conditions.[134] Literature conditions require a mixture of the diene and dienophile, where the dienophile acts as the solvent. To the neat reaction is then added calcium oxide as a desiccant, and the mixture is stirred at 150 °C for 12 h. Following this, a 0.1% EtOH solution is added, followed by further addition of HCl, and final precipitation to the desired pyridoxine•HCl salt. However, scaling down these reaction conditions to lab scale production resulted in little to no solubility, and further burning of the product that resulted in carbon soot. To try and promote better solubility, a series of Diels-Alder compatible solvent additions were incorporated, including DMF, toluene, and xylenes.[135,136] Despite the increase in solubility, little to no conversion was observed, with the only product obtained being a shiny black crystalline solid with no observable LC-MS or NMR correlating to the desired

product. It is possible that industrial reactors allow for better mixing conditions and the suspension sees less contact with direct heat, preventing the burning of reactants. The use of a pressure vessel was also hypothesized to provide better reaction conditions, but despite its use, similar results were observed.

Due to multiple unsuccessful cyclization attempts, it was decided that the Kondrat'eva Diels-Alder route may not be compatible with lab conditions. To further assess this conclusion, the production of PN from alanine was also attempted, to ensure this was not just an incompatibility with the one-carbon homologated aspartic acid. As was observed with previous attempts, the Diels-Alder attempts with alanine also proved unsuccessful. As a result, this reaction pathway was deemed unsuitable and left for future optimization.

2.6 Synthesis of Methylated Cold Standards

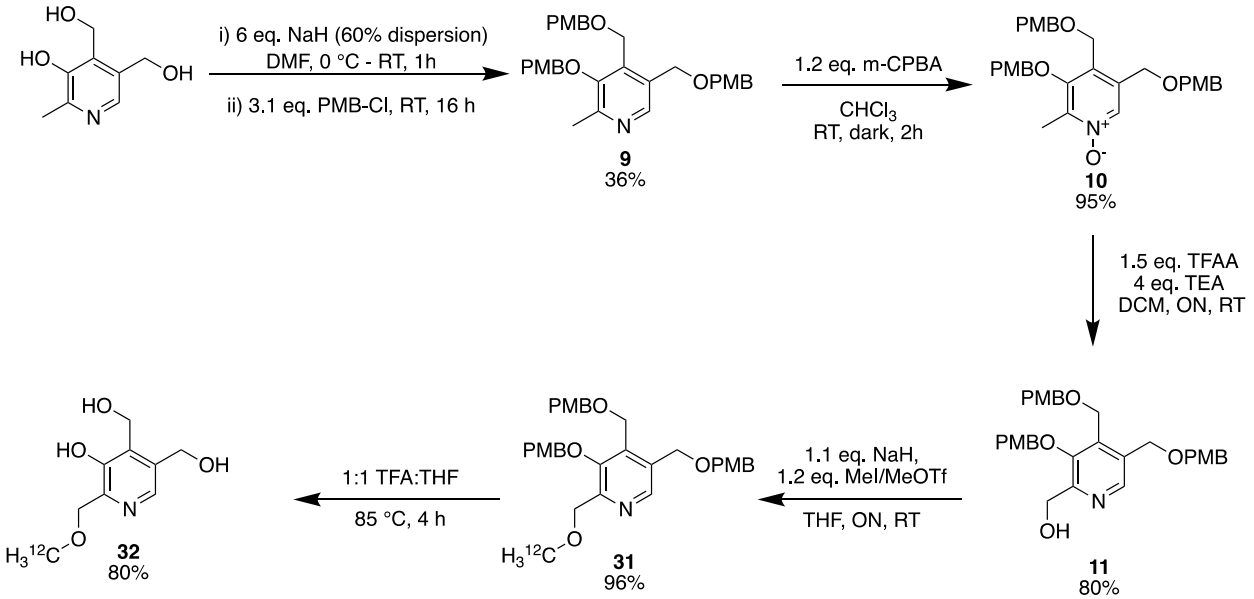

Scheme 10. Synthesis of 2'-O-methyl pyridoxine cold-standard 3. Compounds 9-11 have been previously shown for 2'-fluoro pyridoxine synthesis.

After extensive attempts to homologate the 2'-benzyl position of PN with little success, we returned to literature to find more stable substitutions. From this search, we

discovered antivitamins of PN, which are structurally similar molecules that interact with the same enzymes. More specifically, we found Ginkgotoxin, which is known to interact with only PDXK and PDXP with higher affinity as a competitive substrate.[76] Ginkgotoxin is structurally related to PN but contains a 4'-*O*-methyl substitution that imparts a higher affinity to PDXK than endogenous PN. Finally, this methylation is known to stabilize the 4'-benzyl position from elimination reactions previously observed, which provides a suitable modification and translatable radiolabel that will not degrade *in vivo*.

Through an understanding of the benefits of 4'-*O*-methyl substitution in providing chemical stability, the 2'-benzyl position was first modified following Scheme 10. Synthesis began using previously described **11**, which could be methylated on the 2'-benzyl alcohol using MeI or MeOTf and sodium hydride. For this reaction, both DMF and THF were used as possible solvent choices. THF was ultimately chosen as it is more stable when heated with sodium hydride[137] and is not reactive with TFA for deprotection conditions, with optimal yields after overnight reaction to give **31** in 96% yield. Final deprotection conditions using TFA were then screened, using a temperature range of 40-85 °C (reflux), where it was found that no matter how long the reaction was given, full deprotection was only possible when temperatures approaching 85 °C were used. Additionally, approximately 25% deprotection was observed after 1 hour, but 4 hours was necessary to observe complete conversion to **32**, which was HPLC purified with 80% yield. Unlike Ginkgotoxin, this modification should not affect the metabolic pathway by maintaining the original alcohol groups of pyridoxine. This provides a comparison to assess trapping and metabolism in cells and performance as a radiotracer.

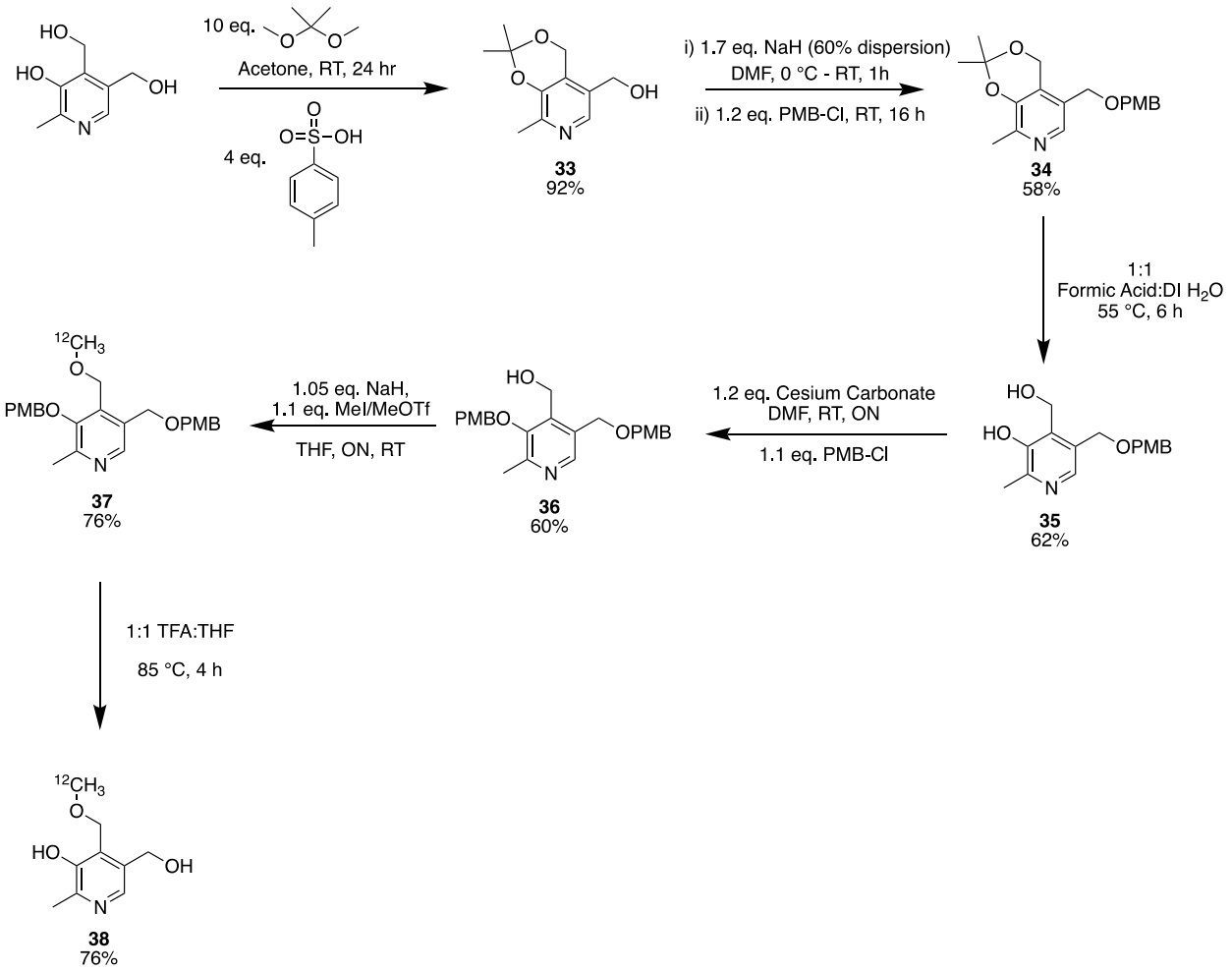

Scheme 11. Synthesis of 4'-O-methyl pyridoxine (Ginkgotoxin) cold-standard 4.

With Ginkgotoxin providing suitable qualities as a radiotracer, we devised **scheme 11** by modifying existing conditions.[138] Protection of the phenolic and 4'-benzyl alcohol of pyridoxine to an acetonide could be performed using 2,2-dimethoxy propane and *p*-TSA in acetone. It was found that unlike literature conditions, isolation of **33** could be performed by precipitation in 5:1 pentanes:diethyl ether to afford **34** with 92% yield, without necessitating chromatography. The 5'-benzyl alcohol could then be selectively protected using sodium hydride and PMB-Cl to afford **35** with 58% yield. This was done to again provide acid-lability that is more suitable to radiochemistry hot-cells, unlike previously reported benzyl ether protecting groups.[138] The acetonide was then selectively

deprotected over the PMB-ether using mild conditions of 1:1 formic acid:DI H_2O at 55 °C, giving **35** with a reasonable 62% yield. Selective deprotonation of the phenolic alcohol with pK_a of 9.8[139] was then performed using cesium carbonate, allowing protection to the PMB-ether product **36** with 60% yield. Methylation of the 4'-benzyl alcohol could then be performed using MeI or MeOTf and sodium hydride in THF to give **37** in 76% yield. Final deprotection using 1:1 TFA:THF at 85 °C for 4 hours allowed for full deprotection conversion, with HPLC purification to afford **38** with 76% yield.

2.7 Evaluation of Metabolism of Cold Standards

With cold-standard pyridoxine derivatives in hand, an understanding of metabolic alterations in cancer cell lines (A549 and H460) was needed. Metabolomics, or metabolic profiling, is a technique widely applied for unveiling novel compound behaviour in biological systems and their metabolism.[140] Through changes of metabolite levels, an understanding can be gained for how molecules interact *in vitro* or *in vivo*, which is critical for compounds intended for monitoring metabolic changes in oncogenic disease states by PET imaging. Currently, many analytical techniques are employed for metabolomics including NMR and MS, but the higher sensitivity of MS makes it the predominant choice. In combination with liquid chromatography (LC), LC-MS can separate and evaluate individual metabolites in either an untargeted (global detection) or targeted (validating known metabolites) fashion with comparison to metabolite databases.[141]

Through collaboration with the uOttawa Metabolomics Core Facility (MCF), a targeted metabolic profiling of our cold standards was performed. A549 and H460 cells were cultured in lab, where they were then incubated with each of the standards to undergo metabolic change and equilibration using the *in vitro* enzymes: PDXK, PDXP,

and PNPO (detailed description in **Materials and Methods Section 4.4).** These cells were then lysed, extracted, and the polar metabolites were evaluated by LC-MS analysis using ESI-MS coupled to the Agilent Metabolomics Dynamic MRM Database for comparison to known precursor and product ion pairs of PN and its derivatives (Figure 19). It is important to note that standards were not prepared for metabolic product validation due to synthetic difficulty, so ion chromatograms and tandem mass spectrometry (MS/MS) detection were used without 100% confirmation.

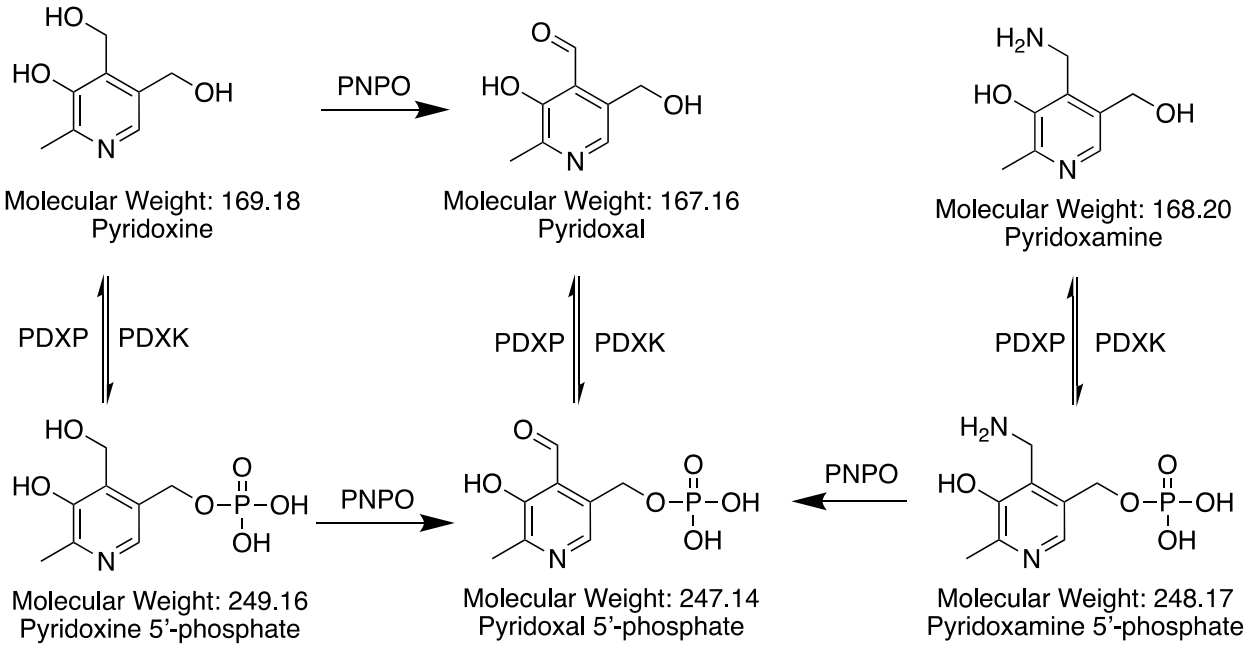

Figure 19. Metabolic alterations of pyridoxine. PDXP, pyridoxal phosphatase; PDXK, Pyridoxal kinase; PNPO, pyridoxine phosphate oxidase.

Cold-standard **1**, C_6-fluoro pyridoxine, was the first compound evaluated for metabolic alterations. Since carbon-6 is not implicated in known metabolism, the proposed metabolic products should mimic pyridoxine, but with the addition of the mass of fluorine (Figure 20).

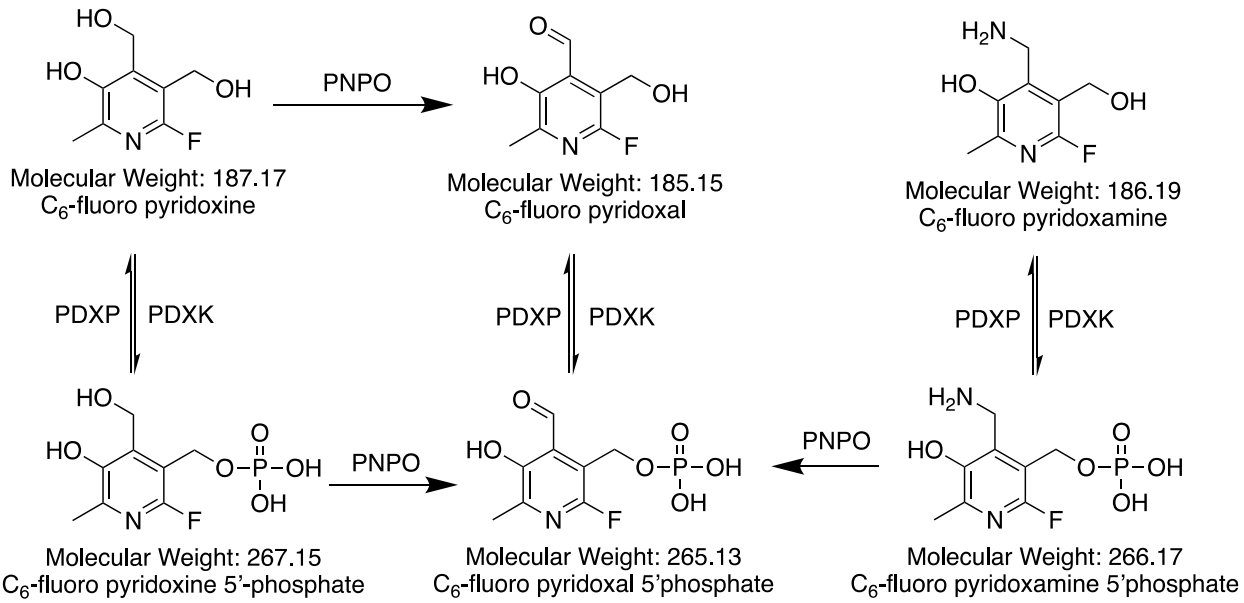

Figure 20. Metabolic alterations of C_6-fluoro pyridoxine. PDXP, pyridoxal phosphatase; PDXK, Pyridoxal kinase; PNPO, pyridoxine phosphate oxidase.

All potential metabolic products were screened, and relevant mass detection, retention times, and ion fragments were recorded in positive and negative ion mode (see Appendix Figure S80). First, the standard of C_6-fluoro pyridoxine was detected readily in both cell lines (Figure 21). Increasing collision energy saw greater fragmentation of the product, with comparable fragments to the pyridoxine standard (see Appendix Figure S81).

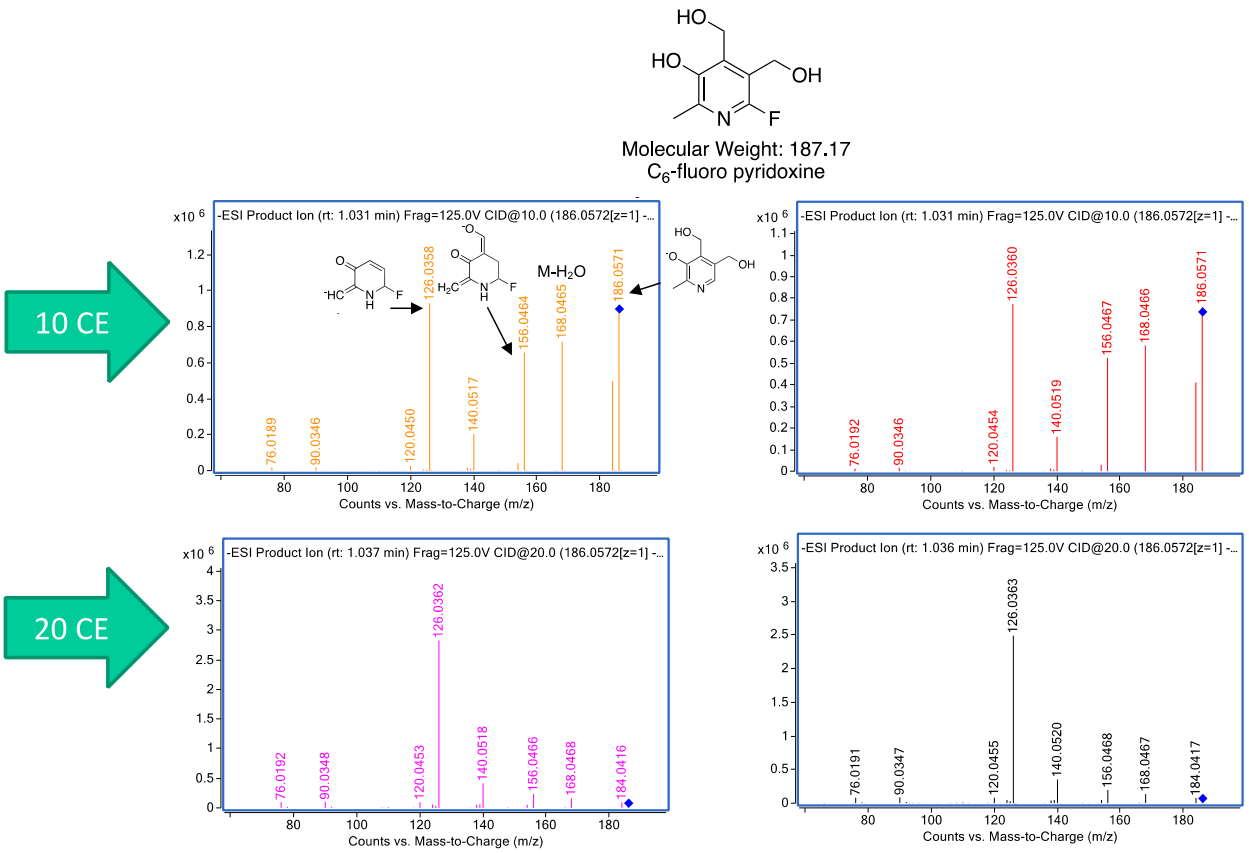

Figure 21. C_6-fluoro pyridoxine MS/MS spectra. Analysis was performed using negative electrospray ionization (-ESI). On the left, H460 human non-small cell lung cancer cells (large cell carcinoma) were tested. On the right, A549 squamous adenocarcinomic human lung alveolar basal epithelial cells were tested. Fragmentation of ions utilized collision induced dissociation (CID) at increasing collision energy (CE), which refers to the rate of acceleration as the ions enter the quadrupole, promoting higher rates of fragmentation.

In addition to the standard, a molecular ion peak corresponding to C_6-fluoro pyridoxal was detected in both cell lines, alongside expected fragment ions (Figure 22). This is an indication that not only is C_6-fluoro pyridoxine transported into the cells but can interact with PNPO to oxidize the 4'-benzyl alcohol position, despite modification at the carbon-6 position.

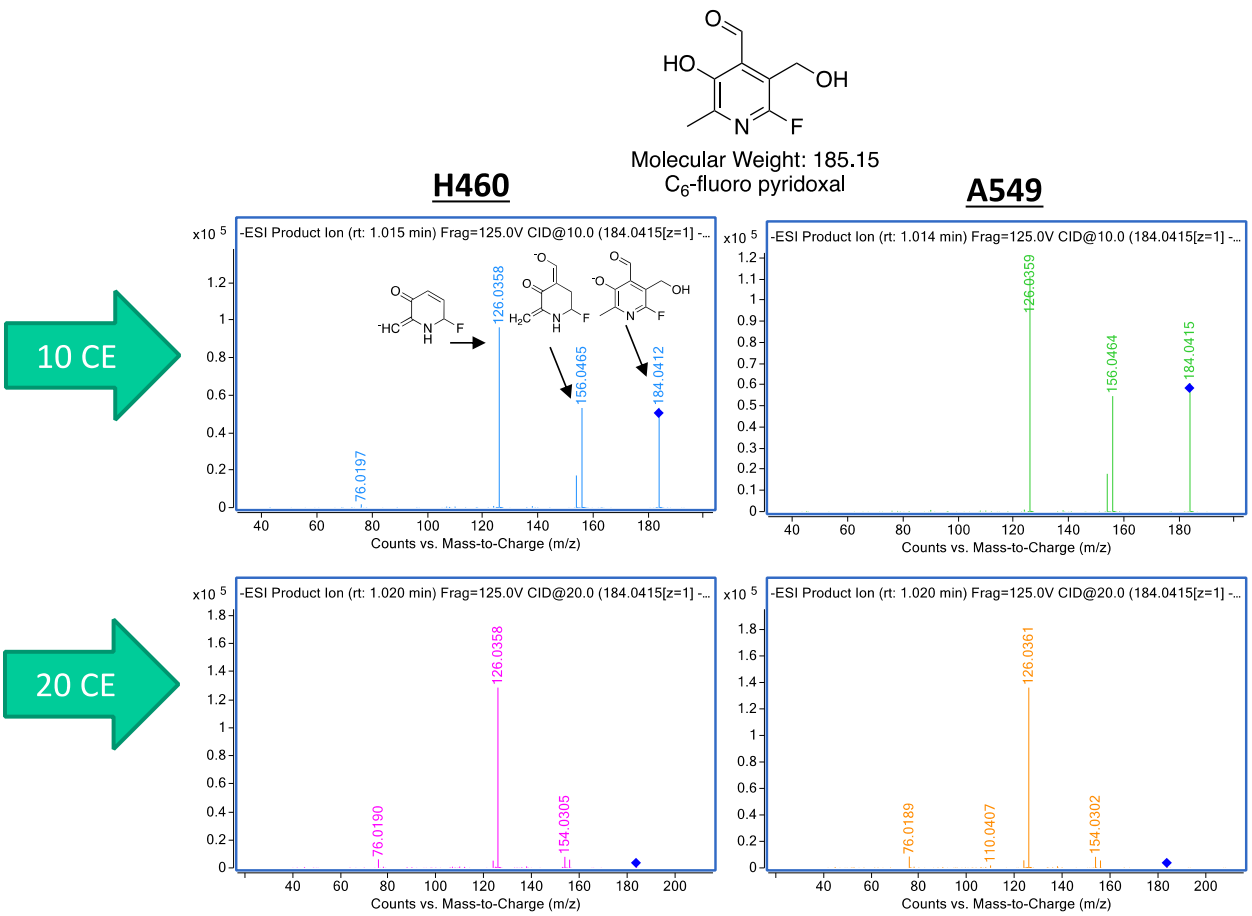

Figure 22. C6-fluoro pyridoxal MS/MS spectra. Analysis was performed using negative electrospray ionization (-ESI). On the left, H460 human non-small cell lung cancer cells (large cell carcinoma) were tested. On the right, A549 squamous adenocarcinomic human lung alveolar basal epithelial cells were tested. Fragmentation of ions utilized collision induced dissociation (CID) at increasing collision energy (CE), which refers to the rate of acceleration as the ions enter the quadrupole, promoting higher rates of fragmentation.

Furthermore, detection of masses corresponding to the C6-fluoro pyridoxine 5'-phosphate metabolite was seen in both cell lines (Figure 23). More specifically, fragments corresponding to the loss of a water molecule, with other MS/MS fragments being present such as the loss of the phosphate group. This is promising, as C6-fluoro pyridoxine can interact with PDXK, the enzyme of interest, and be phosphorylated. However, despite these metabolites being detected, very low abundance of the parent ion and high fragmentation with ions matching defluorinated fragments shows a characteristic loss of

fluorine from the carbon-6 position, indicating instability. The loss of fluorine at this position is concerning, as defluorination *in vivo* can result in high bone uptake of [^{18}F]F^{-}, which impacts imaging quality and patient health by off-target interactions.[142]

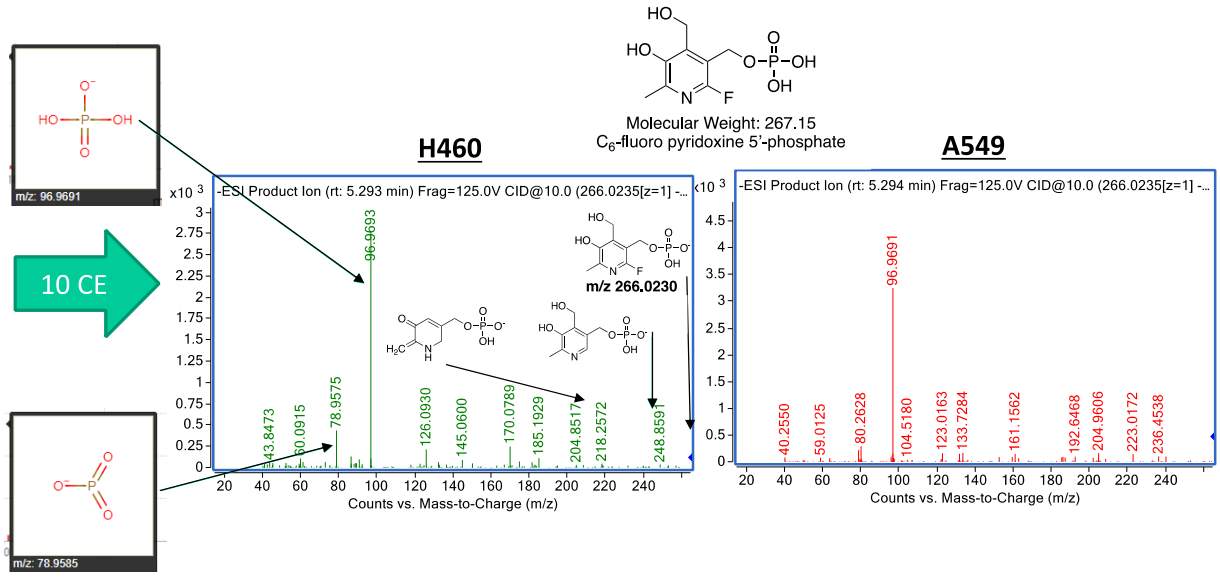

Figure 23. C$_6$-fluoro pyridoxine 5'-phosphate MS/MS spectra. Analysis was performed using negative electrospray ionization (-ESI). On the left, H460 human non-small cell lung cancer cells (large cell carcinoma) were tested. On the right, A549 squamous adenocarcinomic human lung alveolar basal epithelial cells were tested. Fragmentation of ions utilized collision induced dissociation (CID) at increasing collision energy (CE), which refers to the rate of acceleration as the ions enter the quadrupole, promoting higher rates of fragmentation.

Further analysis was performed to identify pyridoxamine and pyridoxal 5'-phosphate products. Standard pyridoxine analysis saw detection of both metabolic derivatives, however C$_6$-fluoro pyridoxal 5'-phosphate or C$_6$-fluoro pyridoxamine products could not be identified. The lack of detection of the fluorinated derivative of PLP is unexpected, since we found independent interactions and products from PDXK and PNPO. It may be possible that due to the instability of the C$_6$-fluorine, or low signal detection, that products may be possible but cannot be detected by MS/MS due to low signal intensity. It may be possible to improve signal intensity by increasing the concentration of standard incubated or increasing cell count. However, despite this

finding, the independent engagement of enzymes can still facilitate metabolic alterations and cell trapping. In addition to not detecting fluorinated-PLP, fluorinated pyridoxamine formation was not seen. This finding is unexpected, and is most likely also a detection limit issue, but is less of a concern for CDDP-resistance monitoring which is focused on PDXK/PDXP interactions. Ultimately, C_6-fluoro pyridoxine (cold-standard **1**) appears to interact with PDXK and PNPO in A549 and H460 cell lines, producing critical metabolic products for monitoring by PET-imaging.

Cold-standard **3**, 2'-*O*-methyl pyridoxine, was the next compound evaluated for metabolic alterations. Since the 2'-benzyl position is not implicated in known metabolic transformations, the proposed metabolic products should mimic pyridoxine, but with the addition of the mass of an *O*-methyl group (Figure 24).

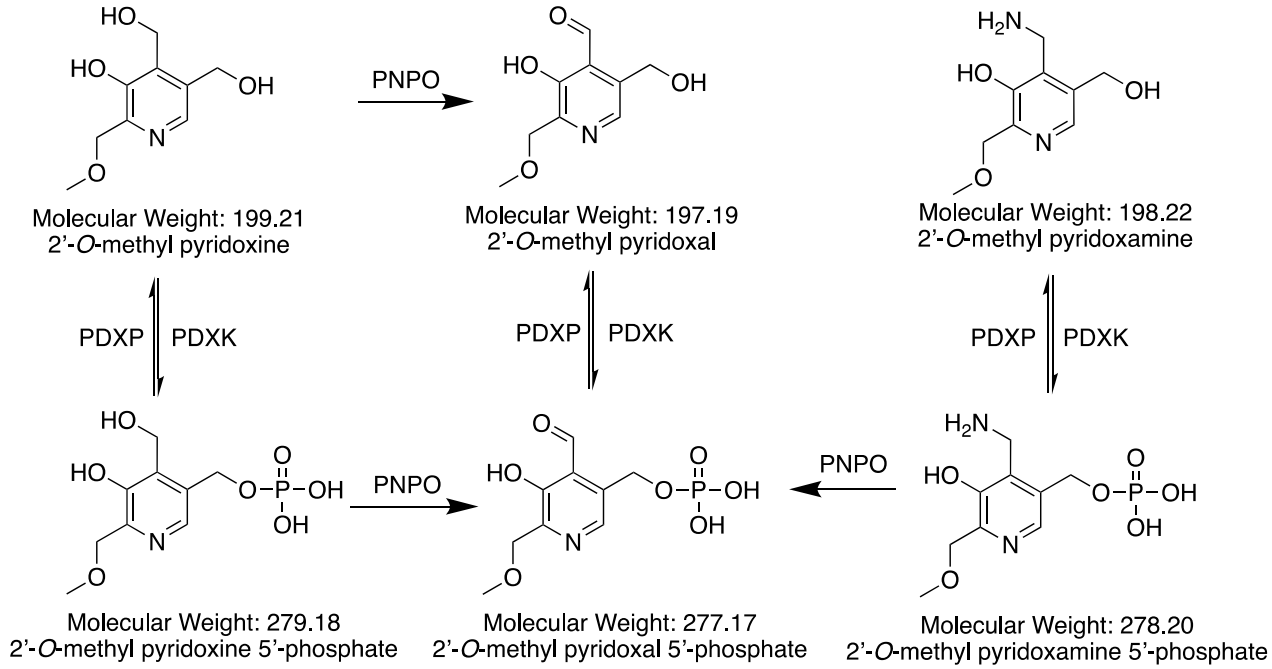

Figure 24. Metabolic alterations of 2'-*O*-methyl pyridoxine. PDXP, pyridoxal phosphatase; PDXK, Pyridoxal kinase; PNPO, pyridoxine phosphate oxidase.

All potential metabolic products were screened, and relevant mass detection, retention times, and ion fragments were recorded in positive and negative ion mode (see Appendix Figure S82). The molecular ion of 2'-*O*-methyl pyridoxine was detected readily in both cell lines, with fragmentation patterns similar to standard pyridoxine (Figure 25). This indicates that cold-standard **3** can be transported into the cancer cell lines.

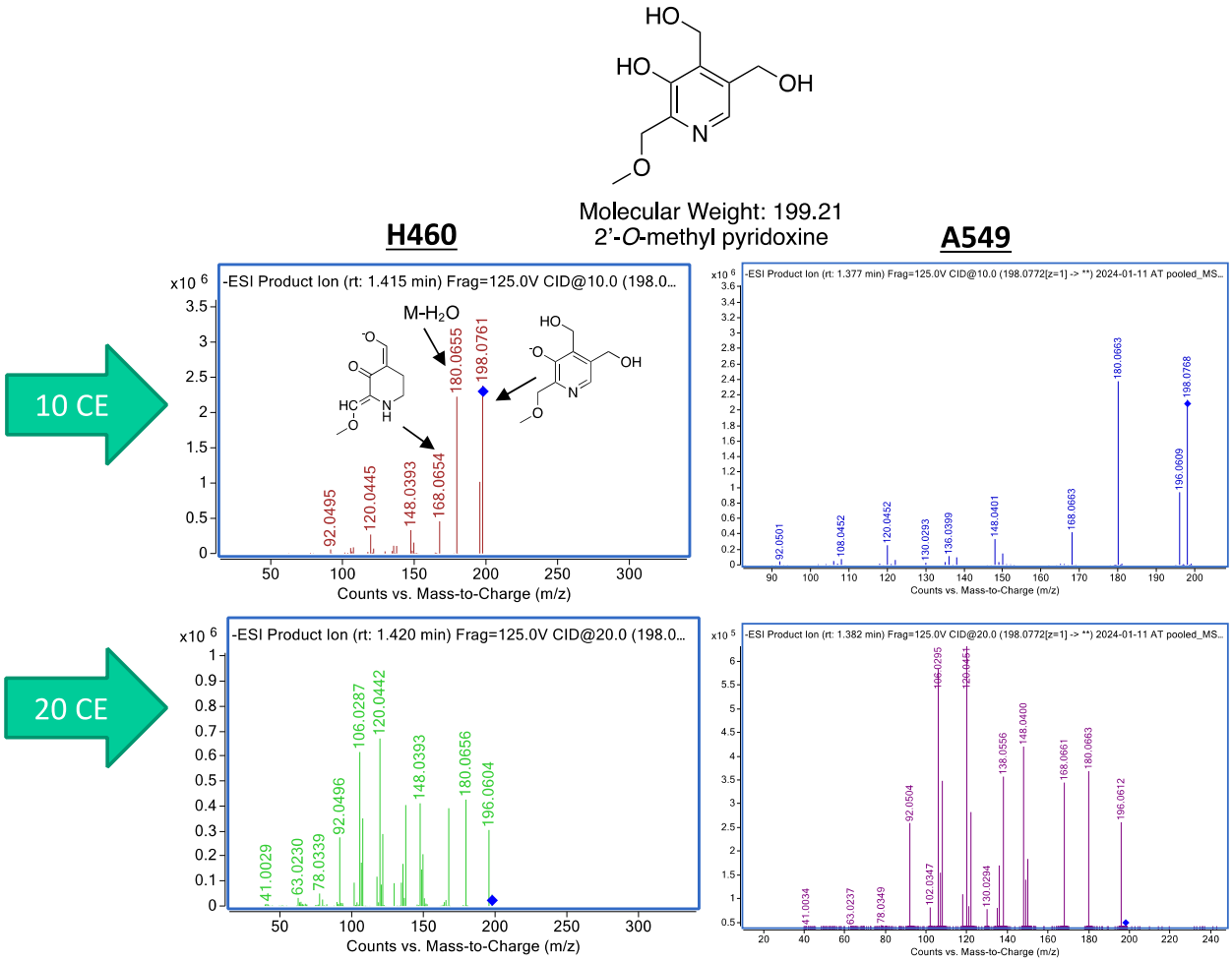

Figure 25. 2'-*O*-methyl pyridoxine MS/MS spectra. Analysis was performed using negative electrospray ionization (-ESI). On the left, H460 human non-small cell lung cancer cells (large cell carcinoma) were tested. On the right, A549 squamous adenocarcinomic human lung alveolar basal epithelial cells were tested. Fragmentation of ions utilized collision induced dissociation (CID) at increasing collision energy (CE), which refers to the rate of acceleration as the ions enter the quadrupole, promoting higher rates of fragmentation.

In addition to the standard, the molecular ion of the metabolite 2'-*O*-methyl pyridoxine 5'-phosphate could be detected in both cell lines, alongside phosphate fragments (Figure 26).

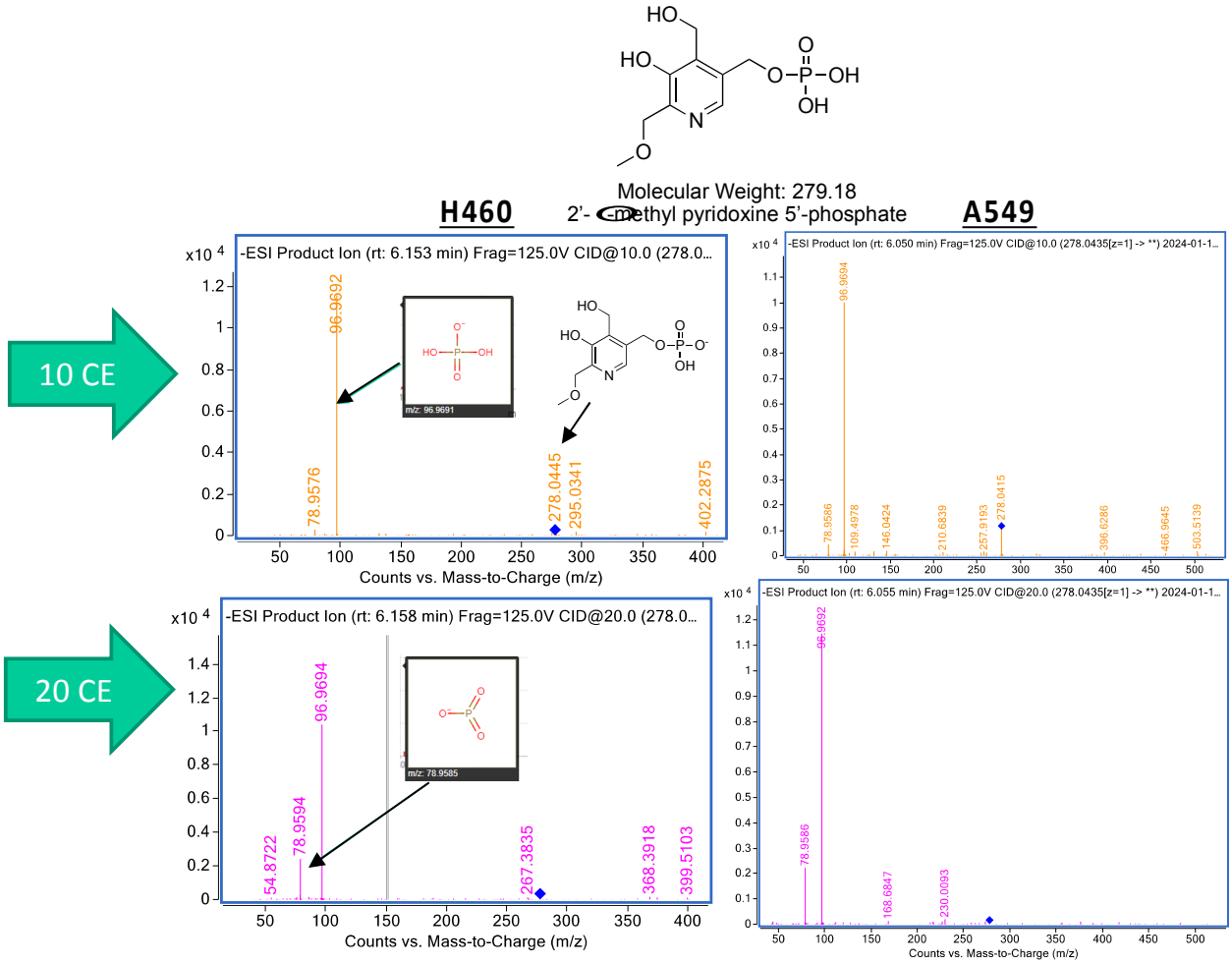

Figure 26. 2'-*O*-methyl pyridoxine 5'-phoshate MS/MS spectra. Analysis was performed using negative electrospray ionization (-ESI). On the left, H460 human non-small cell lung cancer cells (large cell carcinoma) were tested. On the right, A549 squamous adenocarcinomic human lung alveolar basal epithelial cells were tested. Fragmentation of ions utilized collision induced dissociation (CID) at increasing collision energy (CE), which refers to the rate of acceleration as the ions enter the quadrupole, promoting higher rates of fragmentation.

Moreover, the molecular ion corresponding to the metabolic product 2'-*O*-methyl pyridoxal 5'-phosphate were detected in both cell lines (Figure 27).

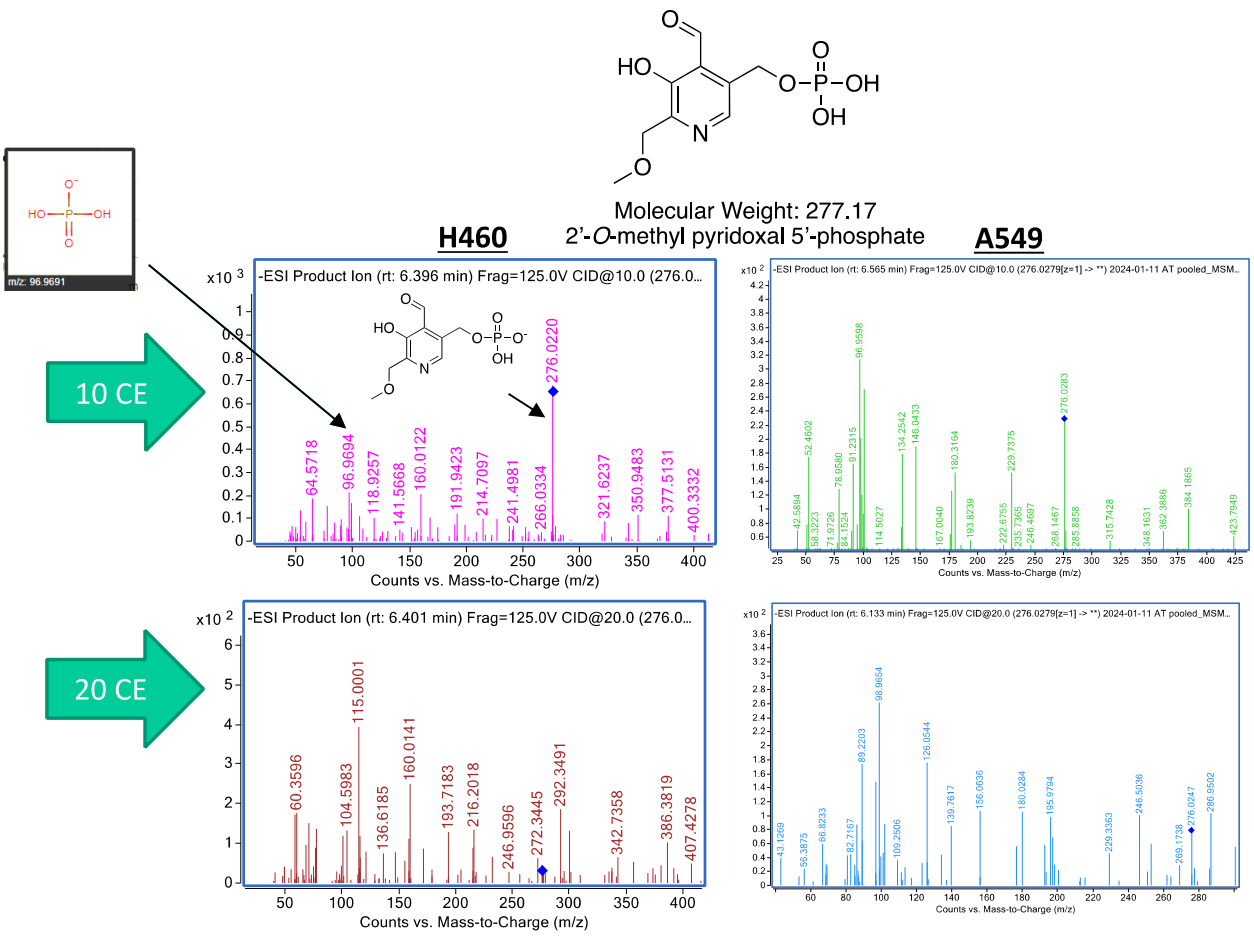

Figure 27. 2'-*O*-methyl pyridoxal 5'-phoshate MS/MS spectra. Analysis was performed using negative electrospray ionization (-ESI). On the left, H460 human non-small cell lung cancer cells (large cell carcinoma) were tested. On the right, A549 squamous adenocarcinomic human lung alveolar basal epithelial cells were tested. Fragmentation of ions utilized collision induced dissociation (CID) at increasing collision energy (CE), which refers to the rate of acceleration as the ions enter the quadrupole, promoting higher rates of fragmentation.

The detection of both phosphorylated and oxidized derivatives of 2'-*O*-methyl pyridoxine indicates a ready interaction with PDXK and PNPO. Unlike the fluorinated cold standard, the detection of a methylated analogue to PLP not only shows enzymatic interactions, but also a more comparable metabolic profile and a product mimicking native pyridoxal 5'-phosphate. Additionally, 2'-*O*-methyl pyridoxamine was detected in H460 cells and suspected to be in A549 cells (low sample quantity limited MS/MS analysis) (Figure 28). As a result, this provides an effective probe with a similar metabolic profile to

pyridoxine, which is translatable to radiochemical synthesis and use for tracking metabolic activity using PET imaging.

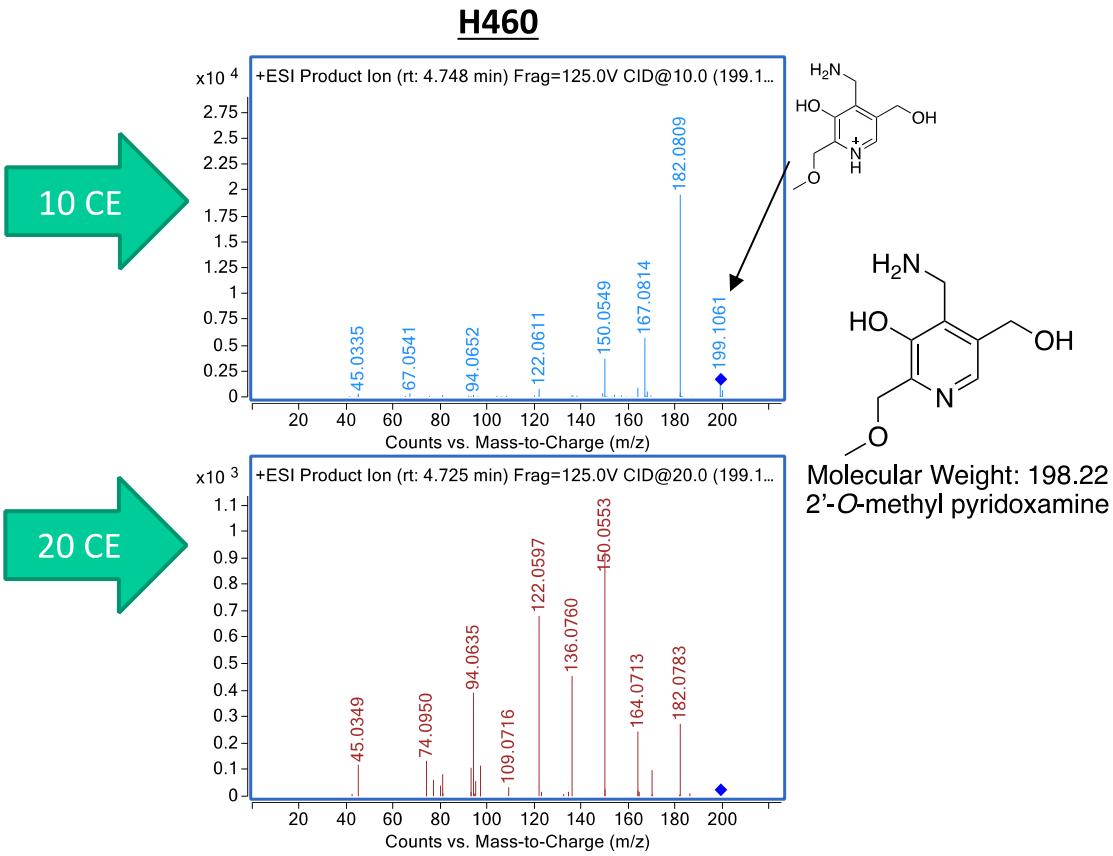

Figure 28. 2'-*O*-methyl pyridoxamine MS/MS spectra. Analysis was performed using positive electrospray ionization (+ESI). H460 human non-small cell lung cancer cells (large cell carcinoma) were tested. Fragmentation of ions utilized collision induced dissociation (CID) at increasing collision energy (CE), which refers to the rate of acceleration as the ions enter the quadrupole, promoting higher rates of fragmentation.

Cold standard **4**, 4'-*O*-methyl pyridoxine, was the next compound evaluated for metabolic interactions. Since the 4'-benzyl position is implicated in typical metabolic transformations, the proposed metabolic products should be limited compared to pyridoxine, with only the phosphorylated and non-phosphorylated products being possible (Figure 29). As previously discussed, this should limit downstream metabolic products, simplifying metabolomics, pharmacokinetics, while still allowing for cell trapping and reporting on the same enzymatic processes of interest. As of the time of writing this

thesis, the standard was submitted to the metabolomics facility, and is awaiting analysis due to a backlog of samples, with results expected to come in May 2024. However, it is expected based on literature precedence, that metabolism will produce the desired products observable by ESI MS/MS analysis.[76]

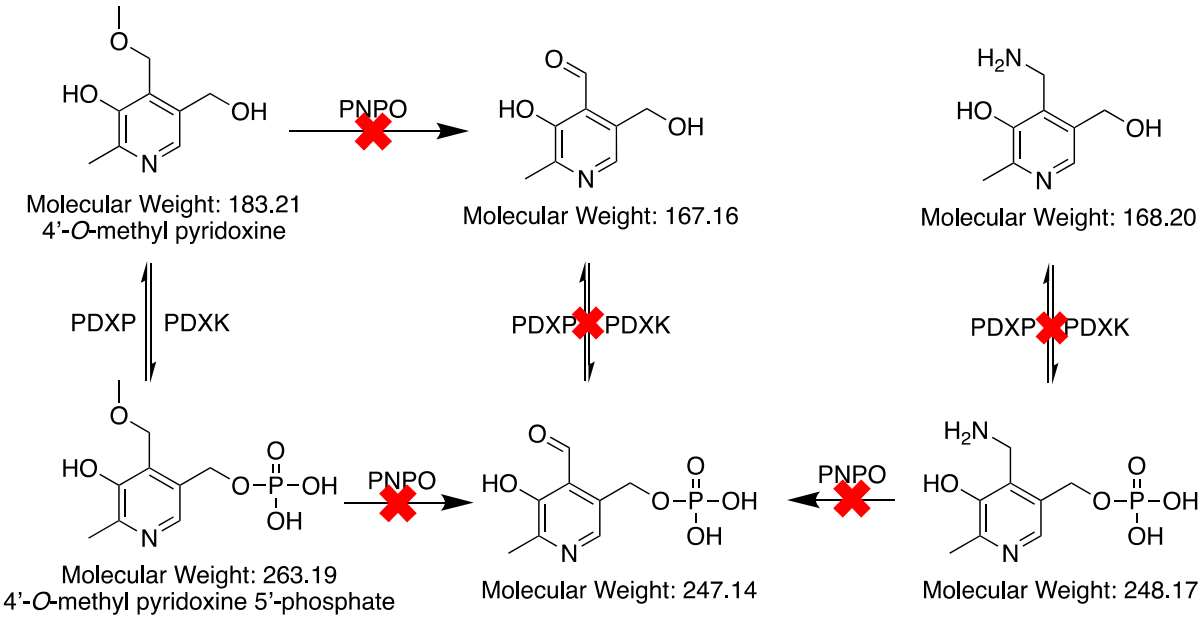

Figure 29. Metabolic alterations of 4'-*O*-methyl pyridoxine. PDXP, pyridoxal phosphatase; PDXK, Pyridoxal kinase; PNPO, pyridoxine phosphate oxidase. Note metabolic conversions and enzymes typical to pyridoxine will not be engaged due to blocking of the 4'-benzyl position with *O*-methyl substitution.

With promising results for cold standards in metabolomics, observing transport and relevant enzyme interactions, these molecules and their precursors were prepared for radiochemical transformation. Radiochemical probes will not be rescreened for metabolomics but are expected to behave in an identical fashion. Metabolic products that are formed will undergo cell trapping, as only the non-phosphorylated and non-oxidized product can be transported from the cell, providing longer residence times for PET-CT imaging before the molecule is shuttled out. Changes in trapped radiolabelled products and their metabolites could then be used to differentiate between resistant and non-resistant CDDP cancer cells, with detectable contrast changes. In healthy patients, with

high vitamin-B_6 metabolism (especially PDXK), we would expect higher contrast in non-resistant cancer cells. During CDDP-resistance onset, less PDXK activity in cancer cells will result in less trapping, reducing imaging contrast.

2.8 Radiochemical Transformations and Validation

To produce radiolabelled counterparts for synthesized and metabolically active cold-standard precursors, work was translated to the University of Ottawa Heart Institute (UOHI) radiochemistry facility. Prior to production, product validation was necessary using an analytical radio-HPLC (**Materials and Methods Section 4.6**) to establish precursor, intermediate, and final product retention times for comparison to radiolabelled products using validated standards previously described (Table 1 and Appendix Figures S83-S92).

Table 1. Cold-standard retention times on analytical radio-HPLC.

Cold-Standard (Compound #)	Retention Time (min)
Pyridoxine	2.6
Methyl Iodide	12
C6-NH2 Pyridoxine (7)	2.9
C6-F Pyridoxine (8)	2.1-3
2'-OH-Pyridoxine (11)	16
2'-O-Methyl PMB Pyridoxine (31)	16.75
2'-O-Methyl Pyridoxine (32)	6.8
4'-OH-Pyridoxine (36)	14.2
4'-*O*-Methyl PMB Pyridoxine (37)	15.7
4'-*O*-Methyl Pyridoxine (38)	7.4

Prior to radiolabelling, standards for methylated intermediates, and final products were also analyzed for retention on Semi-Prep radio-HPLC systems attached to the

automated TRACERlab synthesis modules (Table 2 and Figures S93-S95). By recording these retention times, product peaks from radiochemical conversions could be more easily identified and isolated based on time to elute, especially during initial reaction screenings which provide more complicated spectra.

Table 2. Cold-standard retention times on Semi-Prep radio-HPLC.

Cold-Standard (Compound #)	Retention Time (min)
^{12}C-MeI/^{12}C-MeOTf /^{12}C-MeOH	6-9
2'-*O*-Methyl Pyridoxine (32)	5-7
4'-*O*-Methyl Pyridoxine (38)	4.5-6

For [^{18}F]fluorine labelling, synthesis was conducted on a TRACERlab FX-FN module from GE healthcare. Cyclotron production results in [^{18}F]HF in 2.5 mL of water, which was dispensed directly into the reactor without trapping or azeotropic drying, due to the need of aqueous HF for reaction. A 1-hour proton beam of [^{18}O-H_2O] produced approximately 1600 millicuries (mCi) of [^{18}F]HF (58.5 nmol), which was added directly to the reaction vial containing pre-incubated 6-amino pyridoxine (7) with sodium nitrite as a diazo species and reacted for 1 h at 60 °C (Scheme 12). Long cyclotron beaming was utilized to maximize the effective concentration of HF (~40 μM), which is suggested to occur in the 1 hour provided time by Siemen's engineers. After a NaOH quench and filtration through an aluminum cartridge to trap [^{18}F]NaF, Semi-Prep radioHPLC detected a major radioactive peak from 6-14 minutes, with no corresponding UV peaks (Figure 30).

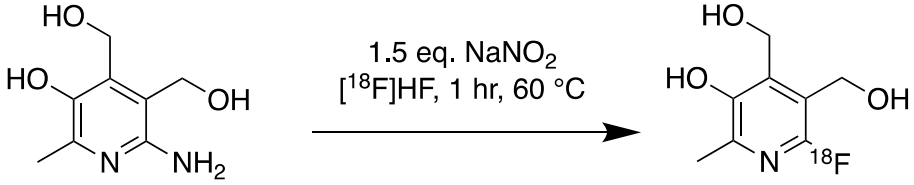

Scheme 12. Radiosynthesis of [^{18}F]C_6-fluoro pyridoxine.

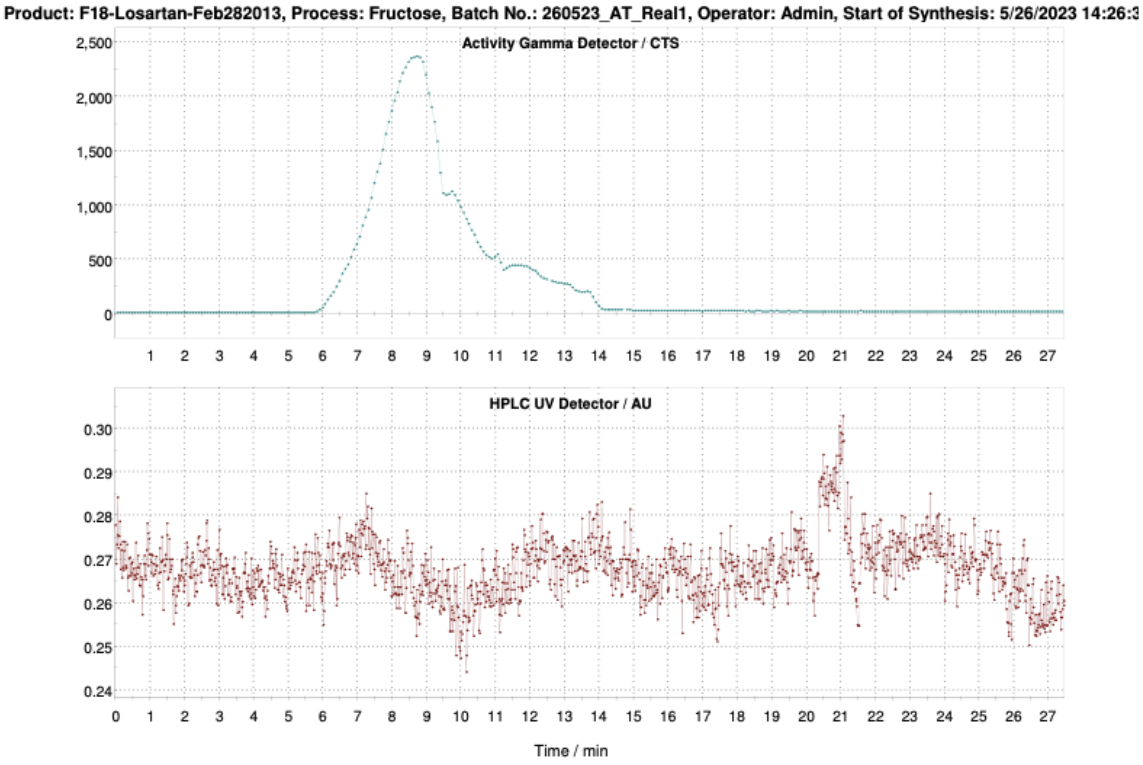

Figure 30. Semi-Prep radio-HPLC trace for synthesis of [^{18}F]C6-fluoro pyridoxine using [^{18}F]-HF, with UV detection at 254 nm.

Isolated product was injected into the analytical radioHPLC, showing one peak at 2.9 min, matching the expected retention time for 6-amino pyridoxine (Figure 31).

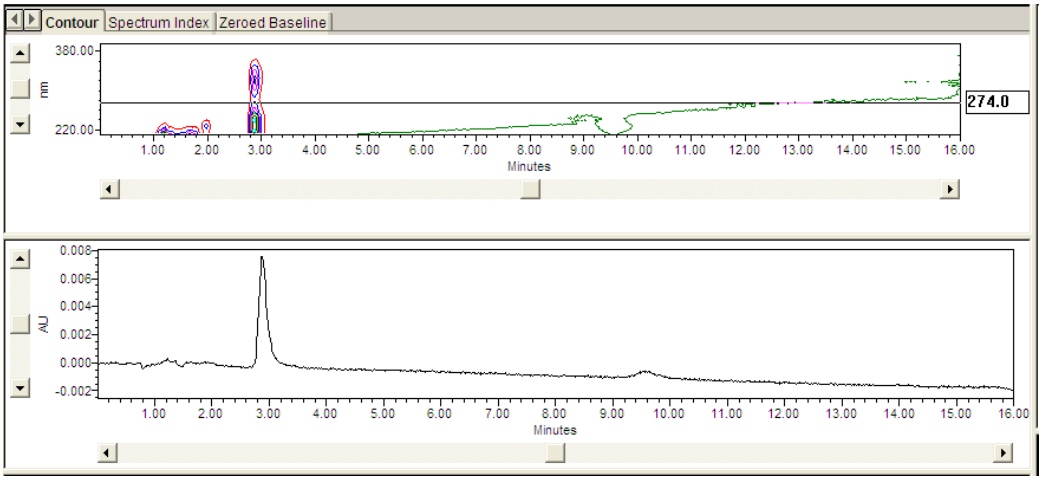

Figure 31. UV chromatogram for C_6-fluoro pyridoxine radiosynthesis using [^{18}F]-HF on analytical radioHPLC. The peak at 2.9 minutes corresponds to the expected retention time for the standard of 6-amino pyridoxine, instead of [^{18}F]C_6-fluoro pyridoxine, measured at 274 nm.

Additionally, radiation detection showed no significant isolated products, with high-background radioactivity (Figure 32). Since no major peaks matched the UV detected product at 2.9 min, it is suspected no significant reaction occurred, with starting material **7** remaining. The high background radioactivity, despite aluminum cartridge filtering, is most likely residual [^{18}F]NaF that does not interact well with the column, and rather broadens out to create high activity throughout. As a result, due to low successful reactivity over multiple attempts, [^{18}F]C_6-fluoro pyridoxine could not be formed due to poor translation of Sandmeyer conditions, which necessitate much higher concentrations of HF to occur (~40 μM in radiochemistry vs. 28.1 M in cold-chemistry).

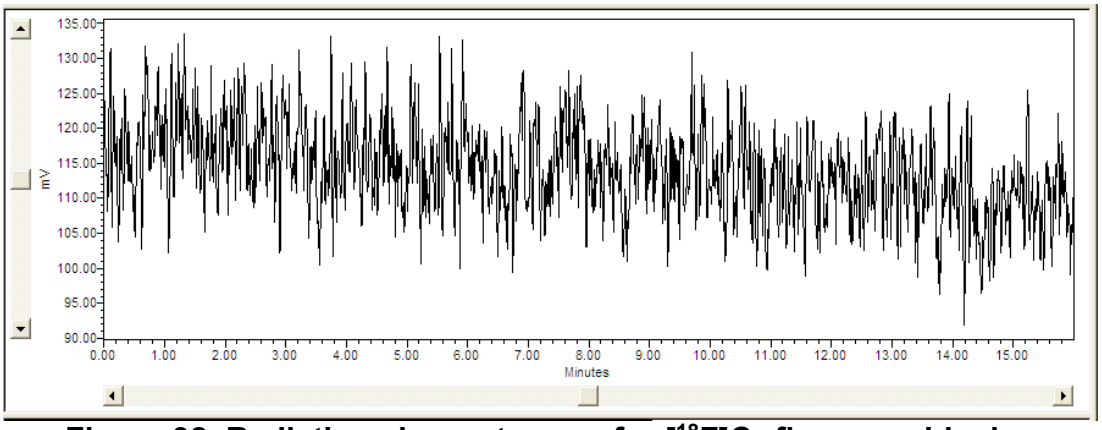

Figure 32. Radiation chromatogram for [^{18}F]C_6-fluoro pyridoxine radiosynthesis using [^{18}F]-HF on analytical radioHPLC. High background radiation detection of [^{18}F]-NaF was observed, with no detection of [^{18}F]C_6-fluoro pyridoxine.

For [^{11}C]-carbon labelling, synthesis was conducted on a TRACERlab FX C Pro module from GE healthcare. Cyclotron production of [^{11}C]CO_2 is further derivatized through a gas-phase in-module system by various stationary phases in a closed loop, with eventual production of either [^{11}C]MeI or [^{11}C]MeOTf (Detailed description provided in **Materials and Methods Section 4.6**). A 20-minute proton beam of ^{14}N was utilized to produce ~500 mCi of [^{11}C]CO_2, which after column conversion, provided on average 300 mCi of methylating agent in the reaction vial after 8-10 min of column circulation.

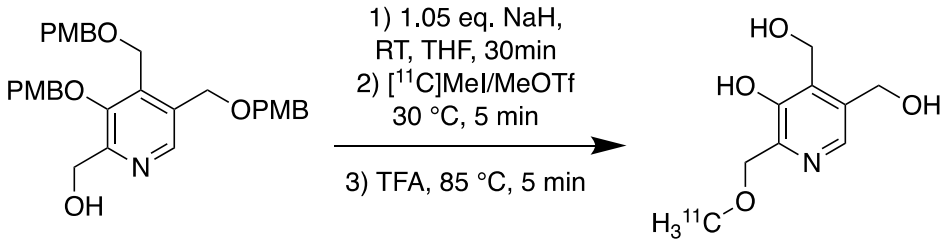

Scheme 13. Radiosynthesis of [^{11}C]2'-O-methyl pyridoxine.

For 2'-*O*-methyl pyridoxine radiosynthesis, precursors were reacted with both [^{11}C]MeI and [^{11}C]MeOTf to establish the best methylating conditions (Scheme 13). Prior testing with cold standard showed a retention time of 5-7 minutes in 80:20 MeCN:H_2O, which was used as reference for isolation. Multiple attempts were made using MeI; however, despite changes in temperature (30-65 °C) and reaction time (5-10 min), the only detected products were between 8-12 minutes by UV and radiation detection (Figure 33). The peaks at these positions are believed to be associated with aqueous conversion of residual methylating agent to [^{11}C]MeOH, which drags through the column starting around 6-8 minutes. As a result, it was determined MeI is not suitable to methylate the precursor in the limited reaction time, so methyl triflate was used in place. Using the same conditions, [^{11}C]MeOTf produced a single UV and radiation peak from 4-6 minutes, which is closer to 2'-*O*-methyl pyridoxine's standard retention time (Figure 34). Longer drying times after acidic deprotection of 3 minutes at 120 °C also assisted in removal of residual unreacted methylating product. 7.38 mCi of isolated [^{11}C]2'-*O*-methyl pyridoxine, with 600 microcuries (μCi) being dispensed for quality control by analytical radio-HPLC.

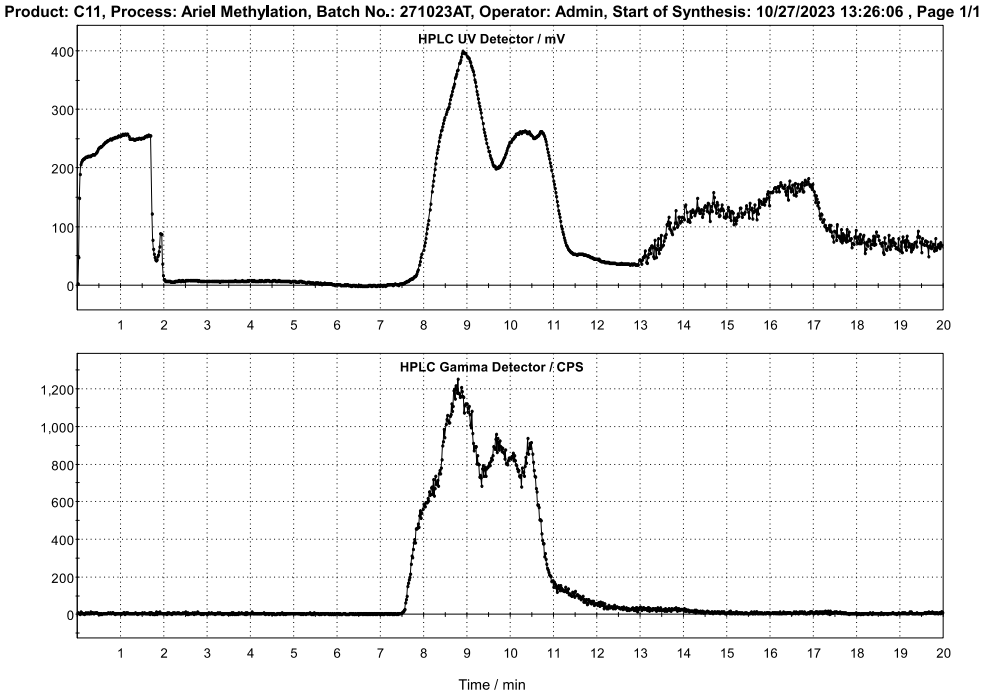

Figure 33. Semi-Prep radio-HPLC trace for synthesis of [^{11}C]2'-O-methyl pyridoxine using [^{11}C]MeI at 280 nm.

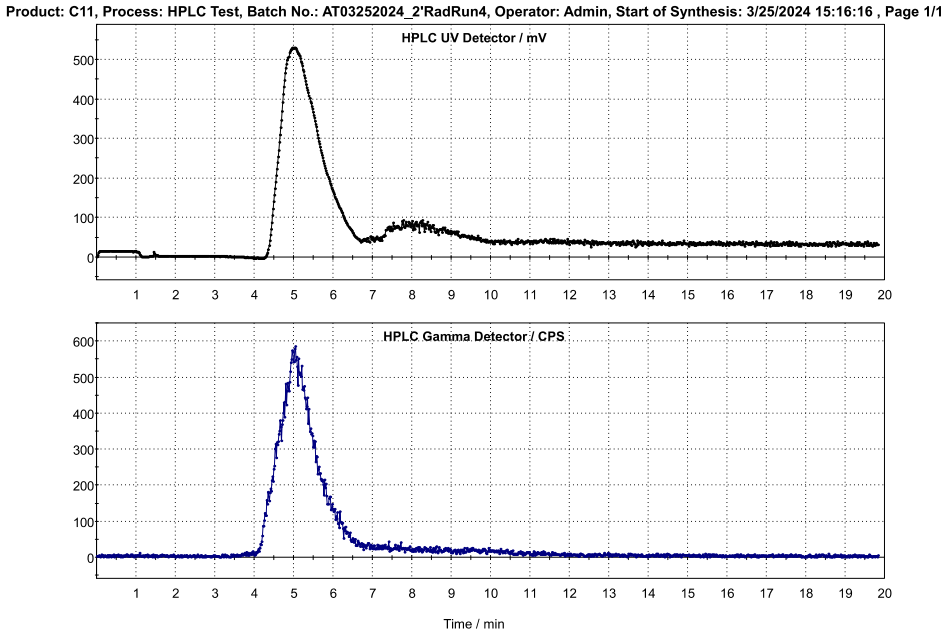

Figure 34. Semi-Prep radio-HPLC tracer for synthesis of [^{11}C]2'-O-methyl pyridoxine using [^{11}C]MeOTf at 280 nm.

Isolated product using [^{11}C]MeOTf was first injected directly into the analytical radioHPLC, without standard product spiking, showing two peaks: 4.5 min for [^{11}C]MeOH and 5.2 min for [^{11}C]2'-*O*-methyl pyridoxine, which exhibited a lower retention time than the cold-standard **3** (Figure 35).

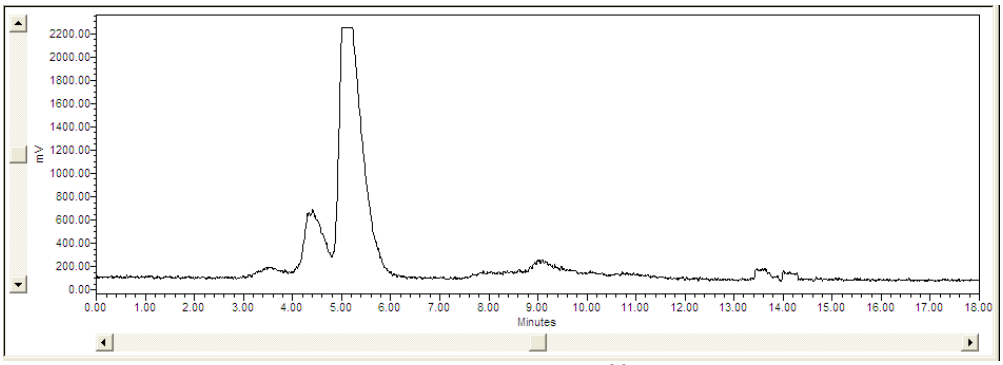

Figure 35. Radiation chromatogram for [^{11}C]2'-O-methyl pyridoxine radiosynthesis using [^{11}C]MeOTf on analytical radioHPLC. The peak at 4.5 minutes correspond to [^{11}C]-MeOH, while the peak at 5.2 minutes corresponds to [^{11}C]2'-*O*-methyl pyridoxine.

To better identify radiotracer peaks, a standard process implemented is co-injection with cold standard. This allows for any differences in pH, salt, and solvent systems to equilibrate between samples and better align peaks, as well as provide a strong UV peak to match the radioactive product. After spiking with 1 mg/mL of 2'-*O*-methyl pyridoxine standard (**compound 32**), the radiation peak appeared to align more closely to the UV standard at 6.8 minutes (Figures 36 and 37). This shift in elution time is slightly more extreme than expected. This difference may result from the high TFA content of the radiochemistry deprotection (approximately 30x more TFA than cold synthesis), which could have made a more polar TFA-salted product compared to cold-standard synthesis. By combining products, it may be possible that they underwent some form of salt exchange and equilibrated at the same pH. With this result, and the presence of two other radioactive peaks at 4 minutes ([^{11}C]MeOH) and 9 minutes (partially

deprotected product), more optimization and characterization of this radiosynthesis is still necessary and is undergoing further testing, including the introduction of a buffered HPLC solvent.

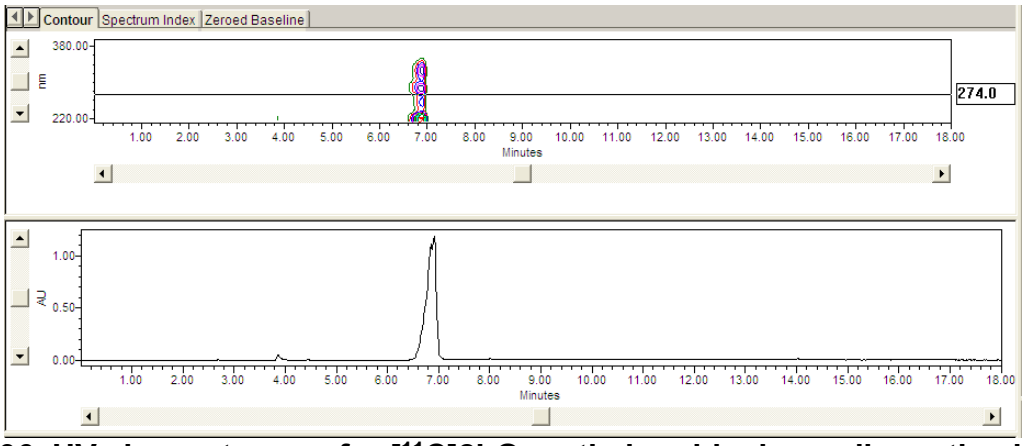

Figure 36. UV chromatogram for [^{11}C]2'-O-methyl pyridoxine radiosynthesis using [^{11}C]MeOTf with cold-standard co-injection on Analytical RadioHPLC. The peak at 6.8 minutes corresponds to the expected retention time for the standard, measured at 274 nm.

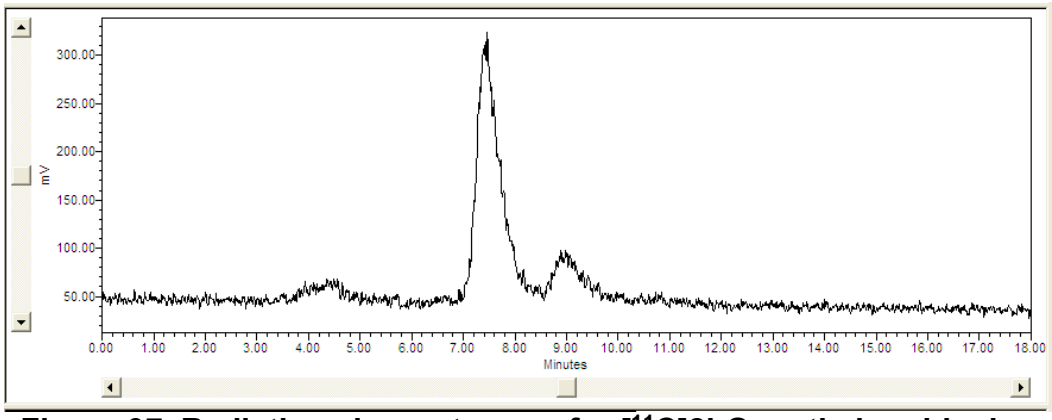

Figure 37. Radiation chromatogram for [^{11}C]2'-O-methyl pyridoxine radiosynthesis using [^{11}C]MeOTf with cold-standard co-injection on Analytical RadioHPLC. The peak at 4.5 minutes corresponds to [^{11}C]MeOH, while the peak at 7.2 minutes aligns with product. The small radioactive peak at 9 minutes is another unidentified impurity, potentially corresponding to partially deprotected product.

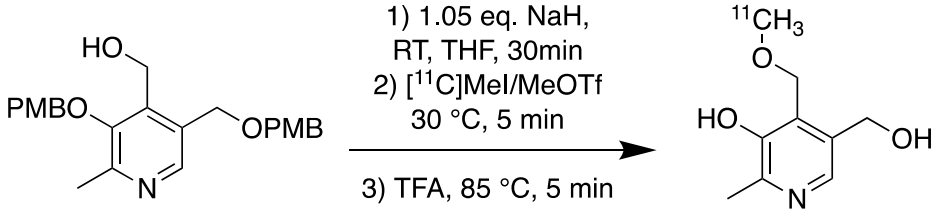

Scheme 14. Radiosynthesis of [^{11}C]4'-O-methyl pyridoxine.

In parallel, [^{11}C]4'-*O*-methyl pyridoxine radiosynthesis was also attempted on the FX-C Pro automated synthesis module. For 4'-*O*-methyl pyridoxine radiosynthesis, precursors were reacted with both [^{11}C]MeI and [^{11}C]MeOTf to establish the best methylating conditions once again (Scheme 14). Prior testing with cold standard showed a retention time of 4.5-6 minutes in 80:20 MeCN:H_2O, which was used as reference for isolation. Multiple attempts were made using [^{11}C]MeI, however, this approach once again showed chromatographically broad peaks from 5-10 min, indicating poor conversion and residual radioactivity from by-products and unincorporated [^{11}C]MeI (Figure 38). Analytical radio-HPLC analysis showed a similar radiation peak at 4-4.5 minutes for [^{11}C]MeOH, with no observed product formation of [^{11}C]4'-*O*-methyl pyridoxine (Figure 39). With low confidence in the success for this methylation reaction, it was opted that [^{11}C]MeOTf would be used.

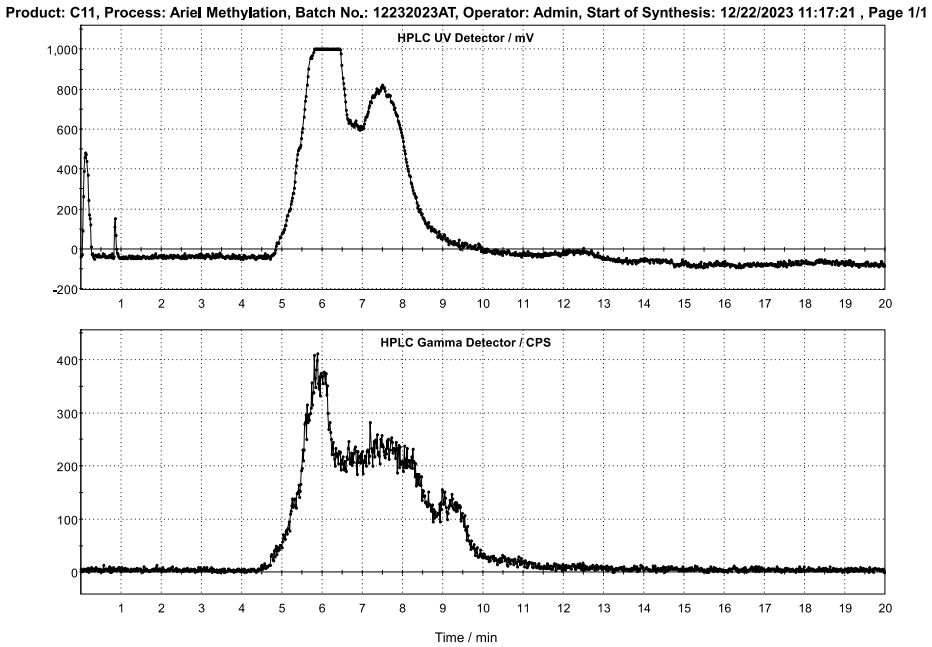

Figure 38. Semi-Prep radio-HPLC tracer for synthesis of [^{11}C]4'-O-methyl pyridoxine using [^{11}C]MeI with UV detection at 280 nm.

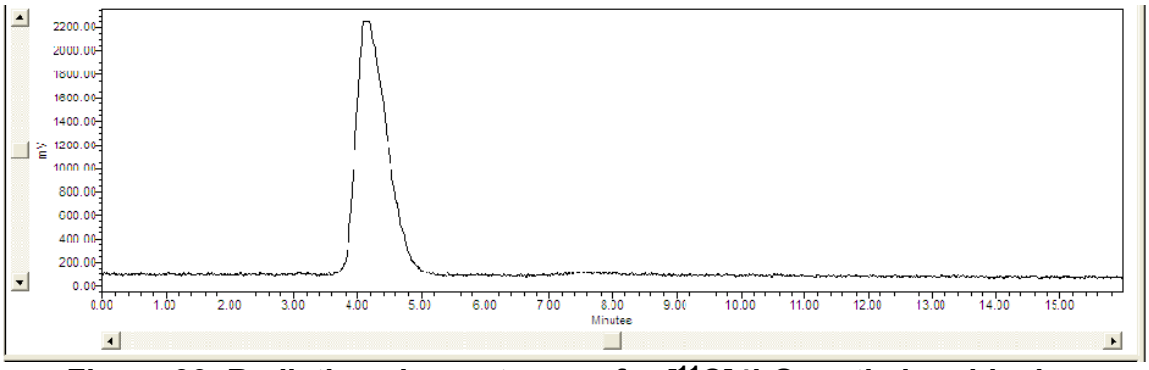

Figure 39. Radiation chromatogram for [^{11}C]4'-O-methyl pyridoxine radiosynthesis using [^{11}C]MeI on Analytical RadioHPLC. The peak at 4-4.5 minutes corresponds to [^{11}C]MeOH.

Using similar conditions, [^{11}C]MeOTf produced two UV peaks and one radioactive peak (Figure 40). The peak from 6-8 minutes was collected, as it matches standard retention times of 4.5-6 min for 4'-*O*-methyl pyridoxine by semi-prep HPLC. 10.48 mCi of product was isolated, with 500 µCi of [^{11}C]4'-*O*-methyl pyridoxine being dispensed for quality control by analytical radio-HPLC. Isolated product was injected into the analytical radioHPLC, showing three peaks: 4 min for [^{11}C]MeOH, 7.6 min for [^{11}C]4'-*O*-methyl pyridoxine, and 9 min for an impurity (Figure 41). Since the peak at 7.6 min is close to the cold standard retention time of 7.4 min, it may be possible that product formation was successful. However, despite this success, there remains the problem of residual activity from radioactive methanol, and a shoulder peak that may represent a product with only partial deprotection of PMB groups. Further optimization is necessary to better isolate this product, necessitating longer drying time before HPLC purification for [^{11}C]MeI/MeOH removal, and longer deprotection times.

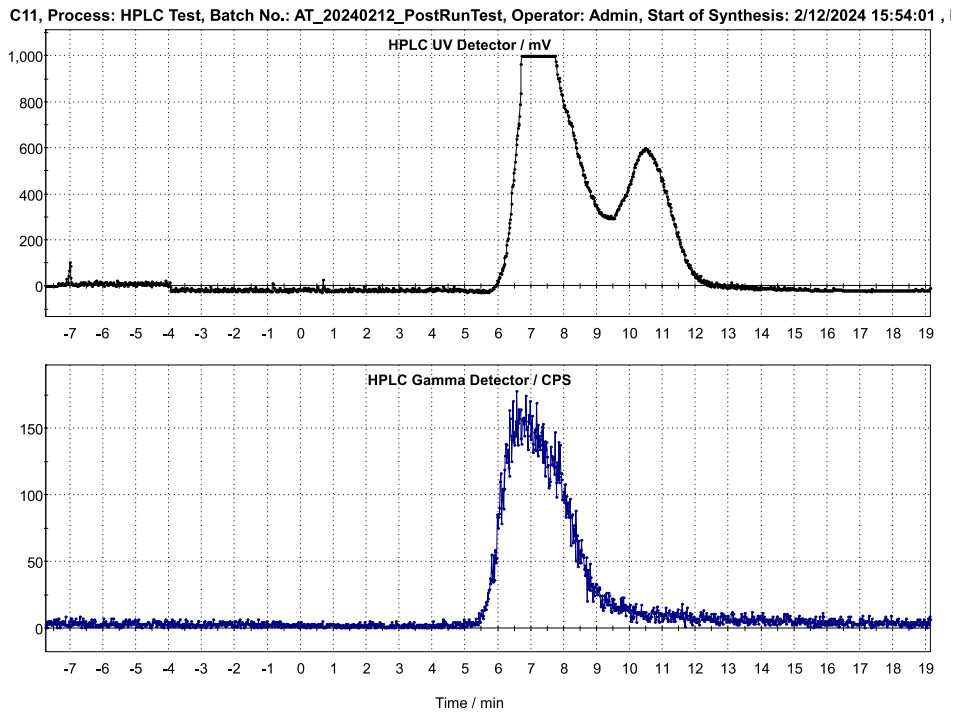

Figure 40. Semi-Prep radio-HPLC tracer for synthesis of [^{11}C]4'-O-methyl pyridoxine using [^{11}C]MeOTf with UV detection at 280nm.

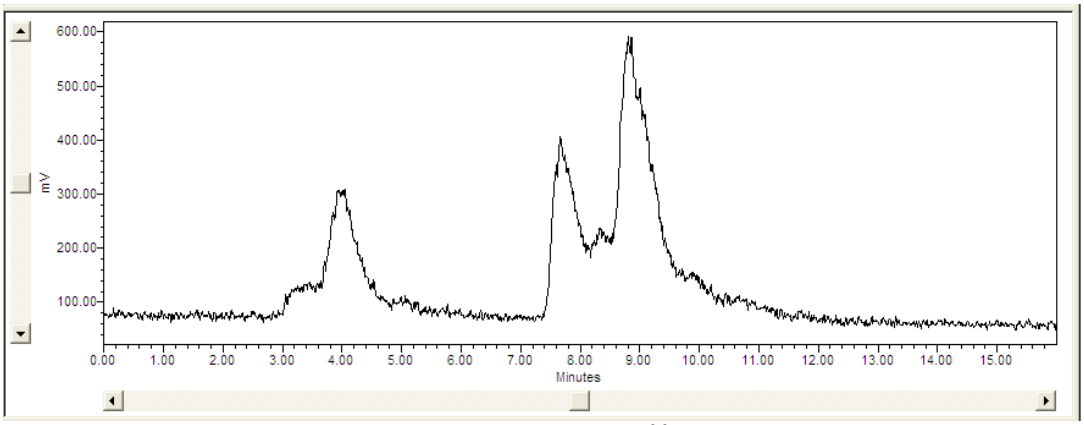

Figure 41. Radiation chromatogram for [^{11}C]4'-O-methyl pyridoxine radiosynthesis using [^{11}C]MeOTf on Analytical RadioHPLC. The peak at 4 min corresponds to [^{11}C]-MeOH, 7.5 min may correspond to 4'-*O*-methyl pyridoxine, and 9 min is an impurity potentially corresponding to a partially deprotected intermediate.

Overall, despite the synthetic ease of cold-standard C_6-fluoro pyridoxine, radiochemical transformation proved to be non-translatable. In contrast, carbon labelling strategies for both 2'- and 4'-*O*-methyl pyridoxine show some success, with the necessity for optimization of radiochemical conversion and purification. Collaborations have now

been made with Peter Scott and the PET Centre at the University of Michigan to assist in production, with hopes that synthetic difficulties can be overcome with in-field experts.

Chapter 3 – Conclusions and Future Work

Lung cancer continues to account for most cancer-related deaths in Canadian men and women, with CDDP remaining the standard of care. With drug resistance being a major clinical challenge, low survival rates necessitate better diagnostic and prognostic care. A strong association has been found between treatment outcomes of lung tumours and the metabolism of PN, providing a useful biomarker for monitoring resistance onset. With changes in metabolic alterations during resistance onset, PET-CT and radiotracer development was explored to quantify and image CDDP sensitive and resistant lung cancer, with the goal of improving patient treatment outcomes.

Cold-standard radiotracer structures were proposed for addressing this issue, beginning with fluorine labelling techniques. Carbon-6 aromatic labelling (cold-standard **1**) experienced significant difficulties with utilizing standard aromatic nucleophilic substitutions with fluorine, even with activated leaving groups, due to PN's high electron density and functional group incompatibility. Unconventional conditions were instead selected, using a Sandmeyer reaction and aqueous HF, allowing for efficient production of C_6-fluoro pyridoxine. Synthesis efforts for 2'-fluoro pyridoxine (cold-standard **2**) were also complicated by known pyridinone-methide eliminations, and therefore necessitated efforts for carbon-homologation. In the effort to prevent significant deviation and metabolic issues, one-carbon homologations were attempted, but fell short under varying conditions due to difficult functional group compatibility and poor reaction conversion.

Cold-standard radiotracer structures involving carbon labelling techniques were also utilized. With an understanding of the anti-vitamin Ginkgotoxin, the 2'-benzyl and 4'-benzyl positions were identified for methylation strategies. Through implementation of PMB and acetonide protecting group strategies, 2'-*O*-methyl pyridoxine (cold-standard **3**) and 4'-*O*-methyl pyridoxine (cold-standard **4**) were synthesized and characterized. Methylation of these positions provided aqueous stability unlike the previous benzyl fluorine substitution and provides comparisons for radionuclides and pharmacokinetics in further studies.

The analysis of cold-standard metabolism showed that despite modification of PN's structure, transport into A549 and H460 cancer cells was still possible. Metabolic alteration of C_6-fluoro pyridoxine interacted with both PDXK and PNPO but suffers from potential defluorination. 2'-*O*-methyl pyridoxine in contrast exhibited great stability, interacting with all relevant enzymes with structures mimicking pyridoxine's PL, PLP and PM, but with *O*-methyl substitution. Unfortunately, due to time constraints, 4'-*O*-methyl pyridoxine (Ginkgotoxin) has not yet been analyzed. However, it has been submitted for analysis but it is expected to behave according to literature as a known substrate.

Finally, radiotracer production of [^{18}F]C_6-fluoro pyridoxine proved to be a difficult translation from cold chemistry, with low concentrations of [^{18}F]HF limiting reaction conversion. [^{11}C]-radiochemical transformation on the 2'-benzyl position also saw extensive attempts, with apparent success in acquiring conversion to the [^{11}C] *O*-methyl derivative with methyl triflate when co-injected and compared to cold-standard by radio-HPLC. Further optimization and characterization efforts are necessary, with translation to partially successful 4'-*O*-methyl pyridoxine.

Overall, this work has identified both fluorine and carbon-labelled derivatives of pyridoxine that are capable of being transporting into lung cancer cells and reporting on metabolism using PN based enzymes PDXK, PDXP, and PNPO. Currently conditions are still being optimized for [^{11}C] labelling, with new collaborations being made with Peter Scott and the PET Centre at the University of Michigan to assist in production. If successful, radiotracer production will be optimized for desired activity and purity. With PN based radiotracers in hand, PET-CT imaging can be performed on mice models to non-invasively evaluate the cancer resistance phenotype prior to and during CDDP-based chemotherapy (Figure 42). We hope to demonstrate that reduced radiolabelled PN retention in lung cancer tissue is associated with resistance, and compare prognostic ability to the clinical radiotracer [^{18}F]FDG. With this new precision cancer medicine approach, treatment outcomes for patients with lung cancer could be improved, and most importantly, the patient would be spared the devastation of learning that their painful and taxing therapy was ineffective against their lung cancer.

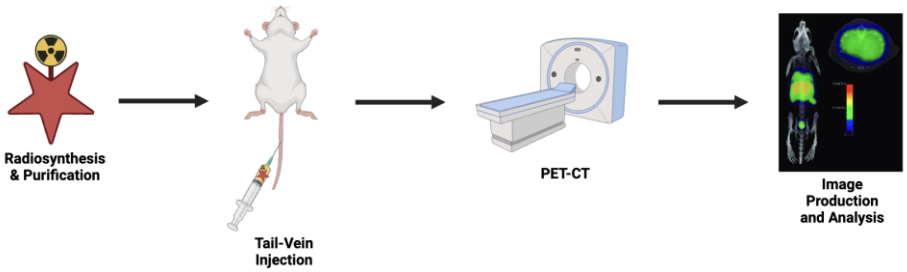

Figure 42. Future radiotracer workflow using PET-CT.

Chapter 4 – Materials and Methods

4.1 General Information

Reagents were commercially available and sourced from Sigma-Aldrich unless otherwise stated and used as received. 4-Methoxybenzyl chloride was sourced from TCI and used as received. Tetrabutylammonium fluoride was sourced from Oakwood Chemicals and used as received. All solvents and acids (TFA) used for HPLC purification were HPLC grade except for water (18.2 MΩ cm Millipore water). All volatiles were removed under reduced pressure using a BUCHI rotary evaporator (R-100, B-100, and V-100), except for final products which were lyophilized using a LABCONCO FreeZone lyopholizer after HPLC purification. Thin-layer chromatography (TLC) was carried out on aluminum backed silica gel plates with compounds visualized by UV light. All ^{1}H, ^{13}C, and 2D COSY NMR spectra were recorded on Bruker 400, 500, and 600 MHz NMR spectrophotometers as reported in the synthesis characterization below and analyzed using MestReNova software. HRMS spectra were obtained using ESI+ ionization mode.

4.2 Separation Protocols

Flash column chromatography was run manually, using solvent gradients consistent of ethyl acetate, hexanes, dichloromethane, and methanol. All columns utilized SiliaFlash Irregular Silica Gels F60, which are particle size 40-64 μm, at 60 Å. Columns were equilibrated for 5 minutes prior to elution with the more non-polar solvent (hexanes in most cases). Introduction of dried crude reaction mixture or dried organic phases from extraction was done by re-dissolving in 1-2 mL running solvent and pipetting onto the top of the silica gel. Sand was then added on top to prevent disruption of the silica gel, and desired solvent systems were added according to reaction procedures in **Materials and**

Methods Section 4.3. Product separation was monitored by TLC analysis in a matching eluent system, with desired product identified by UV light at 254 nm.

LC-MS analysis of synthetic intermediates for evaluation of reaction conversion was performed using a Shimadzu Prominence UFLC HPLC separation module utilizing a LC-20AD liquid chromatography unit connected to an SPD-20A UV-Vis detector (at 210 and 254 nm) and a column warmer set to 40 °C. All samples were prepared by dissolving approximately 1 mg of material in 400 µL of LC-MS grade acetonitrile. An Agilent 959963-902 Eclipse Plus C18 column with 3.5 µm particle size, at 95 Å, with dimensions 4.6x100 mm was used for separation. Eluent A was OMNISolv LC-MS grade water with 0.05% LC-MS grade formic acid, and eluent B was Optima LC-MS grade acetonitrile with 0.05% LC-MS grade formic acid. All samples utilized a gradient profile as follows: flow rate of 1 mL/min, with 2 minutes at 5% acetonitrile, followed by a gradient to 99% acetonitrile over 6 minutes, a static 4 minutes at 99% acetonitrile, then re-equilibration back to 5% acetonitrile over 1 minute and running for 2 more minutes for a total of 15 minutes. A Shimadzu LCMS-2020 mass spectrophotometer was coupled for analysis, with a scanning range of 100-800 *m/z* at a scan speed of 715 u/sec on a single quadrupole. Any HPLC conversion was represented in %area and calculated using the integration of peaks present at 254 nm.

HPLC purification of final cold-standard products was performed using a Shimadzu Prominence HPLC separation module utilizing a LC-20AR liquid chromatography unit connected to an SPD-M20A Diode photodiode array detector (scanning from 190-400 nm) without a column warmer. All samples were prepared by dissolving 25 mg of material in 5 mL of acetonitrile (5 mg/mL). A Phenomenex 00G-4542-P0-AX Luna C18(2) column

with 5 µm particle size, at 100 Å, with dimensions 250 × 21.2 mm was used for separation. Eluent A was 18.2 MΩ cm Millipore water with 0.1% TFA, and eluent B was HPLC grade acetonitrile with 0.1% TFA. All samples utilized a gradient profile as follows: flow rate of 10 mL/min, with an increase from 1 to 92% acetonitrile over 23 minutes, re-equilibrating to 1% acetonitrile over 1 minute, and then running for 6 more minutes (total run time of 30 minutes). Desired final product peaks were identified and collected using a Shimadzu FRC-40 automatic fraction collector.

4.3 Synthetic Procedures

Synthesis of C_6-fluoro pyridoxine using Standard Nucleophilic Aromatic Substitution

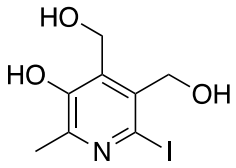

Synthesis of compound 1: 6-Iodopyridoxine. To a round bottom flask charged with a magnetic stir bar was added 2 g (11.8 mmol) of pyridoxine, dissolved in 20 mL 10% aqueous solution of K_2CO_3. Iodine (3.00 g, 23.6 mmol) was then added, and the solution was left to stir for 3 hours at RT while wrapped in aluminum foil to exclude light. The reaction was then quenched using saturated sodium thiosulfate, and pH was adjusted to pH 3 using concentrated HCl. A yellow precipitate formed, which was then vacuum filtered and washed with cold water. Concentration and drying *in vacuo* afforded 6-iodopyridoxine as a yellow solid (2.16 g, 62%). ^{1}H NMR (600 MHz, DMSO) δ 9.49 (s, 1H), 5.80 (s, 1H), 5.06 (t, *J* = 5.2 Hz, 1H), 4.79 (s, 2H), 4.55 (d, *J* = 5.1 Hz, 2H), 3.32 (s, 4H), 2.30 (s, 3H). ^{13}C NMR (151 MHz, DMSO) δ 150.39, 148.19, 136.20, 134.94, 112.09, 63.94, 56.97, 18.90. HRMS (ESI): Mass calc for $C_8H_{10}NO_3$[M+H]+: 294.9705, found: 294.9683.

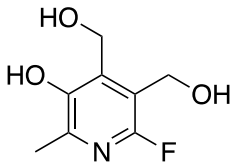

Synthesis of compound 2: C_6-fluoro pyridoxine. To a round bottom flask charged with a magnetic stir bar was added compound **1**, 6-iodopyridoxine (0.02 g, 0.068 mmol), dissolved in either anhydrous acetonitrile of DMF (2 mL). Potassium fluoride (0.004 g, 0.069 mmol) and kryptofix [2.2.2] cryptand ligan (0.026 g, 0.069 mmol) were then added to the flask, a condenser was fixed, and the reaction mixture was left to stir at 80 °C for 2 hours. Reaction progress was monitored by LC-MS. No conversion of starting material was observed.

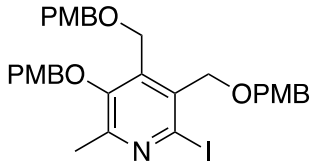

Synthesis of compound 3: 3,4,5-*O*-methoxymethyl 6-iodopyridoxine. To a round bottom flask charged with a magnetic stir bar was added anhydrous DMF (15 mL) and **1** (0.02 g, 0.068 mmol). The reaction mixture was cooled down to 0 °C, and sodium hydride (60% dispersion in mineral oil, 0.0137 g, 0.408 mmol) was added. The mixture was stirred for 5 minutes at 0 °C, and then removed from ice to stir for 1 hour at RT. To the viscous suspension was then added 4-methoxybenzyl chloride (0.033 mL, 0.211 mmol) at 0 °C dropwise, and the resulting mixture was then stirred overnight at RT for a total of 16 hours. Reaction progress was monitored by LC-MS. No conversion of starting material was observed.

Synthesis of C_6-Fluoro Pyridoxine using Hypervalent Iodine

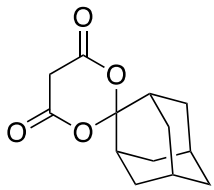

Synthesis of compound 4: Spiroadamantyl-1,3-dioxane-4,6-dion (SPIAd): To round bottom flask charged with a magnetic stir bar was added malonic acid (1 g, 9.610 mmol) and 2-adamantone (1.45, 9.652 mmol), dissolved in acetic anhydride (2 mL). To the mixture was then added 10 uL sulfuric acid (catalytic), and the mixture was stirred at 60 °C for 30 min, and then cooled to RT and stirred a final 1.5 h. Cold hexanes was then added to the flask alongside a small amount of diethyl ether, and sonicated to produce a crystalline solid. The solid was then vacuum filtered and dried *in vacuo* to afford Spiroadamantyl-1,3-dioxane-4,6-dione (SPIAd) as a white crystalline solid (1.86 g, 82%). ^{1}H NMR (600 MHz, $CDCl_3$) δ 3.61 (s, 2H), 2.20 (s, 2H), 2.14 (d, *J* = 13.1 Hz, 4H), 1.94 – 1.90 (m, 2H), 1.82 – 1.74 (m, 6H). ^{13}C NMR (151 MHz, $CDCl_3$) δ 163.17, 109.77, 37.77, 36.84, 36.65, 33.60, 26.18. HRMS (ESI): Mass calc for $C_{14}H_{15}N_3O_3$[M-H]-: 235.0971, found: 235.0963.

C_6-Fluoro Pyridoxine Cold Standard Synthesis using the Sandmeyer Reaction

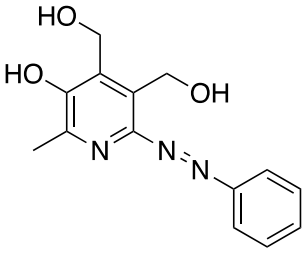

Synthesis of compound 6: 6-Phenylazopyridoxine hydrochloride. 2 g (11.8 mmol) of pyridoxine was dissolved in 30 mL deionized water in a 250 mL Erlenmeyer flask. The solution was adjusted to pH 8 with 2.5 M NaOH, equipped with a stir bar, then placed in

an ice bath. To a round bottom flask charged with a magnetic stir bar, 1 equivalent of aniline (0.54 mL, 5.9 mmol)) was combined with 10 mL 6 M HCl and cooled down to 0 °C. In a separate 10 mL flask, $NaNO_2$ (0.62 g, 8.98 mmol) was dissolved in 2 mL deionized water and the solution was cooled down to 0 °C. The cooled down $NaNO_2$ was added portion wise to the aniline solution at 0 °C to perform diazotization. The diazotized aniline solution was then added portion wise to the pyridoxine solution at 0 °C while maintaining pH 8 by subsequent additions of 2.5 M NaOH. Once addition was finished, the solution was allowed to warm up to room temperature and was stirred for 2 hours, protected from light. Once the reaction was done, the pH was adjusted to 3 with 6 M HCl and the solution was placed on ice to crystallise. The reaction mixture was filtered, and the precipitate was washed with ethanol. The precipitate was then dried under vacuum to give 2.1 g of pure compound **6** as a red solid in 98% yield. ^{1}H NMR (600 MHz, DMSO) δ 7.96 (dd, J = 7.9, 1.3 Hz, 2H), 7.64 – 7.58 (m, 3H), 5.06 (s, 2H), 4.98 (s, 2H), 2.54 (s, 3H). ^{13}C NMR (151 MHz, DMSO) δ 154.47, 152.05, 147.61, 146.05, 137.52, 134.62, 131.97, 129.58, 122.82, 56.55, 54.30, 17.63. HRMS (ESI): Mass calc for $C_{14}H_{16}N_3O_3$[M+H]+: 274.1192, found: 274.1191.

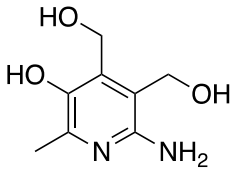

Synthesis of compound 7: 6-Aminopyridoxine hydrochloride. To a Schlenk flask charged with a magnetic stir bar was added **6,** 6-phenylazopyridoxine hydrochloride (2.10 g, 7.69 mmol), dissolved in 50 mL dry methanol. 0.2 g of palladium on carbon (10 weight%) was added to the flask. Three full balloons of hydrogen gas were placed into the flask to saturate, and the solution was stirred overnight. The solution was then filtered

through celite by vacuum filtration, washing with methanol three times. Elution of product off the celite bed could be monitored by UV wand (blue fluorescence). The solvent was then removed by rotary evaporation to give a dark brown solid. The crude solid was then purified by triturating the solid with cold ether, followed by washing over a vacuum filter with multiple portions of cold ether. The precipitate was then dried under vacuum to afford 1.3 g of a yellow solid with 92% yield. ^{1}H NMR (600 MHz, DMSO) δ 9.18 (s, 1H), 7.03 (s, 1H), 5.67 (s, 1H), 5.36 (s, 1H), 4.66 (s, 2H), 4.54 (s, 2H), 2.36 (s, 3H). ^{13}C NMR (151 MHz, DMSO) δ 148.96, 146.33, 140.82, 132.65, 120.77, 54.94, 54.56, 14.13. HRMS (ESI): Mass calc for $C_8H_{13}N_2O_3$[M+H]+: 185.0926, found: 185.0932.

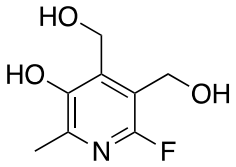

Synthesis of compound 8: C_6-fluoro pyridoxine. To a 25 mL falcon tube charged with a magnetic stir bar was added **7** (0.1 g, 0.543 mmol) and sodium nitrite (0.056g, 0.815 mmol), followed by 0.4 mL of 48% aq. hydrofluoric acid. The mixture was stirred at 0 °C on ice for 20 minutes, and then allowed to heat and stir at 60 °C for 1 hour. To quench the reaction, 1M sodium hydroxide solution was added until neutral. The solution was then concentrated *in vacuo*, and the crude solid was filtered and purified by semi-prep HPLC. Fractions containing product were collected and dried by lyophilization to afford C_6-fluoro pyridoxine as a white powder (0.078 g, 79%). ^{1}H NMR (600 MHz, DMSO) δ 9.15 (s, 1H), 4.77 (d, J = 0.6 Hz, 2H), 4.46 (s, 2H), 2.28 (s, 3H). ^{13}C NMR (151 MHz, DMSO) δ 154.39, 152.88, 147.84, 142.85 (d, J = 15.2 Hz), 138.79, 117.87, 56.33, 53.52, 18.71. 19F NMR (471 MHz, DMSO) δ -74.33, -85.41. HRMS (ESI): Mass calc for $C_8H_{10}FNO_3Na$[M+Na]+: 210.0542, found: 210.0551.

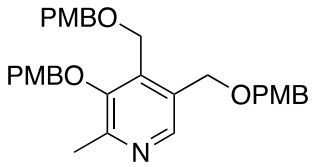

Synthesis of compound 9: 3',4',5'-*O*-methoxybenzyl pyridoxine. To a round bottom flask charged with a magnetic stir bar was added anhydrous DMF (25 mL) and pyridoxine (2 g, 11.8 mmol). The reaction mixture was cooled down to 0 °C, and sodium hydride (60% dispersion in mineral oil, 1.702 g, 42.56 mmol) was added. The mixture was stirred for 5 minutes at 0 °C, and then removed from ice to stir for 1 hour at RT. To the viscous suspension was then added 4-methoxybenzyl chloride (5.29 mL, 39.18 mmol) at 0 °C dropwise, and the resulting mixture was then stirred overnight at RT for a total of 16 hours. The dark brown-green solution was then quenched by adding ice-water to the mixture at 0 °C. The majority of solvent was then removed by rotary evaporation. The solution was then partitioned between H_2O (100 mL) with 25 mL of brine and Et_2O (50 mL), with the organic phase isolated. The aqueous phase was washed with Et_2O (3 x 50 mL) and the organic extracts were combined, dried with Na_2SO_4, and concentrated *in vacuo*. The crude material was purified by column chromatography (hexanes:ethyl acetate = 1:1). Fractions containing product were collected and dried *in vacuo* to afford 3',4',5'-*O*-methoxybenzyl pyridoxine as an orange precipitate (2.25 g, 36%). ^{1}H NMR (400 MHz, $CDCl_3$) δ 8.31 (s, 1H), 7.24 (m, *J* = 17.1, 7.6, 1.7 Hz, 7H), 6.94 – 6.81 (m, 6H), 4.77 (s, 2H), 4.56 (d, *J* = 7.6 Hz, 4H), 4.43 (d, *J* = 11.9 Hz, 4H), 3.83 (s, 3H), 3.80 (s, 3H), 3.79 (s, 3H), 2.52 (s, 3H). ^{13}C NMR (101 MHz, $CDCl_3$) δ 159.82, 159.52, 159.46, 153.30, 152.16, 145.48, 138.04, 132.08, 130.13, 129.92, 129.90, 129.71, 128.98, 114.09, 113.97, 76.46, 73.07, 72.39, 67.15, 62.50, 55.44, 55.42, 55.38, 19.89. HRMS (ESI): Mass calc for $C_{32}H_{36}NO_6$[M+H]+: 530.2543, found: 530.2542.

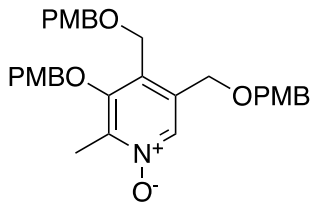

Synthesis of compound 10: 3',4',5'-*O*-methoxybenzyl pyridin-*N*-oxide. To a round bottom flask charged with a magnetic stir bar was added $CHCl_3$ (8 mL) and Compound **9** (2.25g, 4.25 mmol). In a separate flask, m-CPBA (0.88 g, 5.10 mmol) was added to 5 mL $CHCl_3$, which was then transferred dropwise to the reaction slowly over 5 minutes. The reaction was then stirred for 2 hours at RT. Reaction progress was monitored by TLC in 95:5 DCM:MeOH. Once complete, an extraction was performed. The solution was then partitioned between H_2O (100 mL) with 25 mL of brine and $CHCl_3$ (40 mL), with the organic phase isolated. The aqueous phase was washed with $CHCl_3$ (3 x 40 mL) and the organic extracts were combined, dried with Na_2SO_4, and concentrated *in vacuo*. The crude material was purified by column chromatography (hexanes:ethyl acetate = 1:1, followed by ethyl acetate:methanol = 90:10). Fractions containing product were collected and dried *in vacuo* to afford 3',4',5'-*O*-methoxybenzyl pyridine-*N*-oxide as an off-white powder (2.14 g, 95%). ^{1}H NMR (400 MHz, $CDCl_3$) δ 8.28 (s, 1H), 7.28 – 7.16 (m, 6H), 6.93 – 6.81 (m, 6H), 4.77 (s, 2H), 4.48 (d, *J* = 13.7 Hz, 4H), 4.41 (d, *J* = 4.0 Hz, 4H), 3.82 (s, 3H), 3.80 (s, 3H), 3.79 (s, 3H), 2.43 (s, 3H). ^{13}C NMR (101 MHz, $CDCl_3$) δ 160.04, 159.58, 159.51, 153.80, 144.14, 135.49, 134.18, 130.14, 129.92, 129.57, 129.50, 128.42, 127.86, 114.13, 113.99, 113.97, 72.86, 72.61, 66.15, 61.98, 55.38, 55.37, 55.34, 12.00. HRMS (ESI): Mass calc for $C_{32}H_{35}NO_7Na$[M+Na]+: 568.2311, found: 568.2324.

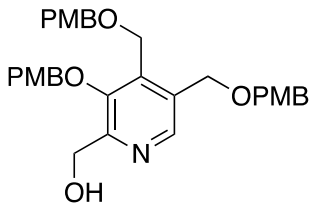

Synthesis of compound 11: 2'-hydroxyl-3',4',5'-*O*-methoxybenzyl pyridoxine. To a round bottom flask charged with a magnetic stir bar was added DCM (20 mL) and Compound **10** (2.14 g, 3.92 mmol). Triethylamine (2.19 mL, 15.7 mmol) was then added to the flask, and stirred for 5 minutes at RT. Then trifluoracetic anhydride (0.818 mL, 5.88 mmol) was added slowly over 10 minutes, and the reaction was left to stir overnight at RT and under nitrogen atmosphere. Reaction progress was monitored by TLC in hexanes:ethyl Acetate 40:60. Once complete, an extraction was performed. The solution was then partitioned between H_2O (100 mL) with 25 mL of brine and DCM (50 mL), with the organic phase isolated. The aqueous phase was washed with DCM (3 x 50 mL) and the organic extracts were combined, dried with Na_2SO_4, and concentrated *in vacuo*. The crude material was purified by column chromatography (hexanes:ethyl acetate = 4:6). Fractions containing product were collected and dried *in vacuo* to afford 2'-hydroxyl-3',4',5'-*O*-methoxybenzyl pyridoxine as a red precipitate (1.72 g, 80%). ^{1}H NMR (400 MHz, $CDCl_3$) δ 8.43 (s, 1H), 7.34 – 7.21 (m, 7H), 6.91 (m, *J* = 14.4, 7.5, 1.9 Hz, 6H), 4.81 (s, 2H), 4.75 (s, 2H), 4.64 (s, 2H), 4.58 (s, 2H), 4.48 (d, *J* = 17.6 Hz, 4H), 3.86 (s, 3H), 3.84 (s, 3H), 3.83 (s, 3H). ^{13}C NMR (101 MHz, $CDCl_3$) δ 159.99, 159.61, 159.51, 152.87, 150.69, 144.49, 138.38, 133.56, 130.05, 129.98, 129.71, 129.66, 128.54, 114.16, 114.01, 73.18, 72.57, 67.03, 62.12, 60.49, 55.43, 55.39. HRMS (ESI): Mass calc for $C_{32}H_{36}NO_7$[M+H]+: 546.2492, found: 546.2492.

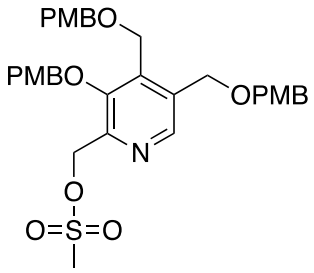

Synthesis of compound 12: 2'-*O*-mesyl-3',4',5'-*O*-methoxybenzyl pyridoxine. To a round bottom flask charged with a magnetic stir bar was added DCM (4 mL) and Compound **11** (0.05 g, 0.092 mmol). Triethylamine (0.066 mL, 0.474 mmol) was then added to the flask, and stirred for 5 minutes at RT. Then methanesulfonyl chloride (0.011 mL, 0.140 mmol) was added, and the reaction was left to stir for 1 hour under nitrogen atmosphere at 0 °C. Reaction progress was monitored by TLC in hexanes:ethyl Acetate 40:60. Once complete, the reaction was concentrated by rotary evaporation. The crude material was purified by column chromatography (hexanes:ethyl acetate = 1:1). Fractions containing product were collected and dried *in vacuo* to afford 2'-*O*-mesyl-3',4',5'-*O*-methoxybenzyl pyridoxine as a light pink oil, used directly in the next reaction due to instability (0.0429 g, 75%). ^{1}H NMR (500 MHz, $CDCl_3$) δ 8.48 (s, 1H), 7.28 – 7.17 (m, 7H), 6.91 – 6.82 (m, 7H), 5.29 (s, 2H), 4.85 (s, 2H), 4.59 (s, 2H), 4.53 (s, 2H), 4.47 (s, 2H), 4.42 (s, 2H), 3.81 (s, 3H), 3.79 (s, 3H), 3.78 (s, 3H), 3.03 (s, 3H). ^{13}C NMR (101 MHz, $CDCl_3$) δ 171.26, 160.06, 159.65, 159.54, 153.01, 147.30, 145.96, 139.14, 136.16, 130.32, 129.99, 129.80, 129.69, 129.45, 128.10, 114.18, 114.02, 114.01, 78.73, 73.25, 72.75, 68.23, 66.80, 62.08, 60.50, 55.41, 55.39, 55.36, 38.32, 21.16, 14.31. HRMS (ESI): Mass calc for $C_{33}H_{37}NO_9SNa$[M+Na]+: 646.2087, found: 646.2075.

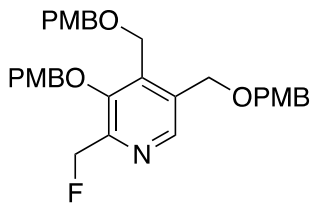

Synthesis of compound 13: 2'-fluoro-3',4',5'-*O*-methoxybenzyl pyridoxine. To a round bottom flask charged with a magnetic stir bar was added anhydrous acetonitrile (2 mL) and Compound **12** (0.0429 g, 0.069 mmol). Tetrabutylammonium fluoride monohydrate (0.022 g, 0.084 mmol) was then added to the flask, and stirred for 4 hours at 60 °C. Reaction progress was monitored by TLC in hexanes:ethyl Acetate 40:60. Once complete, the reaction was concentrated by rotary evaporation to remove acetonitrile, and an extraction was performed. The solution was then partitioned between H_2O (40 mL) with 10 mL of brine and DCM (20 mL), with the organic phase isolated. The aqueous phase was washed with DCM (3 x 20 mL) and the organic extracts were combined, dried with Na_2SO_4, and concentrated *in vacuo*. The crude material was purified by column chromatography (hexanes:ethyl acetate = 4:6). Fractions containing product were collected and dried *in vacuo* to afford 2'-Fluoro-3',4',5'-*O*-methoxybenzyl pyridoxine as an off-white solid (0.032 g, 84%). ^{1}H NMR (400 MHz, $CDCl_3$) δ 8.50 (s, 1H), 7.30 – 7.18 (m, 7H), 6.93 – 6.84 (m, 7H), 5.52 (s, 1H), 5.40 (s, 1H), 4.87 (s, 2H), 4.62 (d, *J* = 1.7 Hz, 2H), 4.56 (s, 2H), 4.47 (s, 2H), 4.42 (s, 2H), 3.83 (s, 3H), 3.81 (s, 3H), 3.80 (s, 3H). ^{13}C NMR (126 MHz, $CDCl_3$) δ 159.99, 159.62, 159.54, 153.28, 153.26, 149.40, 149.28, 145.91, 139.04, 139.02, 135.76, 135.73, 130.19, 129.95, 129.92, 129.70, 129.65, 128.58, 114.14, 114.03, 82.41, 81.09, 78.95, 78.92, 72.90 (d, *J* = 66.8 Hz), 66.93, 62.12, 55.44, 55.42, 55.39. ^{19}F NMR (377 MHz, $CDCl_3$) δ -211.68, -211.80, -211.93. HRMS (ESI): Mass calc for $C_{32}H_{35}FNO_7$[M+H]+: 564.2398, found: 564.2396.

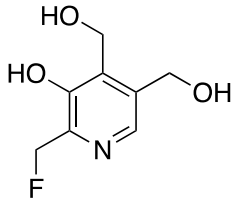

Synthesis of compound 14: 2'-fluoro-pyridoxine. To a round bottom flask charged with a magnetic stir bar was added compound **13**, dissolved in 2 mL anhydrous acetonitrile. 2 mL of synthesis grade TFA was then added, the flask was fixed with a condenser, and the solution was stirred for 4 hours at 70 °C to ensure full conversion. Reaction conversion was monitored by LC-MS, which showed desired product as well as loss of fluorine. Once consumption of starting material was observed, the reaction was stopped by boiling without the condenser to remove residual methyl iodide, quenched with a small amount of water and sodium hydroxide, followed by rotary evaporation. The crude material was then purified by semi-prep HPLC. Fractions containing product were collected and dried by lyophilization, but LC-MS and NMR of the sample showed degradation of product and inability to be isolated.

<u>Synthesis of One-Carbon Homologated Pyridoxine from PMB-Protected Pyridoxine</u>

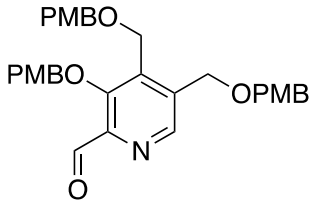

Synthesis of compound 15: 3',4',5'-*O*-methoxybenzyl-2-Pyridoxine carboxaldehyde. To a round bottom flask charged with a magnetic stir bar was added DCM (4 mL) and Compound **12** (0.07 g, 0.128 mmol). Dess–Martin periodinane (0.06 g, 0.141 mmol) was then added to the flask, and stirred for 1 hour at RT. Once complete, the reaction was then partitioned between H_2O (40 mL) with 10 mL of brine and DCM (20

mL), with the organic phase isolated. The aqueous phase was washed with DCM (3 x 15 mL) and the organic extracts were combined, dried with Na_2SO_4, and concentrated *in vacuo*. The crude material was purified by column chromatography (hexanes:ethyl acetate = 7:3). Fractions containing product were collected and dried *in vacuo* to afford 3',4',5'-*O*-methoxybenzyl-2-pyridinecarboxaldehyde as a white solid (0.066 g, 95%). ^{1}H NMR (400 MHz, CDCl3) δ 10.16 (s, 1H), 8.70 (s, 1H), 7.30 – 7.25 (m, 4H), 7.20 (d, *J* = 8.6 Hz, 2H), 6.91 – 6.84 (m, 6H), 4.95 (s, 2H), 4.65 (s, 2H), 4.51 (d, *J* = 7.1 Hz, 4H), 4.39 (s, 2H), 3.81 (d, *J* = 2.3 Hz, 6H), 3.80 (s, 3H). ^{13}C NMR (101 MHz, $CDCl_3$) δ 190.87, 160.11, 159.63, 159.59, 155.40, 146.14, 145.21, 141.72, 140.32, 139.81, 133.03, 131.73, 130.64, 129.89, 129.69, 129.63, 129.50, 128.04, 128.02, 114.14, 114.05, 114.01, 79.03, 73.13, 72.90, 66.77, 61.55, 55.41, 55.38. HRMS (ESI): Mass calc for $C_{32}H_{34}NO_7$[M+H]+: 544.2335, found: 544.2357.

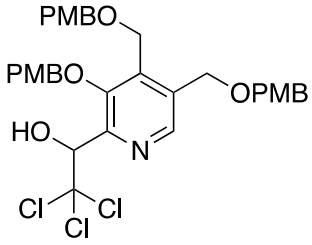

Synthesis of compound 16: 3',4',5'-*O*-methoxybenzyl-2'-hydroxy-(2,2,2-trichloro) pyridoxine. To a round bottom flask charged with a magnetic stir bar was added compound **15** (0.066 g, 0.121 mmol), dissolved in 4 mL $CHCl_3$. To the flask was added 1,8-diazabicyclo(5.4.0)undec-7-ene (DBU) (0.0216 g, 0.142 mmol, 0.0212 mL), and the reaction was left to stir at RT overnight. Reaction progress was monitored by LC-MS, and after approximately 90% conversion, the reaction was stopped by concentrating with rotary evaporation. The crude material was purified directly by column chromatography (hexanes:ethyl acetate = 1:1). Fractions containing product were collected and dried *in*

vacuo to afford 3',4',5'-*O*-methoxybenzyl-2'-hydroxy-(2,2,2-trichloro) pyridoxine as an oil (0.061 g, 76%). ^{1}H NMR (600 MHz, $CDCl_3$) δ 8.51 (s, 1H), 7.29 – 7.27 (m, 2H), 7.26 – 7.24 (m, 2H), 7.22 – 7.20 (m, 2H), 6.93 – 6.90 (m, 4H), 6.87 – 6.85 (m, 2H), 5.43 (d, *J* = 10.2 Hz, 1H), 5.07 (d, *J* = 10.3 Hz, 1H), 4.91 – 4.82 (m, 2H), 4.63 (s, 2H), 4.55 – 4.46 (m, 4H), 4.42 (d, *J* = 3.0 Hz, 2H), 3.83 (s, 3H), 3.81 (s, 4H), 3.80 (s, 3H). ^{13}C NMR (151 MHz, $CDCl_3$) δ 159.94, 159.67, 159.57, 152.59, 147.77, 144.52, 139.04, 136.42, 130.05, 129.78, 129.73, 129.54, 129.40, 128.27, 114.22, 114.04, 102.36, 78.10, 77.61, 73.17, 72.97, 66.83, 65.16, 62.23, 60.51, 55.56, 55.43, 55.41, 55.37, 31.71, 22.78, 22.75, 14.26. HRMS (ESI): Mass calc for $C_{33}H_{34}Cl_3NO_7$[M+H]+: 662.1495, found: 662.1479.

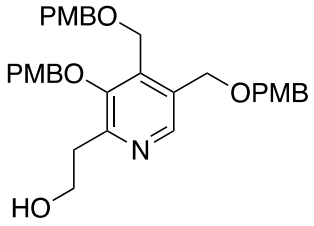

Synthesis of compound 17: 3',4',5'-*O*-methoxybenzyl-2'-(2-hydroxyethyl) pyridoxine. To a Schlenk flask charged with a magnetic stir bar was added compound **16** (0.044 g, 0.066 mmol), placed into an inert nitrogen atmosphere, and dissolved in 2 mL dry isopropyl alcohol. Sodium hydroxide (0.008 g, 0.2 mmol) was ground into a powder and added, followed by addition of lithium borohydride (0.0058 g, 0.266 mmol). Poor solubility was noted, so an additional 2 mL of THF was added to the mixture to assist in solubilizing, and the reaction was left to stir at 60 °C overnight with a condenser. LC-MS was used to monitor reaction progress alongside TLC (1:1 hexanes:ethyl acetate). Desired product mass of *m/z* 560 was observed with little conversion, alongside *m/z* of 546 (starting material) as the major product and *m/z* 574 impurity. The reaction was concentrated by rotary evaporation, and the crude material was purified by column

chromatography (hexanes:ethyl acetate 1:1). No desired product was obtained, and LC-MS of product fractions saw loss of desired product.

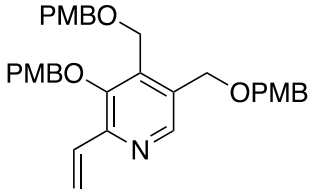

Synthesis of compound 18: 3',4',5'-*O*-methoxybenzyl-2'-vinyl pyridoxine. To a round bottom flask charged with a magnetic stir bar was added 2 mL anhydrous THF with sodium hydride (60% dispersion in mineral oil, 0.0277 g, 1.155 mmol). Methyltriphenylphosphonium bromide (0.0687 g, 0.192 mmol) was then added at 0 °C, and stirred for 1 h to prepare the Wittig reagent. Compound **16** aldehyde (0.07 g, 0.129 mmol) was then added at 0 °C and left to stir for 15 min. The reaction was then warmed to RT, and left to stir under nitrogen atmosphere overnight. Reaction progress was monitored by TLC in hexanes:ethyl acetate 1:1, and once conversion was seen, the reaction was stopped by concentrating by rotary evaporation. Once complete, the reaction was then partitioned between H_2O (20 mL) with 5 mL of brine and EtOAc (15 mL), with the organic phase isolated. The aqueous phase was washed with EtOAc (3 x 15 mL) and the organic extracts were combined, dried with Na_2SO_4, and concentrated *in vacuo*. The crude material was purified by column chromatography (hexanes:ethyl acetate = 1:1). Fractions containing product were collected and dried *in vacuo* to afford 3',4',5'-*O*-methoxybenzyl-2'-vinyl pyridoxine as a colourless oil (0.040 g, 56%). ^{1}H NMR (600 MHz, $CDCl_3$) δ 8.45 (s, 1H), 7.30 – 7.25 (m, 5H), 7.24 – 7.21 (m, 2H), 7.14 (dd, *J* = 17.3, 10.8 Hz, 1H), 6.93 – 6.89 (m, 4H), 6.87 – 6.84 (m, 2H), 6.44 (dd, *J* = 17.3, 2.0 Hz, 1H), 5.52 (dd, *J* = 10.8, 2.0 Hz, 1H), 4.79 (s, 2H), 4.61 (s, 2H), 4.56 (s, 2H), 4.47 (s, 2H), 4.42 (s, 2H), 3.84 (s, 3H), 3.81 (s, 3H), 3.80 (s, 3H). ^{13}C NMR (151 MHz, $CDCl_3$) δ 159.83,

159.51, 159.44, 151.26, 149.49, 146.07, 138.72, 133.50, 130.88, 130.09, 129.89, 129.85, 129.65, 128.75, 119.61, 114.07, 113.95, 77.54, 73.00, 72.34, 67.08, 65.97, 62.27, 55.41, 55.39, 55.35, 53.55, 25.72, 15.40. HRMS (ESI): Mass calc for $C_{33}H_{36}NO_6$[M+H]+: 542.2543, found: 542.2541.

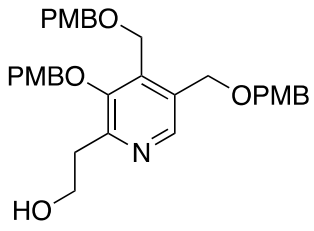

Synthesis of compound 19: 3',4',5'-*O*-methoxybenzyl-2'-(2-hydroxyethyl)pyridoxine. To a round bottom flask charged with a magnetic stir bar was added 2 mL of anhydrous THF, and compound **18** (0.04 g, 0.0738 mmol). The mixture was placed under a nitrogen atmosphere and cooled to 0 °C, and BH_3•THF complex (0.08 mL, 0.835 mmol) was added and stirred for 2 h at RT. Similarly, 9-BBN and BH_3•DMS complexes were also used. This was then followed by addition of 10% aqueous NaOH and 35% hydrogen peroxide. Reaction progress was monitored by LC-MS. Despite multiple attempts, no successful conversion to the desired product was observed.

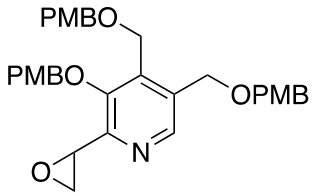

Synthesis of compound 20: 3',4',5'-*O*-methoxybenzyl-2'-(2-(oxiran-2-yl))pyridoxine. To a round bottom flask charged with a magnetic stir bar was added compound **18** (0.128 g, 0.236 mmol), dissolved in 2 mL t-butanol and 2 mL H_2O. Freshly recrystalized N-bromo succinimide (0.046 g, 0.258 mmol) was added slowly. The reaction was then heated to 40 °C and stirred for 1 h. After 1 h, the reaction was cooled to 0 °C, and 0.7 mL of 1 M NaOH solution was added, and stirring continued for 1 h at RT. The reaction was then

stopped by concentration by rotary evaporation, and an extraction was performed. The crude material was partitioned between H_2O (20 mL) with 5 mL of brine and EtOAc (15 mL), with the organic phase isolated. The aqueous phase was washed with EtOAc (3 x 15 mL) and the organic extracts were combined, dried with Na_2SO_4, and concentrated *in vacuo*. The crude material was purified by column chromatography (hexanes:ethyl acetate = 1:1). Fractions containing product were collected and dried *in vacuo* to afford 3',4',5'-*O*-methoxybenzyl-2'-(2- 2-(oxiran-2-yl))pyridoxine as a yellow oil (0.047 g, 36%). The reaction success was evaluated by LC-MS to confirm desired mass, and was used directly in the next reaction without further characterization due to the instability of the epoxide.

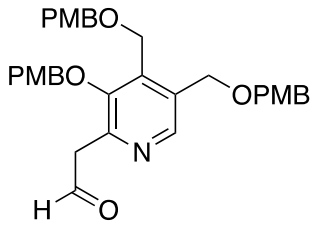

Synthesis of compound 21: 3',4',5'-*O*-methoxybenzyl-(2'-acetaldehyde)-pyridoxine. To a Schleck flask charged with a magnetic stir bar was added compound **20** (0.047 g, 0.0843 mmol), dissolved in 1 mL anhydrous DMF. The reaction mixture was cooled to 0 °C, and $BH_3 \bullet Et_2O$ complex (0.011 mL, 0.089 mmol) was added. The reaction was stirred at RT for 8 h. Reaction progress was assessed by LC-MS, where no desired formation of product was observed.

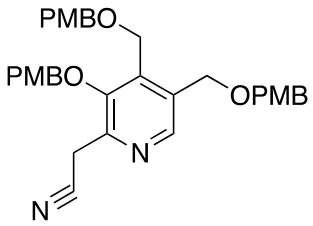

Synthesis of compound 22: 3',4',5'-*O*-methoxybenzyl-2'-(2-cyano)-pyridoxine. To a round bottom flask charged with a magnetic stir bar was added compound **13** (0.369 g, 0.592 mmol), dissolved in 2 mL DMF and 2 mL H_2O. Sodium cyanide (0.06 g, 1.224 mmol) was added carefully. The reaction was then heated to 90 °C and stirred for 2 h. The reaction progress was monitored by LC-MS, and when desired product was formed in high conversion, the reaction was stopped by concentrating *in vacuo* by rotary evaporation. The crude material was partitioned between H_2O (25 mL) with 10 mL of brine and EtOAc (20 mL), with the organic phase isolated. The aqueous phase was washed with EtOAc (3 x 20 mL) and the organic extracts were combined, dried with Na_2SO_4, and concentrated *in vacuo*. The crude material was purified by column chromatography (hexanes:ethyl acetate = 1:1). Fractions containing product were collected and dried *in vacuo* to afford 3',4',5'-*O*-methoxybenzyl-2'-(2-cyano)-pyridoxine as a yellow oil (0.280 g, 85%). LC-MS was used to assess reaction success without further characterization, and used directly in the next reaction.

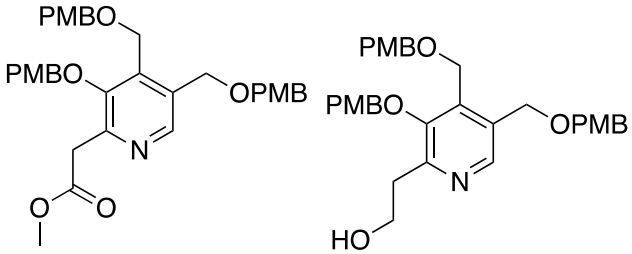

Synthesis of compound 23 and compound i: 3',4',5'-*O*-methoxybenzyl-(2'-acetate)-pyridoxine and 3',4',5'-*O*-methoxybenzyl-2'-(2-hydroxyethyl)-pyridoxine. To a round bottom flask charged with a magnetic stir bar was added compound **22** (0.085 g, 0.153

mmol), dissolved in 2 mL of MeOH. KOH (0.004 g, 0.071 mmol) was then added. The reaction was then left to stir at 80 °C for 8 h. Reaction progress was monitored by LC-MS, where desired methyl ester was observed. To stop the reaction, 5 mL H_2O was then added and stirred for 20 min, where then MeOH was removed by rotary evaporation. The crude material was partitioned between H_2O (25 mL) with 10 mL of brine and EtOAc (20 mL), with the organic phase isolated. The aqueous phase was washed with EtOAc (3 x 20 mL) and the organic extracts were combined, dried with Na_2SO_4, and concentrated *in vacuo*. The material was then used directly in the next reaction without characterization. Compound (0.007 g, 0.012 mmol) was dissolved in 1 mL anhydrous THF, followed by lithium aluminum hydride (0.0003 g, 0.006 mmol). The mixture was left to stir at RT for 1 h. Reaction progress was monitored by LC-MS, where desired product was not observed. As a result, compound **i** was not able to be synthesized.

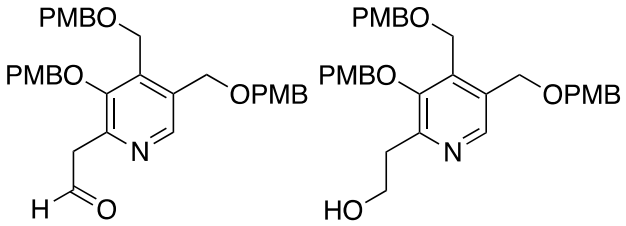

Synthesis of compound 24 and ii: 3',4',5'-*O*-methoxybenzyl-(2'-acetaldehyde)-pyridoxine and 3',4',5'-*O*-methoxybenzyl-2'-(2-hydroxyethyl)-pyridoxine. To a round bottom flask charged with a magnetic stir bar was added compound **22** (0.280 g, 0.505 mmol) and dissolved in 10 mL DCM. The mixture was cooled to -78 °C, where then DIBAL-H (1M in Hexanes, 0.505 mL, 0.505 mmol) was then added dropwise over 2 min. The mixture was then left to stir at -78 °C for 1 h, and was then quenched with 15 mL sat. Rochelle salts while stirring, followed by sat. aqueous ammonium chloride and 2 mL MeOH. The crude mixture was then partitioned between H_2O (25 mL) with 10 mL of brine

and DCM (20 mL), with the organic phase isolated. The aqueous phase was washed with DCM (3 x 20 mL) and the organic extracts were combined, dried with Na_2SO_4, and concentrated *in vacuo*. The crude material was then assessed by LC-MS, where desired product was not observed, but rather full reduction to the amine. Despite multiple attempts, desired product could not be obtained. As a result, compound **ii** was unable to be synthesized.

Diels-Alder/Kondrat'eva Synthesis of One Carbon Homologated Pyridoxine

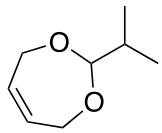

Synthesis of compound 25: 2-isopropyl-4,7-dihydro-[1,3]dioxepine. To a round bottom flask charged with a magnetic stir bar was added isobutyraldehyde (2.00 g, 27.74 mmol), followed by *cis*-1,4-butenediol (2.44 g, 27.693 mmol). 15 mL of hexanes was then added, followed by a spatula tip of 3 Å molecular sieves. The reaction was set to reflux at 70 °C for 12 h. Once complete, the sieves were removed by gravity filtration through paper, and an extraction/wash was performed on the filtrate. Two washes with 25 mL 1 M NaOH were performed, followed by two washes with brine. The organic extracts were collected and dried with Na_2SO_4, and concentrated *in vacuo*. A distillation was then performed using a high vacuum, with an oil bath heated from 40 °C- 70 °C. The distillate was collected into a separate flask. The distillation process afforded 2-isopropyl-4,7-dihydro-[1,3]dioxepine as a colourless oil (0.900 g, 23%). ^{1}H NMR (600 MHz, $CDCl_3$) δ 5.72 – 5.70 (m, 2H), 4.40 (dt, *J* = 16.4, 2.5 Hz, 2H), 4.33 (d, *J* = 7.0 Hz, 1H), 4.20 – 4.11 (m, 2H), 1.95 – 1.84 (m, *J* = 6.8 Hz, 1H), 0.95 (s, 3H), 0.94 (s, 3H). ^{13}C NMR (151 MHz, $CDCl_3$) δ 129.79, 109.15, 65.93, 31.84, 18.05. Obtained NMR matches previously published literature.[143]

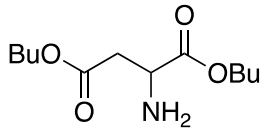

Synthesis of compound 26: di-n-butyl ester of L-aspartic acid. To a round bottom flask charged with a magnetic stir bar was added aspartic acid (2.00 g, 15.02 mmol), dissolved in 50 mL of n-butanol. Thionyl chloride ($SOCl_2$, 4.5 mL, 62.032 mmol) was then added at 0 °C for 30 min, followed by stirring overnight for 12 h at RT. n-butanol was then removed *in vacuo*, azeotropically with toluene, and 50 mL of diethyl ether was then added to the flask. The flask was then placed in the freezer, and once cold, sonicated to promote precipitation of product. The resulting solid was then washed with cold diethyl ether and cold hexanes under vacuum filtration. This afforded the di-n- butyl ester of L-aspartic acid as a white solid (3.73 g, Quant.). ^{1}H NMR (600 MHz, $CDCl_3$) δ 8.87 (s, 2H), 4.54 – 4.51 (m, 1H), 4.25 (d, *J* = 10.7 Hz, 1H), 4.21 – 4.13 (m, 2H), 4.12 (dd, *J* = 6.8, 5.1 Hz, 1H), 3.33 (dd, *J* = 17.9, 5.0 Hz, 1H), 3.20 (dd, *J* = 17.9, 5.1 Hz, 1H), 1.62 (s, 4H), 1.35 (s, 4H), 0.92 (td, *J* = 7.4, 2.1 Hz, 6H). ^{13}C NMR (151 MHz, $CDCl_3$) δ 170.39, 168.11, 66.94, 65.80, 49.78, 34.00, 30.55, 30.41, 19.15, 19.05, 13.80, 13.74. HRMS (ESI): Mass calc for $C_{12}H_{23}NO_4Na$[M+Na]+:268.1525, found: 268.1542.

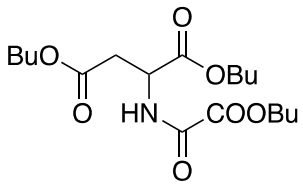

Synthesis of compound 27: di-n-butyl ester-2-oxoacetamido propanoate. To a round bottom flask charged with a magnetic stir bar was added compound **26** (3.73 g, 15.20 mmol), dissolved in 20 mL of DCM. Triethylamine (6.36 mL, 45.60 mmol) was then added, followed by butyl chloroacetate (2.57 mL, 18.24 mmol). The mixture was then stirred overnight at room temperature for 12 h. Reaction progress was monitored by TLC. Once

complete, an extraction performed. The crude material was partitioned between H_2O (50 mL) with 20 mL of brine and DCM (40 mL), with the organic phase isolated. The aqueous phase was washed with DCM (3 x 40 mL) and the organic extracts were combined, dried with Na_2SO_4, and concentrated *in vacuo*. This afforded di-n-butyl ester-2-oxoacetamido propanoate as a dark golden oil (4.94 g, 87%). ^{1}H NMR (600 MHz, $CDCl_3$) δ 8.17 – 7.95 (m, 1H), 4.83 – 4.78 (m, 1H), 4.29 (t, *J* = 6.9 Hz, 1H), 4.22 – 4.05 (m, 5H), 3.10 – 3.02 (m, 1H), 2.89 – 2.81 (m, 1H), 1.75 – 1.70 (m, 1H), 1.65 – 1.56 (m, 5H), 1.45 – 1.32 (m, 6H), 0.96 – 0.90 (m, 9H). ^{13}C NMR (151 MHz, $CDCl_3$) δ 170.63, 170.36, 169.72, 160.00, 158.94, 156.38, 67.26, 66.17, 65.27, 49.15, 36.00, 30.62, 30.53, 30.42, 19.17, 19.12, 19.09, 13.74. HRMS (ESI): Mass calc for $C_{18}H_{31}NO_7Na$[M+Na]+:396.1960, found: 396.1998.

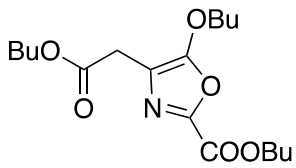

Synthesis of compound 28: 5-Butoxy-4-butyl acetate-2-butyl carboxylate oxazole. To a round bottom flask charged with a magnetic stir bar was added compound **27** (1.55 g, 4.15 mmol), dissolved in 12 mL anhydrous toluene. The mixture was cooled to 0 °C, and triethylamine (1.754 g, 12.45 mmol). Phosphorous oxychloride ($POCl_3$) (0.582 mL, 6.225 mmol) was then addded slowly. After stirring for 30 min, the round bottom flask was fixed with a condenser, and the mixture was heated to 80 °C and stirred overnight. To stop the reaction, the mixture was concentrated by rotary evporation until most solvent was removed, and then an extraction was performed. The crude material was partitioned between H_2O (50 mL) with 20 mL of brine and EtOAc (30 mL), with the organic phase isolated. The aqueous phase was washed with EtOAc (3 x 30 mL) and the organic

extracts were combined, dried with Na_2SO_4, and concentrated *in vacuo*. The crude material was purified by column chromatography (hexanes:ethyl acetate = 9:1 to hexanes:ethyl acetate = 8:2). Fractions containing product were collected and dried *in vacuo* to afford 5-butoxy-4-butyl acetate-2-butyl carboxylate oxazole as a yellow oil (1.062 g, 72%). ^{1}H NMR (300 MHz, DMSO) δ 4.39 – 4.28 (m, 3H), 4.10 (t, *J* = 6.7 Hz, 2H), 3.52 (s, 1H), 1.81 – 1.18 (m, 14H), 1.00 – 0.82 (m, 9H). HRMS (ESI): Mass calc for $C_{18}H_{30}NO_6Na$[M+Na]+: 378.1894, found: 378.1893.

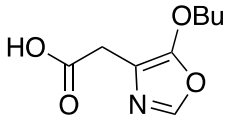

Synthesis of compound 29: 4-(acetic acid)-5-Butoxy-oxazole. To a round bottom flask charged with a magnetic stir bar was added compound **28** (1.00 g, 2.813 mmol), dissolved in 2 mL THF and 2 mL H_2O. Sodium hydroxide (0.282 g, 7.052 mmol) was then added, and the reaction was left to stir for 3 h. The mixture was then adjusted to pH 2 with 1 M HCl, and set to stir at 70 °C for 2 h, monitoring the release of CO_2 by collection with a balloon. Reaction progress was monitored by TLC and LC-MS. The reaction was then stopped by removal of solvent by rotary evaporation, and then an extraction was performed. The crude material was partitioned between H_2O (50 mL) with 20 mL of brine and DCM (30 mL), with the organic phase isolated. The aqueous phase was washed with DCM (3 x 30 mL) and the organic extracts were combined, dried with Na_2SO_4, and concentrated *in vacuo*. After high vacuum overnight, this afforded 4-(acetic acid)-5-Butoxy-oxazole as a yellow solid (0.476 g, 85%). ^{1}H NMR (500 MHz, $CDCl_3$) δ 7.49 (s, 1H), 4.16 (t, *J* = 6.6 Hz, 2H), 3.52 (s, 2H), 1.71 (ddt, *J* = 9.0, 7.8, 6.5 Hz, 2H), 1.50 – 1.39 (m, 3H), 0.95 (t, *J* = 7.4 Hz, 3H). ^{13}C NMR (126 MHz, $CDCl_3$) δ 174.30, 142.69, 74.52,

66.21, 31.43, 30.46, 30.33, 18.93, 13.77. HRMS (ESI): Mass calc for $C_9H_{13}NO_4Na[M+Na]+$: 222.0742, found: 222.0737.

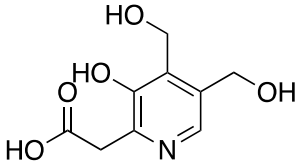

Synthesis of compound 30: 2'-(acetic acid) pyridoxine. To a round bottom flask charged with a magnetic stir bar and fixed with a condenser was added compound **29** (0.042 g, 0.211 mmol), followed by dixoxopene compound (0.06 g, 0.422 mmol). 3 mL of DMF was added, and the mixture was stirred at reflux overnight for 12 h. After this, 4 mL of 95% EtOH and 1 mL of 0.1% aqueous HCl solution were added and stirred for an additional 6 h, followed by 2 h of heating at 60 °C. The mixture was then concentrated by rotary evaporation, and 1 mL of 1 M HCl was added and set to reflux and for 1hr. Finally, 2 mL of 95% EtOH was added and stirred for 10 min. This mixture was then concentrated by rotary evaporation, followed by addition of diethyl ether to precipitate the product. The solid was vacuum filtered and washed twice with diethyl ether to afford a red solid (0.03g). NMR was used to characterize this solid, however, the desired product was not observed, and no carboxylic acid peak was present. LC-MS also further confirmed no desired product masses were present. As a result, compounds iii and iv were not able to be synthesized.

2'-*O*-Methyl Pyridoxine and Gingktoxin Cold Standard Synthesis

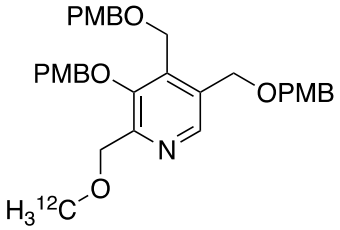

Synthesis of compound 31: 3',4',5'-*O*-methoxy benzyl-2'-*O*-methyl pyridoxine. To a round bottom flask charged with a magnetic stir bar was added compound **11** (0.142 g, 0.262 mmol) in 2 mL anhydrous THF. Sodium hydride (60% dispersion in mineral oil, 0.012 g, 0.30 mmol) was then added at 0 °C and left to stir for 30 minutes. Iodomethane (0.02 mL, 0.32 mmol) was then added to the mixture and left to stir at RT overnight under nitrogen. Reaction progress was monitored by TLC in hexanes:ethyl acetate 4:6. The reaction was then quenched by addition of distilled water, concentrated to remove the majority of THF by rotary evaporation, and then extracted. The solution was partitioned between H_2O (20 mL) with 5 mL of brine and DCM (15 mL), with the organic phase isolated. The aqueous phase was washed with DCM (3 x 15 mL) and the organic extracts were combined, dried with Na_2SO_4, and concentrated *in vacuo*. The crude material was purified by column chromatography (hexanes/ethyl acetate = 4:6). Fractions containing product were collected and dried *in vacuo* to afford 3',4',5'-*O*-methoxy benzyl-2'-*O*-methyl pyridoxine as a yellow oil (0.14 g, 96%). ^{1}H NMR (600 MHz, $CDCl_3$) δ 8.46 (s, 1H), 7.28 – 7.20 (m, 7H), 6.92 – 6.84 (m, 7H), 4.86 (s, 2H), 4.60 (s, 2H), 4.58 (s, 2H), 4.55 (s, 2H), 4.45 (s, 2H), 4.41 (s, 2H), 3.83 (s, 3H), 3.80 (s, 3H), 3.79 (s, 3H). ^{13}C NMR (151 MHz, $CDCl_3$) δ 159.87, 159.57, 159.50, 152.75, 151.69, 145.62, 138.84, 134.33, 130.04, 129.92, 129.79, 129.70, 128.97, 114.09, 114.00, 78.33, 73.10, 72.49, 71.40, 67.03, 62.31,

58.86, 55.44, 55.42, 55.39. HRMS (ESI): Mass calc for $C_{33}H_{37}NO_7Na$[M+Na]+: 582.2438, found: 582.2468.

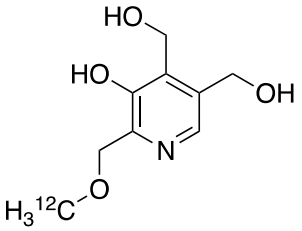

Synthesis of compound 32: 2'-*O*-methyl pyridoxine. To a round bottom flask charged with a magnetic stir bar was added compound **31** (0.13 g, 0.232 mmol), dissolved in 2 mL anhydrous THF. 2 mL of synthesis grade TFA was then added, the flask was fixed with a condenser, and the solution waas stirred for 4 hours at 85 °C to ensure full conversion. Reaction conversion was monitored by LC-MS. Once complete, the reaction was concentrated *in vacuo*. The crude material was then purified by semi-prep HPLC. Fractions containing product were collected and dried by lyophilization to afford 4'-*O*-methylpyridoxine as an off-white solid (0.037 g, 80%). ^{1}H NMR (600 MHz, DMSO) δ 8.14 (s, 1H), 4.78 (s, 2H), 4.69 (s, 4H), 3.42 (s, 3H). ^{13}C NMR (151 MHz, DMSO) δ 150.74, 141.05, 138.90, 132.15, 104.99, 67.35, 58.56, 57.95, 55.60. HRMS (ESI): Mass calc for $C_9H_{14}NO_4$[M+H]+: 200.0950, found: 200.0923.

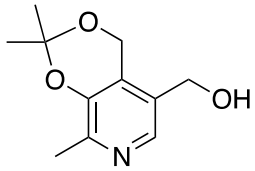

Synthesis of compound 33: 3,4'-*O*-Isopropylidenepyridoxine. To a round bottom flask charged with a magnetic stir bar was added *p*-toluenesulfonic acid monohydrate (13.4 g, 77.80 mmol) and pyridoxine hydrochloride (4 g, 19.46 mmol). 40 mL of dry acetone was added, followed by 2,2-dimethoxypropane (24 mL, 195.86 mmol). The resulting mixture was stirred overnight at room temperature under a nitrogen atmosphere.

The dark brown solution was then neutralized to pH 7 using sat. $NaHCO_3$, concentrated by rotary evaporation, and extracted. The solution was partitioned between H_2O (75 mL) with 25 mL of brine and DCM (50 mL), with the organic phase isolated. The aqueous phase was washed with DCM (3 x 50 mL) and the organic extracts were combined, dried with Na_2SO_4, and concentrated *in vacuo*. The resulting solid was precipitated and triturated in 5:1 pentane:ether, and put in the fridge to promote further precipitation. This was followed by vacuum filtration, where the solid was washed with cold ether three times.The solid was dried *in vacuo* to afford 5'-*O*-methoxybenzyl pyridoxine as a white powder (3.75 g, 92%). ^{1}H NMR (400 MHz, $CDCl_3$) δ 7.78 (s, 1H), 4.92 (s, 2H), 4.53 (s, 2H), 2.35 (s, 3H), 1.54 (s, 6H). ^{13}C NMR (101 MHz, $CDCl_3$) δ 147.83, 146.20, 138.69, 129.58, 126.09, 99.92, 60.28, 58.70, 24.88, 18.38. HRMS (ESI): Mass calc for $C_{11}H_{16}NO_3$[M+H]+: 209.1052, found: 209.1069.

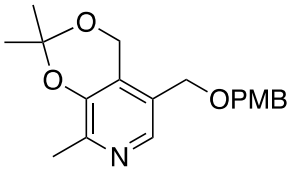

Synthesis of compound 34: 3,4'-*O*-Isopropylidene-5'-*O*-methoxybenzyl pyridoxine. To a round bottom flask charged with a magnetic stir bar was added dry DMF (6 mL), followed by compound **33** (2 g, 9.56 mmol). The reaction mixture was cooled down to 0 °C, and sodium hydride (60% dispersion in mineral oil, 0.674 g, 16.86 mmol) was added. The mixture was stirred for 5 minutes at 0 °C, and then removed from ice to stir for 1 hour at RT. To the suspension was then added 4-methoxybenzyl chloride (1.495 mL, 11.47 mmol) at 0 °C dropwise, and the resulting mixture was then stirred overnight at RT for a total of 16 hours. The dark brown-green solution was then quenched by adding ice-water to the mixture at 0 °C, and then the pH of the mixture was adjusted to pH 8 using sat.

ammonium chloride. The majority of solvent was then removed by rotary evaporation. The solution was then partitioned between H_2O (75 mL) with 25 mL of brine and DCM (50 mL), with the organic phase isolated. The aqueous phase was washed with DCM (3 x 50 mL) and the organic extracts were combined, dried with Na_2SO_4, and concentrated *in vacuo*. The crude material was purified by column chromatography (hexanes/ethyl acetate = 3:1 to hexanes/ethyl acetate = 4:6). Fractions containing product were collected and dried *in vacuo* to afford 3,4'-*O*-isopropylidene-5'-*O*-methoxybenzyl pyridoxine as a yellow oil (2.23 g, 58%). ^{1}H NMR (400 MHz, DMSO) δ 7.92 (s, 1H), 7.25 (d, *J* = 8.6 Hz, 2H), 6.91 (d, *J* = 8.6 Hz, 2H), 4.84 (s, 2H), 4.43 (s, 2H), 4.40 (s, 2H), 3.74 (s, 3H), 2.29 (s, 3H), 1.48 (s, 6H). ^{13}C NMR (101 MHz, DMSO) δ 158.82, 146.43, 145.26, 139.30, 129.95, 129.42, 127.05, 125.84, 113.72, 99.54, 71.17, 66.39, 57.89, 55.06, 24.48, 18.35. HRMS (ESI): Mass calc for $C_{19}H_{24}NO_4$[M+H]+: 330.1690, found: 330.1705.

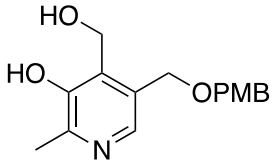

Synthesis of compound 35: 5'-*O*-methoxybenzyl pyridoxine. To a round bottom flask charged with a magnetic stir bar was added compound **34** (1.42 g, 4.31 mmol). 5 mL of distilled water and 5 mL of formic acid (LC-MS grade) were then added. The mixture was stirred at 55 °C for 6 hours. Progress of the deprotection was monitored by LC-MS. The reaction mixture was then concentrated by rotary evaporation. 2 portions of 10 mL acetone were added, and concentrated again by rotary evaporation. 5 mL of cold acetone was then added and sonicated, precipitating product. The flask was then placed in the fridge to promote further precipitation, and was then washed under vacuum filtration 1x with cold acetone, and 2x with cold hexanes. The solid was dried *in vacuo* to afford 5'-*O*-

methoxybenzyl pyridoxine as a white powder (0.763 g, 62%). ^{1}H NMR (600 MHz, DMSO) δ 7.87 (s, 1H), 7.26 (d, *J* = 8.6 Hz, 2H), 6.93 – 6.89 (m, 2H), 4.72 (s, 2H), 4.48 (s, 2H), 4.41 (s, 2H), 3.74 (s, 3H), 2.34 (s, 3H). ^{13}C NMR (151 MHz, DMSO) δ 158.78, 149.89, 146.79, 139.72, 131.70, 130.11, 129.44, 129.33, 113.69, 71.19, 66.93, 56.79, 55.06, 19.32. HRMS (ESI): Mass calc for $C_{16}H_{19}NO_4Na$[M+Na]+: 312.1231, found: 312.1212.

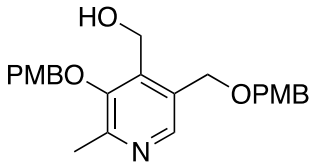

Synthesis of compound 36: 3,5'-*O*-methoxybenzyl pyridoxine. To a round bottom flask charged with a magnetic stir bar was added compound **35** (0.763 g, 2.64 mmol), followed by 5 mL anhydrous DMF. Cesium carbonate (1.031 g, 3.16 mmol) was then added at 0 °C and stirred for 20 min. 4-methoxybenzyl chloride (0.392 mL, 3.00mmol) was then added to the mixture, and left to stir overnight at RT. Progress of reaction was monitored by TLC in 1:1 Hexanes/Ethyl Acetate. Once complete, the majority of solvent was then removed by rotary evaporation. The solution was then partitioned between H_2O (100 mL) with 25 mL of brine and DCM (50 mL), with the organic phase isolated. The aqueous phase was washed with DCM (3 x 50 mL) and the organic extracts were combined, dried with Na_2SO_4, and concentrated *in vacuo*. The crude material was purified by column chromatography (hexanes/ethyl acetate = 1:1 to hexanes:ethyl acetate 3:7). Fractions containing product were collected and dried *in vacuo* to afford 3,5'-*O*-methoxybenzyl pyridoxine as an orange solid (0.64 g, 60%). ^{1}H NMR (600 MHz, $CDCl_3$) δ 8.20 (s, 1H), 7.38 (d, *J* = 8.6 Hz, 2H), 7.29 (d, *J* = 8.6 Hz, 2H), 6.91 (dd, *J* = 10.9, 8.6 Hz, 4H), 4.91 (s, 2H), 4.61 (s, 2H), 4.56 (s, 2H), 3.82 (s, 3H), 3.81 (s, 3H), 2.51 (s, 3H). ^{13}C NMR (151 MHz, $CDCl_3$) δ 159.96, 159.80, 154.62, 152.02, 145.38, 142.07, 130.84,

130.23, 130.06, 128.97, 128.90, 114.23, 114.18, 76.75, 72.76, 68.58, 56.55, 55.46, 55.43, 19.99. HRMS (ESI): Mass calc for $C_{24}H_{27}NO_5Na$[M+Na]+: 432.1761, found: 432.1787.

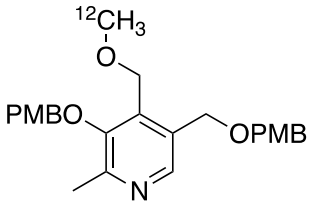

Synthesis of compound 37: 3',5'-*O*-methoxy benzyl-4'-*O*-methyl pyridoxine. To a round bottom flask charged with a magnetic stir bar was added compound **36** (0.3 g, 0.733 mmol) in 4 mL anhydrous THF. Sodium hydride (60% dispersion in mineral oil, 0.03 g, 0.75 mmol) was then added at 0 °C and left to stir for 30 minutes. Iodomethane (0.05 mL, 0.80 mmol) was then added to the mixture and left to stir at RT overnight under nitrogen. Reaction progress was monitored by TLC in hexanes:ethyl acetate 4:6. The reaction was then quenched by addition of distilled water, concentrated to remove the majority of THF by rotary evaporation, and then extracted. The solution was partitioned between H_2O (20 mL) with 5 mL of brine and DCM (15 mL), with the organic phase isolated. The aqueous phase was washed with DCM (3 x 15 mL) and the organic extracts were combined, dried with Na_2SO_4, and concentrated *in vacuo*. The crude material was purified by column chromatography (hexanes/ethyl acetate = 4:6). Fractions containing product were collected and dried *in vacuo* to afford 4'-*O*-methyl-3,5'-*O*-methoxybenzyl pyridoxine as a yellow oil (0.234 g, 76%). ^{1}H NMR (600 MHz, $CDCl_3$) δ 8.31 (s, 1H), 7.36 (d, *J* = 8.5 Hz, 2H), 7.29 (d, *J* = 8.5 Hz, 2H), 6.95 – 6.87 (m, 5H), 4.81 (s, 2H), 4.60 (s, 2H), 4.50 (d, *J* = 5.2 Hz, 5H), 3.83 (s, 4H), 3.81 (s, 4H), 3.33 (d, *J* = 0.8 Hz, 3H), 2.53 (s, 3H). ^{13}C NMR (151 MHz, $CDCl_3$) δ 159.89, 159.50, 153.40, 152.28, 145.59, 137.94, 131.89, 130.14, 129.94, 129.73, 129.06, 114.16, 114.03, 114.01, 76.53, 72.37, 67.13,

65.25, 58.87, 55.47, 55.45, 19.94. HRMS (ESI): Mass calc for $C_{25}H_{29}NO_5Na$[M+Na]+: 446.1943, found: 446.1936.

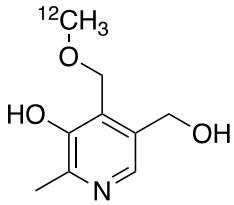

Synthesis of compound 38: 4'-*O*-methylpyridoxine (Ginkgotoxin cold standard). To a round bottom flask charged with a magnetic stir bar was added compound **37** (0.234 g, 0.55 mmol), dissolved in 3 mL anhydrous THF. 3 mL of synthesis grade TFA was then added, the flask was fixed with a condenser, and stirred for 4 hours at 85 °C to ensure full conversion. Reaction conversion was monitored by LC-MS. Once complete, the reaction was concentrated *in vacuo*. The crude material was then purified by semi-prep HPLC. Fractions containing product were collected and dried by lyophilization to afford 4'-*O*-methylpyridoxine (Ginkgotoxin) as a white-yellow solid (0.081 g, 80%). ^{1}H NMR (400 MHz, DMSO) δ 8.20 (s, 1H), 4.69 (s, 2H), 4.63 (s, 2H), 3.30 (s, 3H), 2.57 (s, 3H). ^{13}C NMR (151 MHz, DMSO) δ 151.61, 142.13, 139.49, 137.16, 129.79, 63.84, 58.08, 57.60, 15.47. HRMS (ESI): Mass calc for $C_9H_{14}NO_3$[M+H]+: 184.0995, found: 184.0974.

4.4 Cell Culture of H460 and A549 Cancer Lines

Large-cell lung cancer cells (H460) were grown in RPMI-1640 (RPMI) medium supplemented with 10% fetal bovine serum (FBS) and 1% penicillin-streptomycin (P/S) until 80% confluent, at which point they were passaged approximately every three days. To split cells, trypsin-EDTA was added to the medium and incubated at 37 °C for 5 minutes. Additional medium was then added to wash cells off the flask surface, and cells were transferred to falcon tubes. Centrifugation was then performed at 1000 xg (5 min)

to pit the cells, followed by careful removal of supernatant, which allowed for removal of trypsin-EDTA. Cells were then resuspended in RPI medium, counted, and split to a new flask using 250,000 cells. Cells were passaged three times before use in metabolic assays.

Adenocarcinomic human alveolar basal epithelial cells (A549) were grown in Dulbecco's Modified Eagle Medium (DMEM) supplemented with 10% fetal bovine serum (FBS) and 1% penicillin-streptomycin (P/S) using the same procedure.

4.5 Vitamin B_6 Derivative Metabolism Quantification

Fluorinated pyridoxine and methylated pyridoxine derivatives were quantified in samples by LC-MS.

A549 and H460 cells were seeded in 100-mm tissue culture-treated dishes and cultured with Dulbecco's Modified Eagle Medium (DMEM) supplemented with 10% FBS and 1% P/S in a humidified CO_2 incubator until the cells reached 70% confluency. Twenty-four hours after seeding, the medium was replaced with fresh medium alone. After another 24 h, the medium was replaced with fresh medium alone or containing 25 mM of pyridoxine derivatives and incubated for 4 h at 37 °C. Two technical replicates for each of the three biological replicates were performed. Cells were rinsed with ice cold 150 mM ammonium formate, pH 7.4 and quenched with -20°C equilibrated 50% methanol (360 µL). The cell slurry was transferred to prechilled tubes containing 1.4-mm ceramic beads (Omni International). Cells were lysed by bead beating (MagNA Lyser, Roche Diagnostics) at 2000 RPM for two rounds of one minute. Ice-cold dichloromethane (600 µL) and H_2O (300 µL) were then added, and samples were vortexed and incubated on ice for 10 minutes. Samples were centrifuged at 4,000 RPM for 10 minutes at 1°C and

the supernatants collected and dried by vacuum centrifugation at -4°C (Refrigerated Centrivap, Labconco). The resulting dried polar metabolite extract was stored at -80°C until LC-MS analysis. Samples were resuspended in H_2O and run on a 6470 Triple Quadruple MS equipped with a 1290 Infinity ultraperformance LC system utilizing the Metabolomics Dynamic MRM Database and Method (Agilent), which uses an ion-pairing reverse phase chromatography with negative or positive ionization mode (substrate dependant). This method was optimized for phosphate-containing metabolites with the addition of 5 µM InfinityLab deactivator (Agilent) to mobile phases A and B, which requires decreasing the backflush acetonitrile to 90%. Precursor/product ion pairs for pyridoxamine, pyridoxine, pyridoxal 5-phosphate were present in the database. Relative metabolite quantifications were calculated by interpolating external compound calibration curves in Mass Hunter Quantitative Analysis 10.0 (Agilent).

4.6 FX-FN and FX-C Automated Radiochemistry Module Protocol

TRACERlab FX-FN Automated Synthesis Module

For [^{18}F], an automated in-house time-list program was utilized to attempt synthesis of radiotracer 2, [^{18}F]C_6-fluoro pyridoxine. Typically an azeotropic drying stage is used; however, due to the requirement of [^{18}F]HF for synthesis, this step was removed.

The module was used in its basic configuration, without any modifications (Figure 43). After proton bombardment of [^{18}O-H_2O] for 1 hour (~1600 mCi of activity), the [^{18}F]fluoride produced by the cyclotron is delivered to the FX-FN module. The [^{18}F]HF in 2.5 mL of H_2O was eluted into the reaction vessel containing compound **7** (1 mg) and sodium nitrite (1 mg). The reaction vessel was then heated to 60 °C and stirred for 1 h. After this time, drying under N_2 flow at 110 °C was then performed to remove most residual water and [^{18}F]HF. A small aliquot of 10 M NaOH was then added to ensure quenching of HF, then 2 mL of acetonitrile was added to the reaction vial. The resulting mixture was then passed through an Al_2O_3 cartridge to filter residual salt and [^{18}F]NaF. An additional 2 mL of acetonitrile was used to wash the product out of the cartridge, where the solution was sent for semi-preparative HPLC purification according to the separation procedures outlined below.

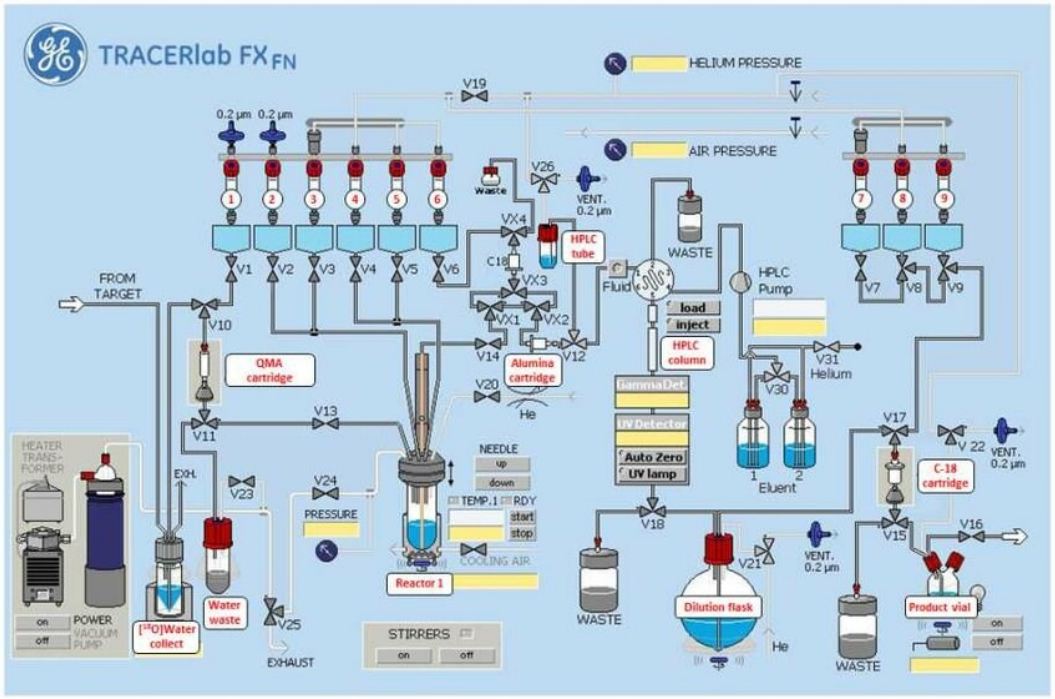

Figure 43. TRACERlab FX-FN Synthesis Module Overlay.

TRACERlab FX-C Pro Automated Carbon Module

For [^{11}C], an automated in-house time-list program was utilized to attempt radiosynthesis of radiotracers 3 and 4, 2'-*O*-methyl pyridoxine and 4'-*O*-methyl pyridoxine.

The module was used in its basic configuration, without significant modifications (Figure 44). After proton bombardment of nitrogen gas ([^{14}N]) in the presence of oxygen for 20 minutes by the cyclotron, [^{11}C]CO_2 was produced (~500 mCi of activity) and delivered to the FX-C Pro module through a Teflon delivery line by helium. A column containing Shimalite-nickel was then sealed under hydrogen gas and heated to 380 °C to convert of [^{11}C]CO_2 to [^{11}C]CH_4 by a gas phase reaction. The [^{11}C]CH_4 was then passed through a desiccant column of phosphorous pentoxide, and trapped on a column of carbosphere at -90 °C with liquid nitrogen. The carbosphere column is then heated at 90 °C to release the gaseous [^{11}C]CH_4, which then enters a circulating oven system. This

contains a gas pump, a column of iodine at 100 °C, a Tracerlab iodine reactor tube at 720 °C, adjacent columns of Ascarite II, and a column of Porapak Q at room temperature. This gaseous mixture was circulated for approximately 5 minutes, which accumulated [^{11}C]MeI, which was either delivered directly to the reaction vessel, or passed through a silver triflate column at 190 °C to form [^{11}C]MeOTf. Once the desired methylation agent entered the reaction vessel, the reaction mixture was stirred for 5 minutes at 60 °C for MeI, or 30 °C for MeOTf. Deprotection can then begin, with introduction of TFA or 2N HCl, for 5 minutes at 85 °C. Once complete, the reaction vessel is heated to 120 °C and opened to a He gas stream to remove unreacted methylation agent and acid. 2 mL of the HPLC eluent (80:20 H_2O:MeCN) is then added, and sent to the semi-prep HPLC for purification according to the procedure outlined below.

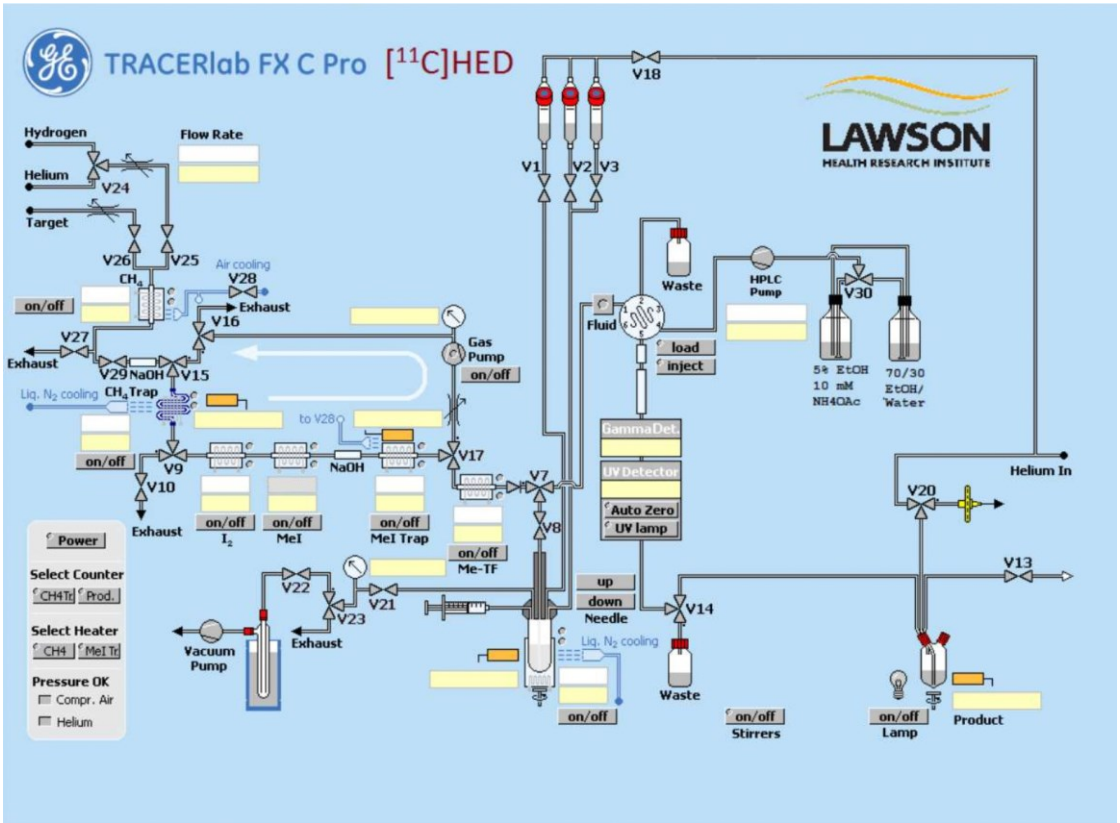

Figure 44. TRACERlab FX-C Pro Synthesis Module Overlay.

Semi-Prep HPLC Separation and Product Validation by Analytical Radio-HPLC

For radiochemical reactions, semi-prep HPLC purification of reaction mixtures were performed using a Sykam HPLC separation module utilizing an S 1122 solvent delivery unit connected to a UV detector (measuring at 254 or 280 nm) without a column warmer. All reaction mixtures were introduced into the column at approximate 3-4 mL total volume. A Phenomenex 00G-4252-N0 Luna C18(2) column with 5 µm particle size, at 100 Å, with dimensions 250x10 mm was used for separation. A pre-made solvent mixture of 20% HPLC grade acetonitrile with 80% 18.2 MΩ cm Millipore water was used. All samples utilized a 2-3 mL/min flow rate. Desired product peaks were identified during the run using a radioactivity and UV detector, and collected into a product vial where the radioactivity in mCi was recorded.

Analytical HPLC product validation of cold-standard products and radiochemistry reactions was performed using a Waters HPLC separation module utilizing a Waters 1525 Binary HPLC pump unit connected to a Waters 2996 photodiode array detector (scanning from 190-400 nm) without a column warmer. A Waters e-SAT/IN detector was coupled, allowing for detection of radioactive peaks. All cold-standards and reactants measured were prepared by dissolving 1 mg of material in 0.5 mL of acetonitrile. All radiolabelled products were HPLC separated for desired product, which was transferred to an HPLC vial with 200-400 µCi of activity.

For fluorine-labelled products, a Supelco 56401AST apHera NH_2 Polymer column with 5 µm particle size, at 300 Å, with dimensions 150x4.6 mm was used for separation. Eluent A was 18.2 MΩ cm Millipore water, and eluent B was HPLC grade acetonitrile. For fluorine labelled cold-standard **1** and its radiotracer counterpart, a gradient profile was

used as follows: flow rate of 1 mL/min, with an increase from 50% acetonitrile to 5% acetonitrile over 10 minutes, running at 5% acetonitrile for 2 more minutes, re-equilibrating to 50% acetonitrile over 1 minute, with a final 3 minutes (16-minute total run) at 50% acetonitrile.

For carbon-labelled products, a Phenomenex 00G-4252-E0 Luna C18(2) column with 5 µm particle size, at 100 Å, with dimensions 250x4.6 mm was used for separation. Eluent A was 18.2 MΩ cm Millipore water, and eluent B was HPLC grade acetonitrile. Carbon labelled cold-standards 3 and 4 and their radiotracer counterparts utilized a gradient profile as follows: flow rate of 1 mL/min, with an increase from 5 to 95% acetonitrile over 12 minutes, running at 95% acetonitrile for 2 more minutes, and then re-equilibrating to 5% acetonitrile over 2 minutes, and then running for a final 2 minutes (18-minute total run) at 5% acetonitrile.

Analysis of radioactive and UV peaks was performed using Empower 2 software, where radioactivity peaks elute and are closely followed by a corresponding UV peak for the same product if successful. Validation of reaction success was performed by matching radiochemical conversion peaks to cold-standard UV traces, and implementation of cold-standard co-injection.

References

(1) Lung and bronchus cancer statistics | Canadian Cancer Society. https://cancer.ca/en/cancer-information/cancer-types/lung/statistics (accessed 2024-02-27).

(2) Torre, L. A.; Bray, F.; Siegel, R. L.; Ferlay, J.; Lortet-Tieulent, J.; Jemal, A. Global Cancer Statistics, 2012. *CA Cancer J Clin* **2015**, *65* (2), 87–108. https://doi.org/10.3322/CAAC.21262.

(3) Biersack, B.; Schobert, R. Current State of Metal-Based Drugs for the Efficient Therapy of Lung Cancers and Lung Metastases. *Adv Exp Med Biol* **2016**, *893*, 211–224. https://doi.org/10.1007/978-3-319-24223-1_11.

(4) Siegel, R. L.; Miller, K. D.; Jemal, A. Cancer Statistics, 2018. *CA Cancer J Clin* **2018**, *68* (1), 7–30. https://doi.org/10.3322/CAAC.21442.

(5) Smit, E.; Moro-Sibilot, D.; Carpeño, J. de C.; Lesniewski-Kmak, K.; Aerts, J.; Villatoro, R.; Kraaij, K.; Nacerddine, K.; Dyachkova, Y.; Smith, K. T.; Girvan, A.; Visseren-Grul, C.; Schnabel, P. A. Cisplatin and Carboplatin-Based Chemotherapy in the First-Line Treatment of Non-Small Cell Lung Cancer: Analysis from the European FRAME Study. *Lung Cancer* **2016**, *92*, 35–40. https://doi.org/10.1016/J.LUNGCAN.2015.11.022.

(6) Du, L.; Morgensztern, D. Chemotherapy for Advanced-Stage Non-Small Cell Lung Cancer. *Cancer J.* **2015**, *21* (5), 366–370. https://doi.org/10.1097/PPO.0000000000000141.

(7) Sarin, N.; Engel, F.; Kalayda, G. V.; Mannewitz, M.; Cinatl, J.; Rothweiler, F.; Michaelis, M.; Saafan, H.; Ritter, C. A.; Jaehde, U.; Frötschl, R. Cisplatin Resistance in Non-Small Cell Lung Cancer Cells Is Associated with an Abrogation of Cisplatin-Induced G2/M Cell Cycle Arrest. *PLoS One* **2017**, *12* (7), e0181081. https://doi.org/10.1371/JOURNAL.PONE.0181081.

(8) Dasari, S.; Bernard Tchounwou, P. Cisplatin in Cancer Therapy: Molecular Mechanisms of Action. *Eur J Pharmacol* **2014**, *740*, 364–378. https://doi.org/10.1016/J.EJPHAR.2014.07.025.

(9) Galluzzi, L.; Marsili, S.; Vitale, I.; Senovilla, L.; Michels, J.; Garcia, P.; Vacchelli, E.; Chatelut, E.; Castedo, M.; Kroemer, G. Vitamin B6 Metabolism Influences the Intracellular Accumulation of Cisplatin. *Cell Cycle* **2013**, *12* (3), 417-421. https://doi.org/10.4161/CC.23275.

(10) Berndtsson, M.; Hägg, M.; Panaretakis, T.; Havelka, A. M.; Shoshan, M. C.; Linder, S. Acute Apoptosis by Cisplatin Requires Induction of Reactive Oxygen Species but Is Not Associated with Damage to Nuclear DNA. *Int J Cancer* **2007**, *120* (1), 175–180. https://doi.org/10.1002/IJC.22132.

(11) Mandic, A.; Hansson, J.; Linder, S.; Shoshan, M. C. Cisplatin Induces Endoplasmic Reticulum Stress and Nucleus-Independent Apoptotic Signaling. *J Biol Chem* **2003**, *278* (11), 9100–9106. https://doi.org/10.1074/JBC.M210284200.

(12) Galluzzi, L.; Vitale, I.; Michels, J.; Brenner, C.; Szabadkai, G.; Harel-Bellan, A.; Castedo, M.; Kroemer, G. Systems Biology of Cisplatin Resistance: Past, Present and Future. *Cell Death Dis* **2014**, *5* (5), e1257. https://doi.org/10.1038/CDDIS.2013.428.

(13) Han, Y.; Wen, P.; Li, J.; Kataoka, K. Targeted Nanomedicine in Cisplatin-Based Cancer Therapeutics. *J Control Release* **2022**, *345*, 709–720. https://doi.org/10.1016/J.JCONREL.2022.03.049.
(14) Alessio, E.; Messori, L. NAMI-A and KP1019/1339, Two Iconic Ruthenium Anticancer Drug Candidates Face-to-Face: A Case Story in Medicinal Inorganic Chemistry. *Molecules* **2019**, *24* (10), 1995-2015. https://doi.org/10.3390/MOLECULES24101995.
(15) Vasan, N.; Baselga, J.; Hyman, D. M. A View on Drug Resistance in Cancer. *Nature 2019 575:7782* **2019**, *575* (7782), 299–309. https://doi.org/10.1038/s41586-019-1730-1.
(16) Nascimento, A. V.; Singh, A.; Bousbaa, H.; Ferreira, D.; Sarmento, B.; Amiji, M. M. Overcoming Cisplatin Resistance in Non-Small Cell Lung Cancer with Mad2 Silencing SiRNA Delivered Systemically Using EGFR-Targeted Chitosan Nanoparticles. *Acta Biomater* **2017**, *47*, 71–80. https://doi.org/10.1016/J.ACTBIO.2016.09.045.
(17) Hryniuk, W.; Bush, H. The Importance of Dose Intensity in Chemotherapy of Metastatic Breast Cancer. *J Clin Oncol* **1984**, *2* (11), 1281–1288. https://doi.org/10.1200/JCO.1984.2.11.1281.
(18) Citron, M. L.; Berry, D. A.; Cirrincione, C.; Hudis, C.; Winer, E. P.; Gradishar, W. J.; Davidson, N. E.; Martino, S.; Livingston, R.; Ingle, J. N.; Perez, E. A.; Carpenter, J.; Hurd, D.; Holland, J. F.; Smith, B. L.; Sartor, C. I.; Leung, E. H.; Abrams, J.; Schilsky, R. L.; Muss, H. B.; Norton, L. Randomized Trial of Dose-Dense versus Conventionally Scheduled and Sequential versus Concurrent Combination Chemotherapy as Postoperative Adjuvant Treatment of Node-Positive Primary Breast Cancer: First Report of Intergroup Trial C9741/Cancer and Leukemia Group B Trial 9741. *J Clin Oncol* **2003**, *21* (8), 1431–1439. https://doi.org/10.1200/JCO.2003.09.081.
(19) Galluzzi, L.; Senovilla, L.; Vitale, I.; Michels, J.; Martins, I.; Kepp, O.; Castedo, M.; Kroemer, G. Molecular Mechanisms of Cisplatin Resistance. *Oncogene* **2012**, *31* (15), 1869–1883. https://doi.org/10.1038/ONC.2011.384.
(20) Siddik, Z. H. Cisplatin: Mode of Cytotoxic Action and Molecular Basis of Resistance. *Oncogene* **2003**, *22* (47), 7265–7279. https://doi.org/10.1038/SJ.ONC.1206933.
(21) Borst, P.; Rottenberg, S.; Jonkers, J. How Do Real Tumors Become Resistant to Cisplatin? *Cell Cycle* **2008**, *7* (10), 1353–1359. https://doi.org/10.4161/CC.7.10.5930.
(22) Gong, J.; Salgia, R. Managing Patients With Relapsed Small-Cell Lung Cancer. *J Oncol Pract* **2018**, *14* (6), 359-366. https://doi.org/10.1200/JOP.18.00204.
(23) Tardy, A. L.; Pouteau, E.; Marquez, D.; Yilmaz, C.; Scholey, A. Vitamins and Minerals for Energy, Fatigue and Cognition: A Narrative Review of the Biochemical and Clinical Evidence. *Nutrients* **2020**, *12* (1), 228-263. https://doi.org/10.3390/NU12010228.
(24) McDowell, L. R. Vitamins in Animal and Human Nutrition. **2000**, 2nd edition, pg 3-14. https://doi.org/10.1002/9780470376911.
(25) Agostoni, C.; Bresson, J.-L.; Fairweather-Tait, S.; Flynn, A.; Golly, I.; Korhonen, H.; Lagiou, P.; Løvik, M.; Marchelli, R.; Martin, A.; Moseley, B.; Neuhäuser-

Berthold, M.; Przyrembel, H.; Salminen, S.; Sanz, Y.; Strain, S.; Strobel, S.; Tetens, I.; Tomé, D.; van Loveren, H.; Verhagen, H.; Becker, W.; van den Berg, H.; Hulshof, K.; Jackson, A. Scientific Opinion on Principles for Deriving and Applying Dietary Reference Values. *EFSA Journal* **2010**, *8* (3), 1458-1488. https://doi.org/10.2903/J.EFSA.2010.1458.

(26) Rippin, H. L.; Hutchinson, J.; Jewell, J.; Breda, J. J.; Cade, J. E. Adult Nutrient Intakes from Current National Dietary Surveys of European Populations. *Nutrients 2017, Vol. 9, Page 1288* **2017**, *9* (12), 1288-1335. https://doi.org/10.3390/NU9121288.

(27) Drummond, J. C. The Nomenclature of the So-Called Accessory Food Factors (Vitamins). *Biochem. J.* **1920**, *14* (5), 660. https://doi.org/10.1042/BJ0140660.

(28) Yang, L.; Scott, P. J. H.; Shao, X.; Yang, L.; Scott, P. J. H.; Shao, X. [11C]Carbon Dioxide: Starting Point for Labeling PET Radiopharmaceuticals. *Carbon Dioxide Chemistry, Capture and Oil Recovery* **2017**. https://doi.org/10.5772/INTECHOPEN.72313.

(29) Ho, E. Y.; Mathy, C. Functional Abdominal Pain Causing Scurvy, Pellagra, and Hypovitaminosis A. *F1000Res* **2014**, *3*. https://doi.org/10.12688/F1000RESEARCH.3-35.V1.

(30) Jukes, T. H. The Prevention and Conquest of Scurvy, Beri-Beri, and Pellagra. *Prev Med (Baltim)* **1989**, *18* (6), 877–883. https://doi.org/10.1016/0091-7435(89)90023-6.

(31) Carpenter, K. J. The Discovery of Thiamin. *Ann Nutr Metab* **2012**, *61* (3), 219–223. https://doi.org/10.1159/000343109.

(32) McCollum, E. V.; Simmonds, N.; Pitz, W. The relation of the unidentified dietary factors, the fat-soluble A, and water soluble B, of the diet to the growthpromoting properties of milk. *J Biol Chem* **1916**, *27* (1), 33–43. https://doi.org/10.1016/S0021-9258(18)86888-0.

(33) Barker, T. Vitamins and Human Health: Systematic Reviews and Original Research. *Nutrients 2023, 15* (13), 2888-2892. https://doi.org/10.3390/NU15132888.

(34) Elmadfa, I.; Meyer, A. L. The Role of the Status of Selected Micronutrients in Shaping the Immune Function. *Endocr Metab Immune Disord Drug Targets* **2019**, *19* (8), 1100–1115. https://doi.org/10.2174/1871530319666190529101816.

(35) Muenst, S.; Läubli, H.; Soysal, S. D.; Zippelius, A.; Tzankov, A.; Hoeller, S. The Immune System and Cancer Evasion Strategies: Therapeutic Concepts. *J Intern Med* **2016**, *279* (6), 541–562. https://doi.org/10.1111/JOIM.12470.

(36) Pecora, F.; Persico, F.; Argentiero, A.; Neglia, C.; Esposito, S. The Role of Micronutrients in Support of the Immune Response against Viral Infections. *Nutrients* **2020**, *12* (10), 1–45. https://doi.org/10.3390/NU12103198.

(37) Sporn, M. B.; Squire, R. A.; Brown, C. C.; Smith, J. M.; Wenk, M. L.; Springer, S. 13-Cis-Retinoic Acid: Inhibition of Bladder Carcinogenesis in the Rat. *Science* **1977**, *195* (4277), 487–489. https://doi.org/10.1126/SCIENCE.835006.

(38) Clamon, G. H. Retinoids for the Prevention of Epithelial Cancers: Current Status and Future Potential. *Med Pediatr Oncol* **1980**, *8* (2), 177–185. https://doi.org/10.1002/mpo.2950080211.

(39) Lotan, R. Effects of Vitamin A and Its Analogs (Retinoids) on Normal and Neoplastic Cells. *Biochim Biophys Acta* **1980**, *605* (1), 33–91. https://doi.org/10.1016/0304-419X(80)90021-9.
(40) Venturelli, S.; Leischner, C.; Helling, T.; Burkard, M.; Marongiu, L. Vitamins as Possible Cancer Biomarkers: Significance and Limitations. *Nutrients* **2021**, *13* (11), 3914-3937. https://doi.org/10.3390/NU13113914.
(41) Ames, B. N. DNA Damage from Micronutrient Deficiencies Is Likely to Be a Major Cause of Cancer. *Mutation Research/Fundamental and Molecular Mechanisms of Mutagenesis* **2001**, *475* (1–2), 7–20. https://doi.org/10.1016/S0027-5107(01)00070-7.
(42) Schmidt, T. T.; Sharma, S.; Reyes, G. X.; Kolodziejczak, A.; Wagner, T.; Luke, B.; Hofer, A.; Chabes, A.; Hombauer, H. Inactivation of Folylpolyglutamate Synthetase Met7 Results in Genome Instability Driven by an Increased DUTP/DTTP Ratio. *Nucleic Acids Res* **2020**, *48* (1), 264–277. https://doi.org/10.1093/NAR/GKZ1006.
(43) Bird, R. P. The Emerging Role of Vitamin B6 in Inflammation and Carcinogenesis. *Adv Food Nutr Res* **2018**, *83*, 151–194. https://doi.org/10.1016/BS.AFNR.2017.11.004.
(44) Percudani, R.; Peracchi, A. The B6 Database: A Tool for the Description and Classification of Vitamin B6-Dependent Enzymatic Activities and of the Corresponding Protein Families. *BMC Bioinformatics* **2009**, *10*, 273, 1-8. https://doi.org/10.1186/1471-2105-10-273.
(45) Wilson, M. P.; Plecko, B.; Mills, P. B.; Clayton, P. T. Disorders Affecting Vitamin B6 Metabolism. *J Inherit Metab Dis* **2019**, *42* (4), 629–646. https://doi.org/10.1002/JIMD.12060.
(46) Hossain, K. S.; Amarasena, S.; Mayengbam, S. B Vitamins and Their Roles in Gut Health. *Microorganisms* **2022**, *10* (6), 1168-1181. https://doi.org/10.3390/MICROORGANISMS10061168.
(47) Middleton, H. M. Intestinal Hydrolysis of Pyridoxal 5'-Phosphate in Vitro and in Vivo in the Rat. Effect of Amino Acids and Oligopeptides. *Dig Dis Sci* **1990**, *35* (1), 113–120. https://doi.org/10.1007/BF01537232.
(48) Mackey, A. D.; McMahon, R. J.; Townsend, J. H.; Gregory, J. F. Uptake, Hydrolysis, and Metabolism of Pyridoxine-5'-Beta-D-Glucoside in Caco-2 Cells. *J Nutr* **2004**, *134* (4), 842–846. https://doi.org/10.1093/JN/134.4.842.
(49) Stolz, J.; Vielreicher, M. Tpn1p, the Plasma Membrane Vitamin B6 Transporter of Saccharomyces Cerevisiae. *J Biol Chem* **2003**, *278* (21), 18990–18996. https://doi.org/10.1074/JBC.M300949200.
(50) Albersen, M.; Bosma, M.; Knoers, N. V. V. A. M.; de Ruiter, B. H. B.; Diekman, E. F.; de Ruijter, J.; Visser, W. F.; de Koning, T. J.; Verhoeven-Duif, N. M. The Intestine Plays a Substantial Role in Human Vitamin B6 Metabolism: A Caco-2 Cell Model. *PLoS One* **2013**, *8* (1), e54113. https://doi.org/10.1371/JOURNAL.PONE.0054113.
(51) Stanulovic, M.; Jeremic, V.; Leskovac, V.; Chaykin, S. New Pathway of Conversion of Pyridoxal to 4-Pyridoxic Acid. *Enzyme* **1976**, *21* (4), 357–369. https://doi.org/10.1159/000458879.

(52) Bohney, J. P.; Fonda, M. L.; Feldhoff, R. C. Identification of Lys190 as the Primary Binding Site for Pyridoxal 5'-Phosphate in Human Serum Albumin. *FEBS Lett* **1992**, *298* (2–3), 266–268. https://doi.org/10.1016/0014-5793(92)80073-P.
(53) Parra, M.; Stahl, S.; Hellmann, H. Vitamin B6 and Its Role in Cell Metabolism and Physiology. *Cells 2018* **2018**, *7* (7), 84-112. https://doi.org/10.3390/CELLS7070084.
(54) Cellini, B.; Bertoldi, M.; Montioli, R.; Laurents, D. V.; Paiardini, A.; Voltattorni, C. B. Dimerization and Folding Processes of Treponema Denticola Cystalysin: The Role of Pyridoxal 5'-Phosphate. *Biochemistry* **2006**, *45* (47), 14140–14154. https://doi.org/10.1021/BI061496L.
(55) Mooney, S.; Hellmann, H. Vitamin B6: Killing Two Birds with One Stone? *Phytochemistry* **2010**, *71* (5–6), 495–501. https://doi.org/10.1016/J.PHYTOCHEM.2009.12.015.
(56) Parletta, N.; Milte, C. M.; Meyer, B. J. Nutritional Modulation of Cognitive Function and Mental Health. *J Nutr Biochem* **2013**, *24* (5), 725–743. https://doi.org/10.1016/J.JNUTBIO.2013.01.002.
(57) Galluzzi, L.; Vitale, I.; Senovilla, L.; Olaussen, K. A.; Pinna, G.; Eisenberg, T.; Goubar, A.; Martins, I.; Michels, J.; Kratassiouk, G.; Carmona-Gutierrez, D.; Scoazec, M.; Vacchelli, E.; Schlemmer, F.; Kepp, O.; Shen, S.; Tailler, M.; Niso-Santano, M.; Morselli, E.; Criollo, A.; Adjemian, S.; Jemaà, M.; Chaba, K.; Pailleret, C.; Michaud, M.; Pietrocola, F.; Tajeddine, N.; de La Motte Rouge, T.; Araujo, N.; Morozova, N.; Robert, T.; Ripoche, H.; Commo, F.; Besse, B.; Validire, P.; Fouret, P.; Robin, A.; Dorvault, N.; Girard, P.; Gouy, S.; Pautier, P.; Jägemann, N.; Nickel, A. C.; Marsili, S.; Paccard, C.; Servant, N.; Hupé, P.; Behrens, C.; Behnam-Motlagh, P.; Kohno, K.; Cremer, I.; Damotte, D.; Alifano, M.; Midttun, Ø.; Ueland, P. M.; Lazar, V.; Dessen, P.; Zischka, H.; Chatelut, E.; Castedo, M.; Madeo, F.; Barillot, E.; Thomale, J.; Wistuba, I. I.; Sautès-Fridman, C.; Zitvogel, L.; Soria, J. C.; Harel-Bellan, A.; Kroemer, G. Prognostic Impact of Vitamin B6 Metabolism in Lung Cancer. *Cell Rep* **2012**, *2* (2), 257–269. https://doi.org/10.1016/J.CELREP.2012.06.017.
(58) Panaretakis, T. Cisplatin-Induced Apoptosis and Development of Resistance Are Transcriptionally Distinct Processes. *Cell Cycle* **2012**, *11* (20), 3723-3729. https://doi.org/10.4161/CC.22114.
(59) Galluzzi, L.; Vitale, I.; Senovilla, L.; Olaussen, K. A.; Pinna, G.; Eisenberg, T.; Goubar, A.; Martins, I.; Michels, J.; Kratassiouk, G.; Carmona-Gutierrez, D.; Scoazec, M.; Vacchelli, E.; Schlemmer, F.; Kepp, O.; Shen, S.; Tailler, M.; Niso-Santano, M.; Morselli, E.; Criollo, A.; Adjemian, S.; Jemaà, M.; Chaba, K.; Pailleret, C.; Michaud, M.; Pietrocola, F.; Tajeddine, N.; de La Motte Rouge, T.; Araujo, N.; Morozova, N.; Robert, T.; Ripoche, H.; Commo, F.; Besse, B.; Validire, P.; Fouret, P.; Robin, A.; Dorvault, N.; Girard, P.; Gouy, S.; Pautier, P.; Jägemann, N.; Nickel, A. C.; Marsili, S.; Paccard, C.; Servant, N.; Hupé, P.; Behrens, C.; Behnam-Motlagh, P.; Kohno, K.; Cremer, I.; Damotte, D.; Alifano, M.; Midttun, Ø.; Ueland, P. M.; Lazar, V.; Dessen, P.; Zischka, H.; Chatelut, E.; Castedo, M.; Madeo, F.; Barillot, E.; Thomale, J.; Wistuba, I. I.; Sautès-Fridman, C.; Zitvogel, L.; Soria, J. C.; Harel-Bellan, A.; Kroemer, G. Prognostic Impact of

Vitamin B6 Metabolism in Lung Cancer. *Cell Rep* **2012**, *2* (2), 257–269. https://doi.org/10.1016/J.CELREP.2012.06.017.
(60) Percudani, R.; Peracchi, A. A Genomic Overview of Pyridoxal-Phosphate-Dependent Enzymes. *EMBO Rep* **2003**, *4* (9), 850-854. https://doi.org/10.1038/SJ.EMBOR.EMBOR914.
(61) Johansson, M.; Relton, C.; Ueland, P. M.; Vollset, S. E.; Midttun, Ø.; Nygård, O.; Slimani, N.; Boffetta, P.; Jenab, M.; Clavel-Chapelon, F.; Boutron-Ruault, M. C.; Fagherazzi, G.; Kaaks, R.; Rohrmann, S.; Boeing, H.; Weikert, C.; Bas Buenode-Mesquita, H.; Ros, M. M.; Van Gils, C. H.; Peeters, P. H. M.; Agudo, A.; Barricarte, A.; Navarro, C.; Rodríguez, L.; Sánchez, M. J.; Larrañaga, N.; Khaw, K. T.; Wareham, N.; Allen, N. E.; Crowe, F.; Gallo, V.; Norat, T.; Krogh, V.; Masala, G.; Panico, S.; Sacerdote, C.; Tumino, R.; Trichopoulou, A.; Lagiou, P.; Trichopoulos, D.; Rasmuson, T.; Hallmans, G.; Riboli, E.; Vineis, P.; Brennan, P. Serum B Vitamin Levels and Risk of Lung Cancer. *JAMA* **2010**, *303* (23), 2377–2385. https://doi.org/10.1001/JAMA.2010.808.
(62) Brun, E. M. S. P. T.; Calvert, N. D.; Suchý, M.; Kirby, A.; Melkus, G.; Garipov, R.; Addison, C. L.; Shuhendler, A. J. Mapping Vitamin B6 Metabolism by HydrazoCEST Magnetic Resonance Imaging. *Chem Commun (Camb)* **2021**, *57* (83), 10867–10870. https://doi.org/10.1039/D1CC03704H.
(63) Kraus-Berthier, L.; Jan, M.; Guilbaud, N.; Naze, M.; Pierré, A.; Atassi, G. Histology and Sensitivity to Anticancer Drugs of Two Human Non-Small Cell Lung Carcinomas Implanted in the Pleural Cavity of Nude Mice. *Clin Cancer Res* **2000**, 6 (1), 297-304.
(64) Korpal, M.; Feala, J.; Puyang, X.; Zou, J.; Ramos, A. H.; Wu, J.; Baumeister, T.; Yu, L.; Warmuth, M.; Zhu, P. Implementation of In Vitro Drug Resistance Assays: Maximizing the Potential for Uncovering Clinically Relevant Resistance Mechanisms. *J Vis Exp* **2015**, *2015* (106). https://doi.org/10.3791/52879.
(65) Zelder, F.; Sonnay, M.; Prieto, L. Antivitamins for Medicinal Applications. *ChemBioChem* **2015**, *16* (9), 1264–1278. https://doi.org/10.1002/CBIC.201500072.
(66) Harrison, D. C.; Mellanby, E. Phytic Acid and the Rickets-Producing Action of Cereals. *Biochem J* **1939**, *33* (10), 1660-1680. https://doi.org/10.1042/BJ0331660.
(67) Stern, E. Ergebnisse Der Medizinischen Grundlagenforschung. *AMA Arch Intern Med* **1956**, *98* (6), 825–825. https://doi.org/10.1001/ARCHINTE.1956.00250300143019.
(68) Dundas, C. M.; Demonte, D.; Park, S. Streptavidin-Biotin Technology: Improvements and Innovations in Chemical and Biological Applications. *Appl Microbiol Biotechnol* **2013**, *97* (21), 9343–9353. https://doi.org/10.1007/S00253-013-5232-Z.
(69) Ravel, J. M.; Shive, W. Biochemical Transformations as Determined by Competitive Analogue-Metabolite Growth Inhibitions: IV. Prevention of Pantothenic Acid Synthesis by Cysteic Acid. *J Biol Chem* **1946**, *166* (2), 407–415. https://doi.org/10.1016/S0021-9258(17)35174-8.

(70) Shive, W. The Utilization of Antimetabolites in the Study of Biochemical Processes in Living Organisms. *Ann N Y Acad Sci* **1950**, *52* (8), 1212–1234. https://doi.org/10.1111/J.1749-6632.1950.TB54026.X.
(71) MUELLER, J. F.; VILTER, R. W. Pyridoxine Deficiency in Human Beings Induced with Deoxypyridoxine. *J Clin Invest* **1950**, *29* (2), 193-201. https://doi.org/10.1172/JCI102246.
(72) Hawkins, W. W. Skin Symptoms of Vitamin-B6 Deficiency in the Dog. *Science* **1955**, *121* (3155), 880. https://doi.org/10.1126/science.121.3155.880.
(73) Jang, H.; Roh, S. Y.; Jeong, E. H.; Kim, B.-S.; Sunwoo, M. K. Ginkgotoxin Induced Seizure Caused by Vitamin B6 Deficiency. *J Epilepsy Res* **2015**, *5* (2), 104-106. https://doi.org/10.14581/JER.15018.
(74) Mei, N.; Guo, X.; Ren, Z.; Kobayashi, D.; Wada, K.; Guo, L. Review of Ginkgo Biloba-Induced Toxicity, from Experimental Studies to Human Case Reports. *J Environ Sci Health C* **2017**, *35* (1), 1–28. https://doi.org/10.1080/10590501.2016.1278298.
(75) van Beek, T. A.; Montoro, P. Chemical Analysis and Quality Control of Ginkgo Biloba Leaves, Extracts, and Phytopharmaceuticals. *J Chromatogr A* **2009**, *1216* (11), 2002–2032. https://doi.org/10.1016/J.CHROMA.2009.01.013.
(76) Kästner, U.; Hallmen, C.; Wiese, M.; Leistner, E.; Drewke, C. The Human Pyridoxal Kinase, a Plausible Target for Ginkgotoxin from Ginkgo Biloba. *FEBS J* **2007**, *274* (4), 1036–1045. https://doi.org/10.1111/J.1742-4658.2007.05654.X.
(77) Tarkin, J. M.; Joshi, F. R.; Rudd, J. H. F. PET Imaging of Inflammation in Atherosclerosis. *Nat Rev Cardiol* **2014**, *11* (8), 443–457. https://doi.org/10.1038/NRCARDIO.2014.80.
(78) Djekidel, M.; Das, J. M. Nuclear Medicine Neuro PET Assessment, Protocols, and Interpretation. *StatPearls* **2023**. https://www.ncbi.nlm.nih.gov/books/NBK570591/.
(79) O'Connor, J. P. B.; Aboagye, E. O.; Adams, J. E.; Aerts, H. J. W. L.; Barrington, S. F.; Beer, A. J.; Boellaard, R.; Bohndiek, S. E.; Brady, M.; Brown, G.; Buckley, D. L.; Chenevert, T. L.; Clarke, L. P.; Collette, S.; Cook, G. J.; Desouza, N. M.; Dickson, J. C.; Dive, C.; Evelhoch, J. L.; Faivre-Finn, C.; Gallagher, F. A.; Gilbert, F. J.; Gillies, R. J.; Goh, V.; Griffiths, J. R.; Groves, A. M.; Halligan, S.; Harris, A. L.; Hawkes, D. J.; Hoekstra, O. S.; Huang, E. P.; Hutton, B. F.; Jackson, E. F.; Jayson, G. C.; Jones, A.; Koh, D. M.; Lacombe, D.; Lambin, P.; Lassau, N.; Leach, M. O.; Lee, T. Y.; Leen, E. L.; Lewis, J. S.; Liu, Y.; Lythgoe, M. F.; Manoharan, P.; Maxwell, R. J.; Miles, K. A.; Morgan, B.; Morris, S.; Ng, T.; Padhani, A. R.; Parker, G. J. M.; Partridge, M.; Pathak, A. P.; Peet, A. C.; Punwani, S.; Reynolds, A. R.; Robinson, S. P.; Shankar, L. K.; Sharma, R. A.; Soloviev, D.; Stroobants, S.; Sullivan, D. C.; Taylor, S. A.; Tofts, P. S.; Tozer, G. M.; Van Herk, M.; Walker-Samuel, S.; Wason, J.; Williams, K. J.; Workman, P.; Yankeelov, T. E.; Brindle, K. M.; McShane, L. M.; Jackson, A.; Waterton, J. C. Imaging Biomarker Roadmap for Cancer Studies. *Nat Rev Clin Oncol* **2017**, *14* (3), 169–186. https://doi.org/10.1038/NRCLINONC.2016.162.
(80) Rong, J.; Haider, A.; Jeppesen, T. E.; Josephson, L.; Liang, S. H. Radiochemistry for Positron Emission Tomography. *Nat Commun 2023 14:1* **2023**, *14* (1), 1–23. https://doi.org/10.1038/s41467-023-36377-4.

(81) Phelps, M. E. Positron Emission Tomography Provides Molecular Imaging of Biological Processes. *Proc Natl Acad Sci U S A* **2000**, *97* (16), 9226-9233. https://doi.org/10.1073/PNAS.97.16.9226.
(82) Ametamey, S. M.; Honer, M.; Schubiger, P. A. Molecular Imaging with PET. *Chem Rev* **2008**, *108* (5), 1501–1516. https://doi.org/10.1021/cr0782426.
(83) Carter, L. M.; Kesner, A. L.; Pratt, E. C.; Sanders, V. A.; Massicano, A. V. F.; Cutler, C. S.; Lapi, S. E.; Lewis, J. S. The Impact of Positron Range on PET Resolution, Evaluated with Phantoms and PHITS Monte Carlo Simulations for Conventional and Non-Conventional Radionuclides. *Mol Imaging Biol* **2020**, *22* (1), 73-84. https://doi.org/10.1007/S11307-019-01337-2.
(84) Phelps, M. E. Positron Emission Tomography Provides Molecular Imaging of Biological Processes. *Proc Natl Acad Sci U S A* **2000**, *97* (16), 9226–9233. https://doi.org/10.1073/PNAS.97.16.9226.
(85) Gambhir, S. S. Molecular Imaging of Cancer with Positron Emission Tomography. *Nat Rev Cancer* **2002**, *2* (9), 683–693. https://doi.org/10.1038/NRC882.
(86) Preshlock, S.; Tredwell, M.; Gouverneur, V. 18F-Labeling of Arenes and Heteroarenes for Applications in Positron Emission Tomography. *Chem Rev* **2016**, *116* (2), 719–766. https://doi.org/10.1021/acs.chemrev.5b00493.
(87) Conti, M.; Eriksson, L. Physics of Pure and Non-Pure Positron Emitters for PET: A Review and a Discussion. *EJNMMI Phys* **2016**, *3* (1), 1-17. https://doi.org/10.1186/S40658-016-0144-5.
(88) Jacobson, O.; Kiesewetter, D. O.; Chen, X. Fluorine-18 Radiochemistry, Labeling Strategies and Synthetic Routes. *Bioconjug Chem* **2015**, *26* (1), 1-18. https://doi.org/10.1021/BC500475E.
(89) Wheeler, O. H.; Roman, F.; Rosado, O.; Org Chem, J.; J Loozen, H. J.; M Drouen, J. J.; Piepers, O.; Org, J.; Wilczynski, J. J.; Johnson, H. W.; Ido, T.; C-N Wan, Ib; Fowler, J. S.; Wolf, A. P. Fluorination with F2. A Convenient Synthesis of 2-Deoxy-2-Fluoro-D-Glucosela. *J. Org. Chem* **1977**, *42* (13), 2341-2342. https://doi.org/10.1021/jo00433a037.
(90) Nielsen, M. K.; Ugaz, C. R.; Li, W.; Doyle, A. G. PyFluor: A Low-Cost, Stable, and Selective Deoxyfluorination Reagent. *J Am Chem Soc* **2015**, *137* (30), 9571–9574. https://doi.org/10.1021/JACS.5B06307.
(91) Deng, H.; Cobb, S. L.; Gee, A. D.; Lockhart, A.; Martarello, L.; McGlinchey, R. P.; O'Hagan, D.; Onega, M. Fluorinase Mediated C–18F Bond Formation, an Enzymatic Tool for PET Labelling. *Chem Commun* **2006**, *6* (6), 652–654. https://doi.org/10.1039/B516861A.
(92) Topczewski, J. J.; Tewson, T. J.; Nguyen, H. M. Iridium-Catalyzed Allylic Fluorination of Trichloroacetimidates. *J Am Chem Soc* **2011**, *133* (48), 19318–19321. https://doi.org/10.1021/JA2087213.
(93) Kamlet, A. S.; Neumann, C. N.; Lee, E.; Carlin, S. M.; Moseley, C. K.; Stephenson, N.; Hooker, J. M.; Ritter, T. Application of Palladium-Mediated 18F-Fluorination to PET Radiotracer Development: Overcoming Hurdles to Translation. *PLoS One* **2013**, *8* (3), 59187-59197. https://doi.org/10.1371/JOURNAL.PONE.0059187.
(94) Deng, X.; Rong, J.; Wang, L.; Vasdev, N.; Zhang, L.; Josephson, L.; Liang, S. H. Chemistry for Positron Emission Tomography: Recent Advances in 11C-, 18F-,

13N-, and 15O-Labeling Reactions. *Angew Chem Int Ed* **2019**, *58* (9), 2580–2605. https://doi.org/10.1002/ANIE.201805501.
(95) Lanzenberger, R. R.; Mitterhauser, M.; Spindelegger, C.; Wadsak, W.; Klein, N.; Mien, L. K.; Holik, A.; Attarbaschi, T.; Mossaheb, N.; Sacher, J.; Geiss-Granadia, T.; Kletter, K.; Kasper, S.; Tauscher, J. Reduced Serotonin-1A Receptor Binding in Social Anxiety Disorder. *Biol Psychiatry* **2007**, *61* (9), 1081–1089. https://doi.org/10.1016/J.BIOPSYCH.2006.05.022.
(96) Dahl, K.; Schou, M.; Amini, N.; Halldin, C. Palladium-Mediated [11C]Carbonylation at Atmospheric Pressure: A General Method Using Xantphos as Supporting Ligand. *Eur J Org Chem* **2013**, *2013* (7), 1228–1231. https://doi.org/10.1002/EJOC.201201708.
(97) Rahman, O.; Långström, B.; Halldin, C. Alkyl Iodides and [11C]CO in Nickel-Mediated Cross-Coupling Reactions: Successful Use of Alkyl Electrophiles Containing a β Hydrogen Atom in Metal-Mediated [11C]Carbonylation. *Chem Sel* **2016**, *1* (10), 2498–2501. https://doi.org/10.1002/SLCT.201600643.
(98) Lee, H. G.; Milner, P. J.; Placzek, M. S.; Buchwald, S. L.; Hooker, J. M. Virtually Instantaneous, Room-Temperature [11C]-Cyanation Using Biaryl Phosphine Pd(0) Complexes. *J Am Chem Soc* **2015**, *137* (2), 648–651. https://doi.org/10.1021/JA512115S/SUPPL_FILE/JA512115S_SI_001.PDF.
(99) Miller, P. W.; Bender, D. [11C]Carbon Disulfide: A Versatile Reagent for PET Radiolabelling. *Chem Eur J* **2012**, *18* (2), 433–436. https://doi.org/10.1002/CHEM.201103128.
(100) Szydło, M.; Jadwiński, M.; Chmura, A.; Gorczewski, K.; Sokół, M. Synthesis, Isolation and Purification of [11C]-Choline. *Contemp Oncol* **2016**, *20* (3), 229-236. https://doi.org/10.5114/WO.2016.61566.
(101) Svensson, J. E.; Schain, M.; Plavén-Sigray, P.; Cervenka, S.; Tiger, M.; Nord, M.; Halldin, C.; Farde, L.; Lundberg, J. Validity and Reliability of Extrastriatal [11C]Raclopride Binding Quantification in the Living Human Brain. *Neuroimage* **2019**, 202, 116-143. https://doi.org/10.1016/J.NEUROIMAGE.2019.116143.
(102) Dahl, K.; Halldin, C.; Schou, M. New Methodologies for the Preparation of Carbon-11 Labeled Radiopharmaceuticals. *Clin Transl Imaging* **2017**, *5* (3), 275–289. https://doi.org/10.1007/S40336-017-0223-1/SCHEMES/7.
(103) Franzius, C.; Hermann, K.; Weckesser, M.; Kopka, K.; Juergens, K. U.; Vormoor, J.; Schober, O. Whole-Body PET/CT with 11 C-Meta-Hydroxyephedrine in Tumors of the Sympathetic Nervous System: Feasibility Study and Comparison with 123 I-MIBG SPECT/CT. *J Nucl Med* **2006**, 47 (10), 1635-1642. https://jnm.snmjournals.org/content/47/10/1635/tab-article-info.
(104) Salminen, E.; Mac Manus, M. FDG-PET Imaging in the Management of Non-Small-Cell Lung Cancer. *Annals of Oncology* **2002**, *13* (3), 357–360. https://doi.org/10.1093/annonc/mdf106.
(105) Kaseda, K. Recent and Current Advances in FDG-PET Imaging within the Field of Clinical Oncology in NSCLC: A Review of the Literature. *Diagnostics* **2020**, *10* (8), 561-576. https://doi.org/10.3390/DIAGNOSTICS10080561.
(106) Farsad, M. FDG PET/CT in the Staging of Lung Cancer. *Curr Radiopharm* **2020**, *13* (3), 195-203. https://doi.org/10.2174/1874471013666191223153755.

(107) Yu, J. X.; Cui, W.; Bourke, V. A.; Mason, R. P. 6-Trifluoromethylpyridoxine: Novel 19F NMR PH Indicator for in Vivo Detection. *J Med Chem* **2012**, *55* (15), 6814–6821. https://doi.org/10.1021/JM300520Q/ASSET/IMAGES/LARGE/JM-2012-00520Q_0004.JPEG.
(108) Dollé, F. [18F]Fluoropyridines: From Conventional Radiotracers to the Labeling of Macromolecules Such as Proteins and Oligonucleotides. *Ernst Schering Res Found Workshop* **2007**, 62, 113–157. https://doi.org/10.1007/978-3-540-49527-7_5.
(109) Xiong, H.; Hoye, A. T.; Fan, K. H.; Li, X.; Clemens, J.; Horchler, C. L.; Lim, N. C.; Attardo, G. Facile Route to 2-Fluoropyridines via 2-Pyridyltrialkylammonium Salts Prepared from Pyridine N-Oxides and Application to (18)F-Labeling. *Org Lett* **2015**, *17* (15), 3726–3729. https://doi.org/10.1021/ACS.ORGLETT.5B01703.
(110) Boekelheide, V.; Linn, W. J. Rearrangements of N-Oxides. A Novel Synthesis of Pyridyl Carbinols and Aldehydes. *J Am Chem Soc* **1954**, *76* (5), 1286–1291. https://doi.org/10.1021/ja01634a026.
(111) Fontenas, C.; Bejan, E.; Haddou, H. A.; Balavoine, G. G. A. The Boekelheide Reaction: Trifluoroacetic Anhydride as a Convenient Acylating Agent. *Synth Commun* **1995**, *25* (5), 629–633. https://doi.org/10.1080/00397919508011399.
(112) Rotstein, B. H.; Wang, L.; Liu, R. Y.; Patteson, J.; Kwan, E. E.; Vasdev, N.; Liang, S. H. Mechanistic Studies and Radiofluorination of Structurally Diverse Pharmaceuticals with Spirocyclic Iodonium(III) Ylides. *Chem Sci* **2016**, *7* (7), 4407–4417. https://doi.org/10.1039/C6SC00197A.
(113) Ross, T. L.; Ermert, J.; Hocke, C.; Coenen, H. H. Nucleophilic 18F-Fluorination of Heteroaromatic Iodonium Salts with No-Carrier-Added [18F]Fluoride. *J Am Chem Soc* **2007**, *129* (25), 8018–8025. https://doi.org/10.1021/JA066850H/ASSET/IMAGES/MEDIUM/JA066850HE00001.GIF.
(114) Rotstein, B. H.; Stephenson, N. A.; Vasdev, N.; Liang, S. H. Spirocyclic Hypervalent Iodine(III)-Mediated Radiofluorination of Non-Activated and Hindered Aromatics. *Nat Commun 2014 5:1* **2014**, *5* (1), 1–7. https://doi.org/10.1038/ncomms5365.
(115) Wuts, P. G. M. Greene's Protective Groups in Organic Synthesis: Fifth Edition. *Greene's Protective Groups in Organic Synthesis: Fifth Edition* **2014**, *9781118057483*, 1–1360. https://doi.org/10.1002/9781118905074.
(116) Turner, J. A. Pyridine and Its Derivatives, Part Two. *Adv. Heterocycl. Chem* **1983**, *48* (5), 3137.
(117) Jacobson, O.; Kiesewetter, D. O.; Chen, X. Fluorine-18 Radiochemistry, Labeling Strategies and Synthetic Routes. *Bioconjug Chem* **2015**, *26* (1), 1-18. https://doi.org/10.1021/BC500475E.
(118) Teare, H.; Robins, E. G.; Kirjavainen, A.; Forsback, S.; Sandford, G.; Solin, O.; Luthra, S. K.; Gouverneur, V. Radiosynthesis and Evaluation of [18F]Selectfluor Bis(Triflate). *Angew Chem Int Ed* **2010**, *49* (38), 6821–6824. https://doi.org/10.1002/ANIE.201002310.
(119) He, S.; Mason, R. P.; Hunjan, S.; Mehta, V. D.; Arora, V.; Katipally, R.; Kulkarni, P. V.; Antich, P. P. Development of Novel 19F NMR PH Indicators: Synthesis and

Evaluation of a Series of Fluorinated Vitamin B6 Analogues. *Bioorg Med Chem* **1998**, *6* (9), 1631–1639. https://doi.org/10.1016/S0968-0896(98)00104-7.
(120) Cresswell, A. J.; Davies, S. G.; Roberts, P. M.; Thomson, J. E. Beyond the Balz-Schiemann Reaction: The Utility of Tetrafluoroborates and Boron Trifluoride as Nucleophilic Fluoride Sources. *Chem Rev* **2015**, *115* (2), 566–611. https://doi.org/10.1021/cr5001805.
(121) Craig, R.; Litvajova, M.; Cronin, S. A.; Connon, S. J. Enantioselective Acyl-Transfer Catalysis by Fluoride Ions. *Chem Commun* **2018**, *54* (72), 10108–10111. https://doi.org/10.1039/C8CC05692G.
(122) Adamczyk, M.; Akireddy, S. R.; Reddy, R. E. Transformation of Vitamin B6 to (+)-Deoxypyridinoline, a Useful Biochemical Marker for Diagnosis of Bone Diseases. *Tetrahedron* **2000**, *56* (16), 2379–2390. https://doi.org/10.1016/S0040-4020(00)00121-6.
(123) Perry-Feigenbaum, R.; Baran, P. S.; Shabat, D. The Pyridinone-Methide Elimination. *Org Biomol Chem* **2009**, *7* (23), 4825–4828. https://doi.org/10.1039/B915265B.
(124) Kuchar, M.; Mamat, C. Methods to Increase the Metabolic Stability of 18F-Radiotracers. *Molecules* **2015**, *20* (9), 16186-16220. https://doi.org/10.3390/MOLECULES200916186.
(125) Pan, Y. The Dark Side of Fluorine. *ACS Med Chem Lett* **2019**, *10* (7), 1016–1019. https://doi.org/10.1021/acsmedchemlett.9b00235.
(126) Li, Z.; Gupta, M. K.; Snowden, T. S. One-Carbon Homologation of Primary Alcohols and the Reductive Homologation of Aldehydes Involving a Jocic-Type Reaction. *Eur J Org Chem* **2015**, *2015* (32), 7009–7019. https://doi.org/10.1002/EJOC.201501089.
(127) Ishida, N.; Moriya, T.; Goya, T.; Murakami, M. Synthesis of Pyridine-Borane Complexes via Electrophilic Aromatic Borylation. *J of Org Chem* **2010**, *75* (24), 8709–8712. https://doi.org/10.1021/jo101920p.
(128) Li, Y.; Liu, Y.; Bu, W.; Guo, J.; Wang, Y. A Mixed Pyridine–Phenol Boron Complex as an Organic Electroluminescent Material. *Chem Commun* **2000**, No. 16, 1551–1552. https://doi.org/10.1039/B003774P.
(129) Walsh, S. P.; Shahripour, A.; Tang, H.; Teumelsan, N.; Frie, J.; Zhu, Y.; Priest, B. T.; Swensen, A. M.; Liu, J.; Margulis, M.; Visconti, R.; Weinglass, A.; Felix, J. P.; Brochu, R. M.; Bailey, T.; Thomas-Fowlkes, B.; Alonso-Galicia, M.; Zhou, X.; Pai, L. Y.; Corona, A.; Hampton, C.; Hernandez, M.; Bentley, R.; Chen, J.; Shah, K.; Metzger, J.; Forrest, M.; Owens, K.; Tong, V.; Ha, S.; Roy, S.; Kaczorowski, G. J.; Yang, L.; Parmee, E.; Garcia, M. L.; Sullivan, K.; Pasternak, A. Discovery of a Potent and Selective ROMK Inhibitor with Pharmacokinetic Properties Suitable for Preclinical Evaluation. *ACS Med Chem Lett* **2015**, *6* (7), 747–752. https://doi.org/10.1021/ML500440U/SUPPL_FILE/ML500440U_SI_001.PDF.
(130) Tan, C. K.; Er, J. C.; Yeung, Y. Y. Synthesis of Chiral Butenolides Using Amino-Thiocarbamate-Catalyzed Asymmetric Bromolactonization. *Tetrahedron Lett* **2014**, *55* (6), 1243–1246. https://doi.org/10.1016/J.TETLET.2014.01.009.
(131) Koval, A. B.; Wuest, W. M. An Optimized Synthesis of the Potent and Selective Pak1 Inhibitor FRAX-1036. *Tetrahedron Lett* **2016**, *57* (3), 449–451. https://doi.org/10.1016/J.TETLET.2015.12.059.

(132) Großkopf, J.; Plaza, M.; Seitz, A.; Breitenlechner, S.; Storch, G.; Bach, T. Photochemical Deracemization at Sp3-Hybridized Carbon Centers via a Reversible Hydrogen Atom Transfer. *J Am Chem Soc* **2021**, *143* (50), 21241–21245. https://doi.org/10.1021/jacs.1c11266.
(133) Yoon, N. M.; Gyoung, Y. S. Reaction of Diisobutylaluminum Hydride with Selected Organic Compounds Containing Representative Functional Groups. *J Org Chem* **1985**, *50* (14), 2443–2450. https://doi.org/10.1021/JO00214A009.
(134) Zou, Y.; Shi, X.; Zhang, G.; Li, Z.; Jin, C.; Su, W. Improved "Oxazole" Method for the Practical and Efficient Preparation of Pyridoxine Hydrochloride (Vitamin B6). *Org Process Res Dev* **2013**, *17* (12), 1498–1502. https://doi.org/10.1021/op4001687.
(135) Breslow, R.; Guo, T. Diels-Alder Reactions in Nonaqueous Polar Solvents. Kinetic Effects of Chaotropic and Antichaotropic Agents and of β-Cyclodextrin. *J Am Chem Soc* **1988**, *110* (17), 5613–5617. https://doi.org/10.1021/ja00225a003.
(136) Soares, M. I. L.; Cardoso, A. L.; Pinho E Melo, T. M. V. D. Diels–Alder Cycloaddition Reactions in Sustainable Media. *Molecules* **2022**, *27* (4), 1304-1350. https://doi.org/10.3390/MOLECULES27041304.
(137) Yang, Q.; Sheng, M.; Henkelis, J. J.; Tu, S.; Wiensch, E.; Zhang, H.; Zhang, Y.; Tucker, C.; Ejeh, D. E. Explosion Hazards of Sodium Hydride in Dimethyl Sulfoxide, N, N-Dimethylformamide, and N, N-Dimethylacetamide. *Org Process Res Dev* **2019**, *23* (10), 2210–2217. https://doi.org/10.1021/acs.oprd.9b00276.
(138) Huang, B.; Danso-Danquah, R.; Safo, M. K.; Zhang, Y. Effective and Versatile Synthesis of Ginkgotoxin and Its 4′-O-Derivatives through Regioselective 4′-O-Alkylation and 4′-O-Chlorination of 3,5′-O-Dibenzylpyridoxine. *SynOpen* **2020**, *04* (03), 51–54. https://doi.org/10.1055/S-0040-1707242.
(139) Bueno, C.; Guerrero, J.; Encinas, M. V. Spectroscopic Properties of 4-Pyridoxic Acid as a Function of PH and Solvent. *Helv Chim Acta* **2004**, *87* (4), 940–948. https://doi.org/10.1002/HLCA.200490087.
(140) Liu, W.; Jin, F.; Gao, D.; Song, L.; Ding, C.; Liu, H. Metabolomics Analysis Reveals Aminoquinazolin Derivative 9d-Induced Oxidative Stress and Cell Cycle Arrest in A549 Cells. *RSC Adv* **2017**, *7* (22), 13149–13158. https://doi.org/10.1039/C7RA00185A.
(141) Schrimpe-Rutledge, A. C.; Codreanu, S. G.; Sherrod, S. D.; McLean, J. A. Untargeted Metabolomics Strategies – Challenges and Emerging Directions. *J Am Soc Mass Spectrom* **2016**, *27* (12), 1897-1905. https://doi.org/10.1007/S13361-016-1469-Y.
(142) Kuchar, M.; Mamat, C. Methods to Increase the Metabolic Stability of 18F-Radiotracers. *Molecules* **2015**, *20* (9), 16186-16220. https://doi.org/10.3390/MOLECULES200916186.
(143) Hilf, S.; Berger-Nicoletti, E.; Grubbs, R. H.; M Kilbinger, A. F.; Hilf, S.; Berger-Nicoletti, E.; M Kilbinger, A. F.; Grubbs Arnold, R. H.; Beckman, M. Monofunctional Metathesis Polymers via Sacrificial Diblock Copolymers. *Angew Chem Int Ed* **2006**, *45* (47), 8045–8048. https://doi.org/10.1002/ANIE.200602323.

Appendix

NMR Spectra

*Peak description can be found in the Materials and Methods Section.

Common residual solvent peaks in DMSO-d_6: 3.33 ppm H_2O, 5.76 ppm DCM, 1.99 ppm-4.03 ppm-1.17 ppm EtOAc, 0 ppm TMS

Common residual solvent peaks in $CDCl_3$: 1.56 ppm H_2O, 5.30 ppm DCM, 1.26 ppm-2.05 ppm-4.12 ppm EtOAc 0 ppm TMS

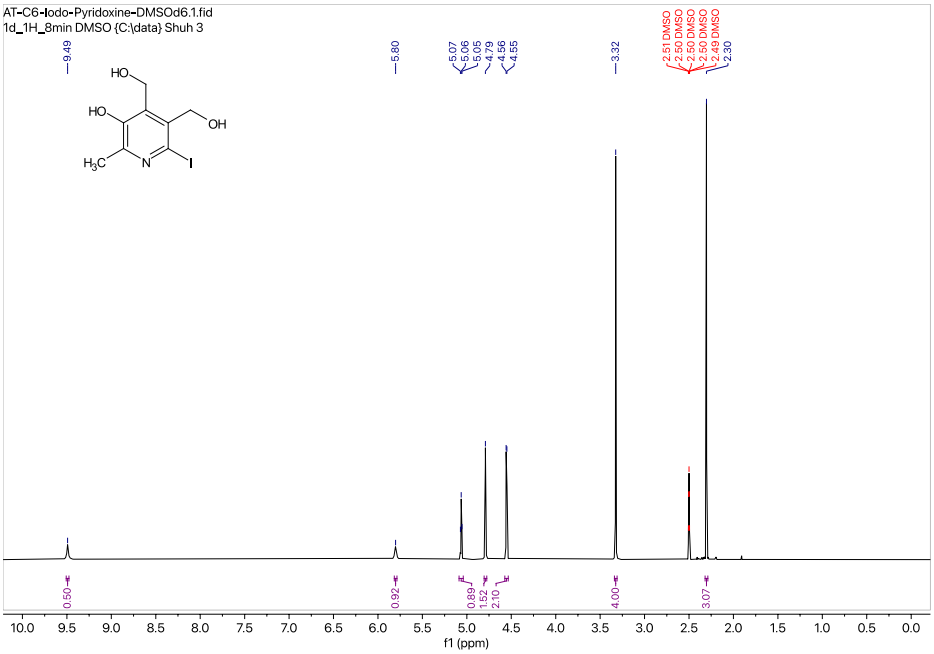

Figure S1. ^{1}H-NMR spectrum of Compound 1.

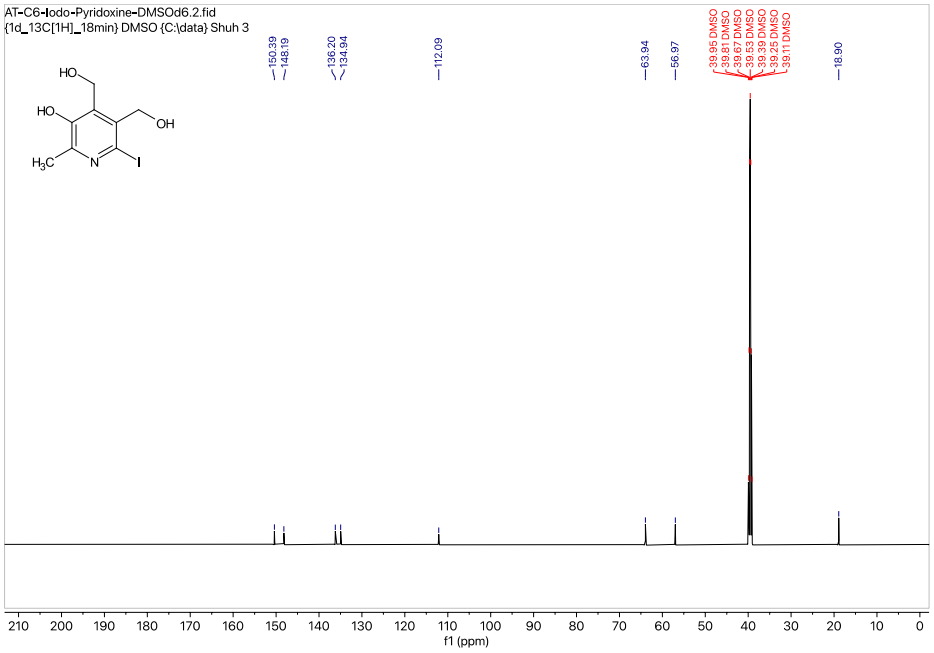

Figure S2. ^{13}C-NMR spectrum of Compound 1.

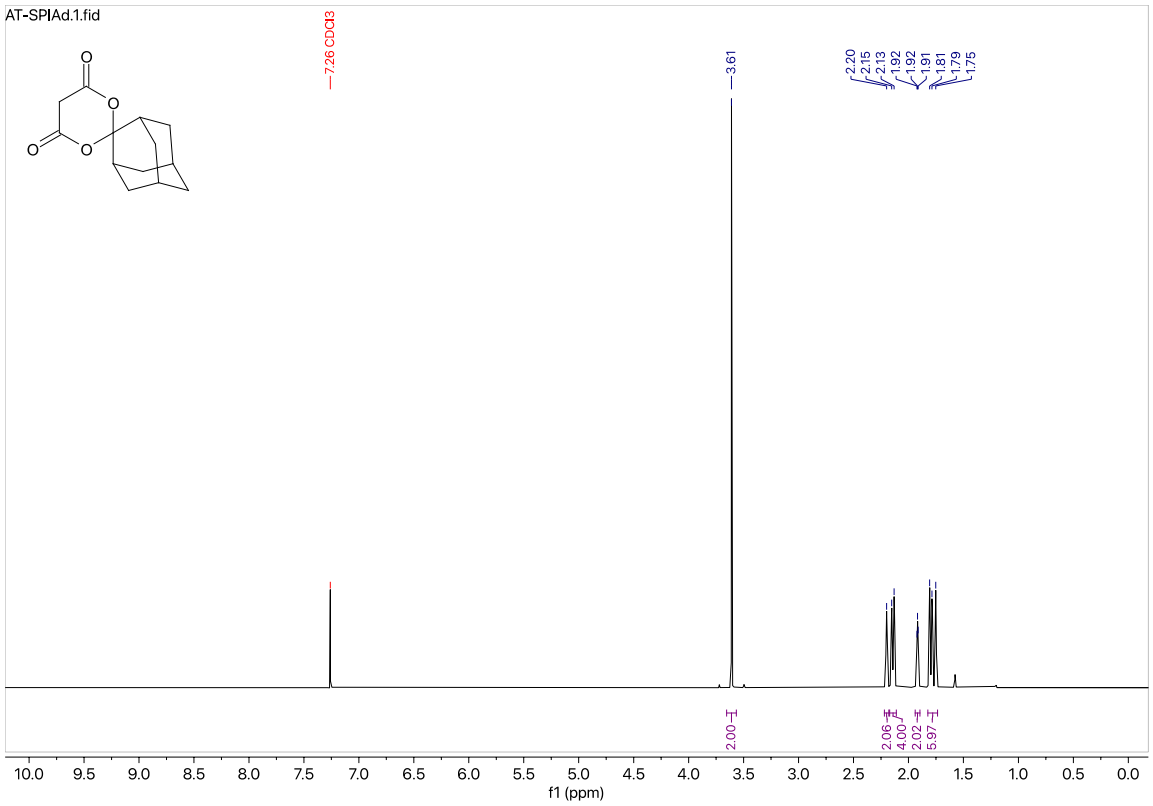

Figure S3. ^{1}H-NMR spectrum of Compound 4.

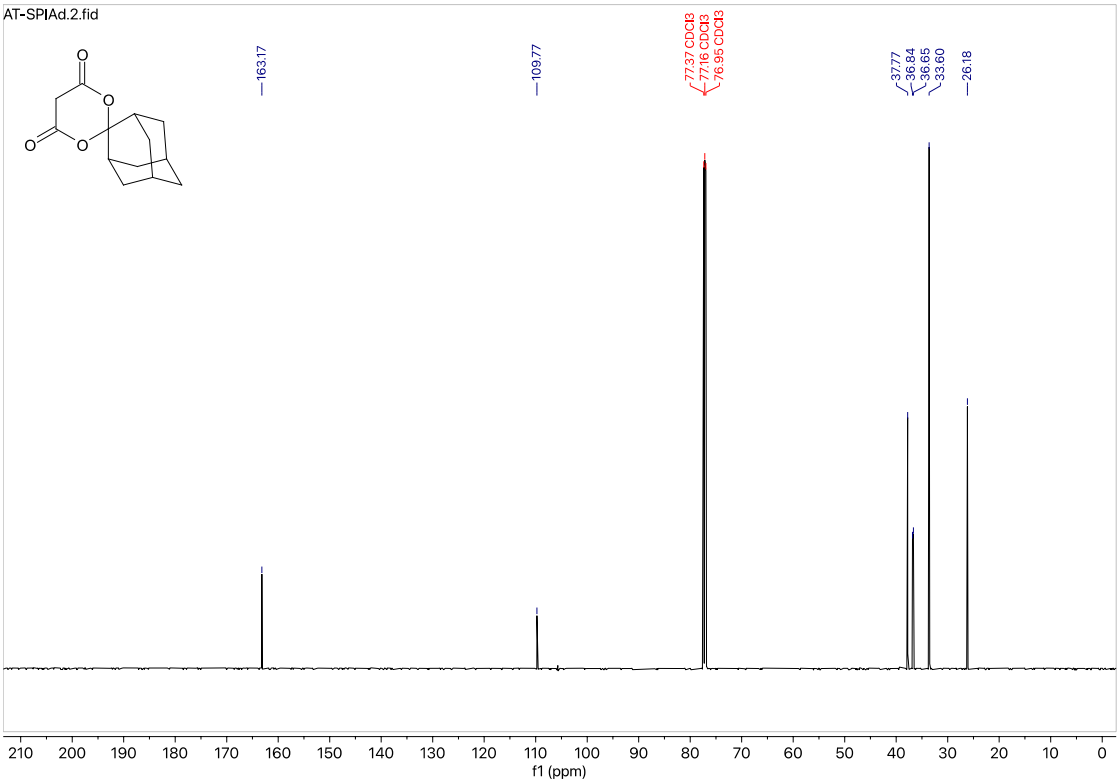

Figure S4. ^{13}C-NMR spectrum of Compound 4.

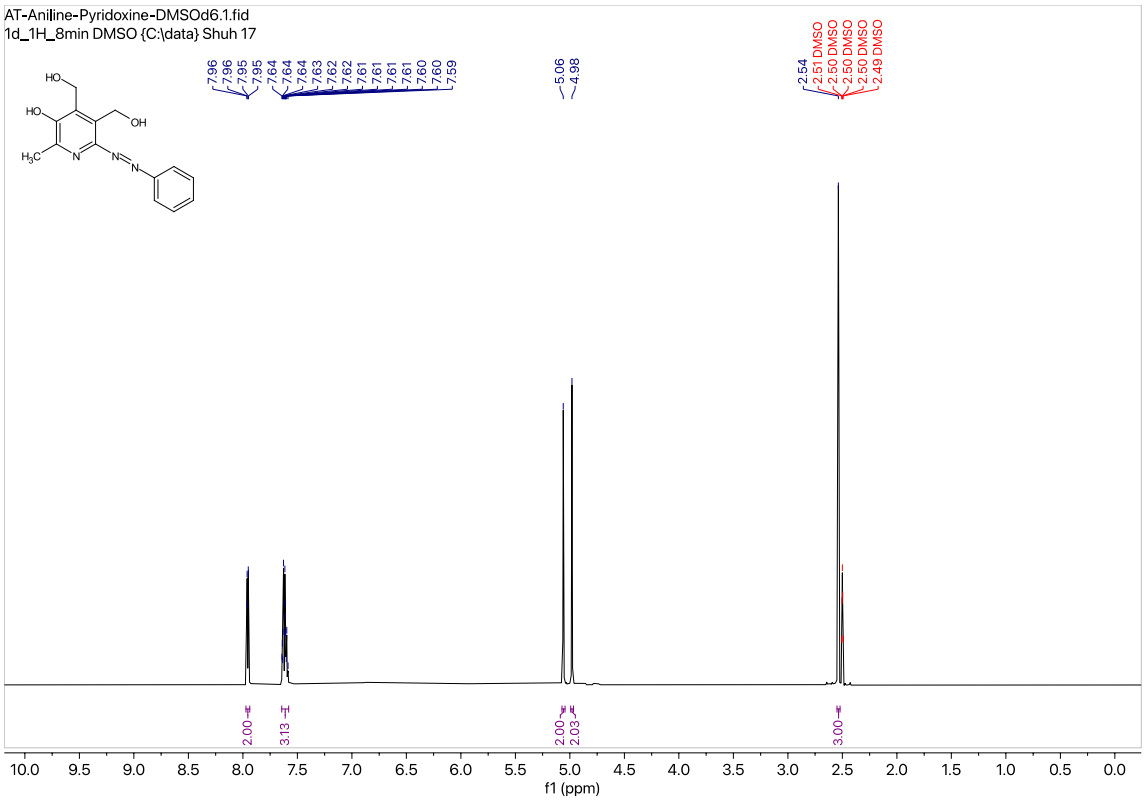

Figure S5. ^{1}H-NMR spectrum of Compound 6.

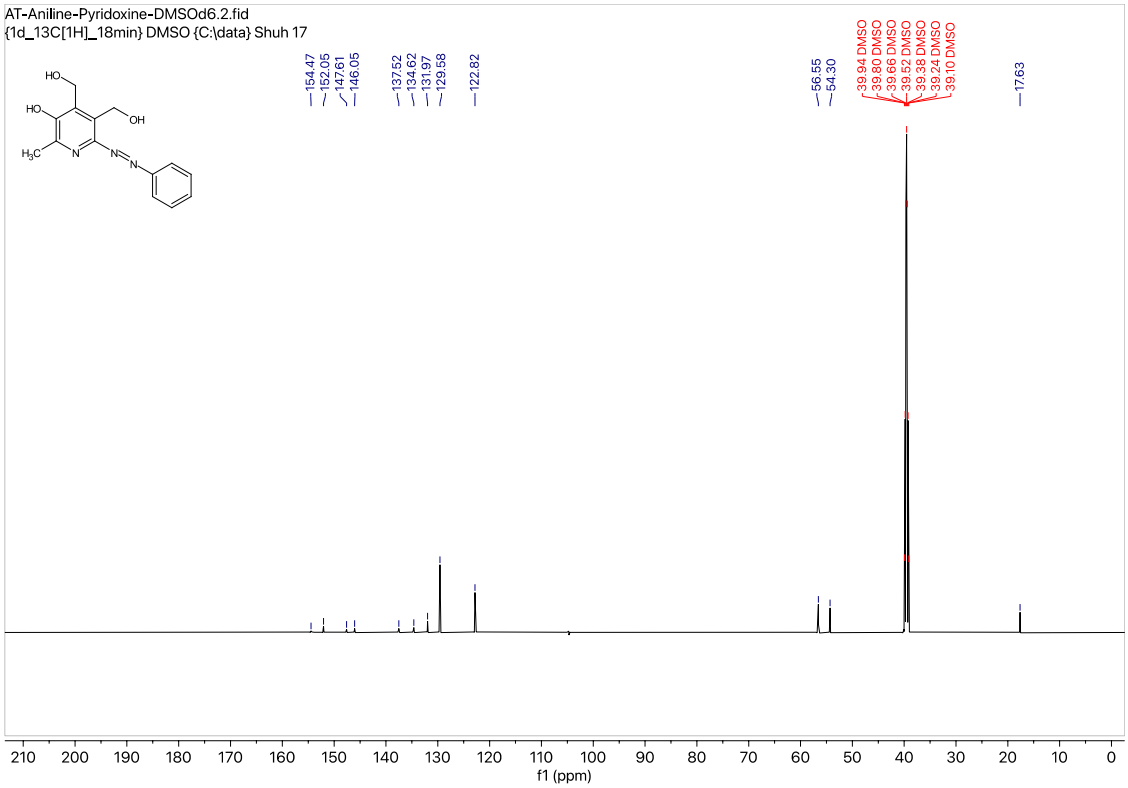

Figure S6. ^{13}C-NMR spectrum of Compound 6.

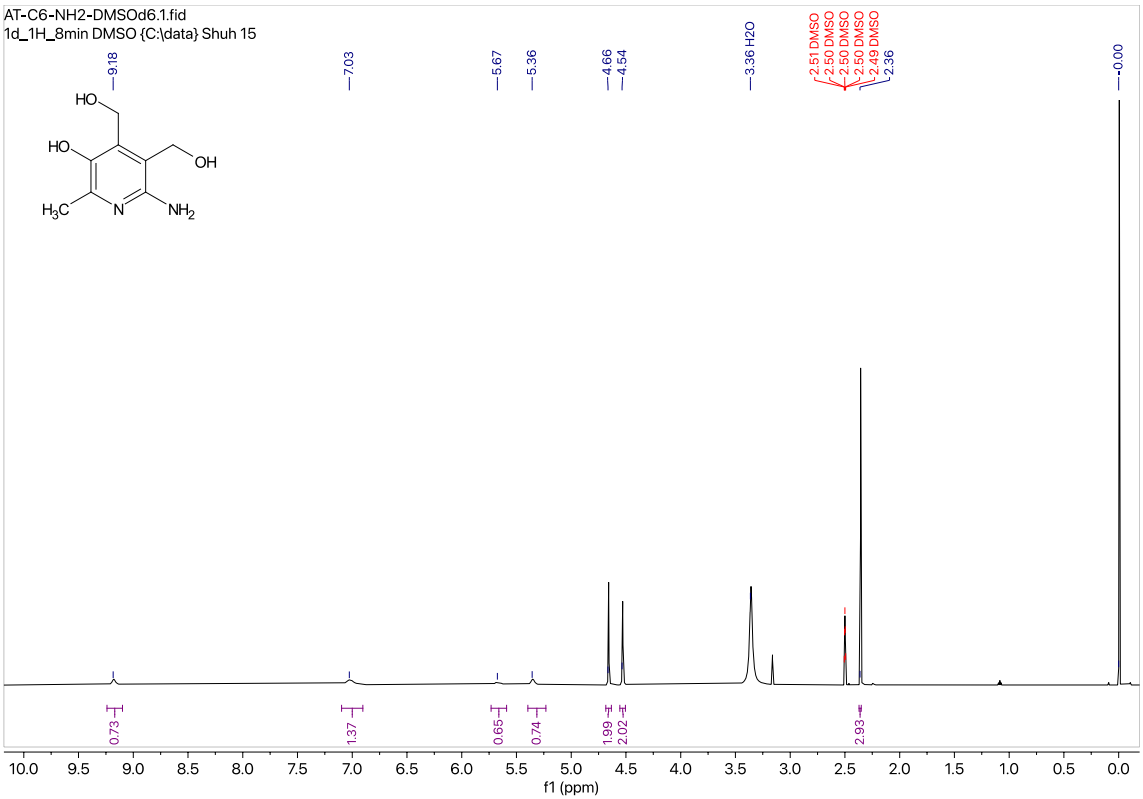

Figure S7. ^{1}H-NMR spectrum of Compound 7.

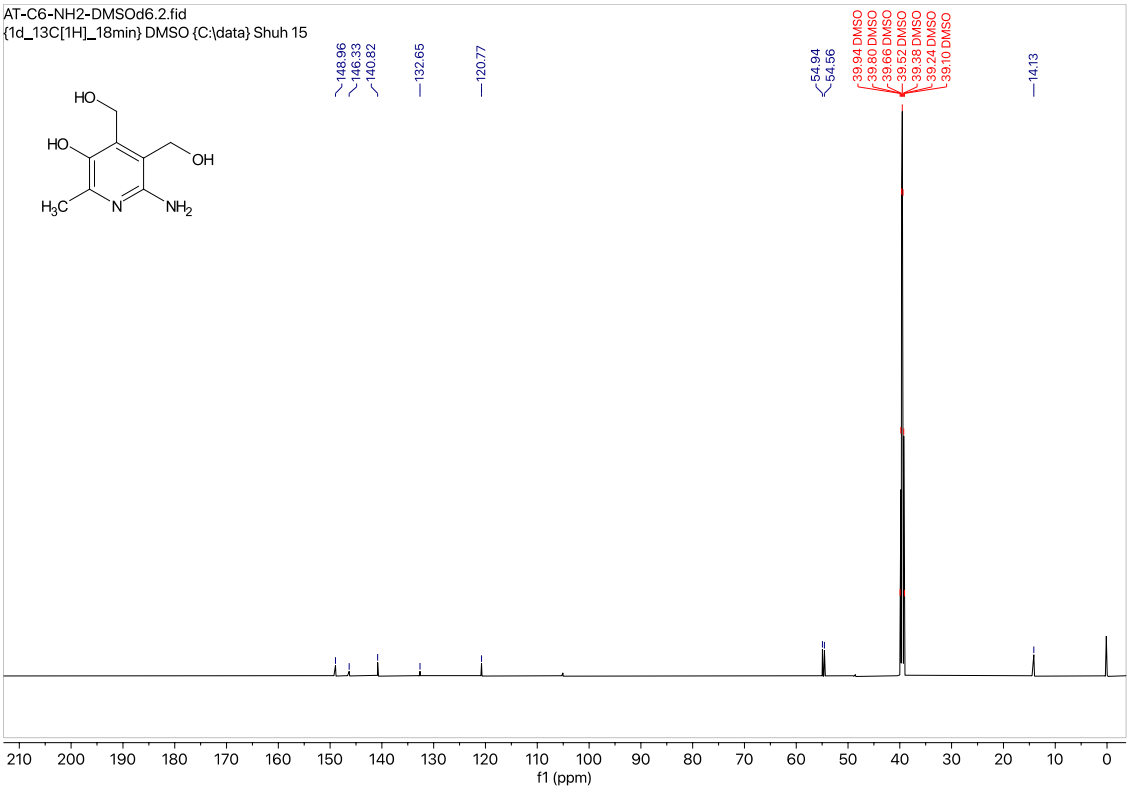

Figure S8. ^{13}C-NMR spectrum of Compound 7.

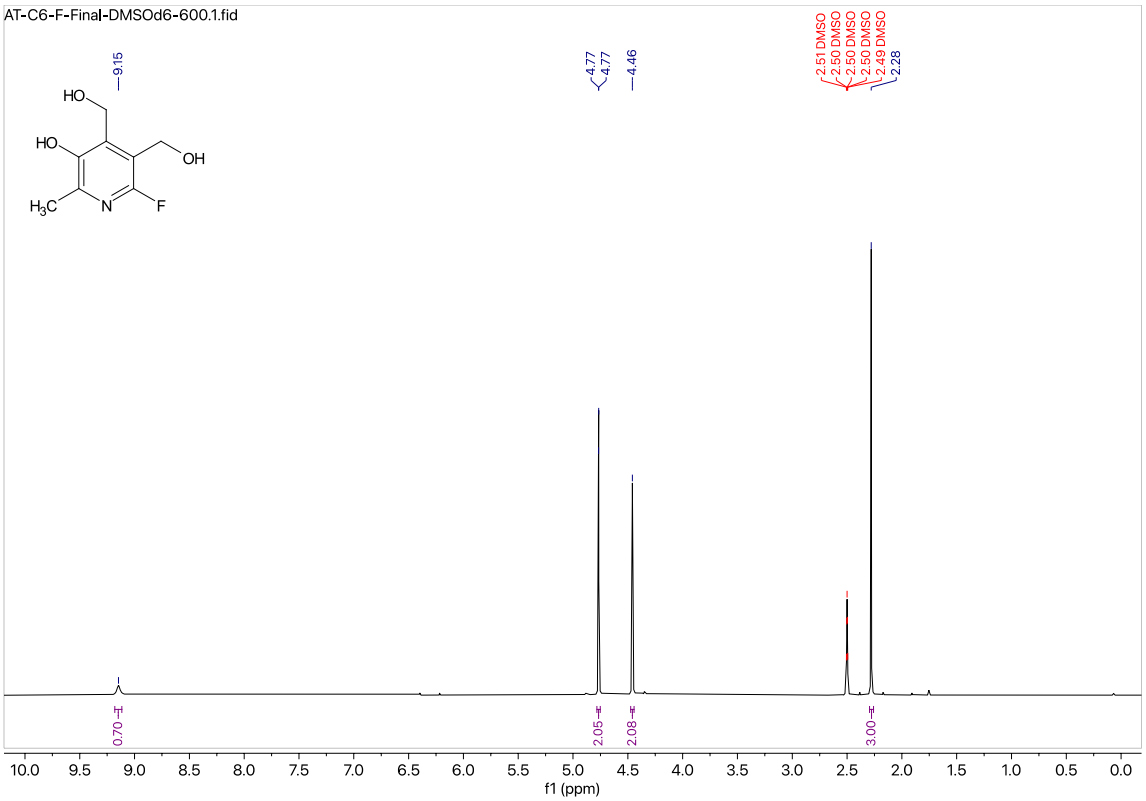

Figure S9. ^{1}H-NMR spectrum of Compound 8.

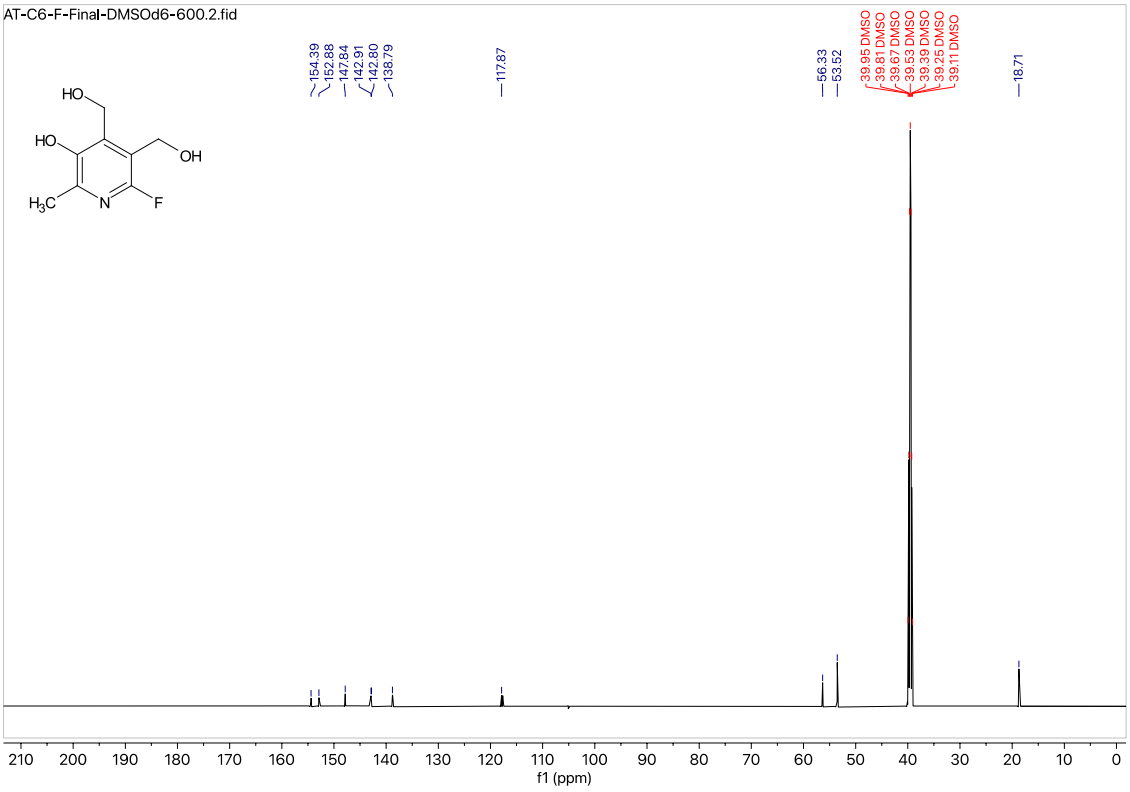

Figure S10. ^{13}C-NMR spectrum of Compound 8.

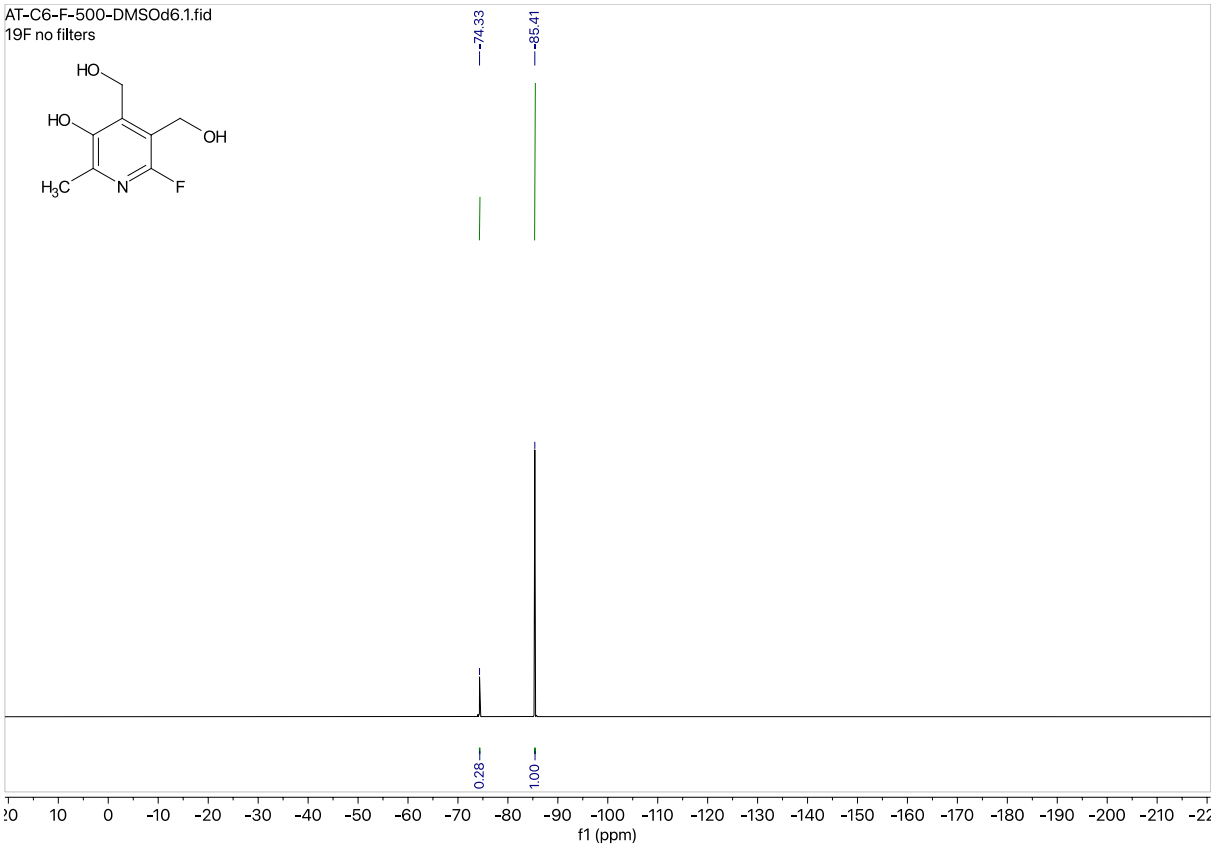

Figure S11. ^{19}F-NMR proton decoupled spectrum of Compound 8.

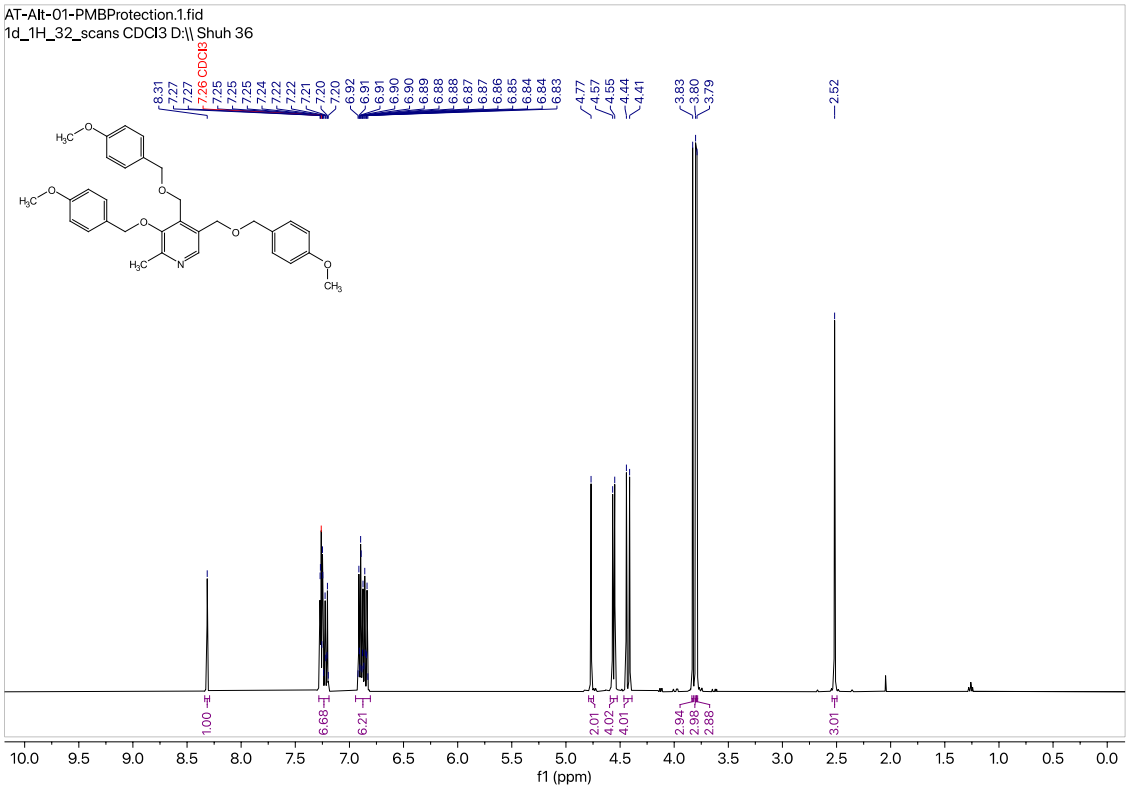

Figure S12. ^{1}H-NMR spectrum of Compound 9.

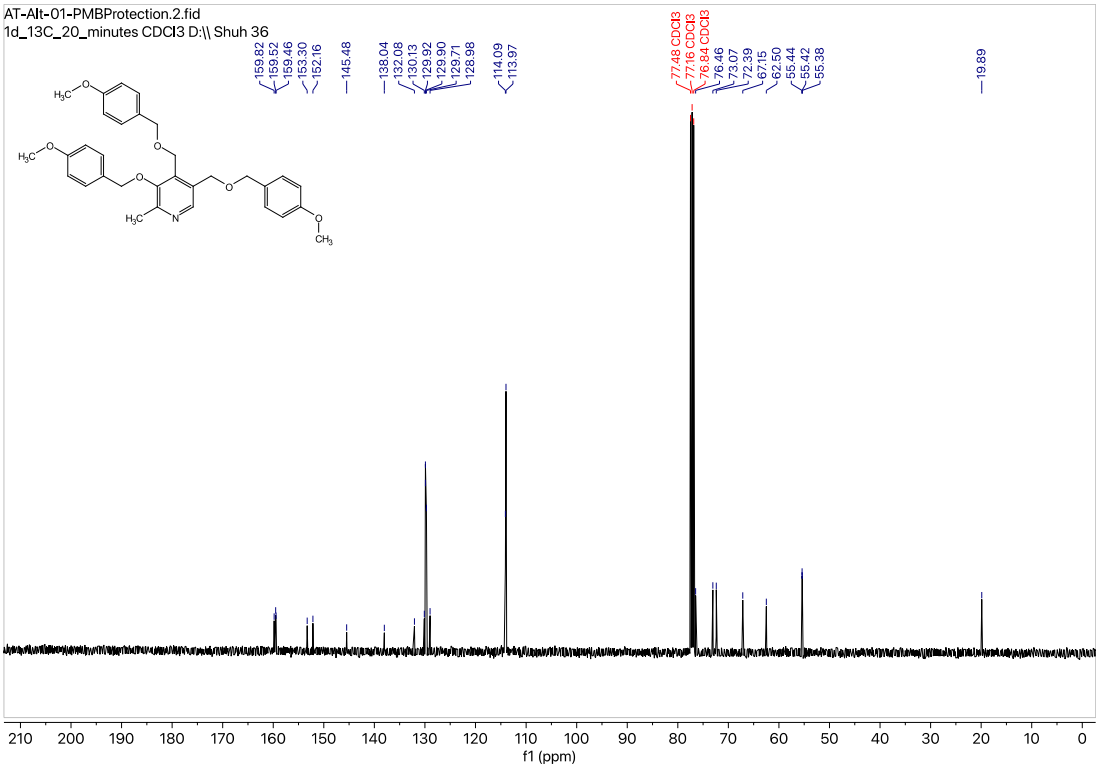

Figure S13. ^{13}C-NMR spectrum of Compound 9.

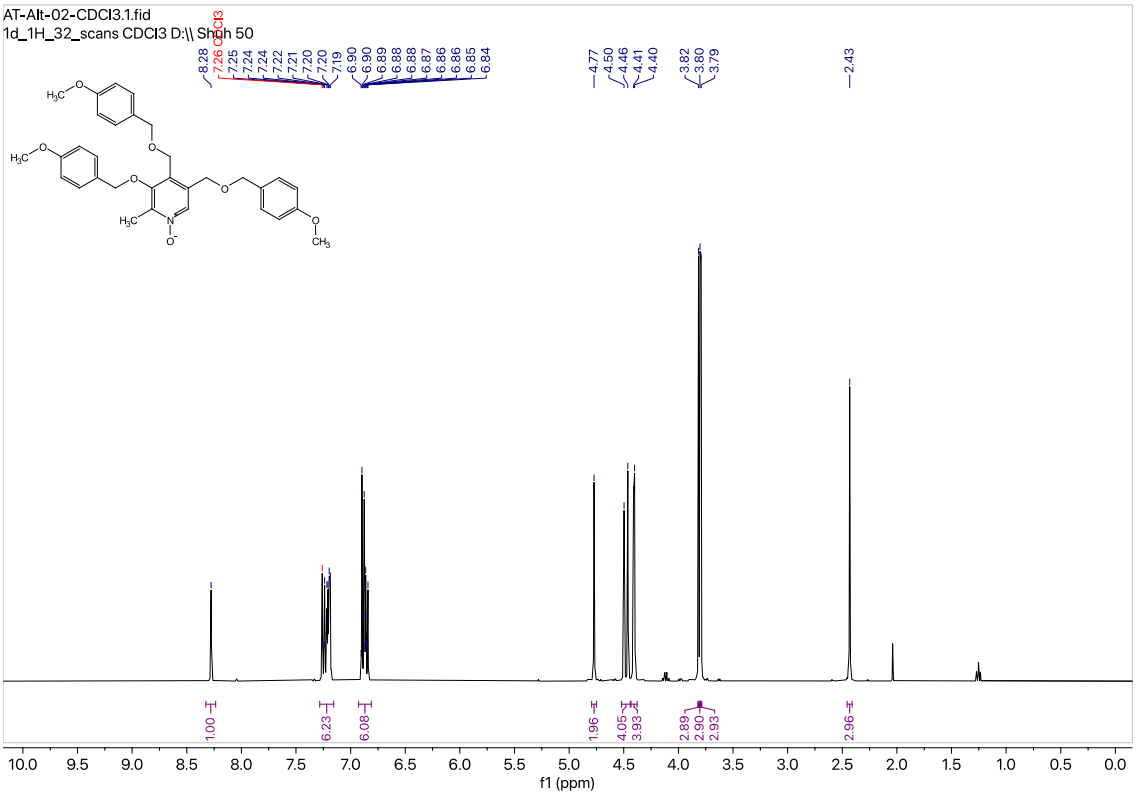

Figure S14. ^{1}H-NMR spectrum of Compound 10.

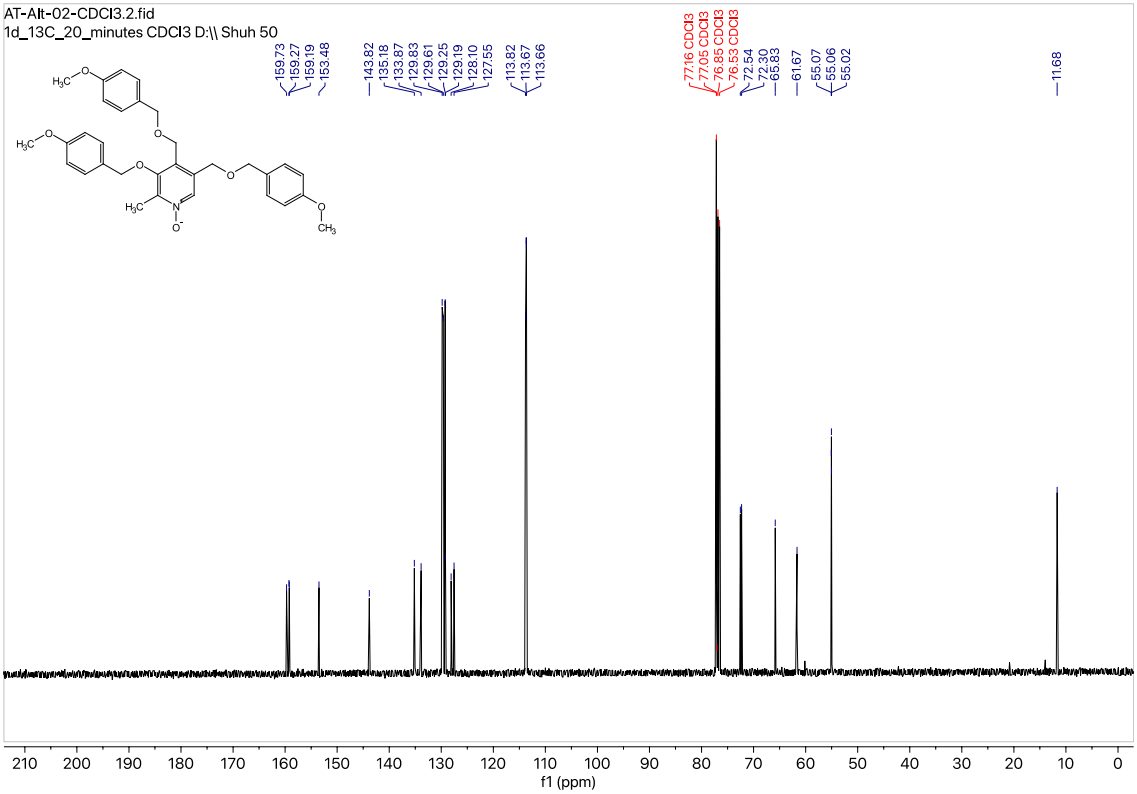

Figure S15. ^{13}C-NMR spectrum of Compound 10.

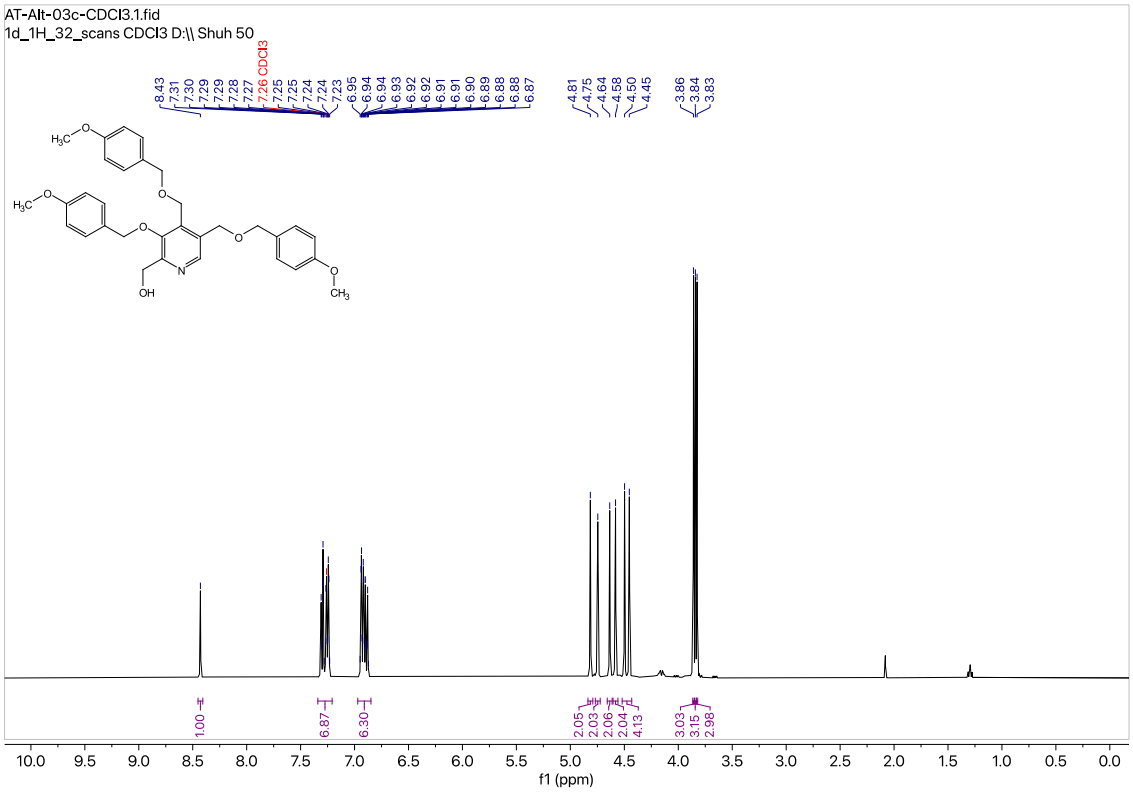

Figure S16. ^{1}H-NMR spectrum of Compound 11.

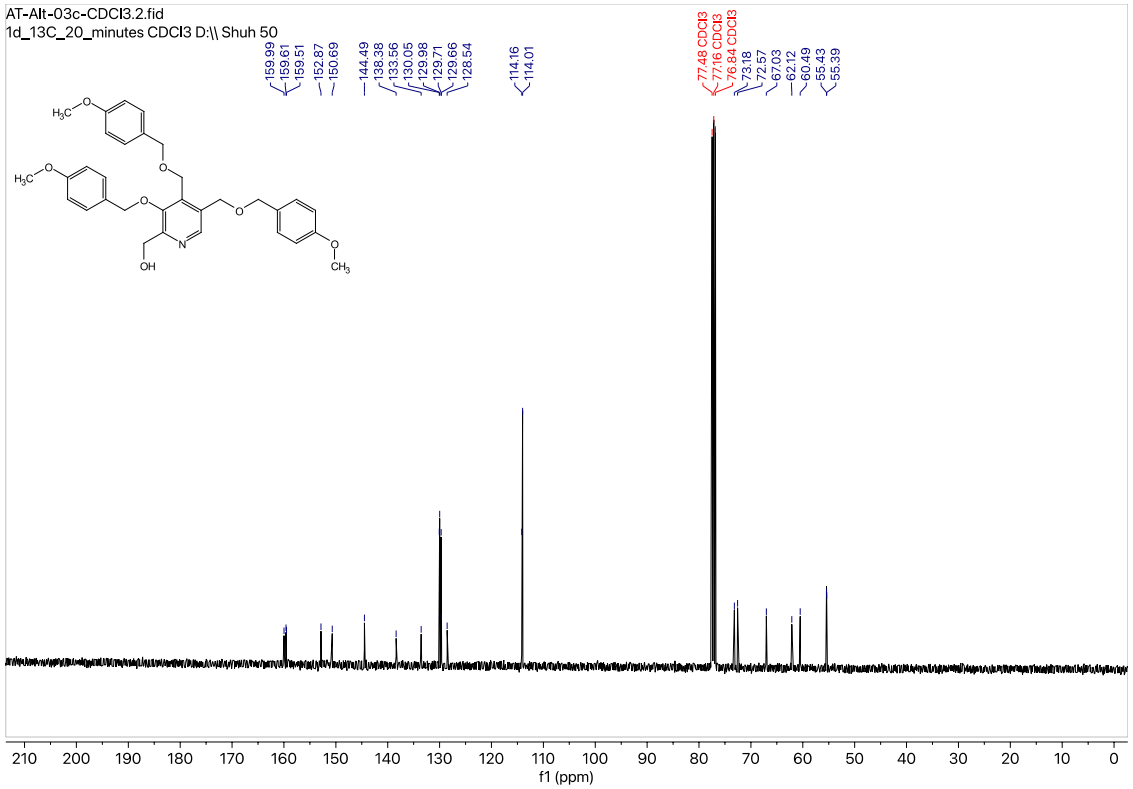

Figure S17. ^{13}C-NMR spectrum of Compound 11.

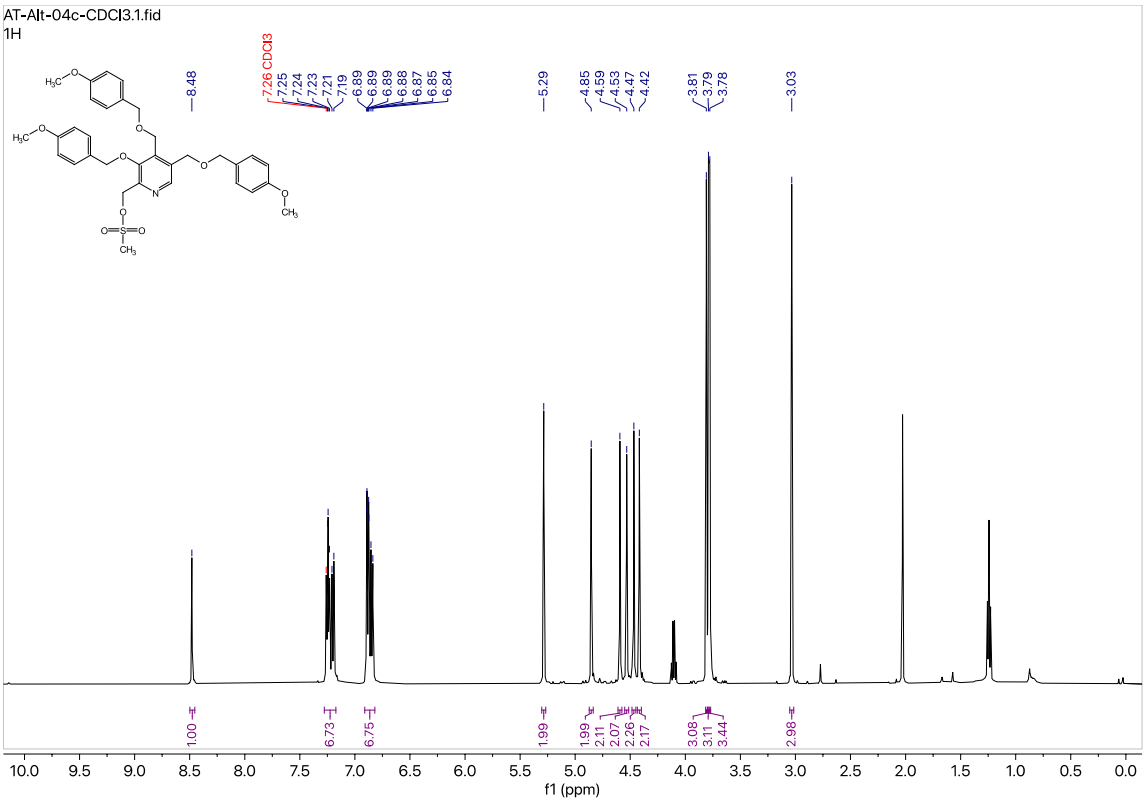

Figure S18. ^{1}H-NMR spectrum of Compound 12.

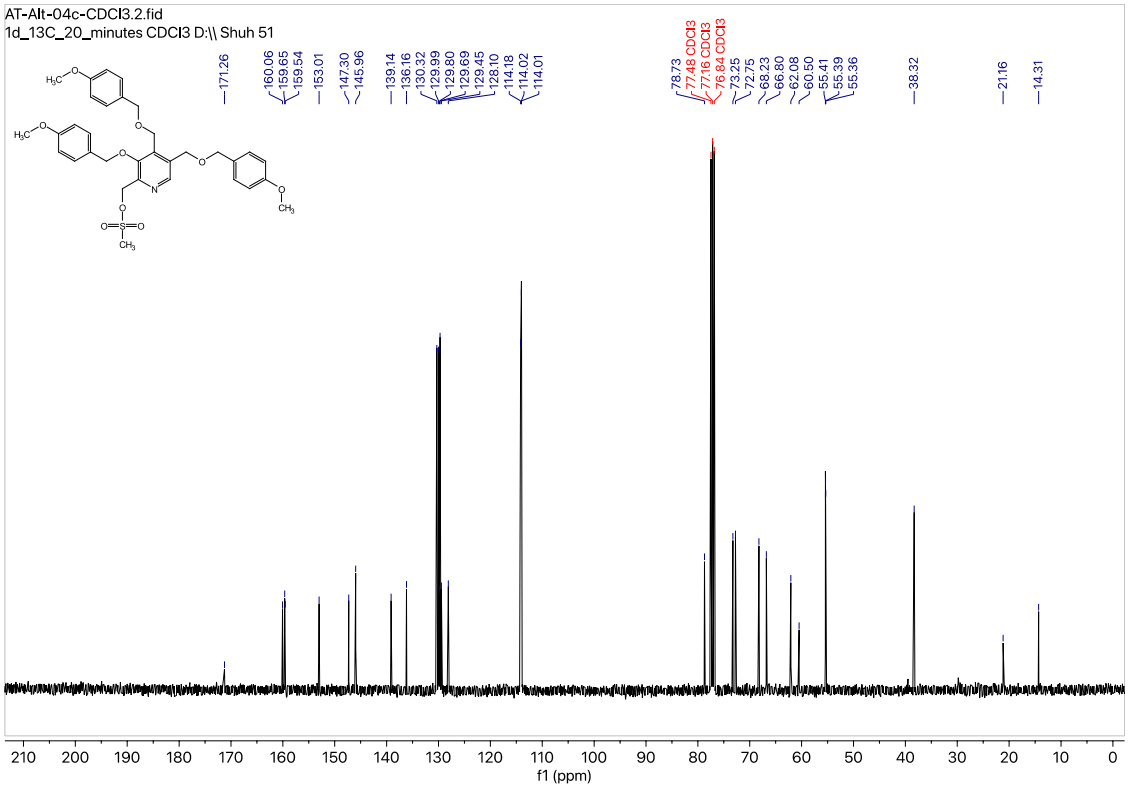

Figure S19. ^{13}C-NMR spectrum of Compound 12.

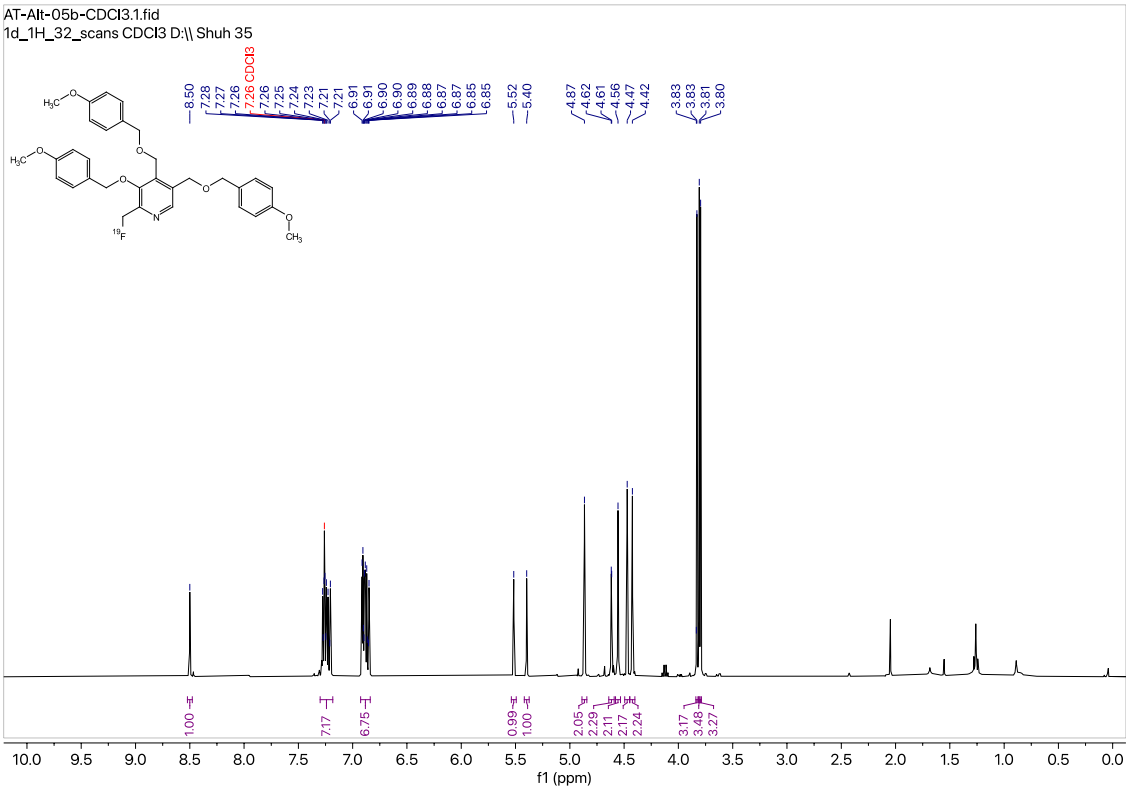

Figure S20. ^{1}H-NMR spectrum of Compound 13.

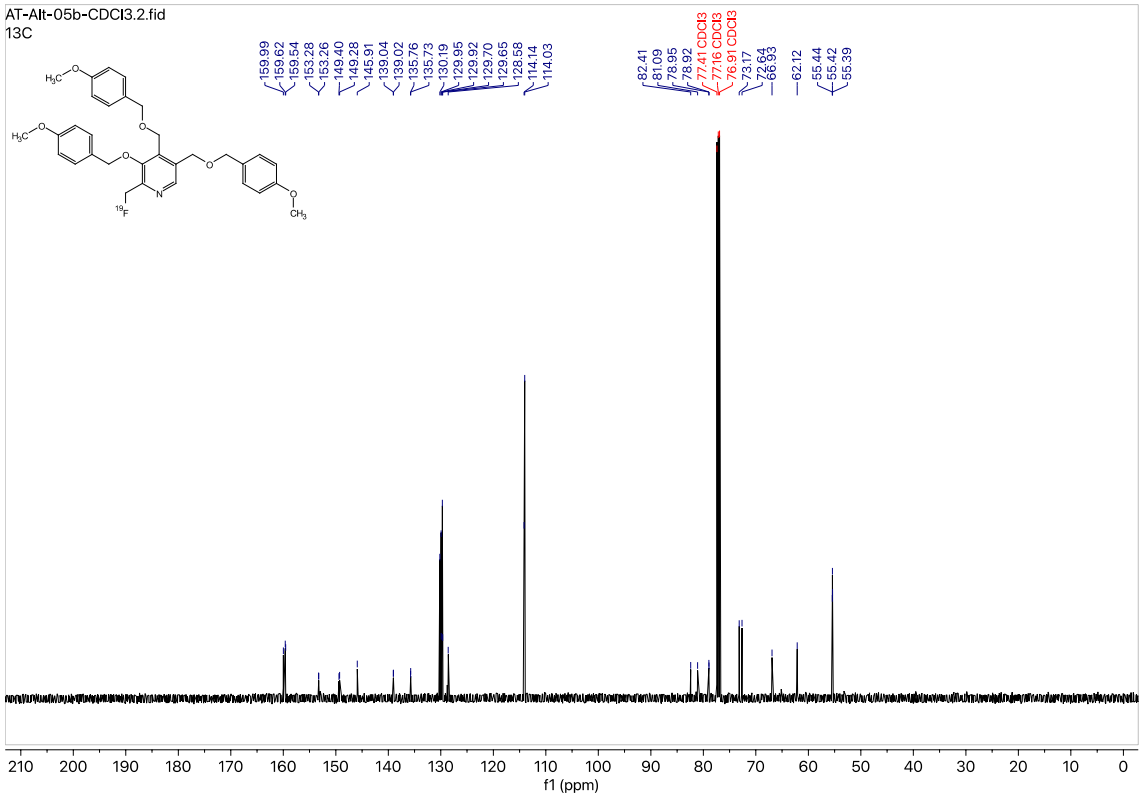

Figure S21. ^{13}C-NMR spectrum of Compound 13.

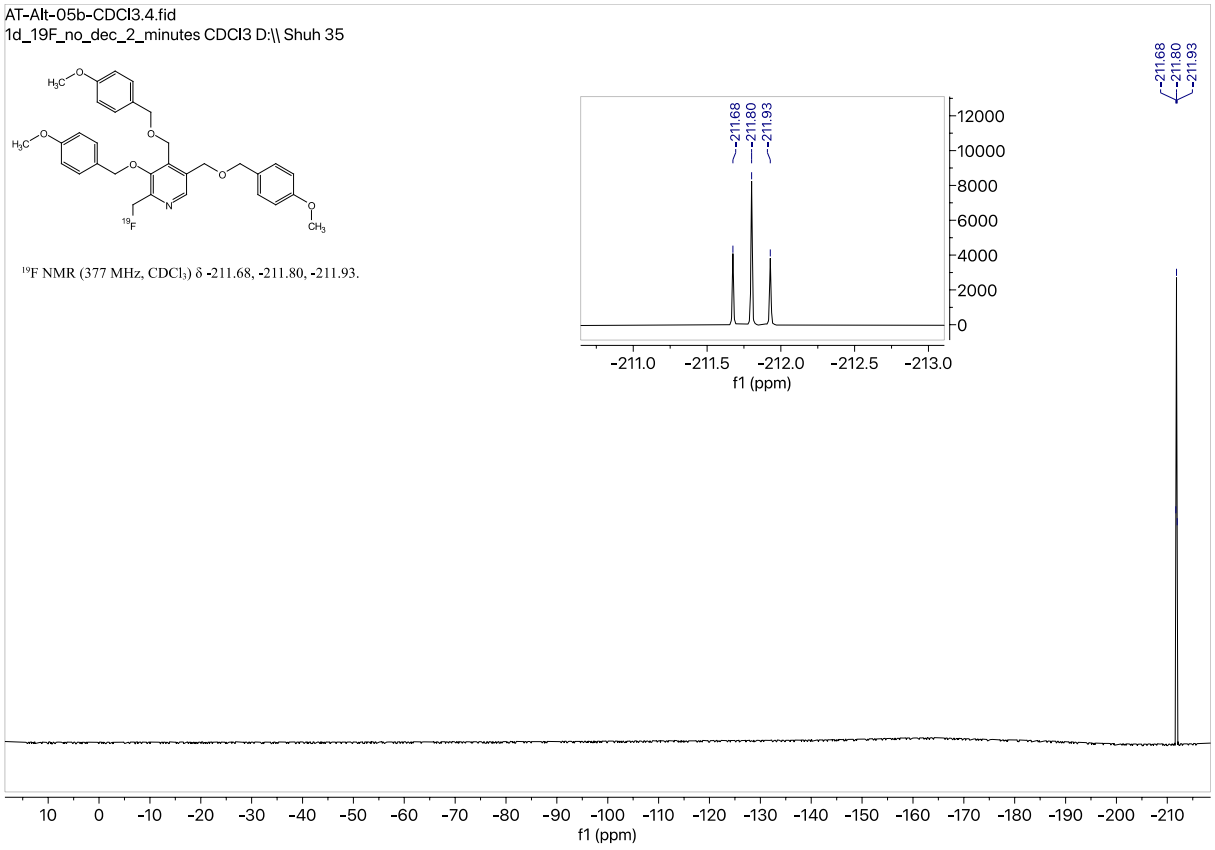

Figure S22. ^{19}F-NMR proton decoupled spectrum of Compound 13.

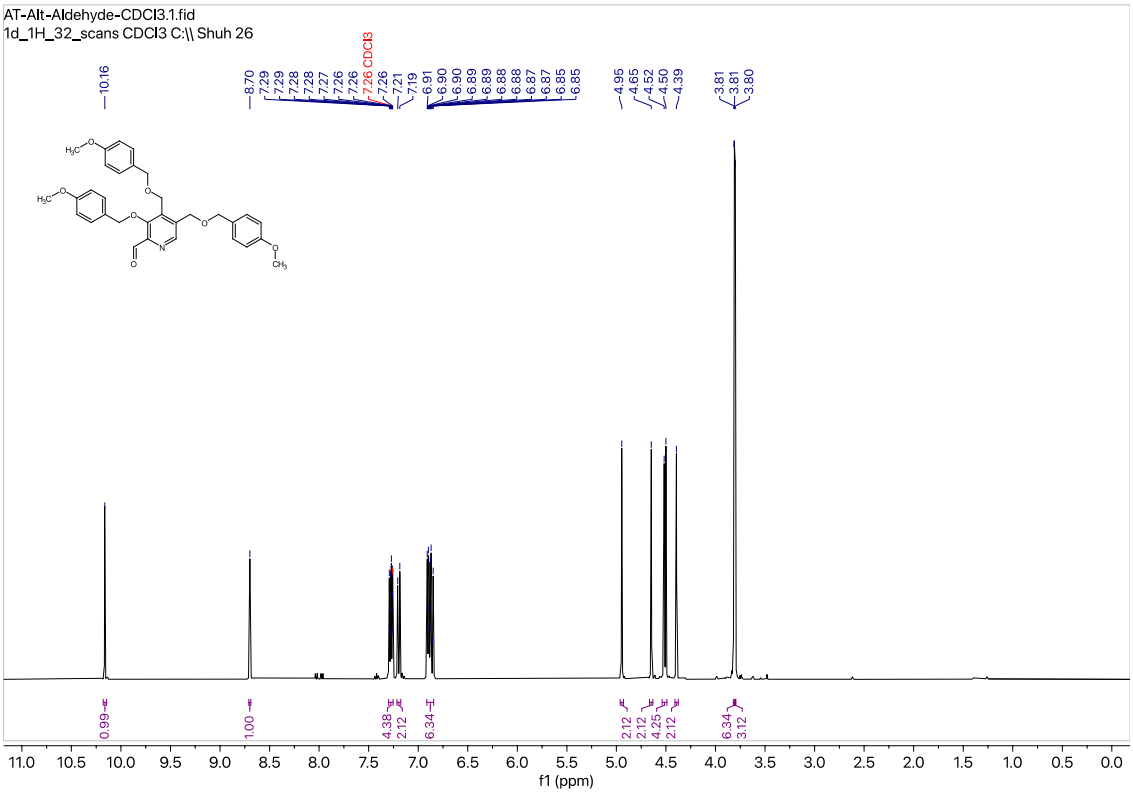

Figure S23. ^{1}H-NMR spectrum of Compound 15.

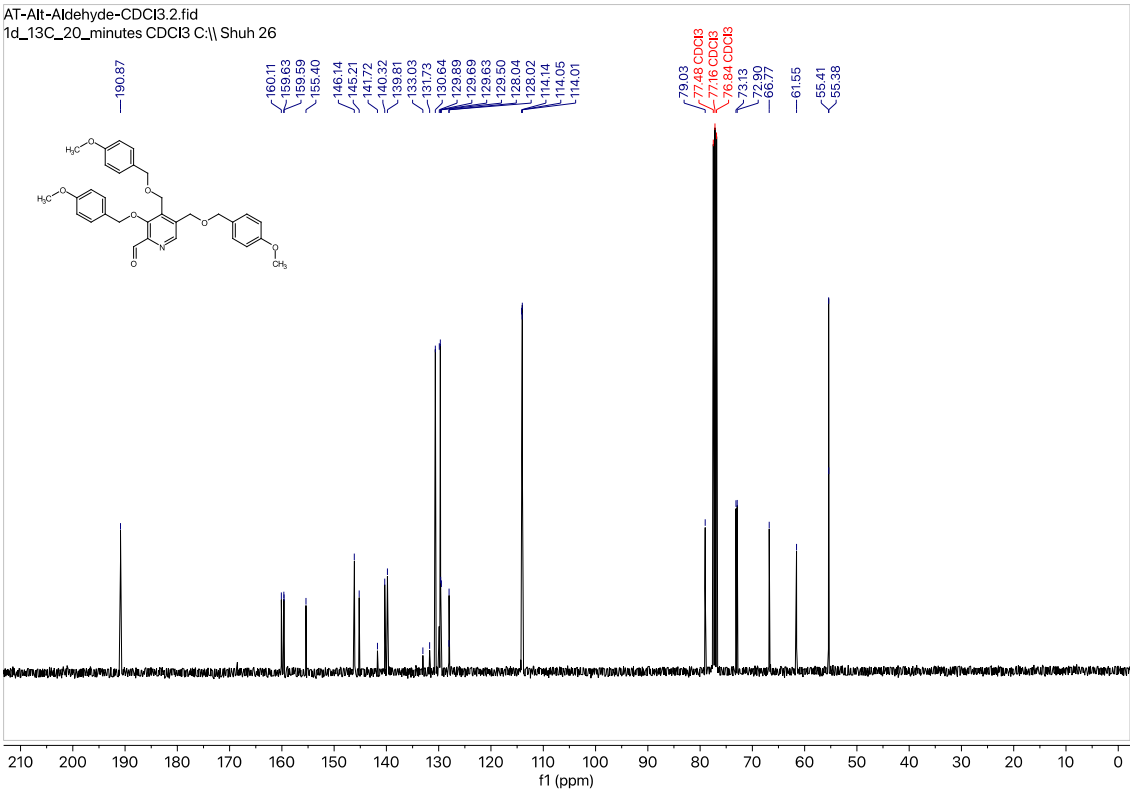

Figure S24. ^{13}C-NMR spectrum of Compound 15.

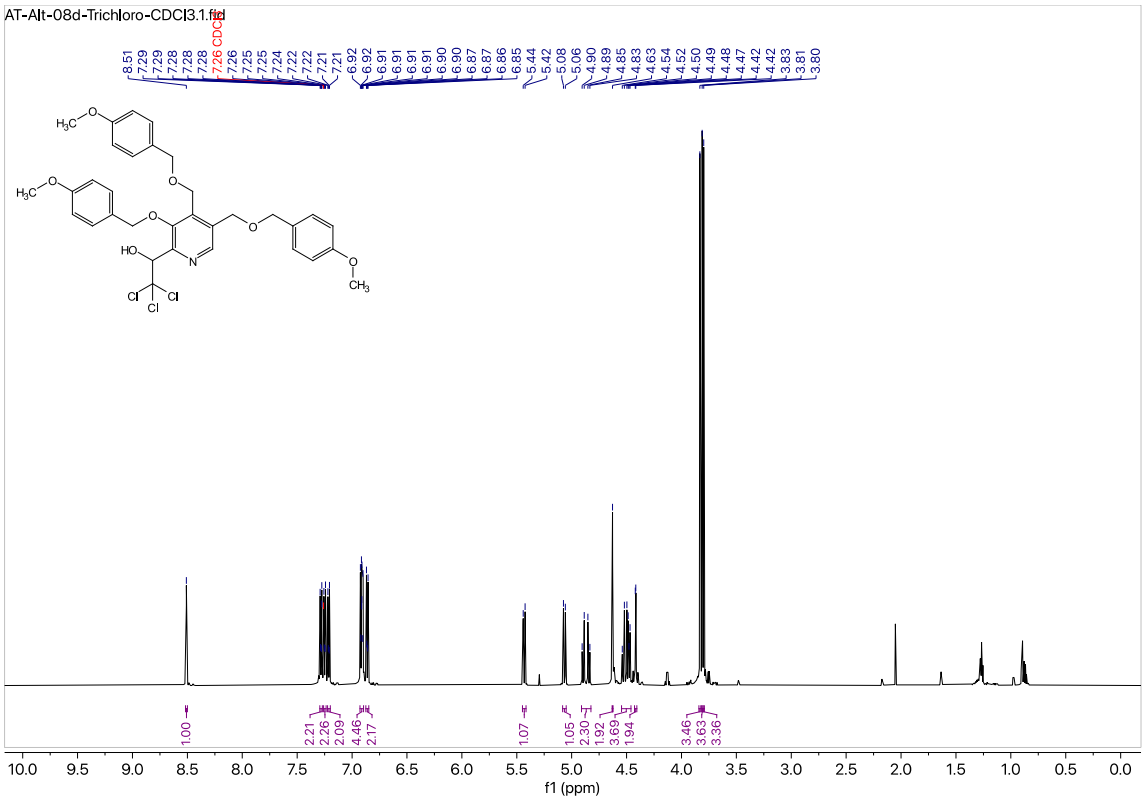

Figure S25. ^{1}H-NMR spectrum of Compound 16.

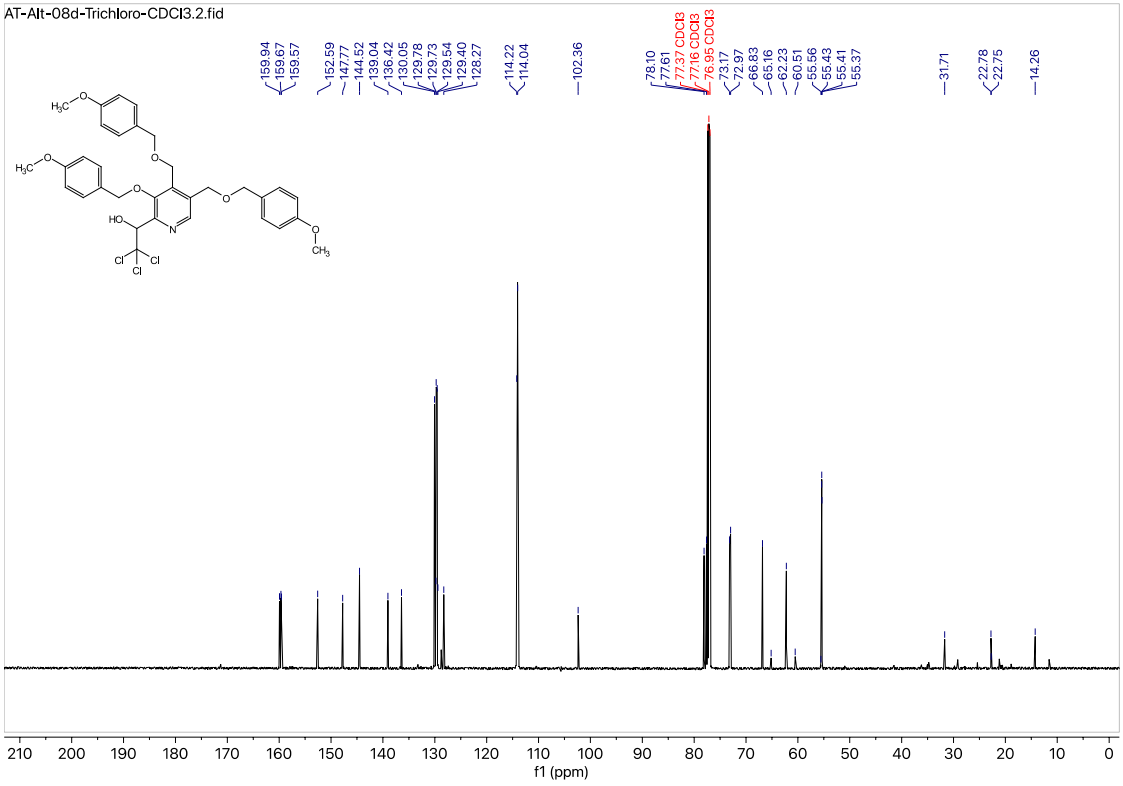

Figure S26. ^{13}C-NMR spectrum of Compound 16.

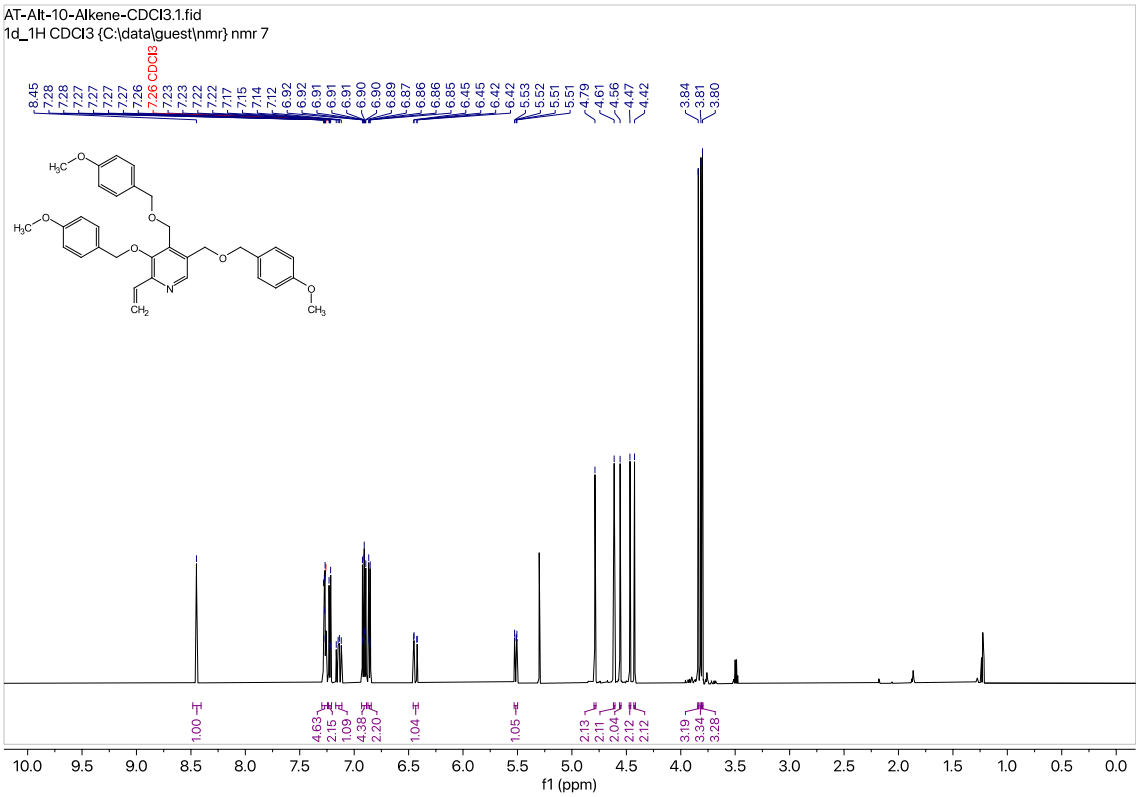

Figure S27. ^{1}H-NMR spectrum of Compound 18.

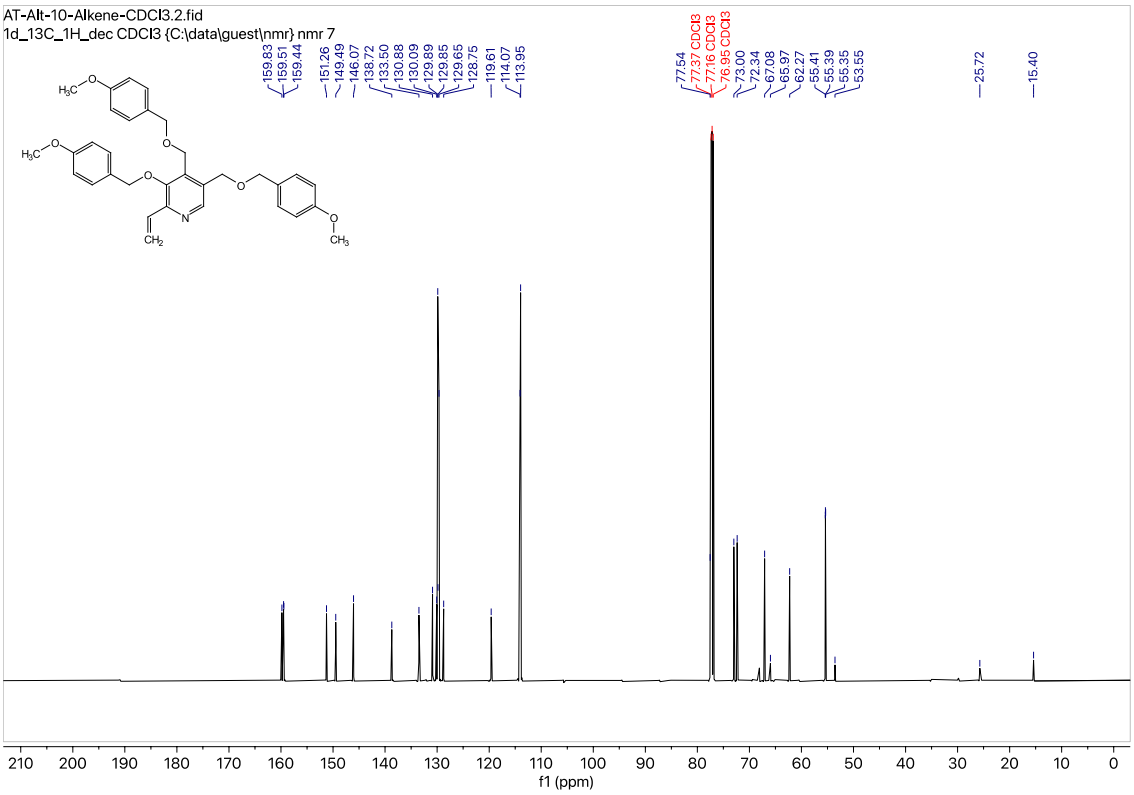

Figure S28. ^{13}C-NMR spectrum of Compound 18.

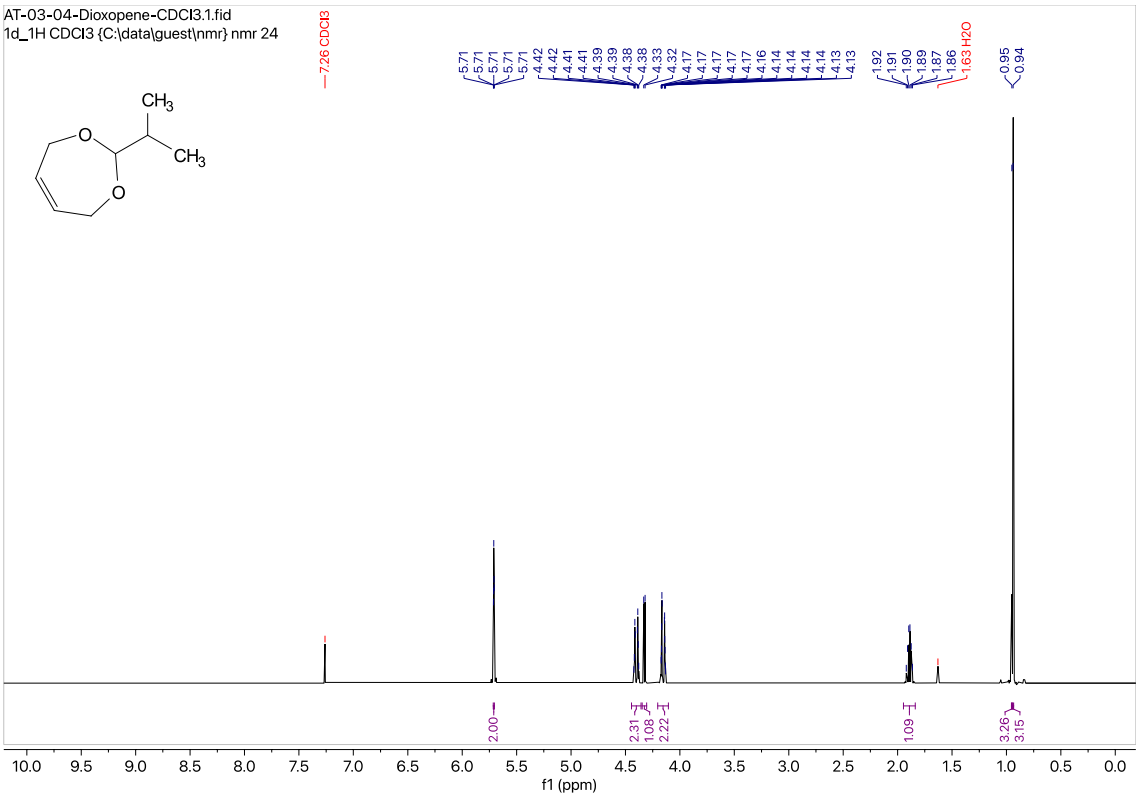

Figure S29. ^{1}H-NMR spectrum of Compound 25.

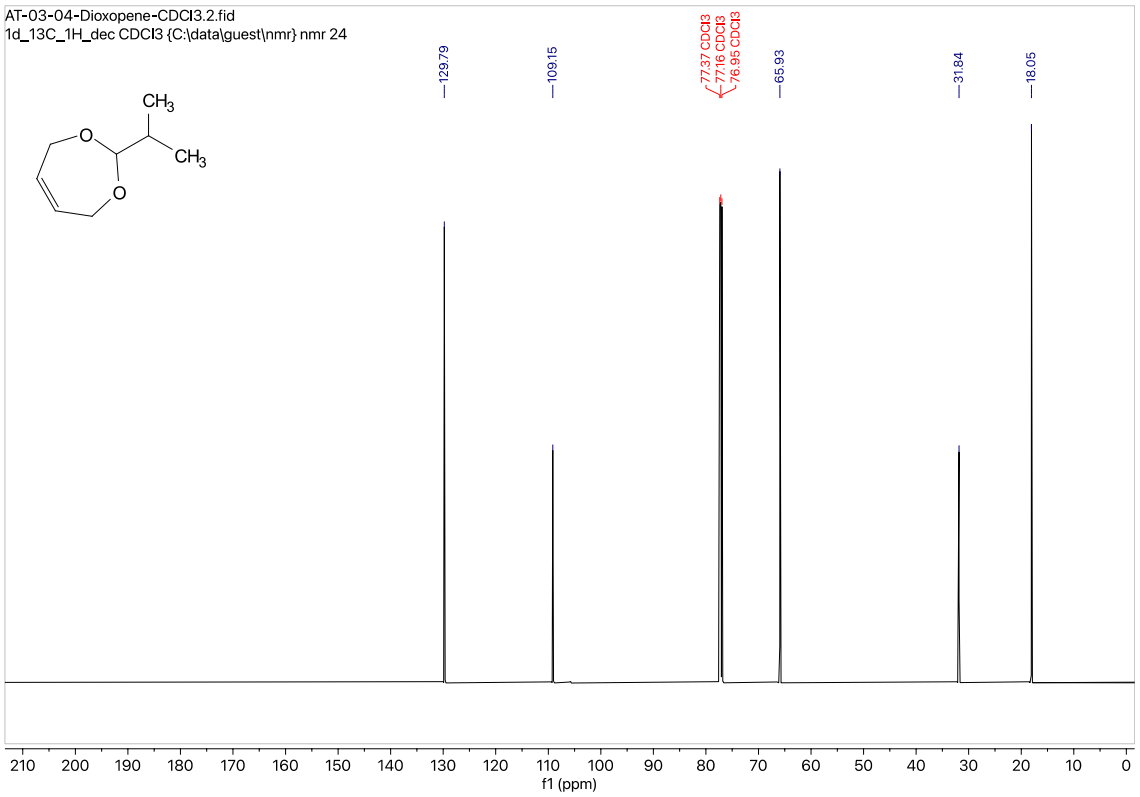

Figure S30. ^{13}C-NMR spectrum of Compound 25.

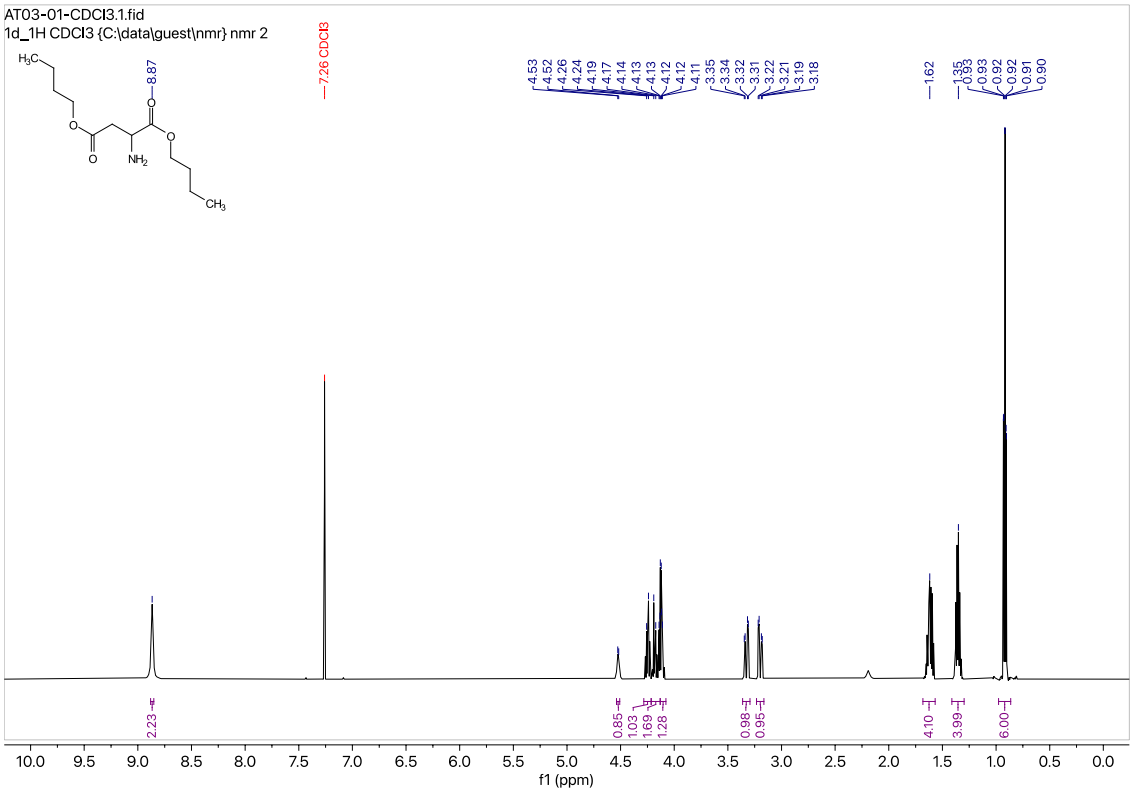

Figure S31. ^{1}H-NMR spectrum of Compound 26.

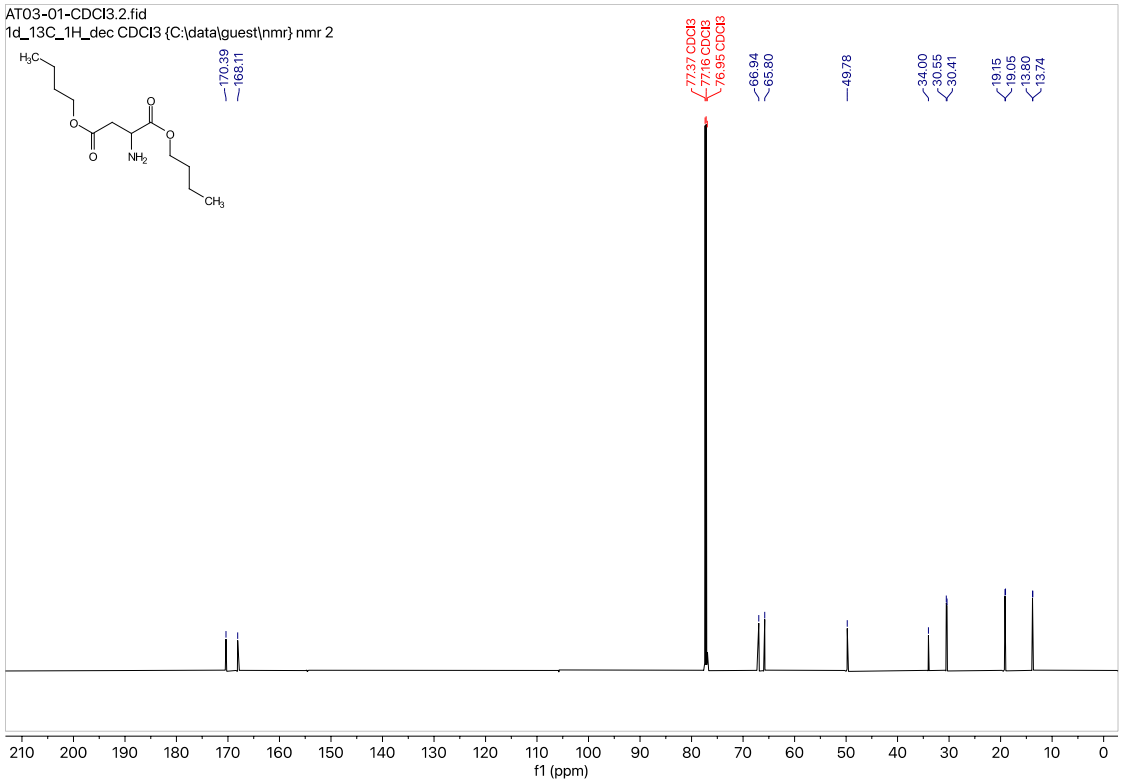

Figure S32. ^{13}C-NMR spectrum of Compound 26.

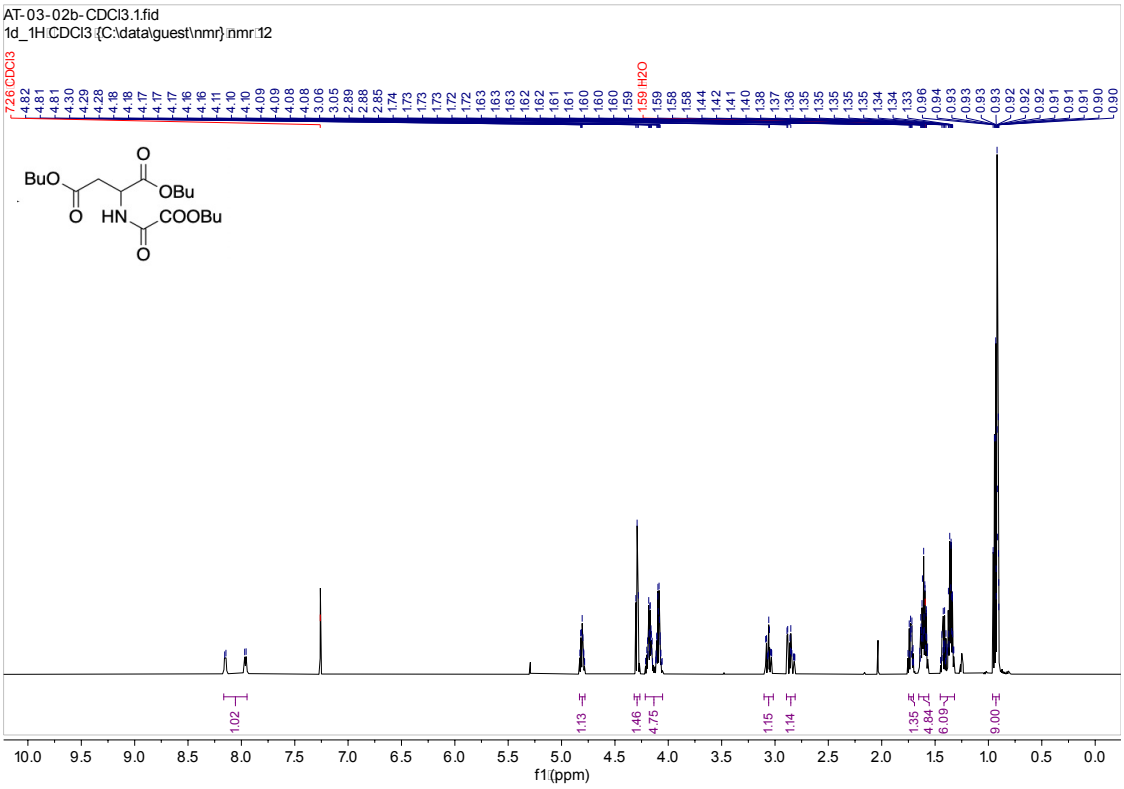

Figure S33. ^{1}H-NMR spectrum of Compound 27.

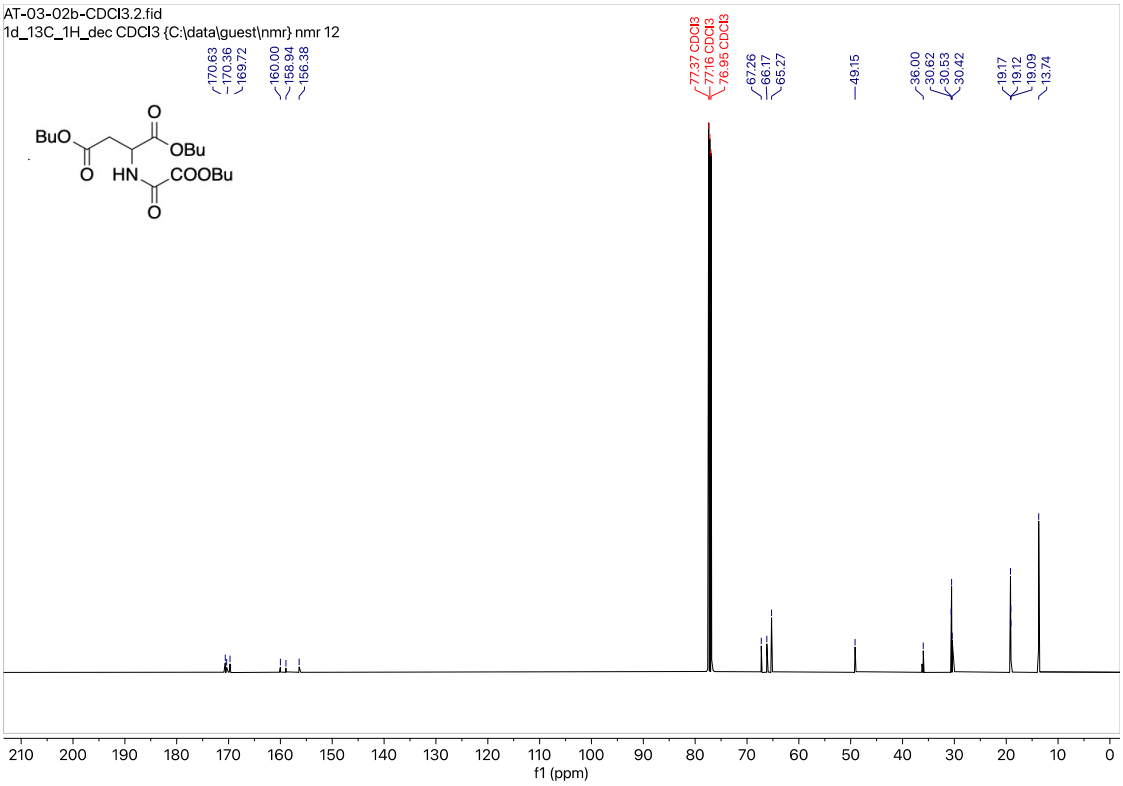

Figure S34. ^{13}C-NMR spectrum of Compound 27.

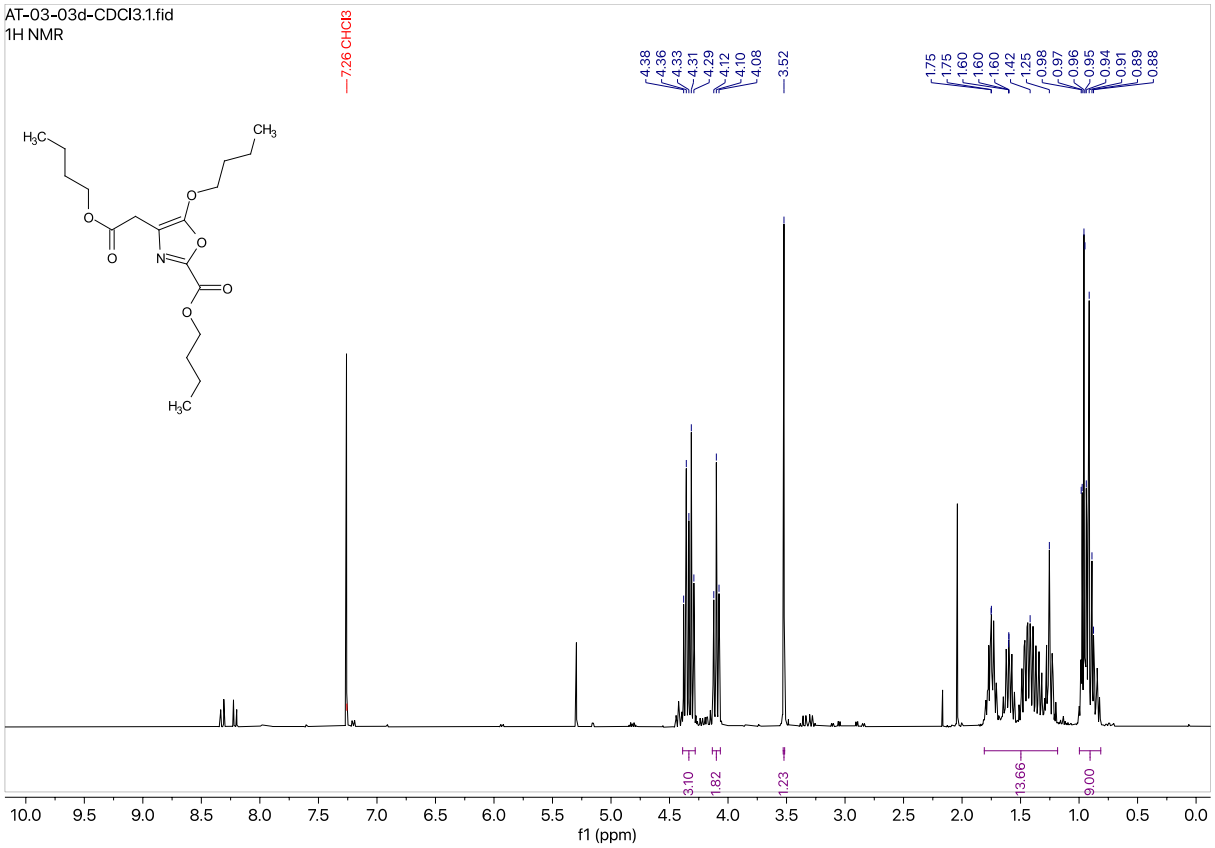

Figure S35. ^{1}H-NMR spectrum of Compound 28.

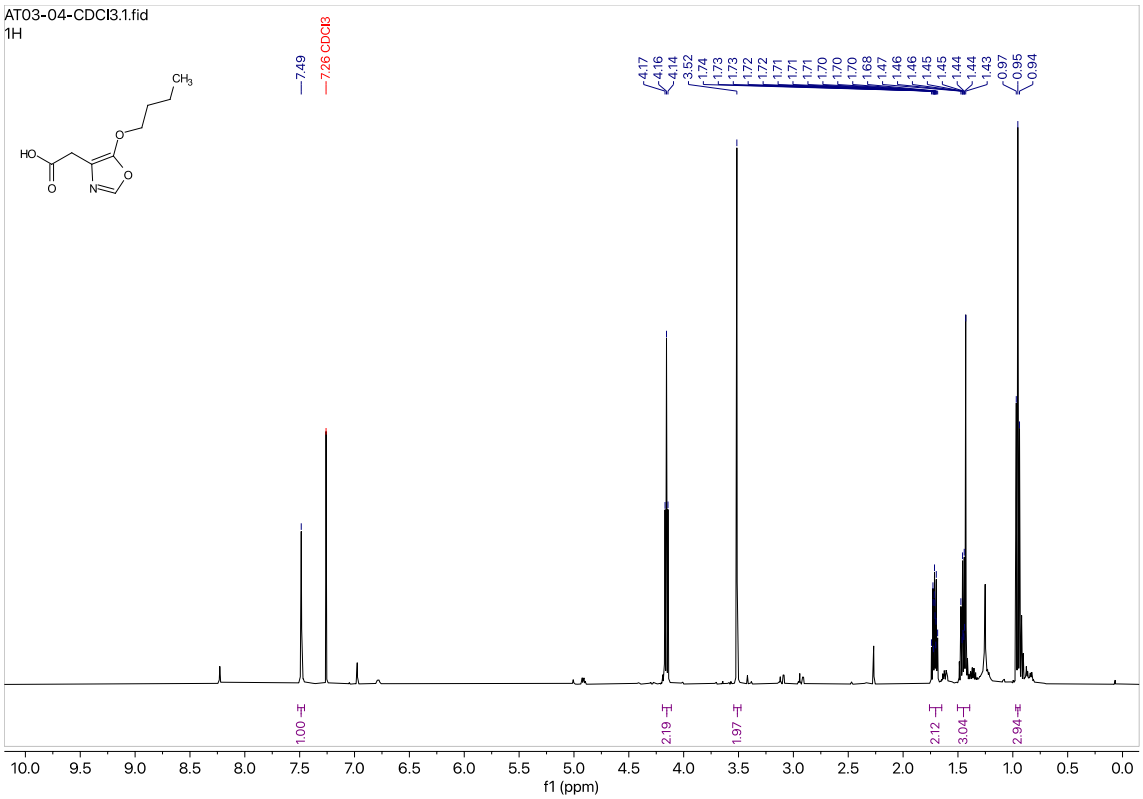

Figure S36. ^{1}H-NMR spectrum of Compound 29.

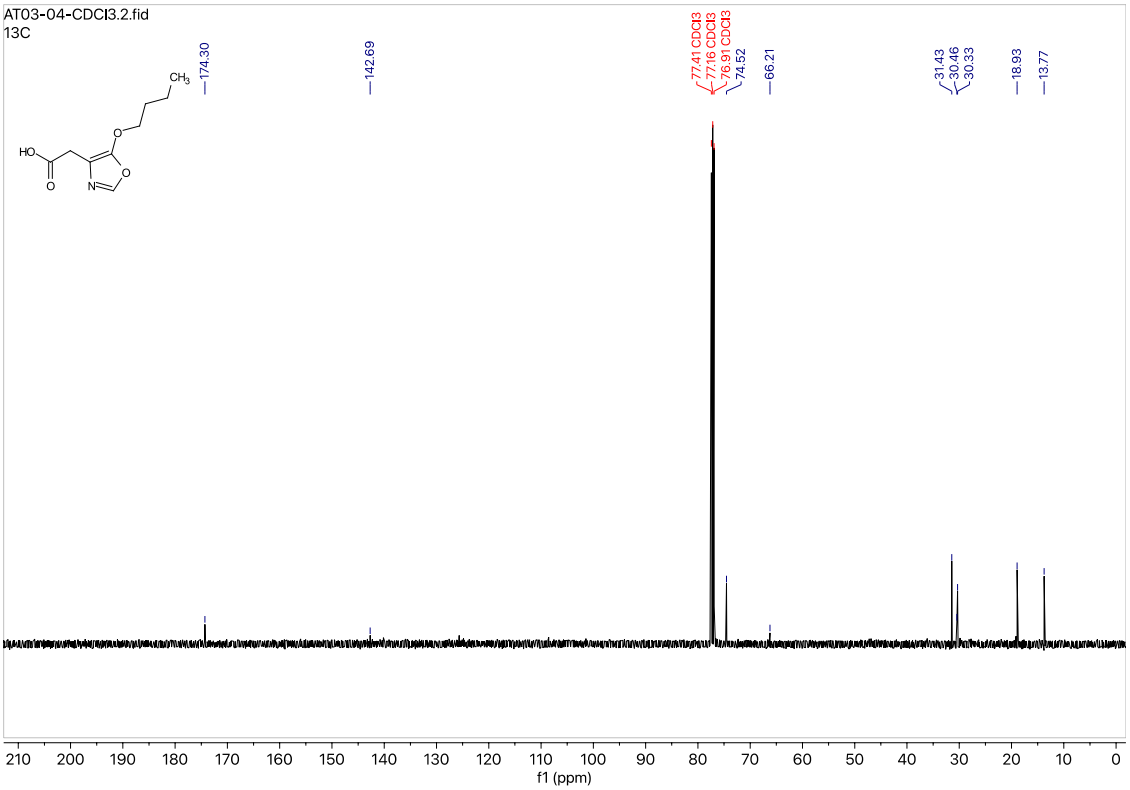

Figure S37. ^{13}C-NMR spectrum of Compound 29.

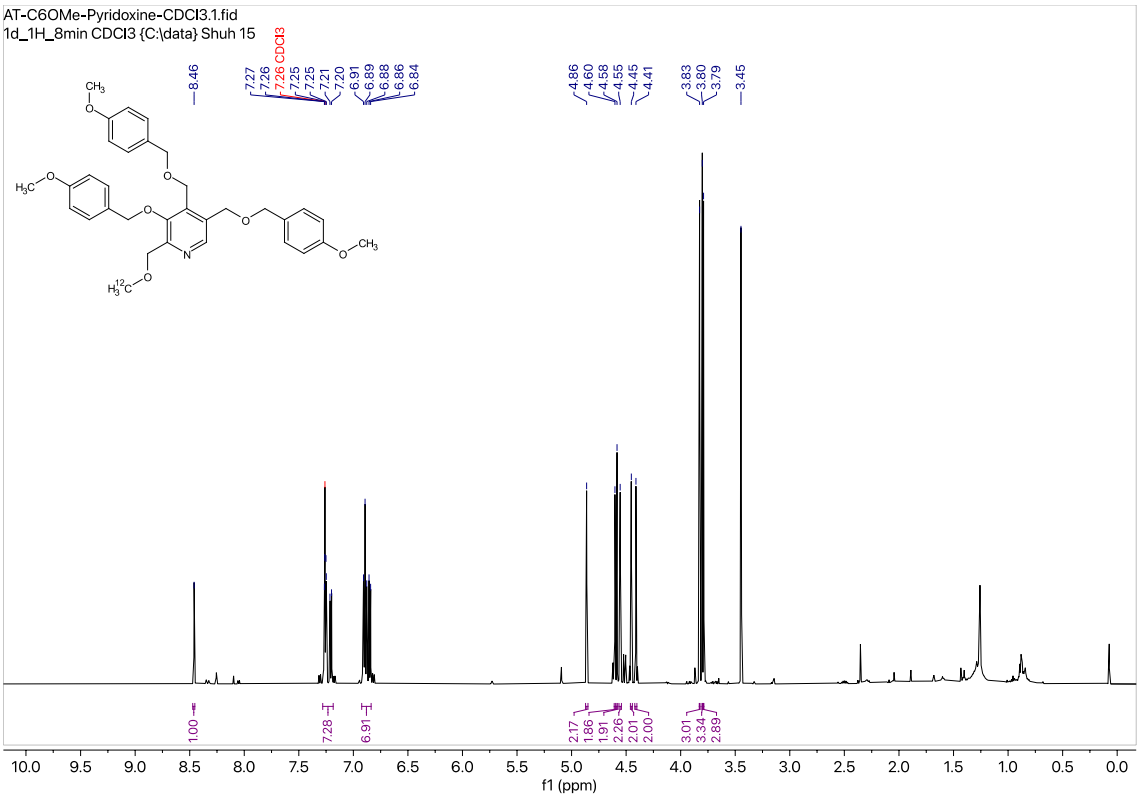

Figure S38. ^{1}H-NMR spectrum of Compound 31.

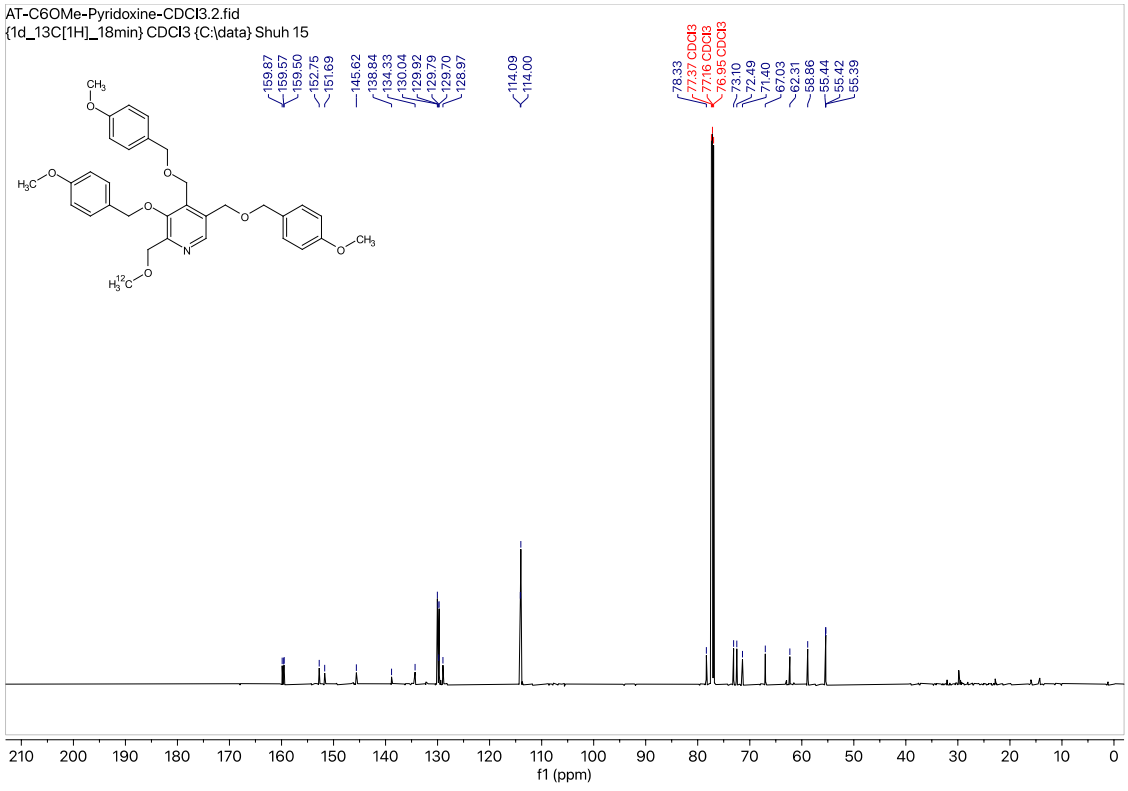

Figure S39. ^{13}C-NMR spectrum of Compound 31.

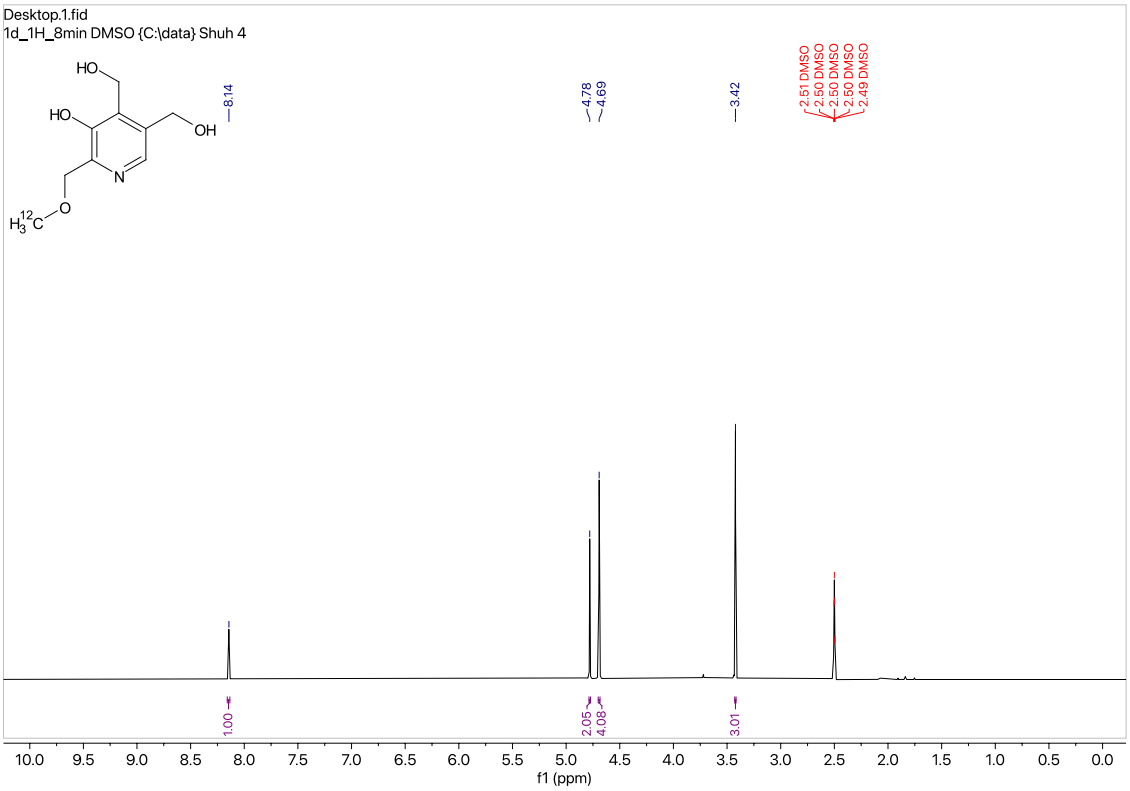

Figure S40. ^{1}H-NMR spectrum of Compound 32.

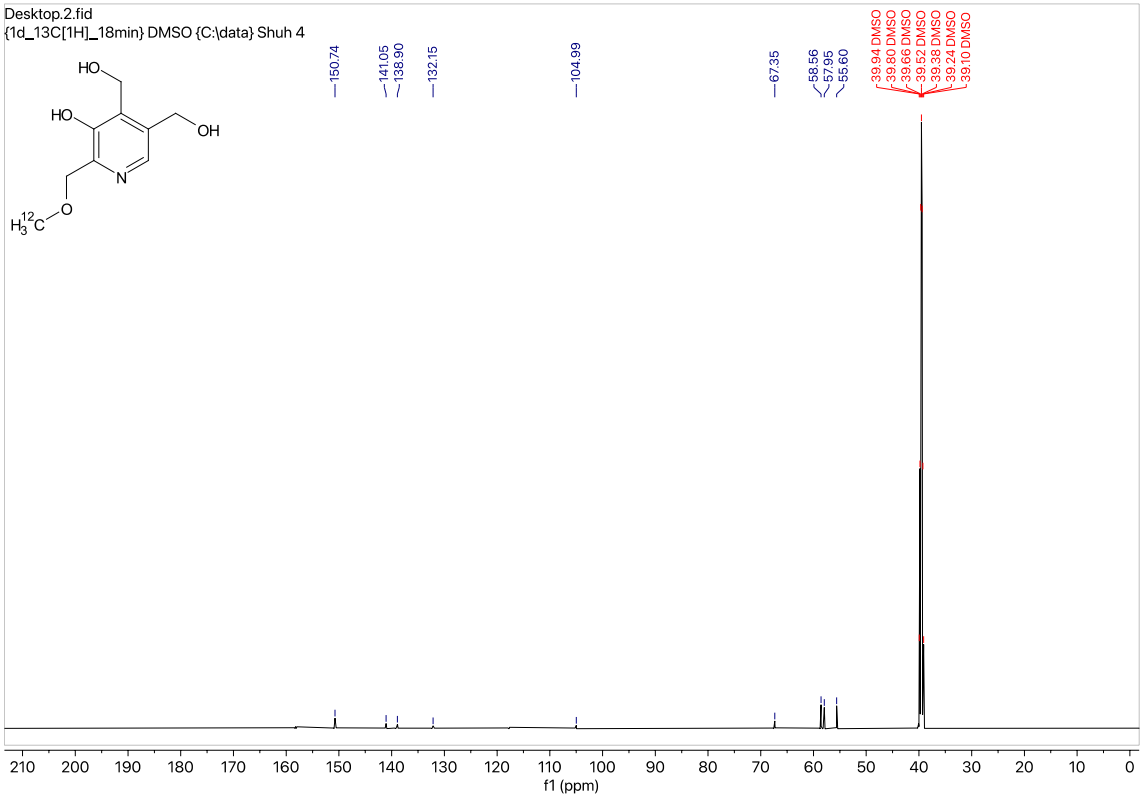

Figure S41. ^{13}C-NMR spectrum of Compound 32.

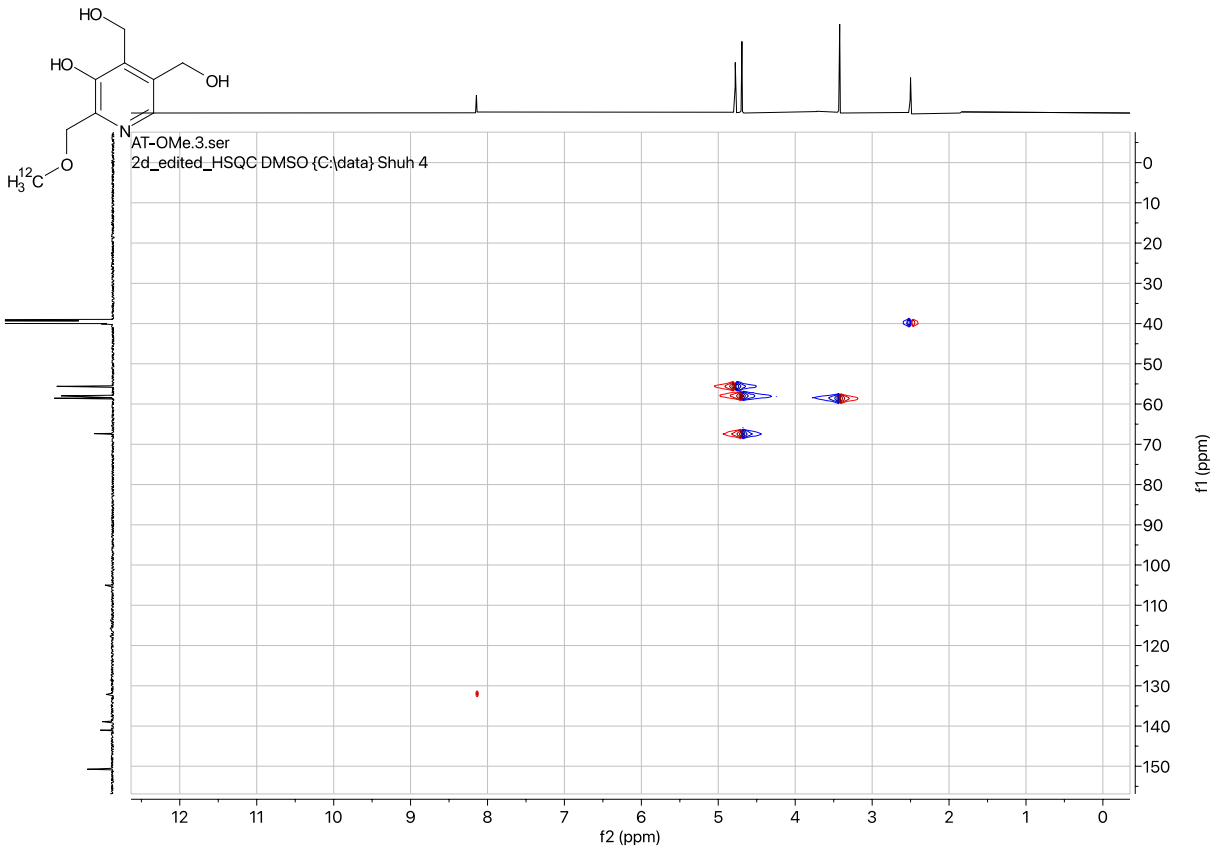

Figure S42. 2D-Edited HSQC NMR spectrum of Compound 32.

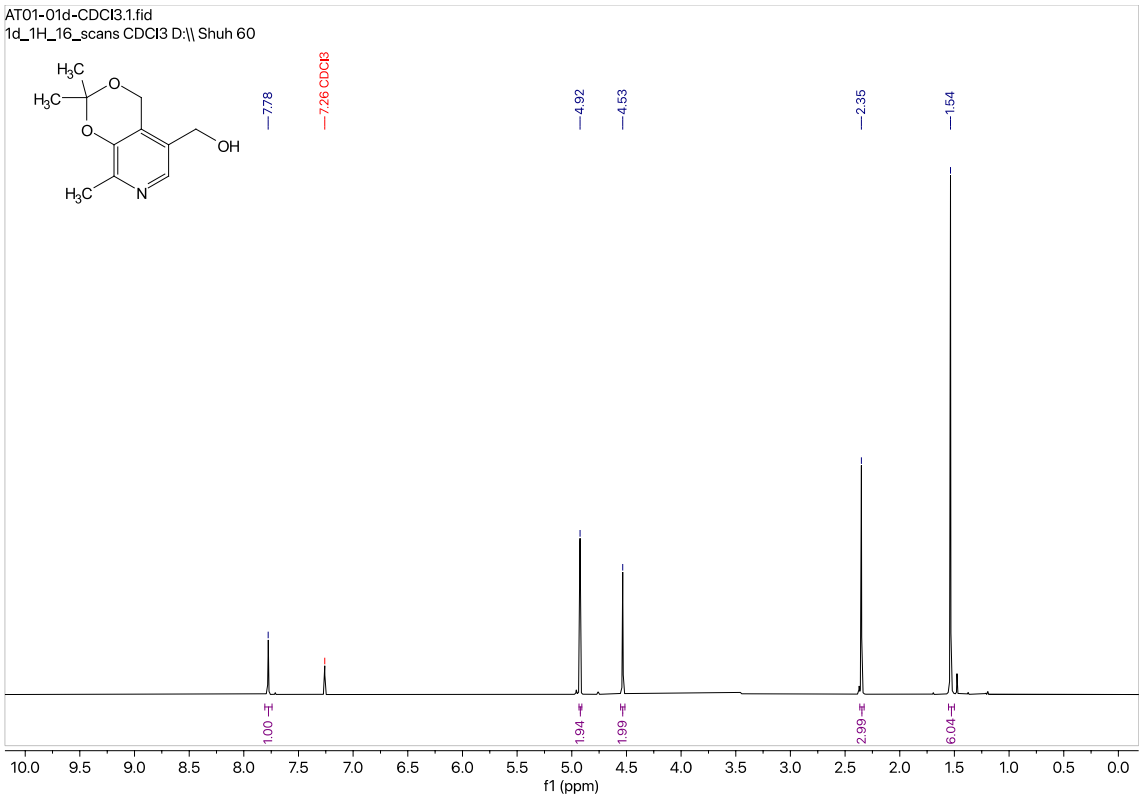

Figure S43. ^{1}H-NMR spectrum of Compound 33.

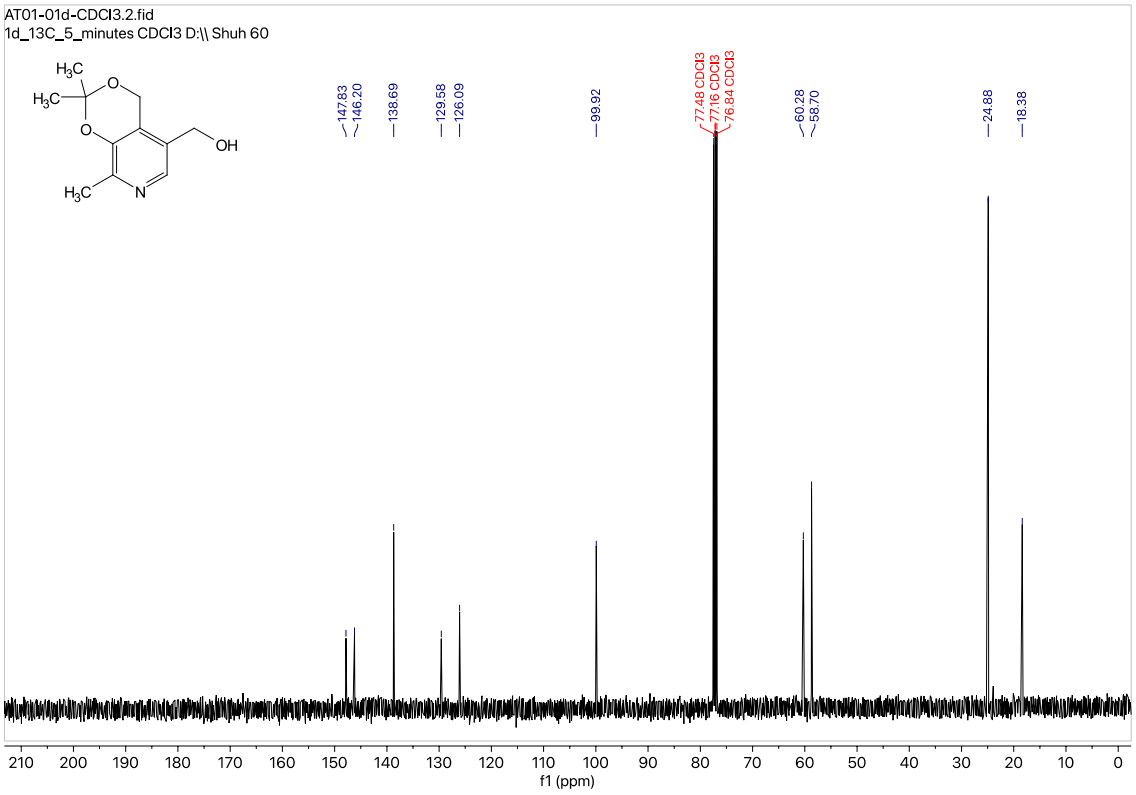

Figure S44. ^{13}C-NMR spectrum of Compound 33.

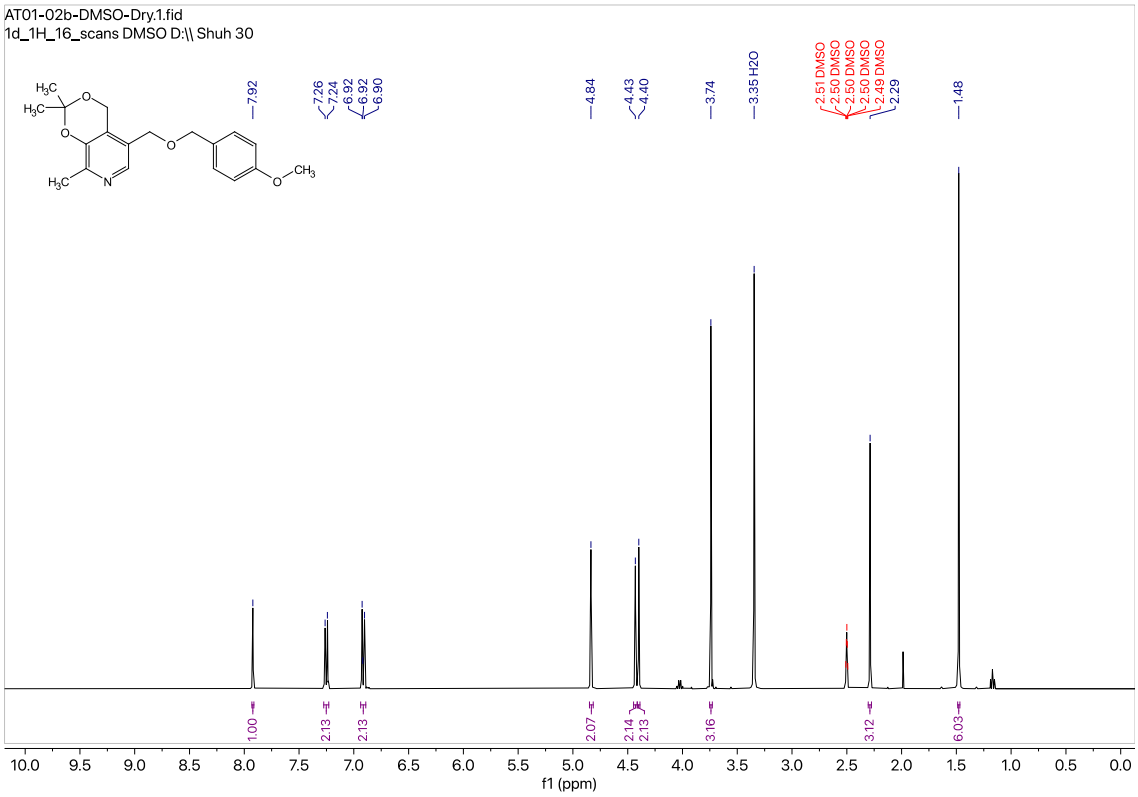

Figure S45. ^{1}H-NMR spectrum of Compound 34.

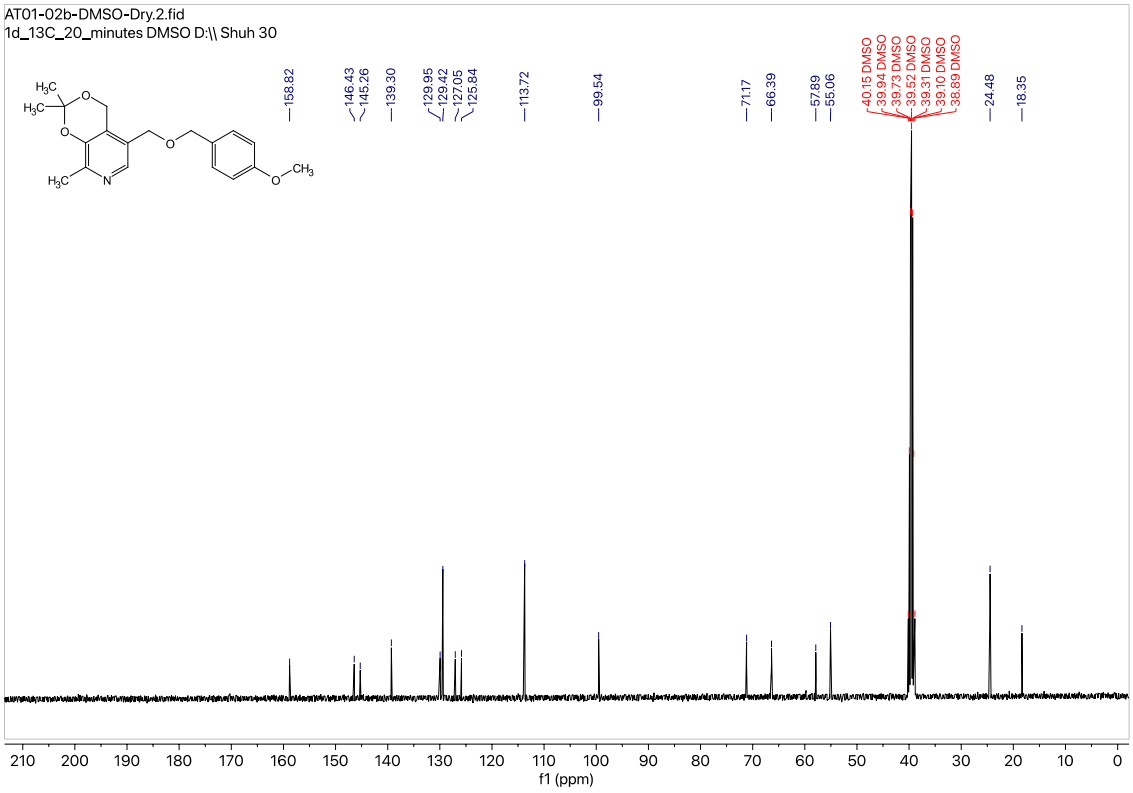

Figure S46. ^{13}C-NMR spectrum of Compound 34.

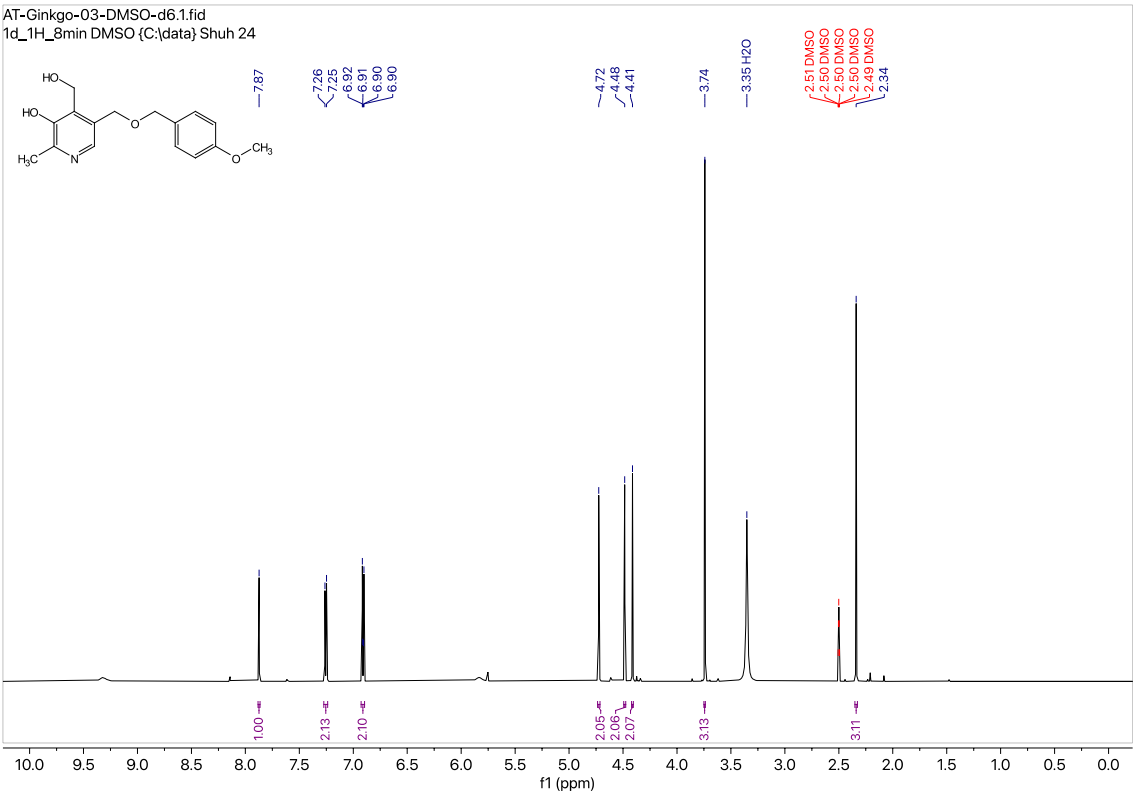

Figure S47. ^{1}H-NMR spectrum of Compound 35.

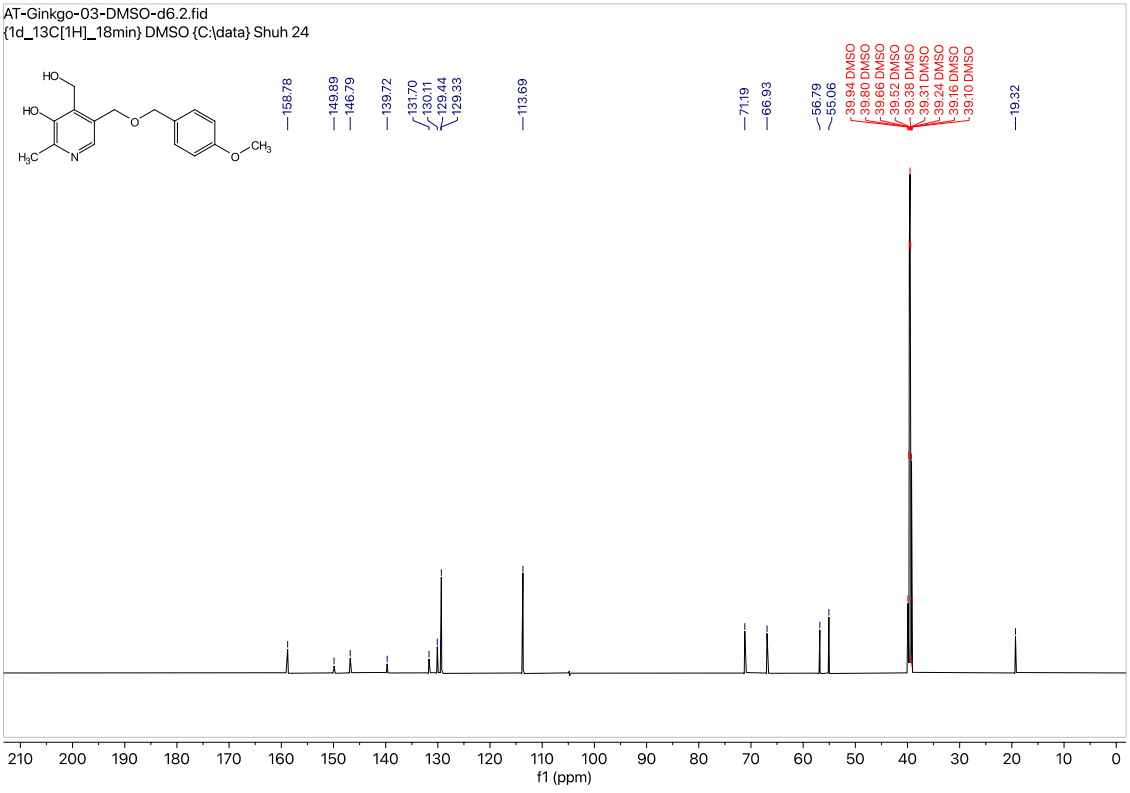

Figure S48. ^{13}C-NMR spectrum of Compound 35.

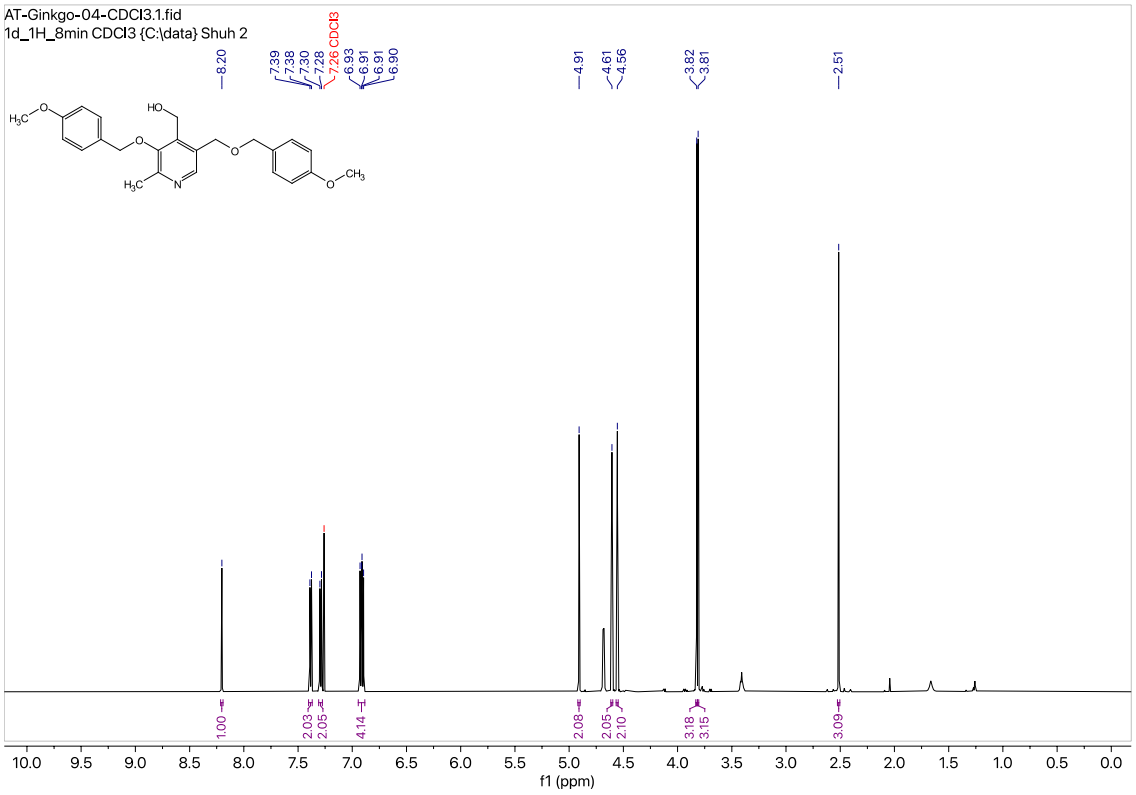

Figure S49. ^{1}H-NMR spectrum of Compound 36.

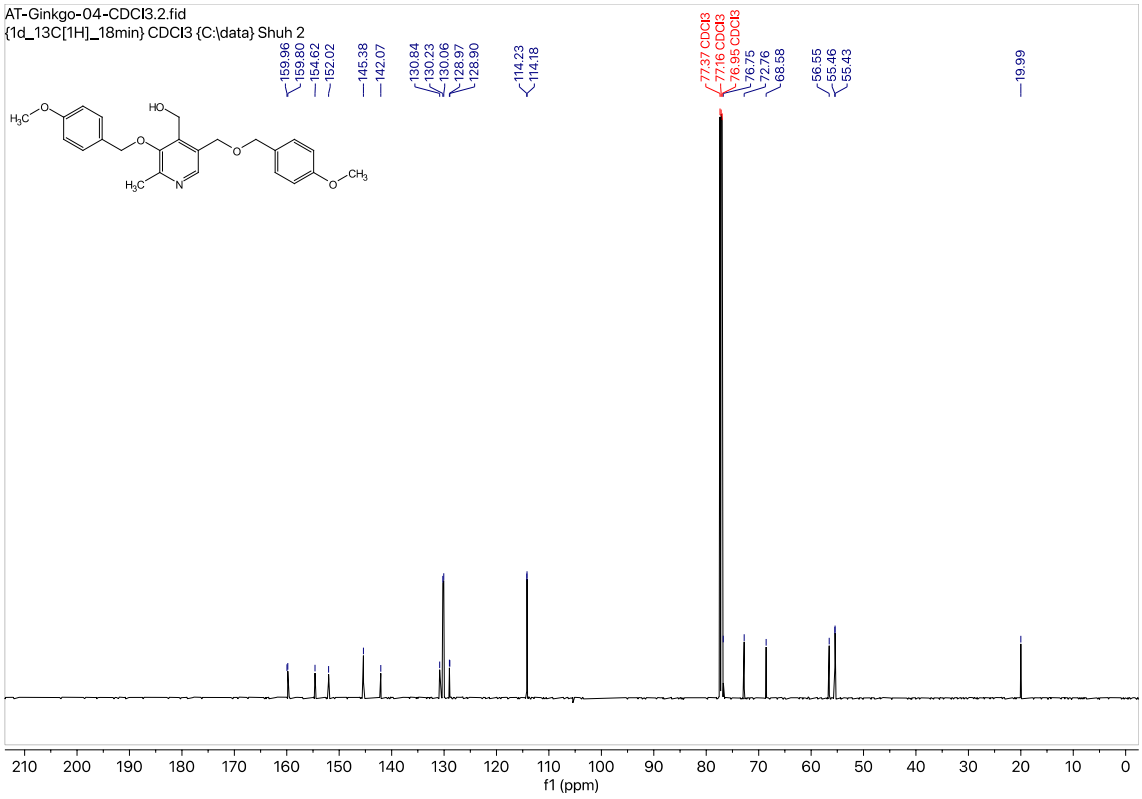

Figure S50. ^{13}C-NMR spectrum of Compound 36.

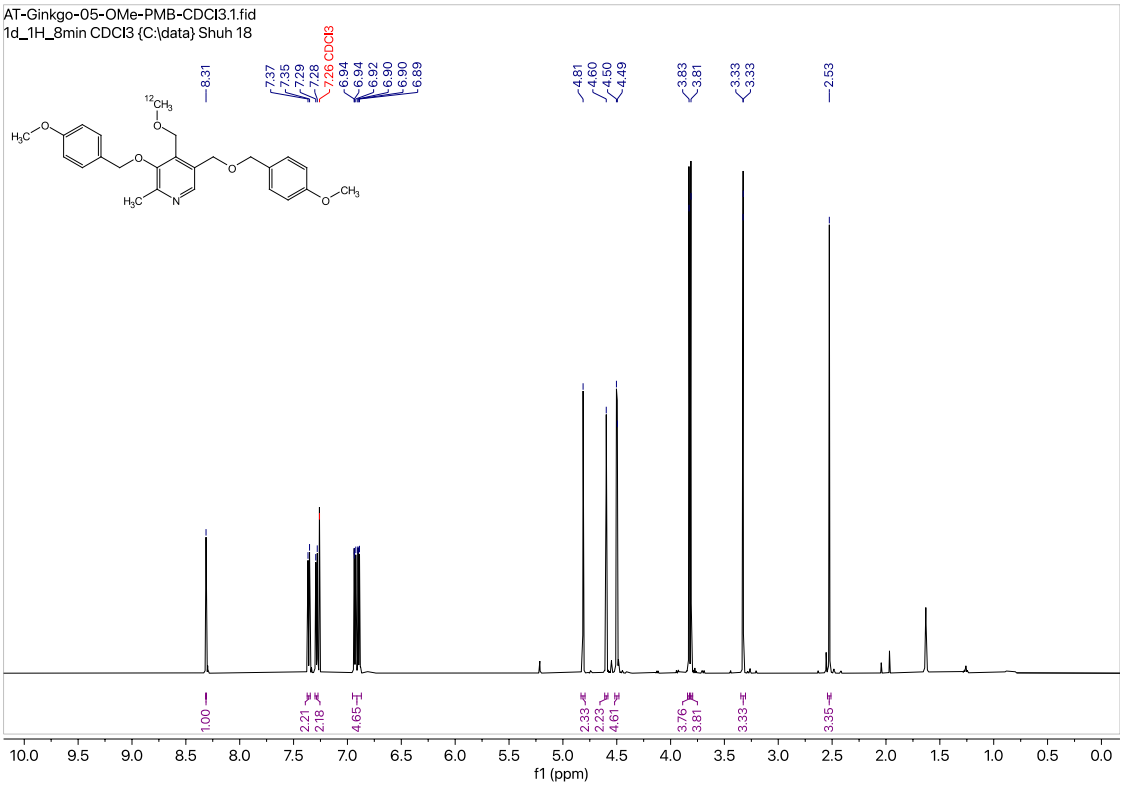

Figure S51. ^{1}H-NMR spectrum of Compound 37.

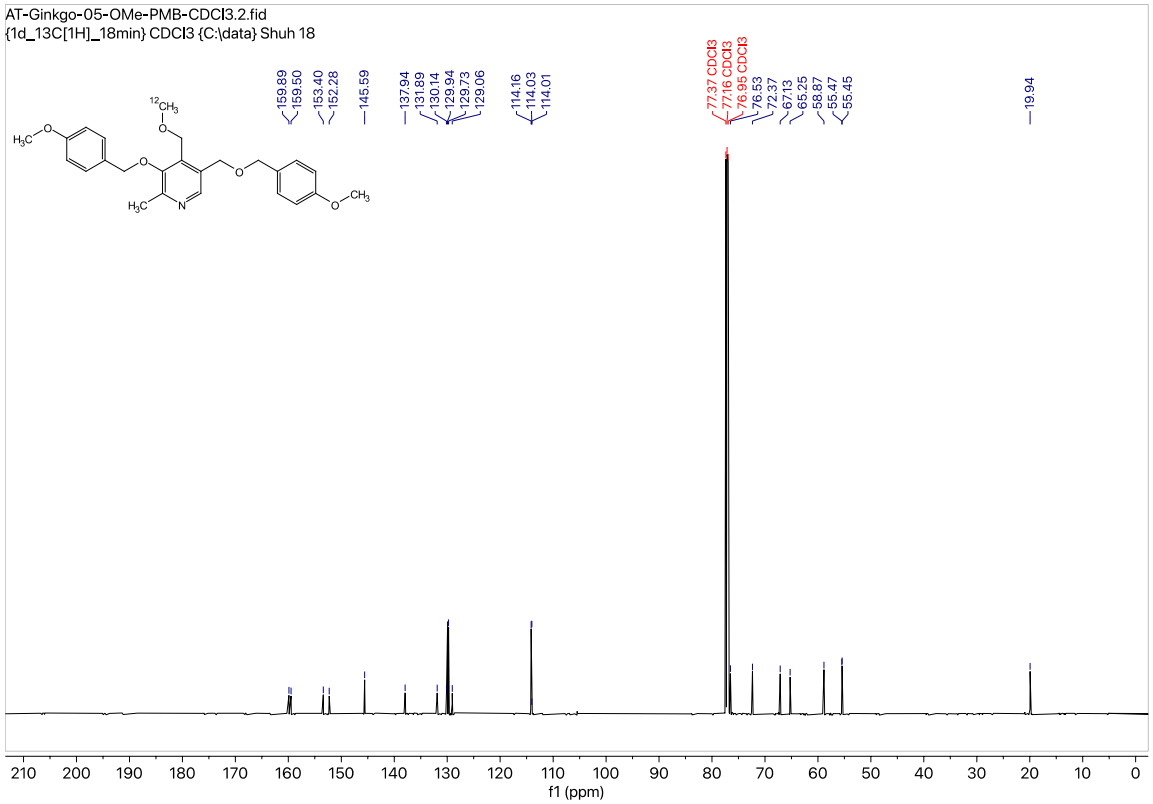

Figure S52. ^{13}C-NMR spectrum of Compound 37.

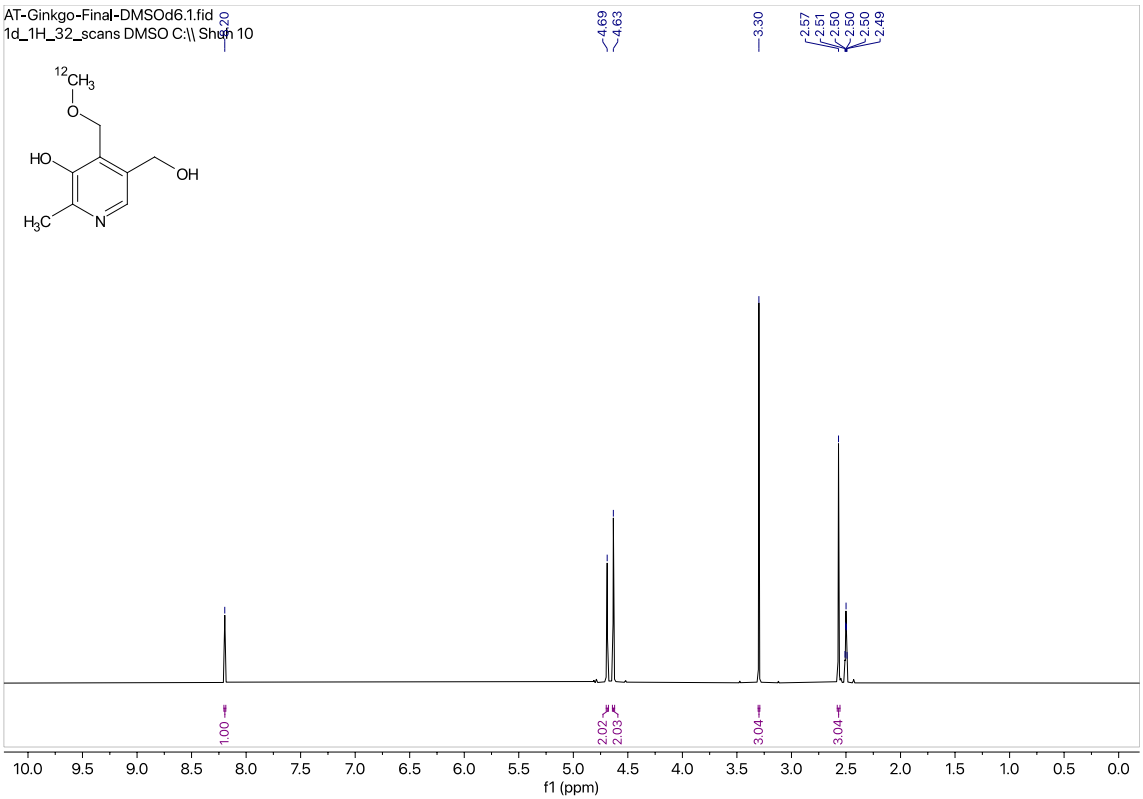

Figure S53. ^{1}H-NMR spectrum of Compound 38.

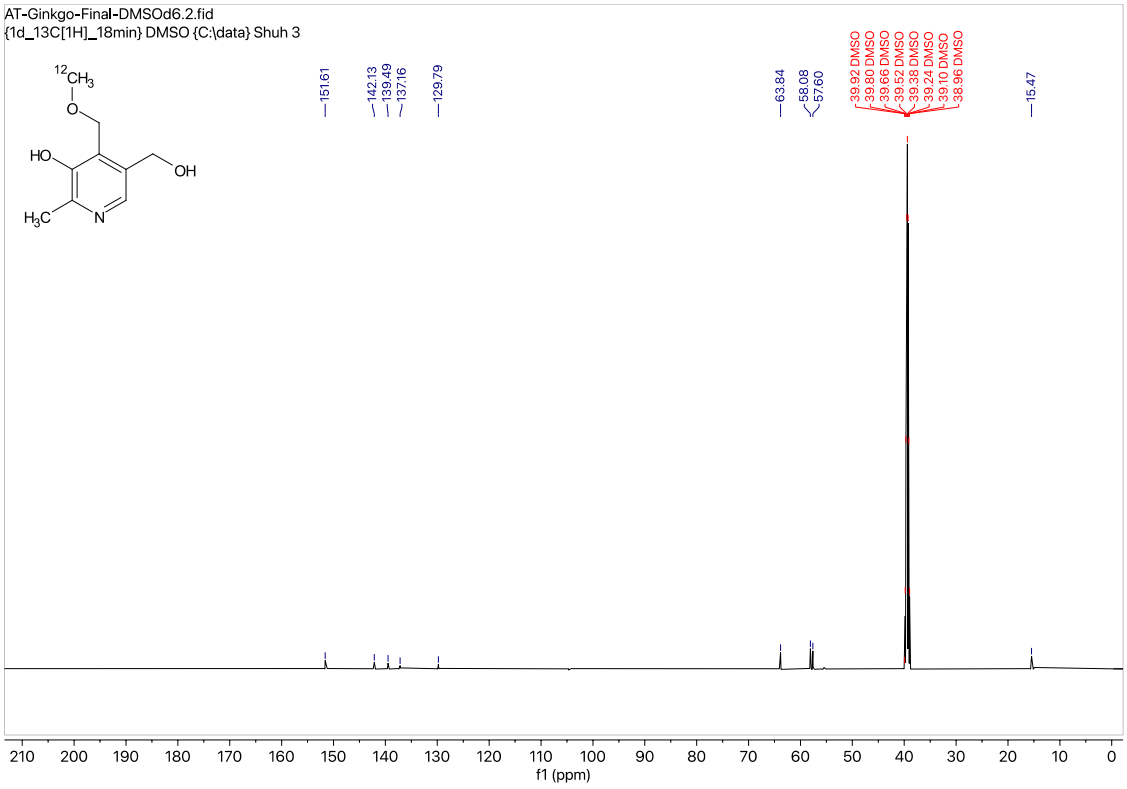

Figure S54. ^{13}C-NMR spectrum of Compound 38.

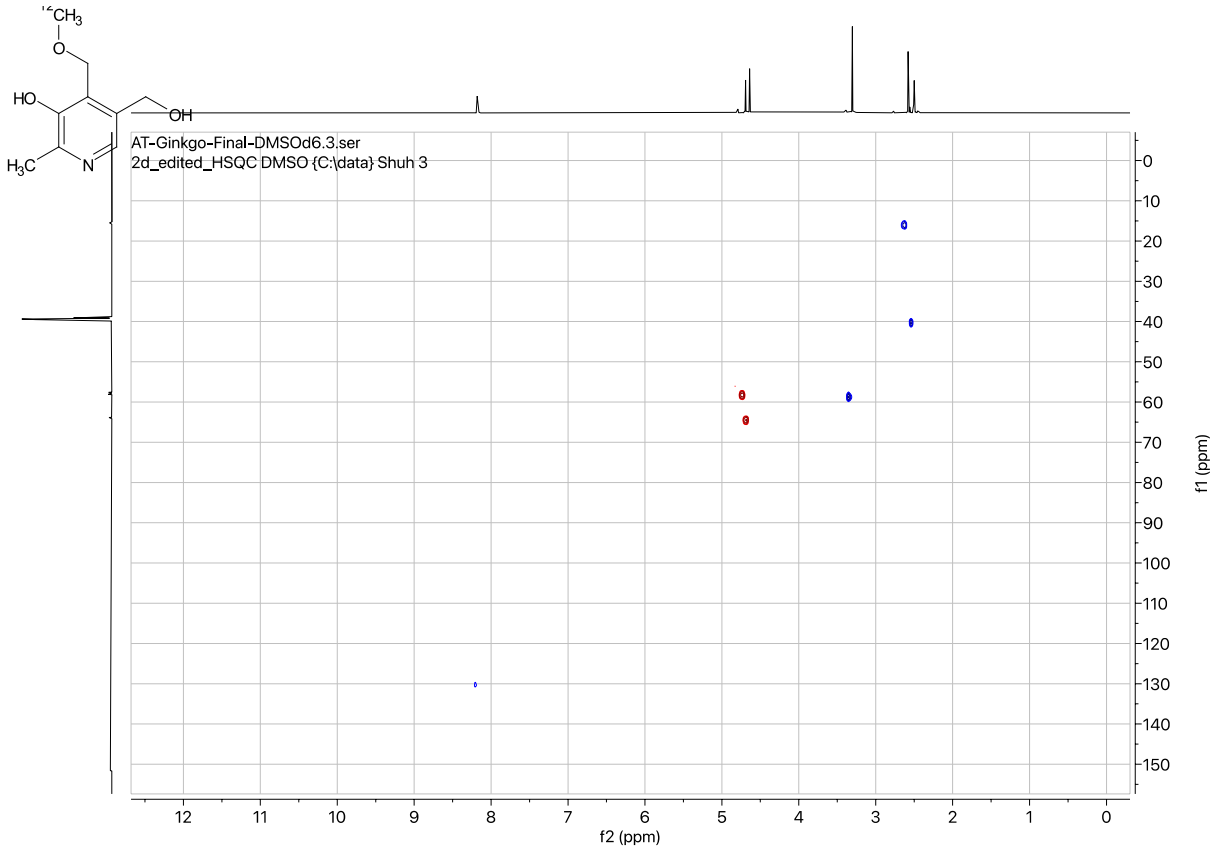

Figure S55. 2D-Edited HSQC NMR spectrum of Compound 38.

LC-MS Reaction Monitoring Traces

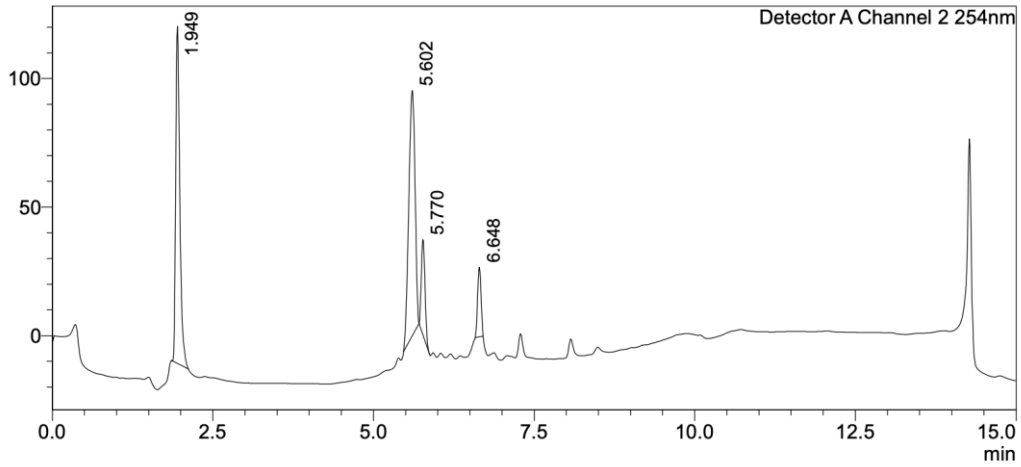

Figure S56. LC-MS UV-Chromatogram for the reaction of Compound 2.

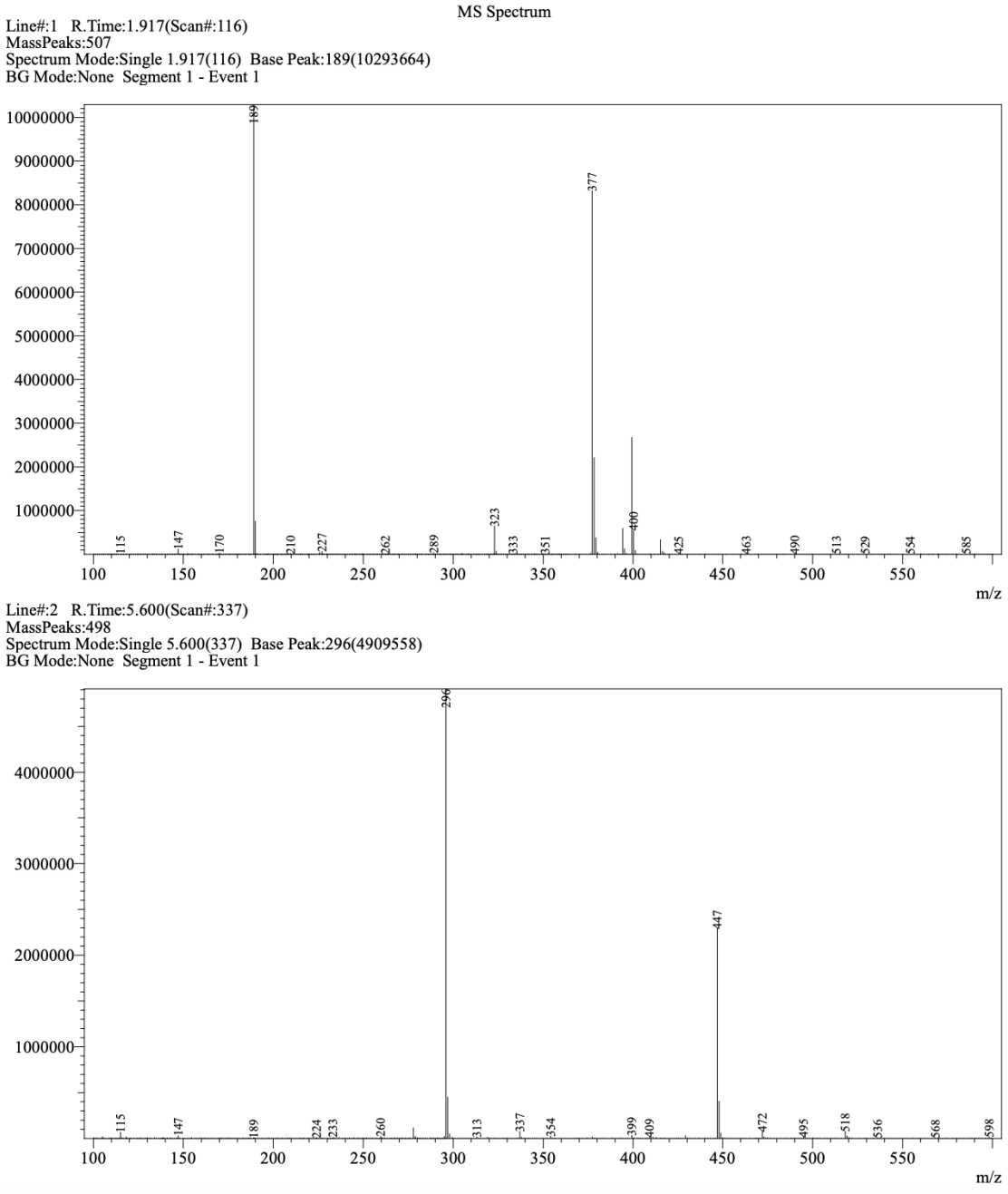

Figure S57. LC-MS Mass Spectrum for the reaction of Compound 2.

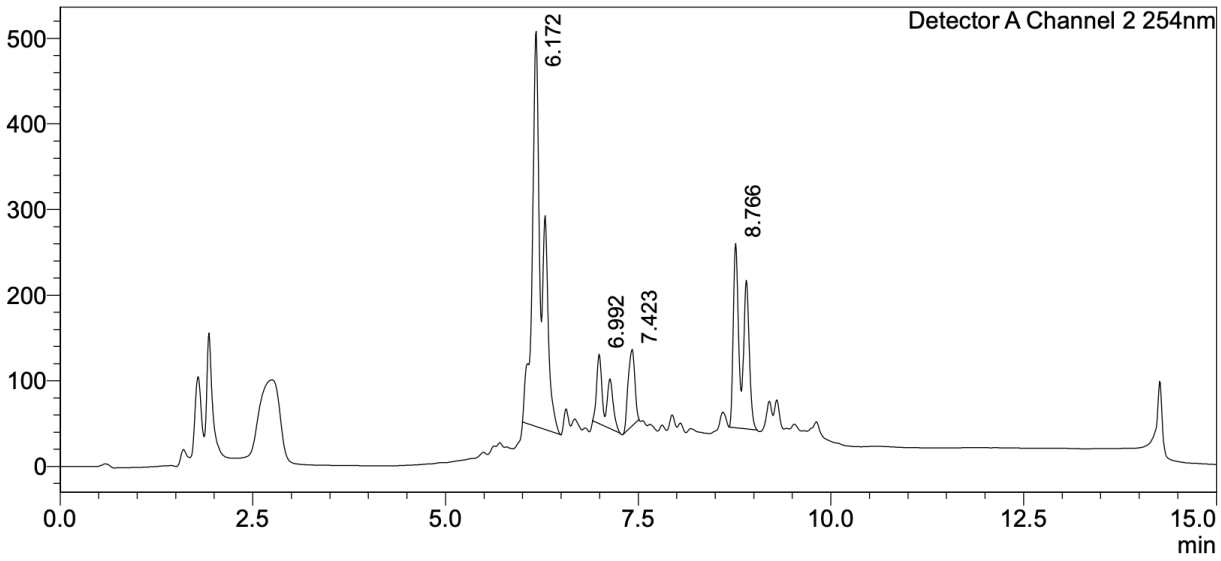

Figure S58. LC-MS UV-Chromatogram for the reaction of Compound 3.

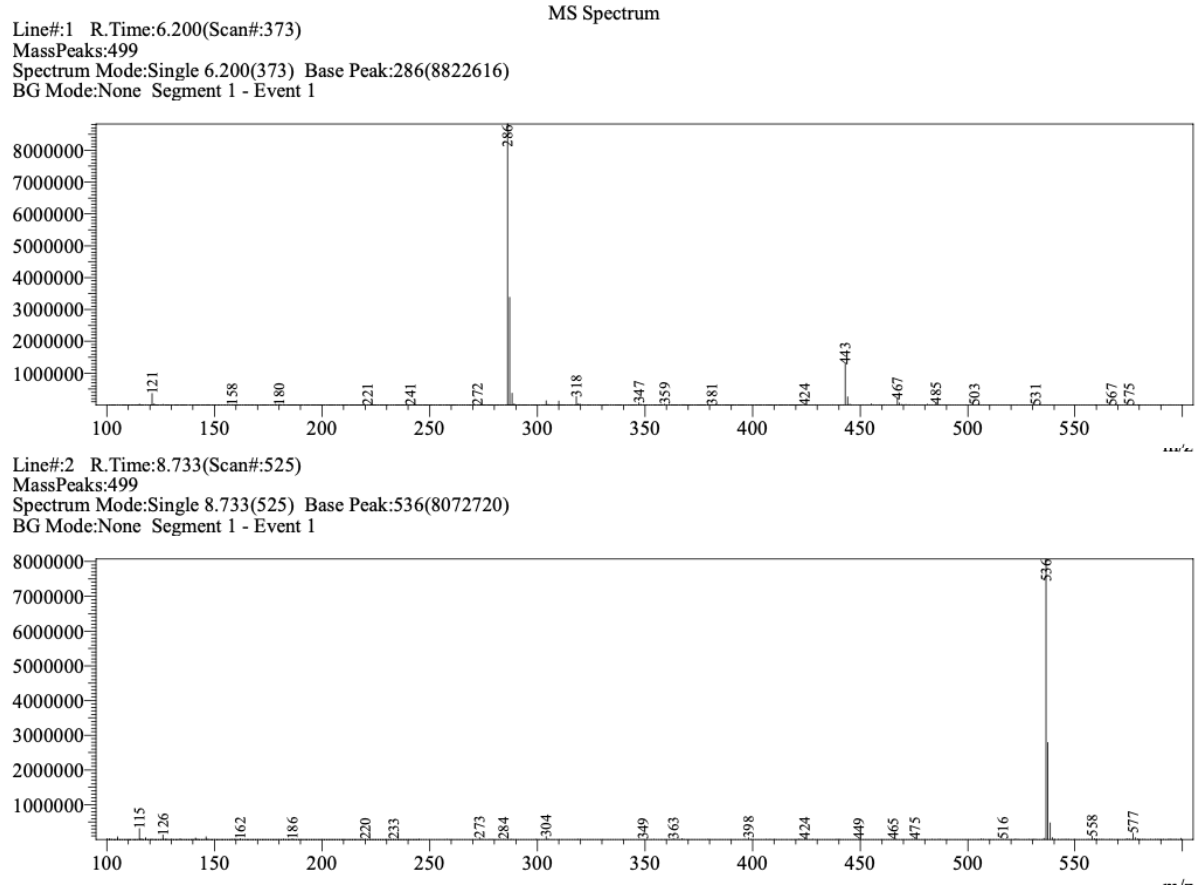

Figure S59. LC-MS Mass Spectrum for the reaction of Compound 3.

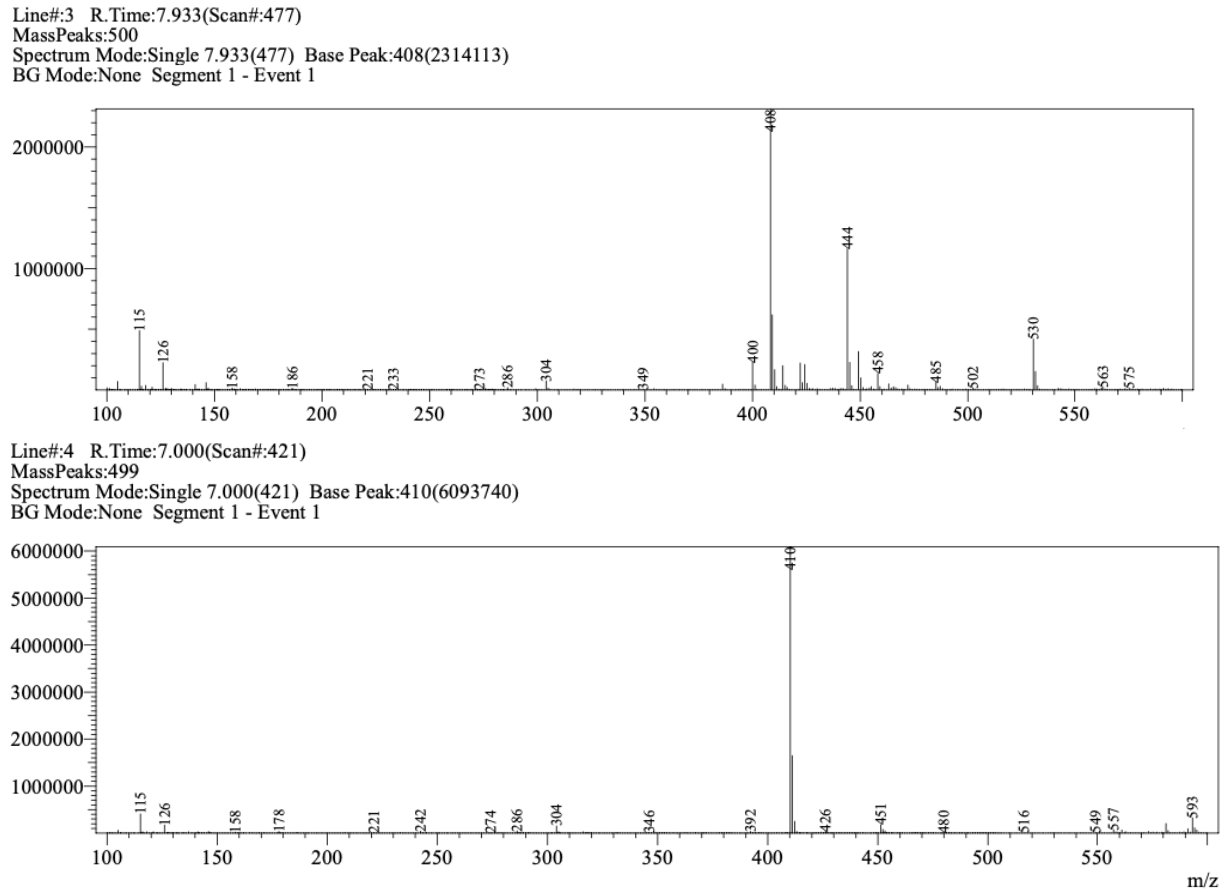

Figure S60. LC-MS Mass Spectrum for the reaction of Compound 3.

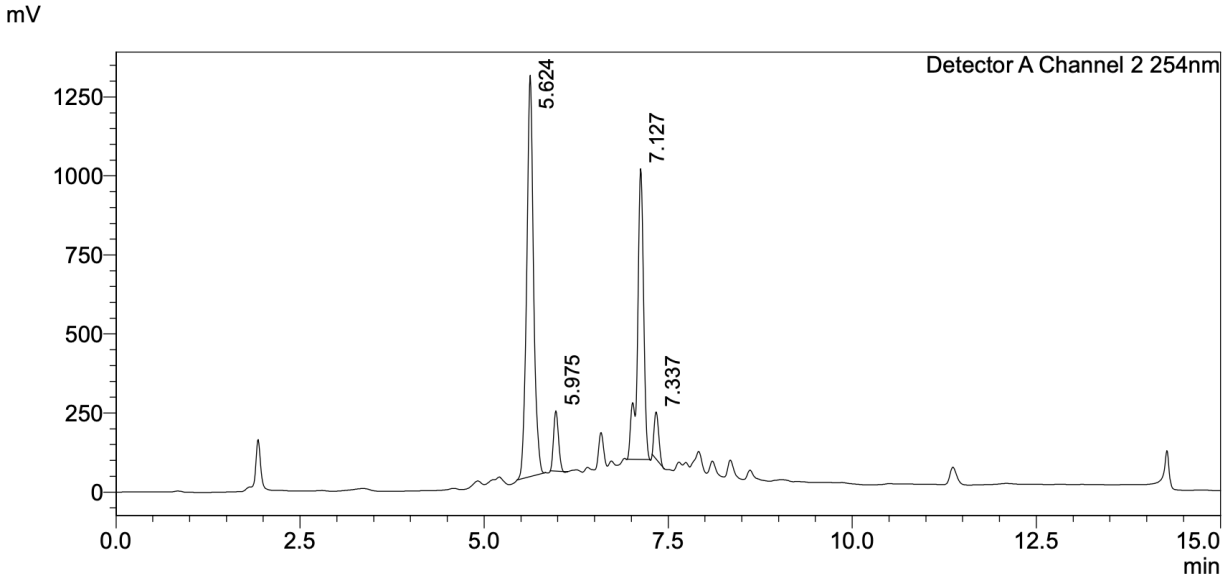

Figure S61. LC-MS UV-Chromatogram for the reaction of Compound 5.

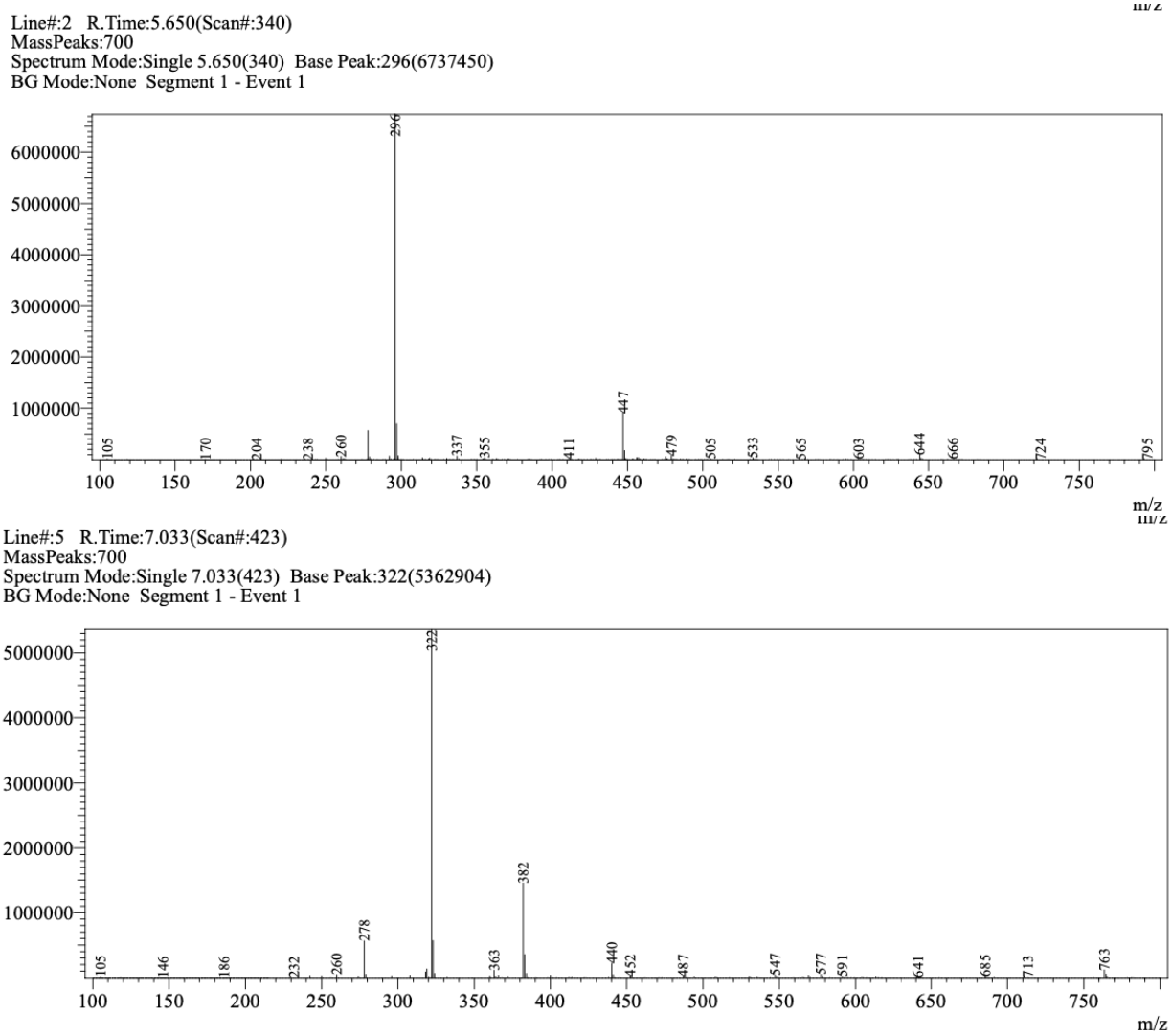

Figure S62. LC-MS Mass Spectrum for the reaction of Compound 5.

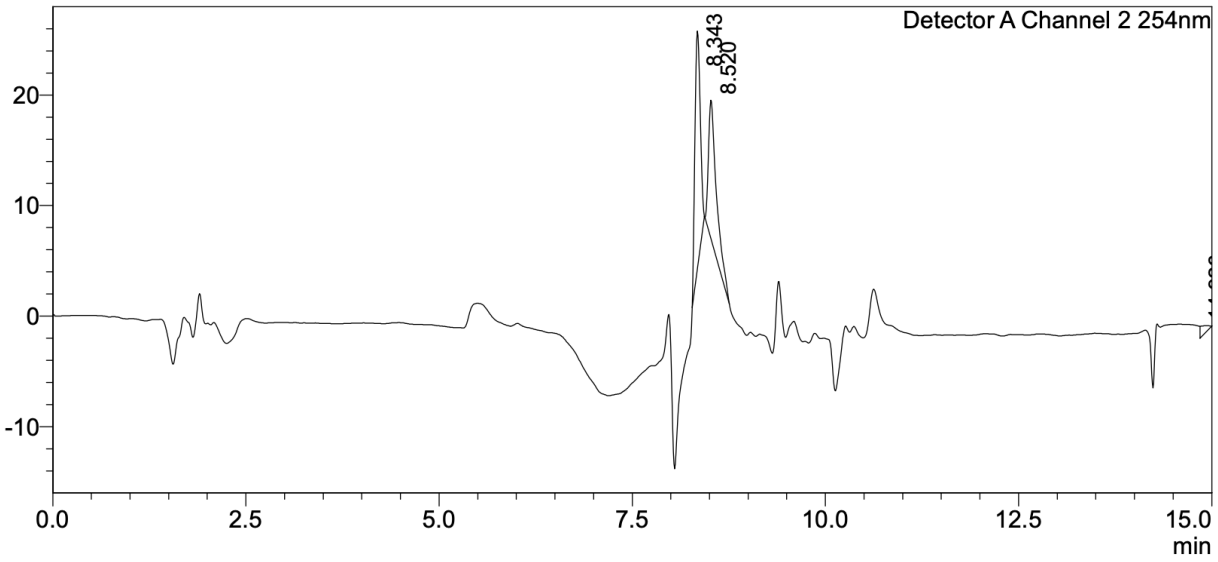

Figure S63. LC-MS UV-Chromatogram for the reaction of Compound 17.

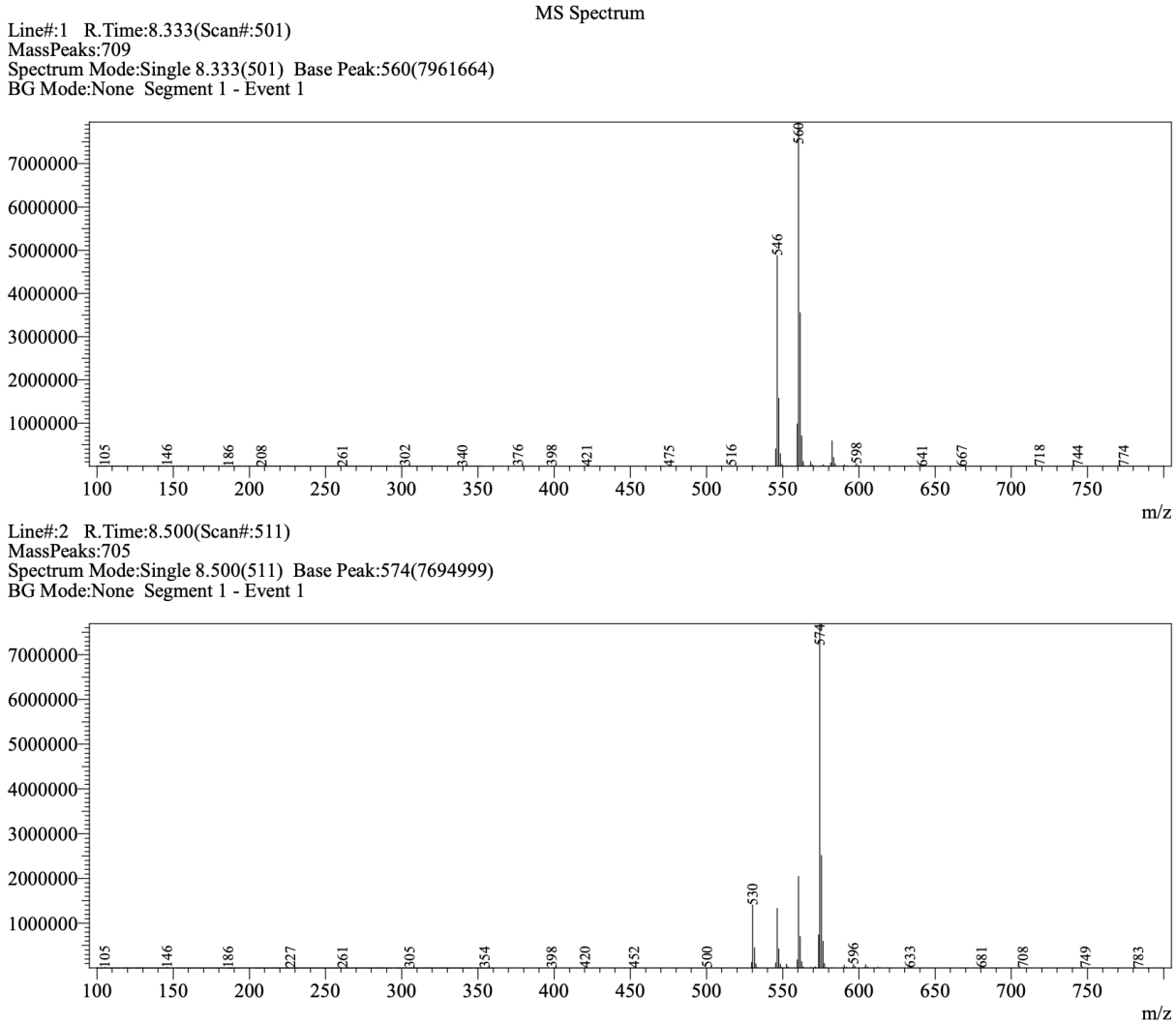

Figure S64. LC-MS Mass Spectrum for the reaction of Compound 17.

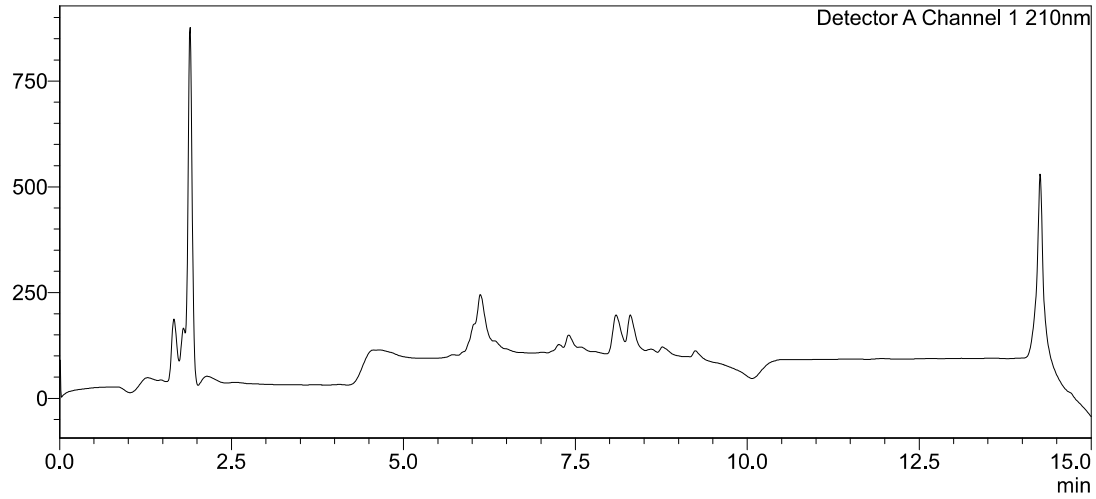

Figure S65. LC-MS UV-Chromatogram for the reaction of Compound 19.

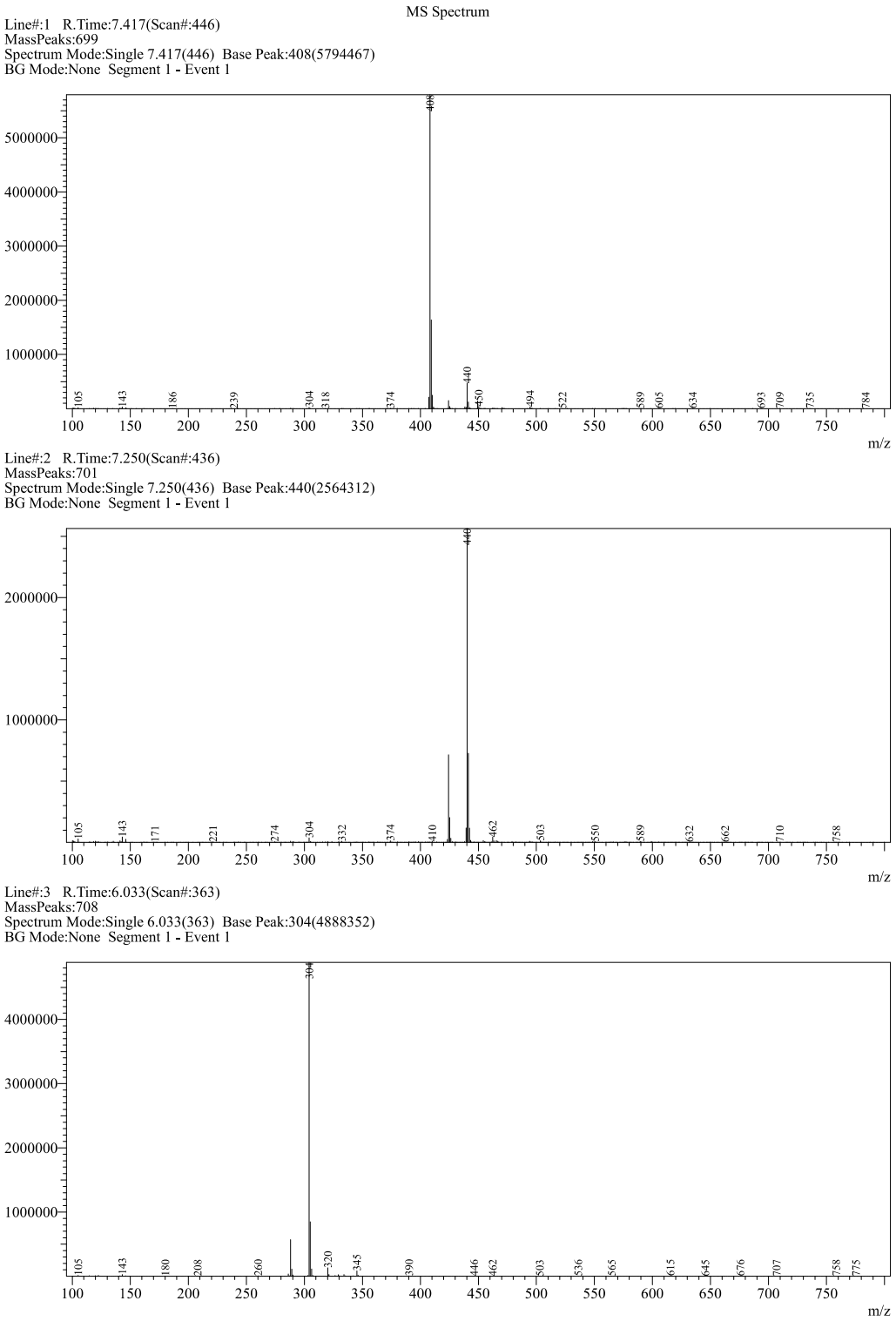

Figure S66. LC-MS Mass Spectrum for the reaction of Compound 19.

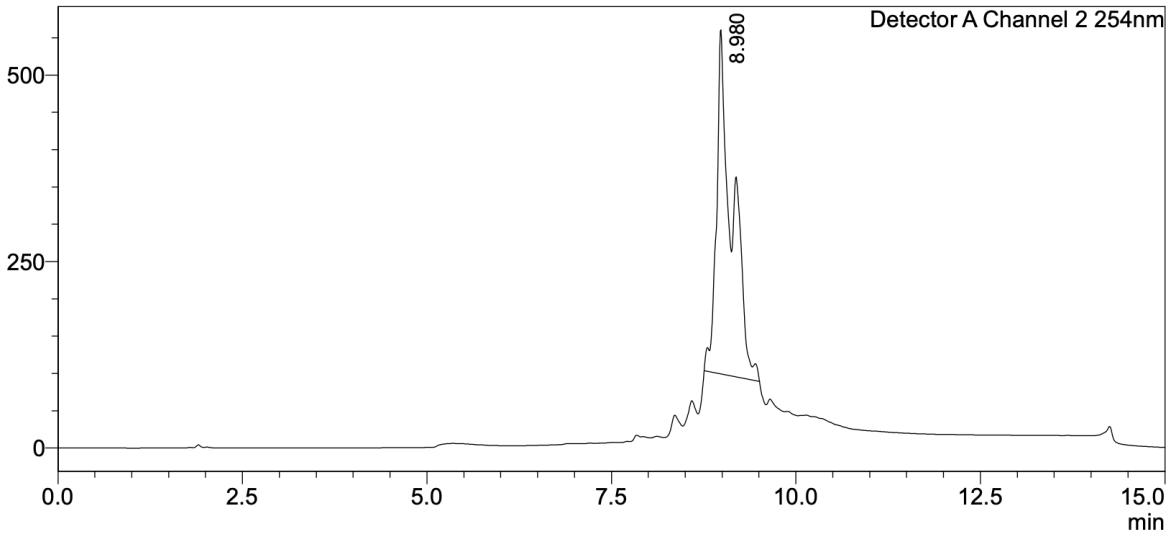

Figure S67. LC-MS UV-Chromatogram for the reaction of Compound 20.

MS Spectrum

Line#:1 R.Time:9.017(Scan#:542)
MassPeaks:699
Spectrum Mode:Single 9.017(542) Base Peak:558(6679328)
BG Mode:None Segment 1 - Event 1

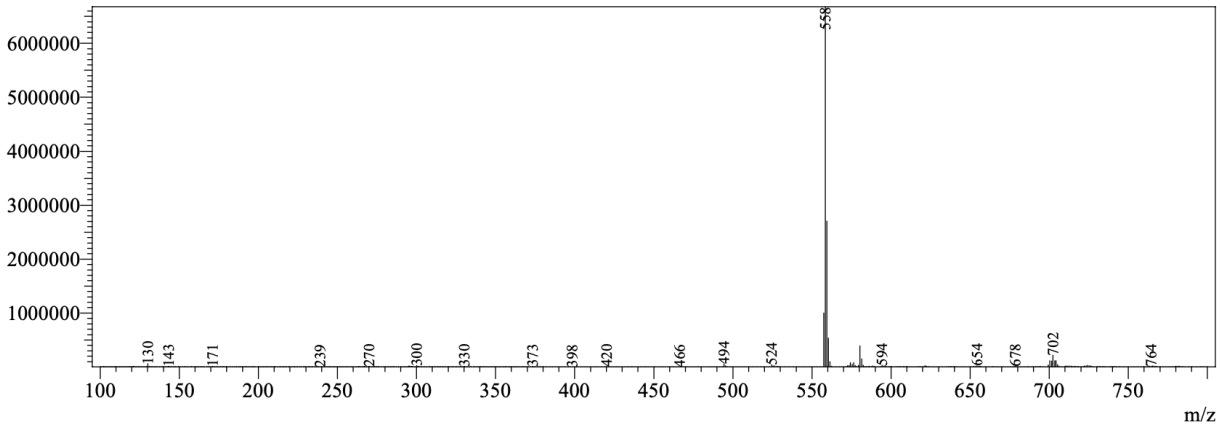

Figure S68. LC-MS Mass Spectrum for the reaction of Compound 20.

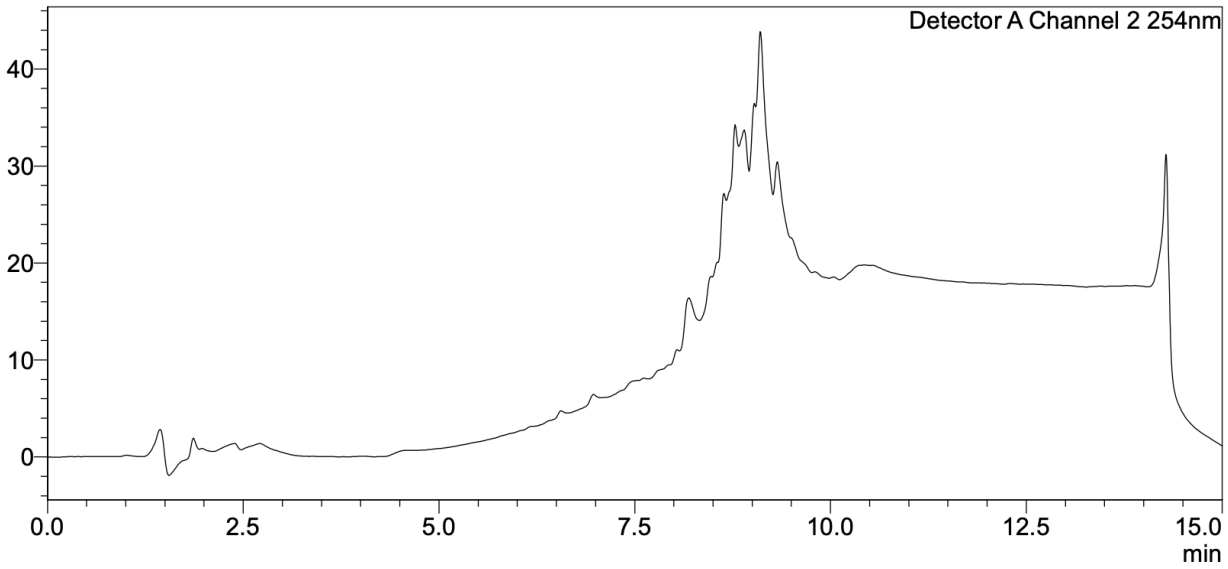

Figure S69. LC-MS UV-Chromatogram for the reaction of Compound 21.

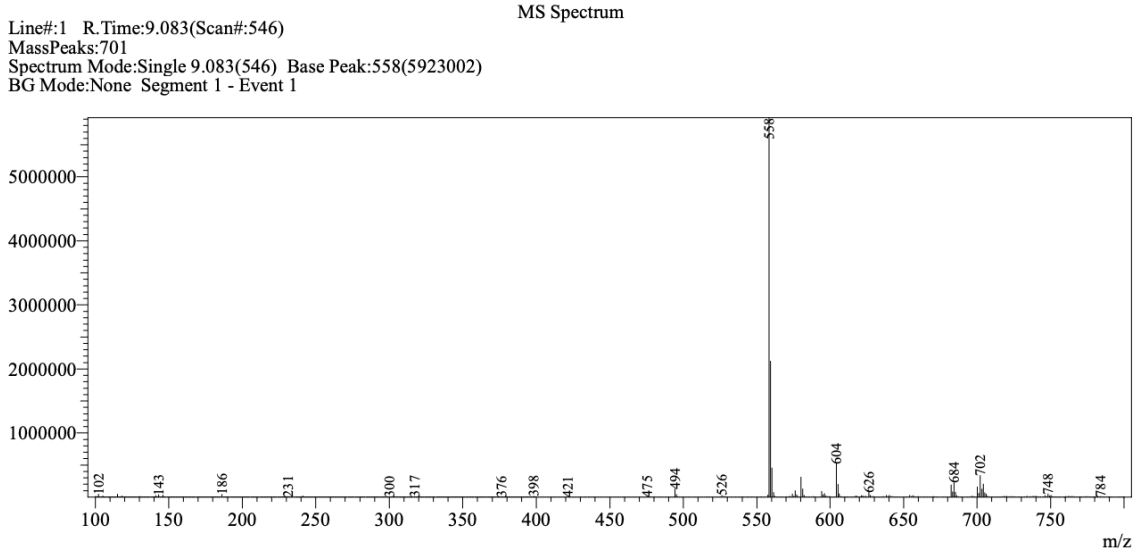

Figure S70. LC-MS Mass Spectrum for the reaction of Compound 21.

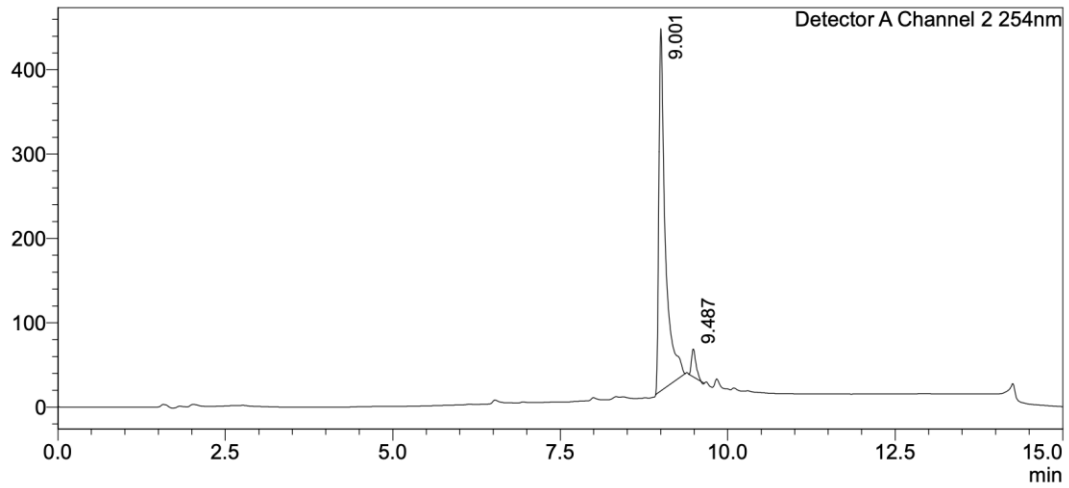

Figure S71. LC-MS UV-Chromatogram for the reaction of Compound 22.

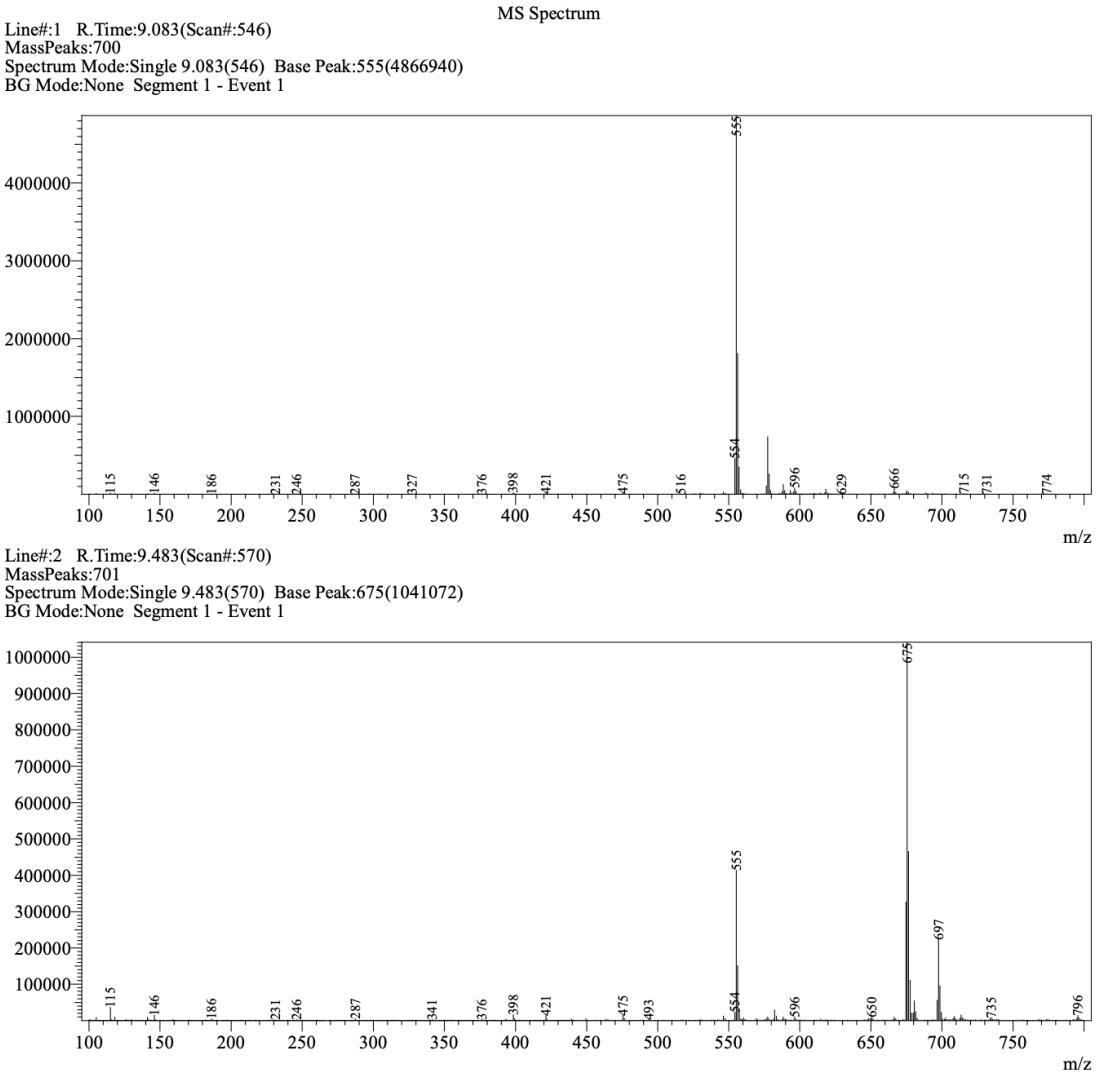

Figure S72. LC-MS Mass Spectrum for the reaction of Compound 22.

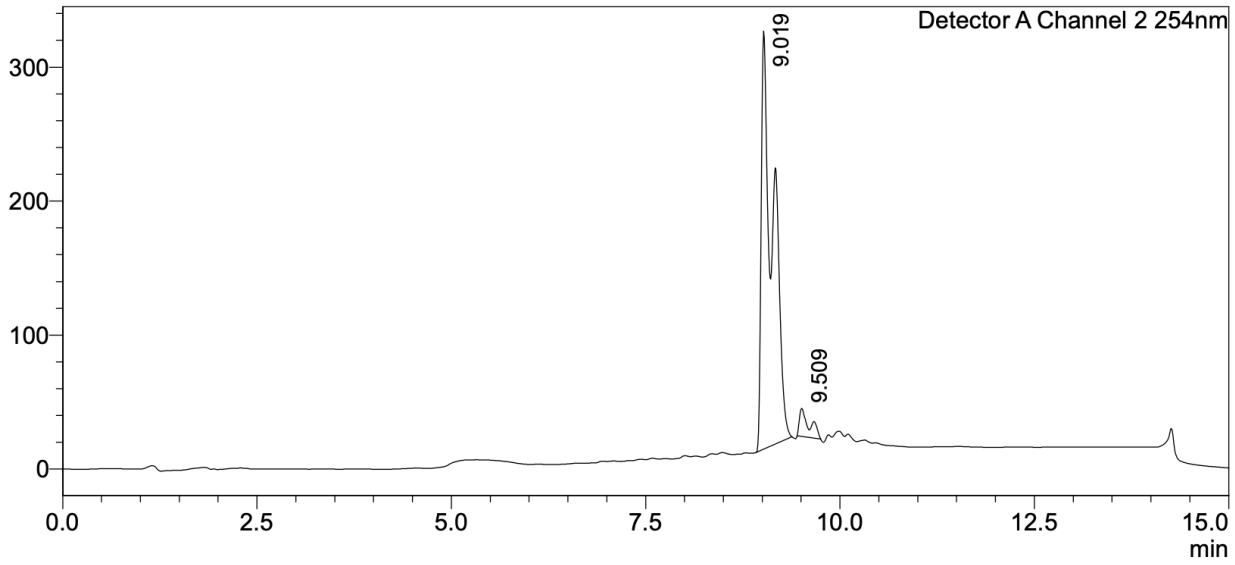

Figure S73. LC-MS UV-Chromatogram for the reaction of Compound 23.

MS Spectrum

Line#:1 R.Time:9.117(Scan#:548)
MassPeaks:699
Spectrum Mode:Single 9.117(548) Base Peak:588(3775401)
BG Mode:None Segment 1 - Event 1

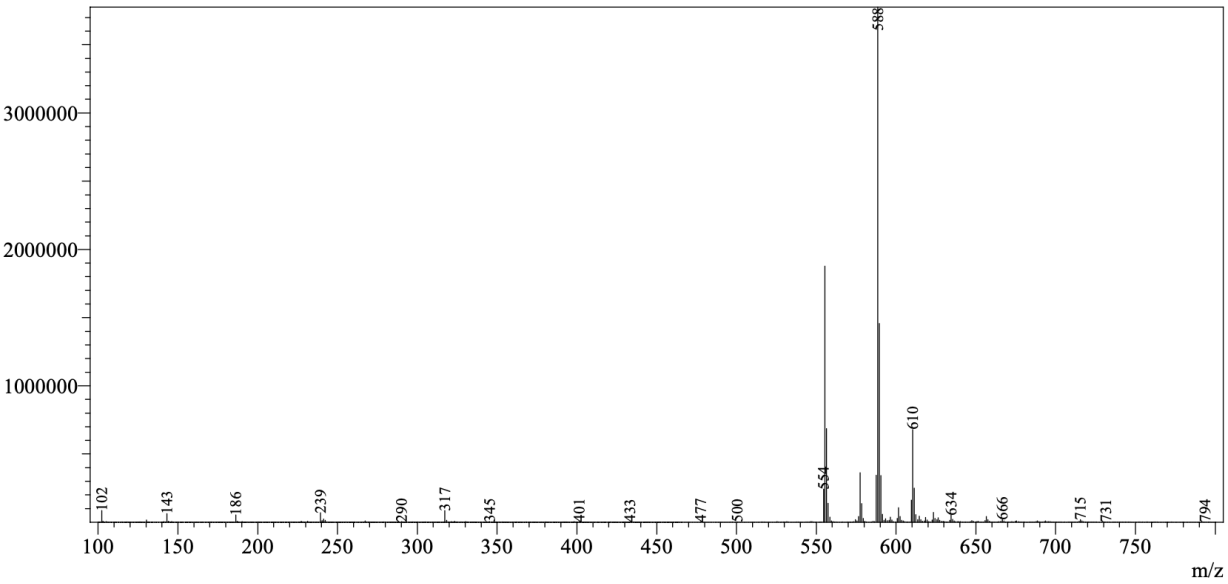

Figure S74. LC-MS Mass Spectrum for the reaction of Compound 23.

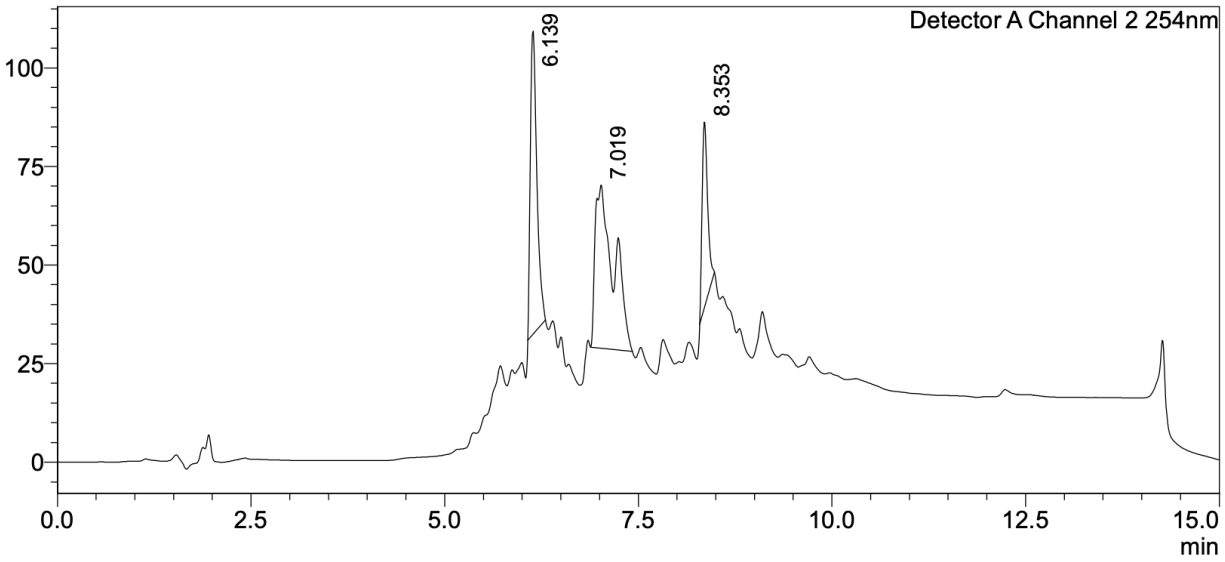

Figure S75. LC-MS UV-Chromatogram for the reaction of Compound i.

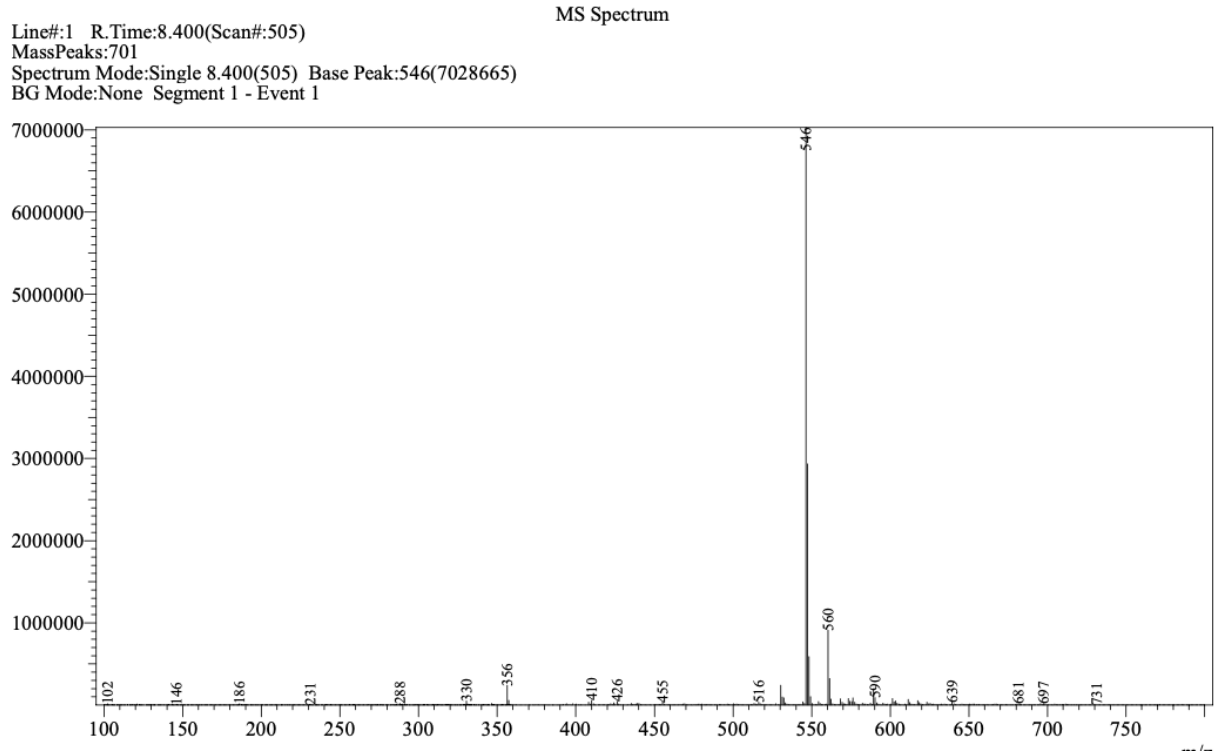

Figure S76. LC-MS Mass Spectrum for the reaction of Compound i.

Line#:2 R.Time:7.200(Scan#:433)
MassPeaks:703
Spectrum Mode:Single 7.200(433) Base Peak:410(5060953)
BG Mode:None Segment 1 - Event 1

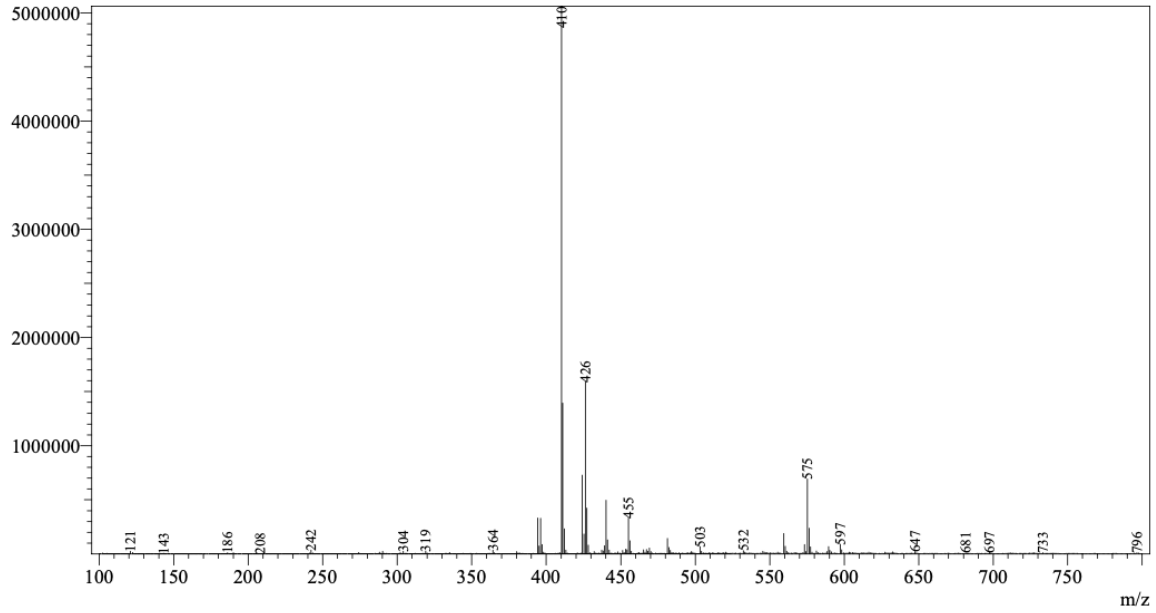

Line#:3 R.Time:6.967(Scan#:419)
MassPeaks:701
Spectrum Mode:Single 6.967(419) Base Peak:426(6425213)
BG Mode:None Segment 1 - Event 1

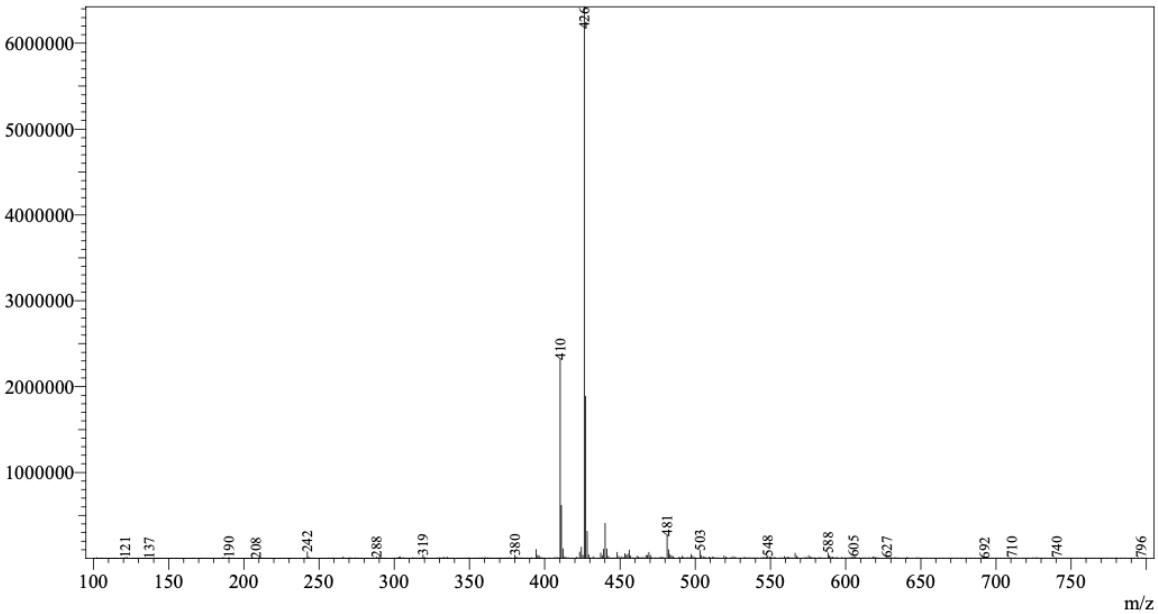

Figure S77. LC-MS Mass Spectrum for the reaction of Compound i.

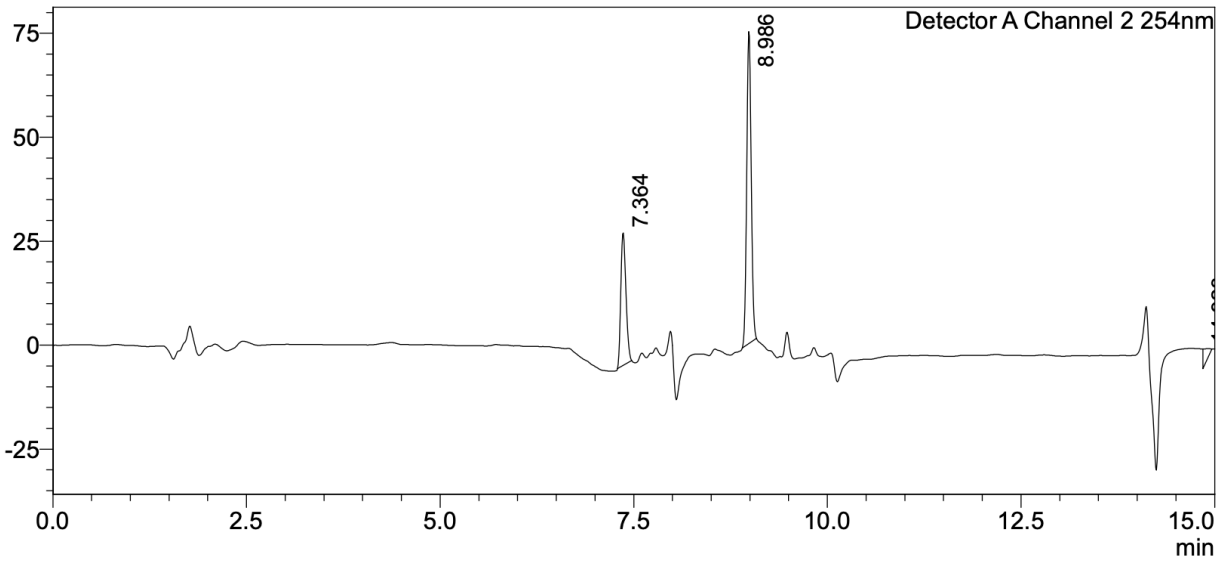

Figure S78. LC-MS UV-Chromatogram for the reaction of Compound 24.

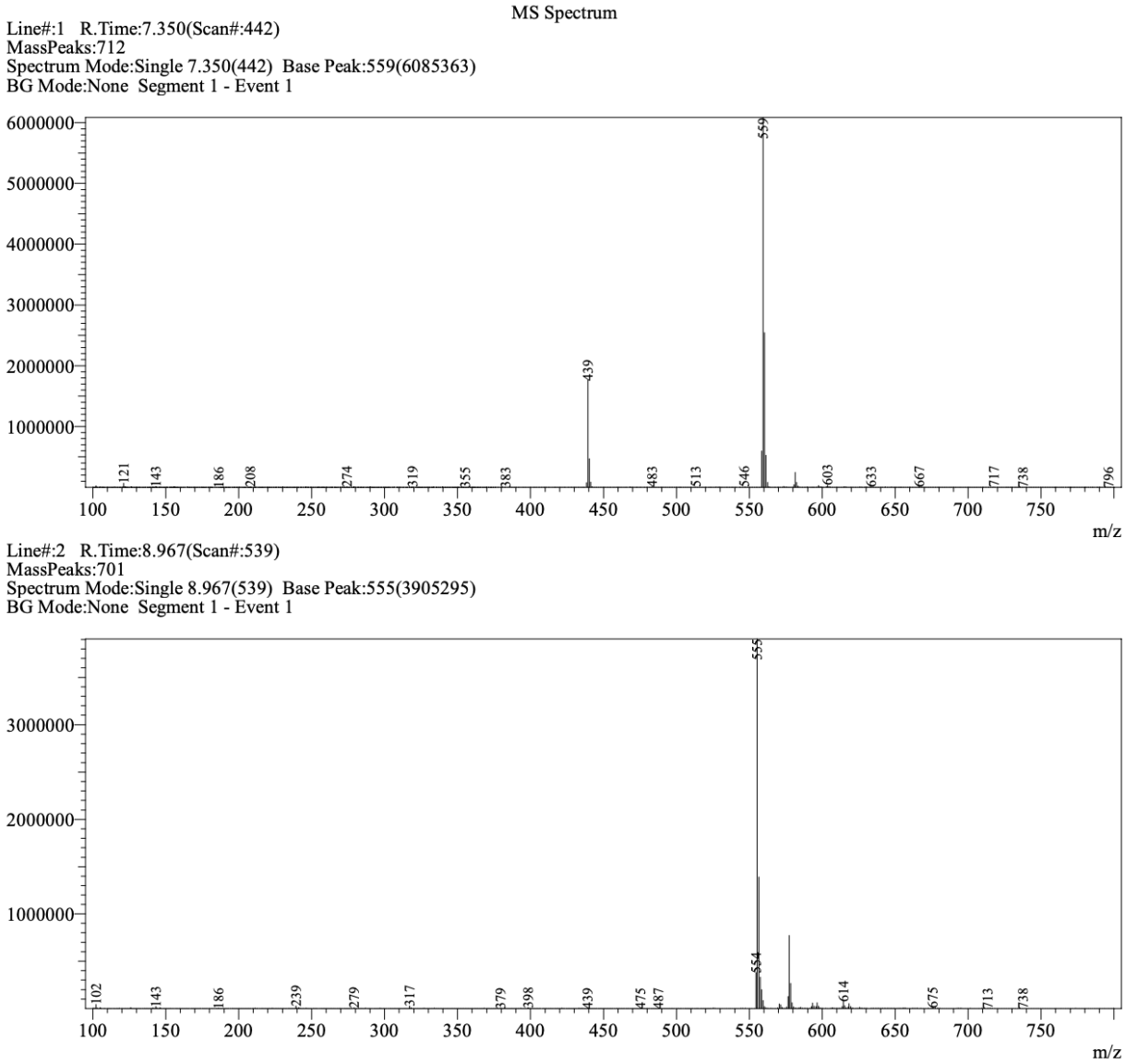

Figure S79. LC-MS Mass Spectrum for the reaction of Compound 24.

LC-MS Metabolomics Raw Compiled Data

Name	Formula	Mass	M-H	RT (Min)	MSMS	Control	Treated	Comments
4-pyridoxic acid	C8H9NO4	183.0532	182.0459	1.2	Yes (No STD)	Present	Present	Small peak present in samples but low Signal to noise ratio. Small peak present in all standards (Degradation by-product?) Need STD to confirm
Fluoro 4-pyridoxic acid	F1C8H8NO4	201.0437	200.0365	0.96	May be yes (No STD)	-	Present	Small peak present in 6 fluoro-pyridoxine standard. May be based on MSMS assumption Need STD to confirm
Pyridoxine	C8H11NO3	169.0739	168.0666	1.47	Yes	Present	Present	Small unlabled fraction present in 6 FluoroPyridoxine standards.
Fluoro pyridoxine	F1C8H10NO3	187.0645	186.0572	0.97	Yes	-	Present	Use 0.1 uM standard and 1/100 dilution for samples.
Pyridoxal	C8H9NO3	167.0582	166.051	1.54	Yes	-	-	Not detected in samples
Fluoro Pyridoxal	F1C8H8NO3	185.0488	184.0415	1	May be yes	-	Present	Small peak present in 6 fluoro-pyridoxine standard. Need STD to confirm
Pyridoxamine	C8H12N2O2	168.0899	167.0826	3.89	Yes	-	-	Not detected in samples
Fluoro Pyridoxamine	F1C8H11N2O2	186.0805	185.0732	?	No STD	-	-	Not detected in samples.
Pyridoxine 5'-phosphate	C8H12NO6P	249.0402	248.0329	?	No STD	-	-	Not detected in samples.
Fluoro Pyridoxine 5'-phosphate	F1C8H11NO6P	267.0308	266.0235	5.27	May be yes (No STD)	-	Present	Small peak present in all treated samples but very low signal. Need standards to confirm.
Pyridoxal 5'-phosphate	C8H10NO6P	247.0246	246.0173	7.44	Yes	-	-	Detected at 7.45 min in individual standard but bad peak shape. Carry over in the next running standards, blanks, and first samples. Not detected in samples.
Fluoro Pyridoxal 5'-phosphate	F1C8H9NO6P	265.0152	264.0079	?	No STD	-	-	Not detected in samples.
Pyridoxamine 5'-phosphate	C8H13N2O5P	248.0562	247.0489	5	MSMS very noisy (no STD)	Present	Present	Peak present in samples Need standards for confirmation.
Fluoro Pyridoxamine 5'-phosphate	F1C8H12N2O5P	266.0468	265.0395	?	No STD	-	-	Not detected in samples.

Figure S80. Compiled metabolomics MS/MS data for C_6-fluoro pyridoxine. Chemical name, formulas, masses, MS/MS matching, cell lines, and ionization mode are reported for each metabolic product of the standard.

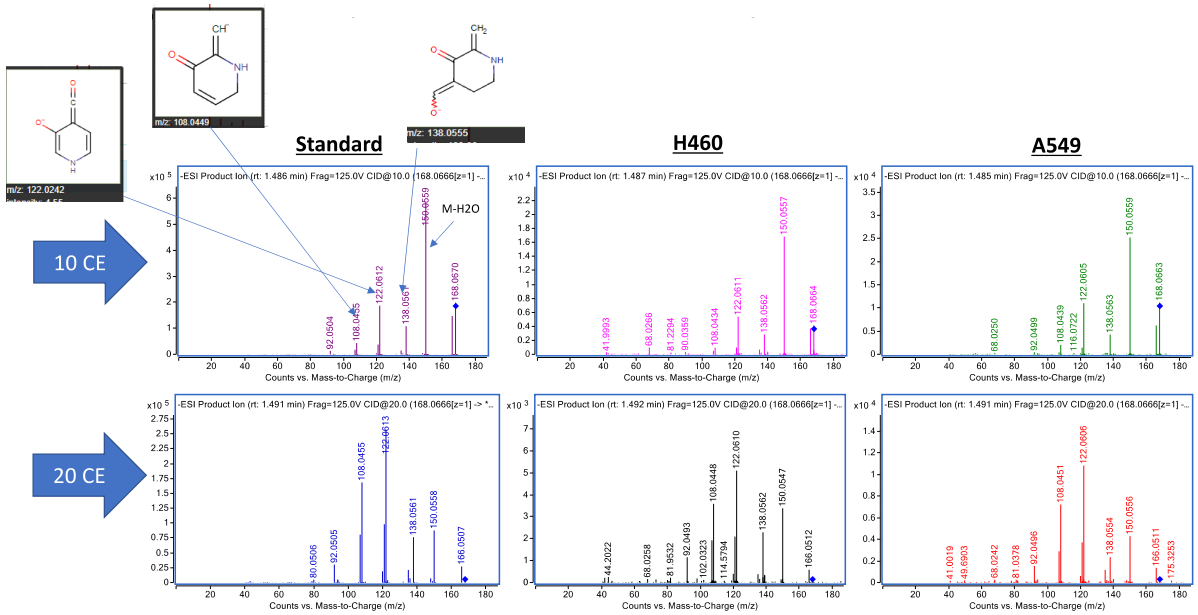

Figure S81. Pyridoxine standard MS/MS spectra. Analysis was performed using negative electrospray ionization (-ESI). Non-enzymatic product, H460 human non-small cell lung cancer cells (large cell carcinoma), and A549 squamous adenocarcinomic human lung alveolar basal epithelial cells were tested for presence of product. Fragmentation of ions utilized collision induced dissociation (CID) at increasing collision energy (CE), which refers to the rate of acceleration as the ions enter the quadrupole, promoting higher rates of fragmentation. Common fragments are shown.

Name	Formula	Mass	M+H	M-H	RT	MSMS	A- cells	H cells	ESI (+)	ESI (-)
Pyridoxal	C8H9NO3	167.0582	168.0655	166.0510	1.54	MSMS confirmed (STD)	Peak present in all samples Low in controls	Peak present in all samples Low in controls	Detected in STD mix Peak intensity better in positive	Detected in STD mix
Pyridoxamine	C8H12N2O2	168.0899	169.0972	167.0826	3.89	-	Not detected	Not detected	Detected in STD mix	Detected in STD mix
Pyridoxine	C8H11NO3	169.0739	170.0812	168.0666	1.47	MSMS confirmed (STD)	Peak present in all samples Saturated thus injected x100 dilution	Peak present in all samples Saturated thus injected x100 dilution	Detected in STD mix	Detected in STD mix
4-pyridoxic acid	C8H9NO4	183.0532	184.0604	182.0459	1.2 (?)	MSMS confirmed (no STD)	Peak present in treated cells only Need standard for 100% confirmation	Peak present in treated cells only Need standard for 100% confirmation	Not detected in +ESI	Detected in STD mix
O-MethylPyridoxal	C9H11NO4	197.0688	198.0761	196.0615	1.39 (?)	MSMS confirmed (no STD)	Peak present in all samples, low in controls Need standard for 100% confirmation	Peak present in all samples, low in controls Need standard for 100% confirmation	Detected in Samples Peak intensity better in positive	Detected in Samples
O-MethylPyridoxamine	C9H14N2O3	198.1004	199.1077	197.0932	4.7 (?)	May be, MSMS confirmed (no STD)	Detected in +ESI mode in treated cells	Detected in +ESI mode in treated cells	Peak detected in sample	Not detected
O-MethylPyridoxine	C9H13NO4	199.0845	200.0917	198.0772	1.37	MSMS confirmed (STD)	Peak present in all samples Saturated thus injected x100 dilution Still saturated signal	Peak present in all samples Saturated thus injected x100 dilution Still saturated signal	Detected in STD mix	Detected in STD mix
Pyridoxal 5'-phosphate	C8H10NO6P	247.0246	248.0319	246.0173	7.44	-	Not detected	Not detected	Not detected	Not detected
Pyridoxamine 5'-phosphate	C8H13N2O5P	248.0562	249.0635	247.0489	4.8 (?)	MSMS does not match with online database (no STD)	Not detected	Peak present in all samples Low intensity MSMS does not match Need standard for 100% confirmation	Detected in samples need MSMS to confirm	Detected in samples but not confirmed
Pyridoxine 5'-phosphate	C8H12NO6P	249.0402	250.0475	248.0329	?		Not detected	Not detected	Not detected	Not detected
O-Methyl Pyridoxal 5P	C9H12NO7P	277.0351	278.0424	276.0279	6.47 (?)	no MSMS spectra generated (no STD)	Not detected	Peak present in all samples Low intensity MSMS does not match Need standard for 100% confirmation	Not detected	Detected in samples but not confirmed
O-MethylPyridoxamine 5P	C9H15N2O6P	278.0668	279.0740	277.0595	1.16 (?)	-	Not detected	Not detected	Not detected	Not detected
O-MethylPyridoxine 5P	C9H14NO7P	279.0508	280.0581	278.0435	6.23 (?)	MSMS confirmed (no STD)	Peak present in treated cells only Need standard for 100% confirmation	Peak present in treated cells only Need standard for 100% confirmation	Not detected	Detected in Samples

Figure S82. Compiled metabolomics MS/MS data for 2'-*O*-methyl pyridoxine. Chemical name, formulas, masses, MS/MS matching, cell lines, and ionization mode are reported for each metabolic product of the standard.

RadioHPLC Analytical Cold Standard UV Chromatograms

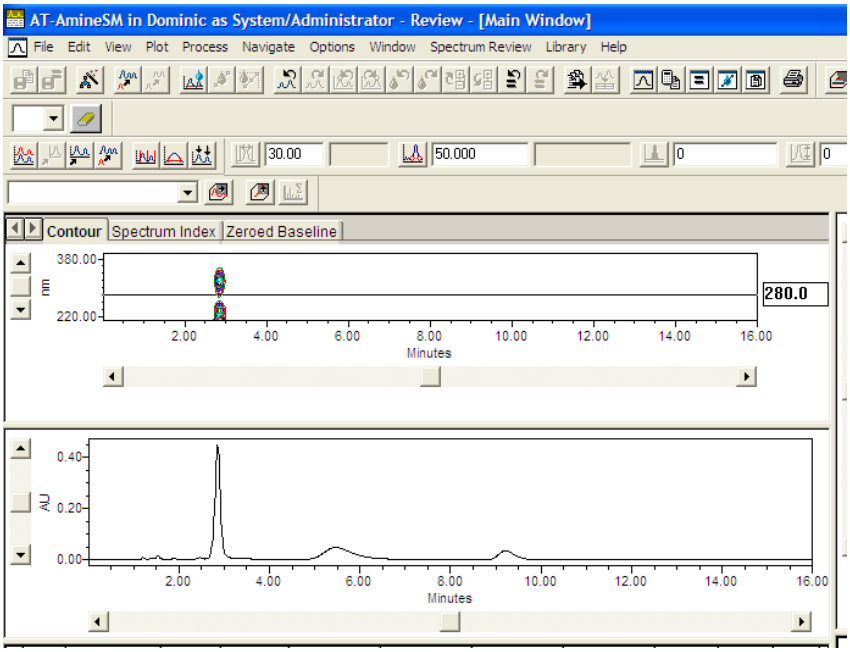

Figure S83. UV Chromatogram for cold-standard for C_6-amino pyridoxine Precursor (7) on Analytical RadioHPLC.

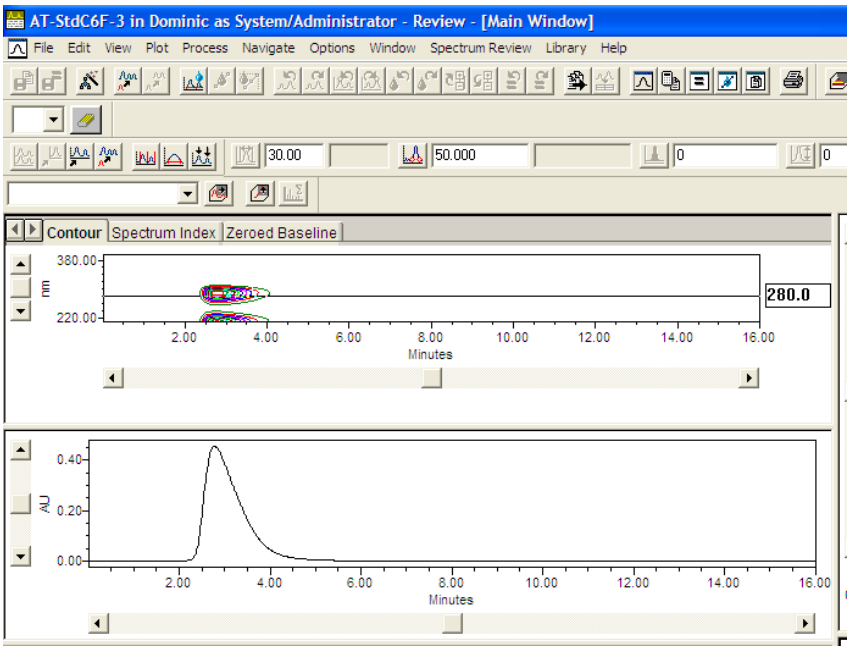

Figure S84. UV Chromatogram for cold-standard for C_6-fluoro (8) on Analytical RadioHPLC.

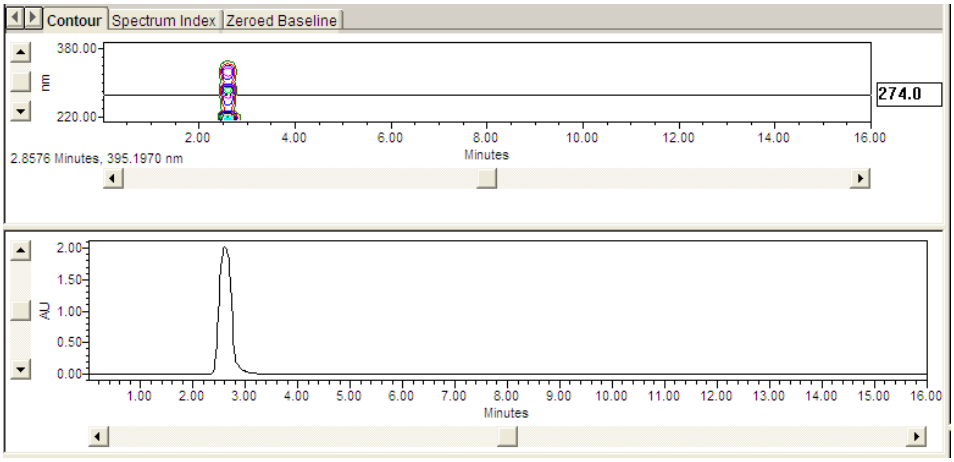

Figure S85. UV Chromatogram for cold-standard for unmodified pyridoxine on Analytical RadioHPLC.

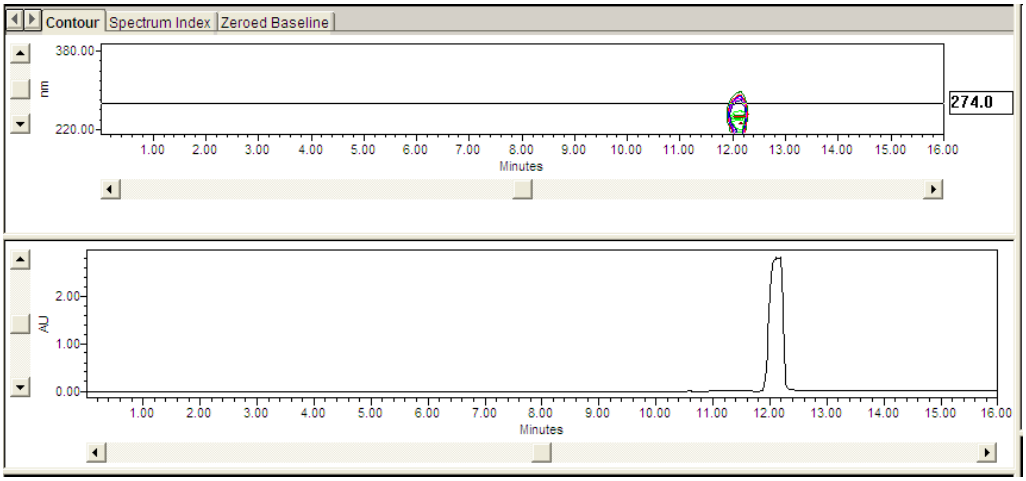

Figure S86. UV Chromatogram for cold-standard for unmodified methyl iodide on Analytical RadioHPLC.

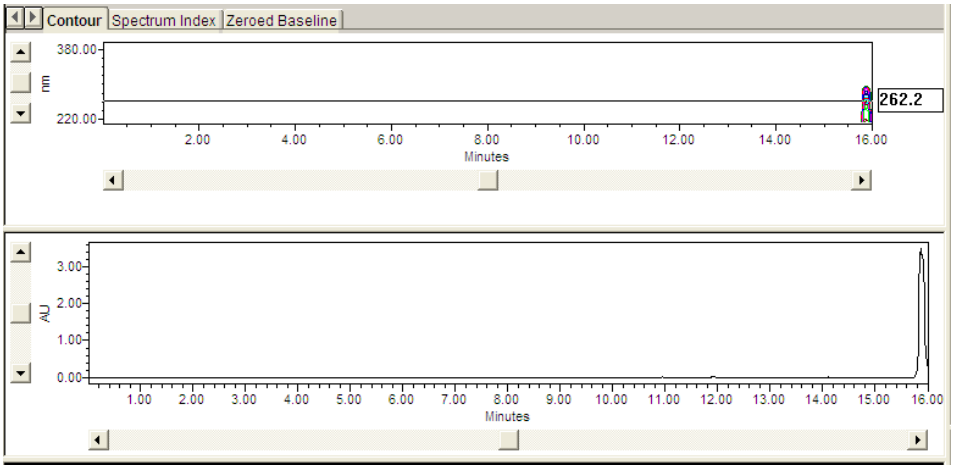

Figure S87. UV Chromatogram for cold-standard for 2'-*O*-Benzyl OH precursor (11) on Analytical RadioHPLC.

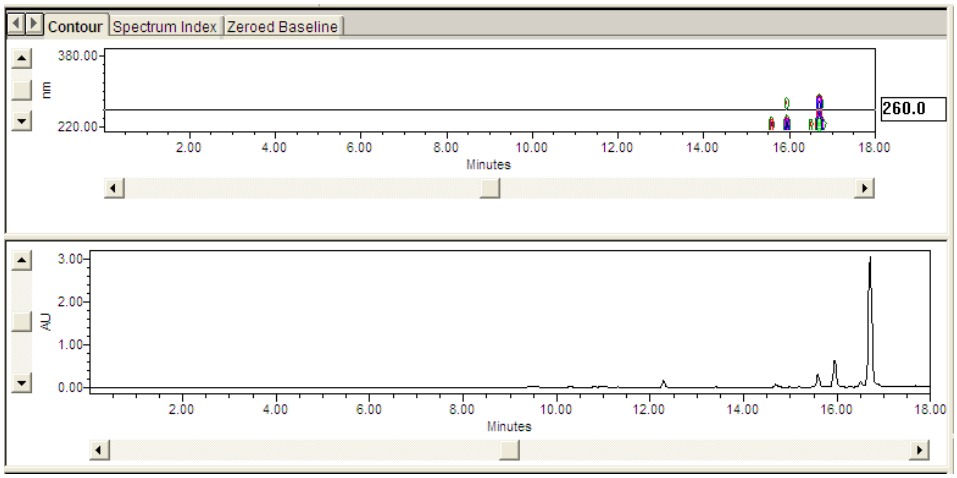

Figure S88. UV Chromatogram for cold-standard for 2'-*O*-methyl pyridoxine PMB protected intermediate (31) on Analytical RadioHPLC.

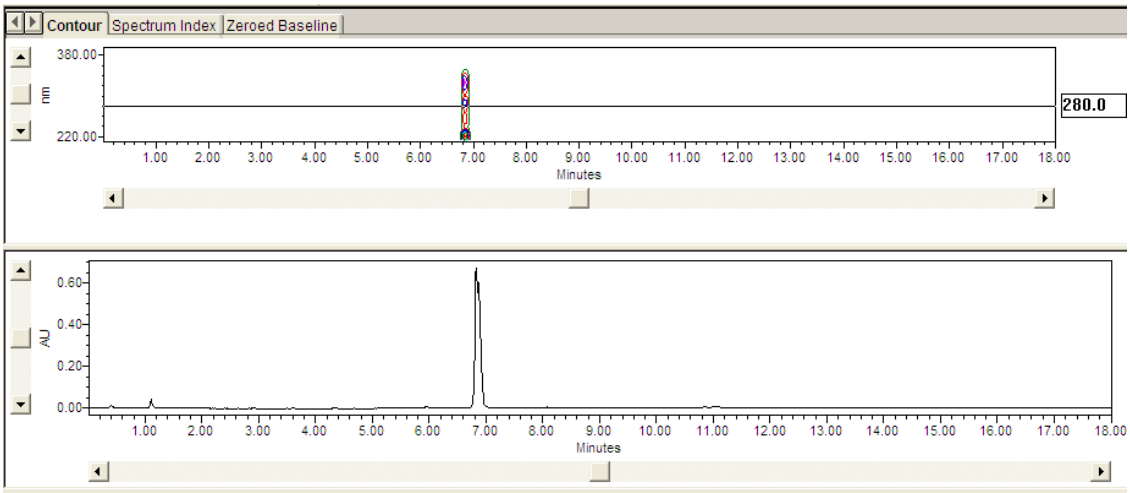

Figure S89. UV Chromatogram for cold-standard for 2'-*O*-methyl pyridoxine final product (32) on Analytical RadioHPLC.

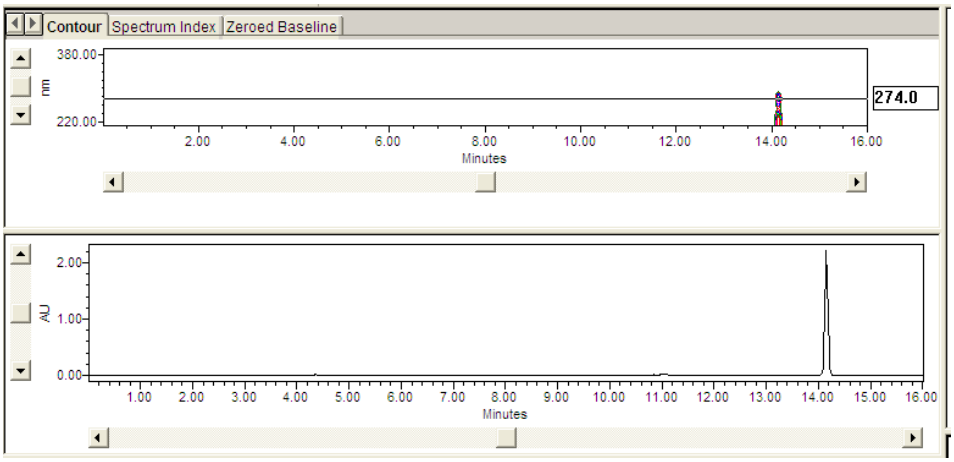

Figure S90. UV Chromatogram for cold-standard for 4'-*O*-benzyl OH precursor (36) on Analytical RadioHPLC.

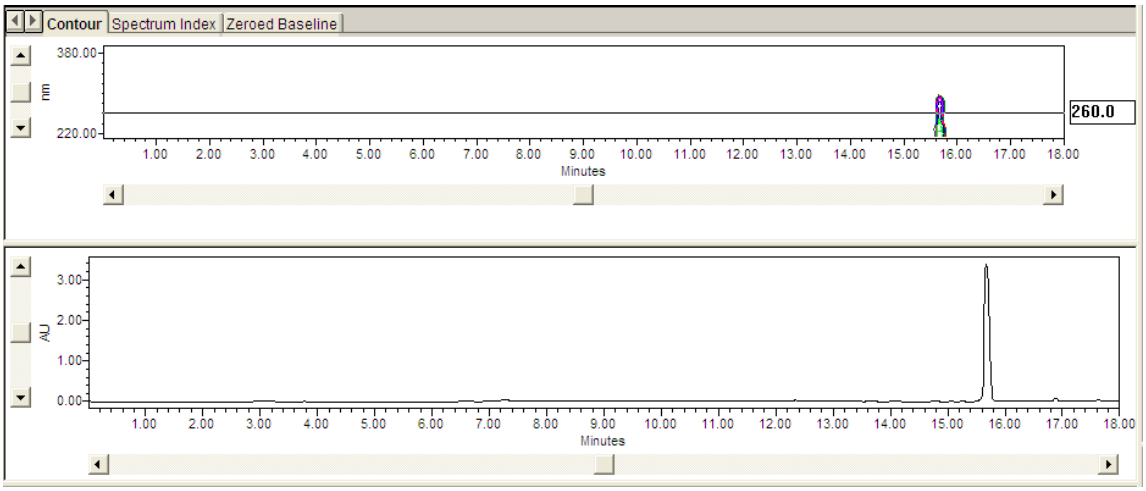

Figure S91. UV Chromatogram for cold-standard for 4'-*O*-methyl pyridoxine PMB protected Intermediate (37) on Analytical RadioHPLC.

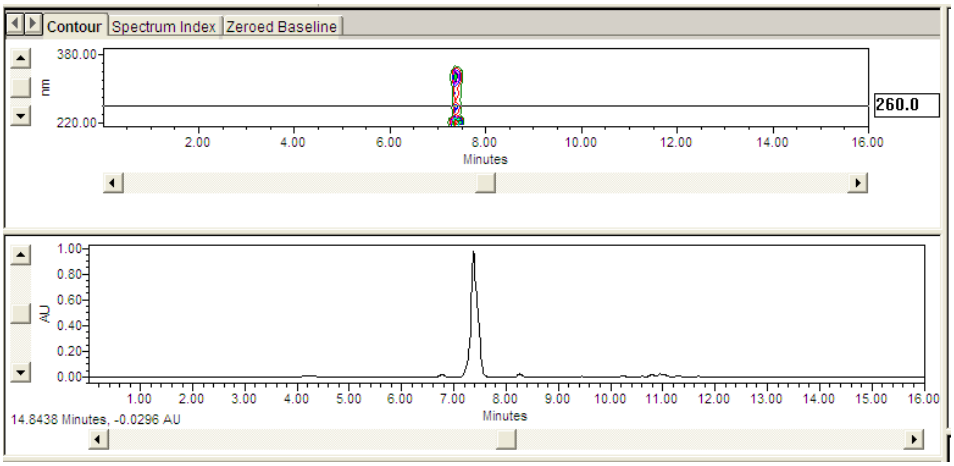

Figure S92. UV Chromatogram for cold-standard for 4'-*O*-methyl pyridoxine Product - Ginkgotoxin (38) on Analytical RadioHPLC.

Semi-Prep HPLC Analytical Cold Standard UV Chromatograms

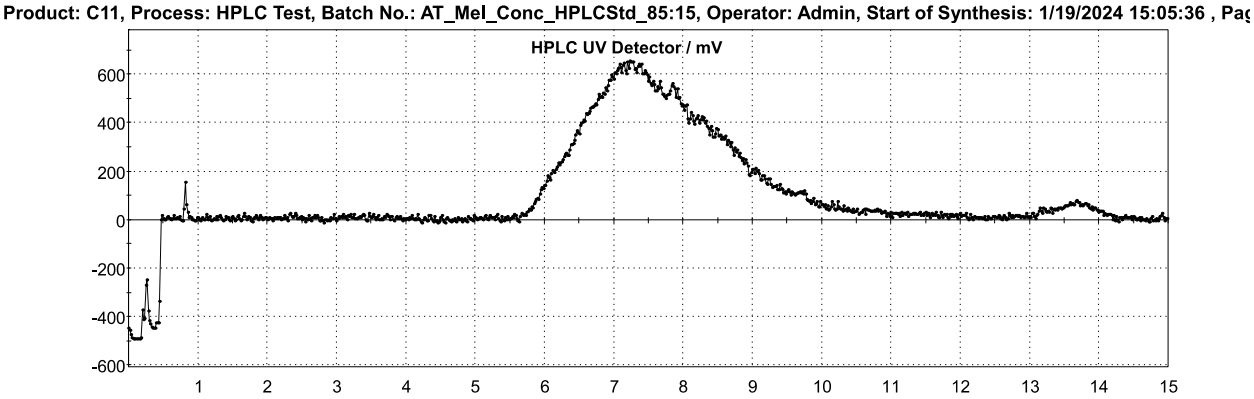

Figure S93. UV Chromatogram for cold-standard for methyl iodide, methanol, and methyl triflate mixture on Semi-Prep RadioHPLC, with similar retention times.

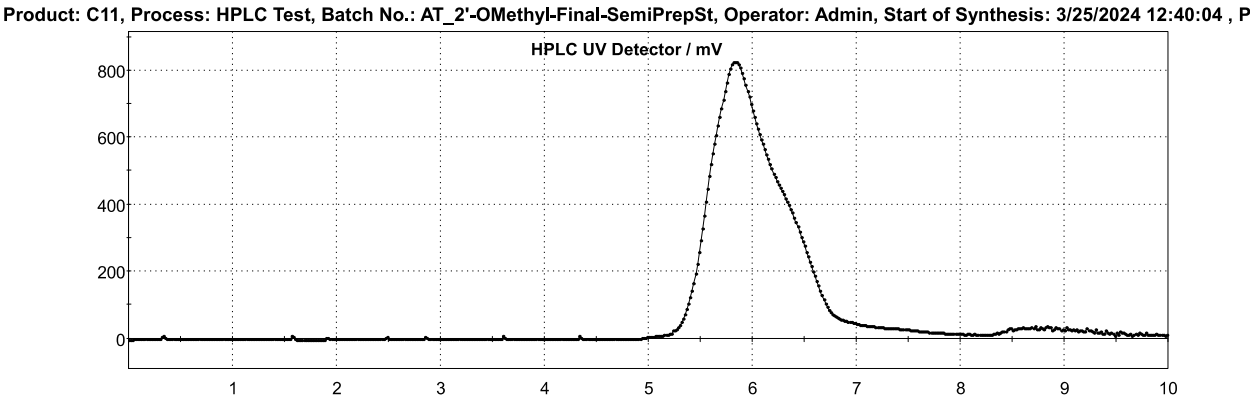

Figure S94. UV Chromatogram for cold-standard 2'-*O*-methyl pyridoxine (32) on Semi-Prep RadioHPLC.

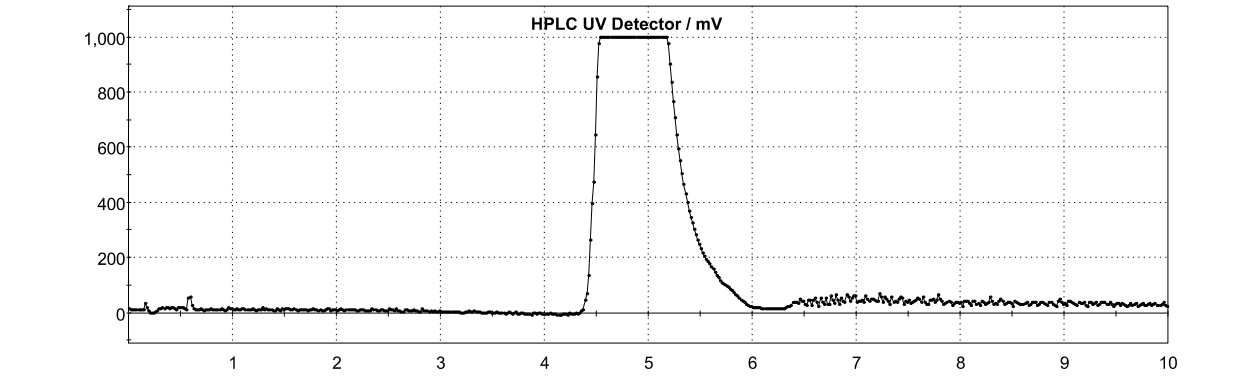

Figure S95. UV Chromatogram for cold-standard 4'-*O*-methyl pyridoxine (38) on Semi-Prep RadioHPLC.